Modeling and unsteady simulation of turbulent multi-phase flow including fuel injection in IC-engines

Vom Fachbereich Maschinenbau
an der Technischen Universität Darmstadt
zur
Erlangung des Grades eines Doktor-Ingenieurs (Dr.-Ing.)
genehmigte

Dissertation

vorgelegt von

MSc. Kaushal Prasad Nishad

aus Akoli (Durg), Indien

Berichterstatter:	Prof. Dr.-Ing. Johannes Janicka
Mitberichterstatter:	Prof. Dr. habil Amsini Sadiki
Mitberichterstatter:	Prof. Dr. habil Eva Gutheil
Tag der Einreichung:	11. Dezember 2012
Tag der mündlichen Prüfung:	14. Februar 2013

D-17, Darmstadt 2013

Hiermit erkläre ich an Eides Statt, dass ich die vorliegende Dissertation selbstständig verfasst und keine anderen als die von mir angegebenen Hilfsmittel verwendet habe. Ich erkläre außerdem, dass ich bisher noch keinen Promotionsversuch unternommen habe.

Kaushal Prasad Nishad

Darmstadt, den 11. Dezember 2012

" There is an eternal struggle going on between destiny and human endeavour. Let us continue to endeavour and leave the results to God."
(M.K. Gandhi, 16-03-1945)
" The failures are the good starting point for the future success."
(Anonyms)

Acknowledgements

The present PhD thesis is a scientific work carried out at the Institute of Energy and Power-plant Technology and Graduate School of Computational Engineering, Technische Universität Darmstadt. This work is supported by the 'Excellence Initiative' of the German Federal and State Governments and the Graduate School of Computational Engineering at Technische Universität Darmstadt.

First of all, I would like to thank my supervisor, the head of the institute Prof. Dr.-Ing. Johannes Janicka, for giving me opportunity to carry out my PhD program and for providing optimum work conditions. I also would like to thank Prof. Dr. habil. Amsini Sadiki for his regular guidance and constant encouragement throughout my PhD. His pesistent enthusiasm and patience have been a source of inspiration throughout the course of this work. I would also like to extend my deep gratitude to Prof. Dr. habil. Eva Gutheil from Interdisciplinary Center for Scientific Computing, Heidelberg University, Germany, for her interest in my thesis work and for agreeing and taking over the referee task.

I am grateful to the head of Graduate School of Computational Engineering Prof. Dr. rer. nat. Michael Schäfer for providing me excellent infrastructure and resources to carry out my research and numerical simulation. I would also like to thank Prof. Dr.-Ing. Reinhold Kneer, Institute of Heat and Mass Transfer, RWTH Aachen University, Germany, for providing experimental data in the early stage of my research. I also appreciate the fruitful technical interaction with Dipl.-ing. Philipp Pischke.

I would like to thank Pradeep, Lukas, Wahid, Anna, Amir, and Fernando for their friendship and useful discussions, suggestions as well as technical and moral support during my stay in Darmstadt. Special thanks to my colleagues Dmitry, Thomas, Chao, and Matteo for their technical help related to KIVA, with whom I had very good teamwork throughout my scientific work including a very good cooperation and useful professional discussions.

A lot of thanks to my family especially my dear wife Chandrakanta for having so much patience and faith in me, while providing enough time and environment by taking care of other tasks by her own so that I could devote much of the time and energy to reach my goals in my life. I would also like to acknowledge the presence of my lovely son Kshitij, whose adorable smile and activities provided a new way of happiness in my daily life.

Darmstadt, December 2012
Kaushal Nishad

Abstract

In internal combustion engine (ICE), researchers have to face with stringent environment regulations concerning pollutants while improving engine thermal efficiency, making the engine design a complex task. To meet these requirements, an understanding of the salient features of all the engine processes are very important. Being the primitive process of engine operations, fuel injection influences whole engine cycle via fuel-air mixture preparation, thereby the combustion behavior and subsequently the emission performance. The inhospitable environment inside a combustion chamber makes the experimental investigations more complex and expensive. In contrast, a CFD based investigation can provide comprehensive insight about in-cylinder flow field, spray injection phenomena as encountered in IC-engine.

In the present study, a CFD tool that enables to investigate the real unsteady behavior of realistic engine configuration is developed by coupling Large Eddy Simulation (LES) together with a spray module using the KIVA4-mpi Code. It is based on an Eulerian-Lagrangian framework to describe the spray evolution including primary and secondary atomization. A linear instability sheet atomization (LISA) based sub-model is integrated to represent the primary atomization. The secondary atomization is modeled by an available Taylor analogy break-up (TAB) model. In dense spray region, the droplet-droplet interaction considerably influences the overall spray dynamics. The first novelty of the proposed methodology is to include droplet-droplet interaction processes via an appropriate collision sub-model that is independent of mesh size and type. Thereby, taking account of different regimes, such as bouncing, separation, stretching separation, reflective separation and coalescence. The formation of wall film on hot cylinder surface is a critical process in an IC-engine, since it largely influences the engine performance and emission characteristics. The second novelty of this spray module is the implementation of an improved wall film model that includes the combined effects of droplet kinetic energy and wall temperature into KIVA4-mpi code.

To perform an IC-engine simulation, a good quality mesh generation in ICEM-CFD for an engine geometry is challenging task. The KIVA4-mpi is compatible only with block structured mesh without any use of O-grid. Due to this reason, only certain degree of mesh refinement is possible. This makes it difficult to achieve a good quality fine mesh required for LES simulation. In the present study, a new meshing strategy is proposed to generate suitable mesh for real IC-engine configurations. The new method clearly demonstrates the improvement in resolving the in-cylinder flow structures. First, the simulated results for motored case (no fuel injection and no combustion) are compared with the experimental data for a transparent combustion chamber (TCC) engine configuration from Engine Combustion Network (ECN). Second, to demonstrate the importance of fuel injection sub-models, further simulations are carried out including the evolution of evaporating fuel spray with wall impingement. Third, using the new meshing strategy, simulations are also performed for a real complex canted 4-valve engine configuration. Simulated results are compared well with available experimental data.

Kurzfassung

Bei der Entwicklung von Verbrennungsmotoren sind Forscher mit der komplexen Aufgabe konfrontiert, strenge Schadstoffauflagen mit der Verbesserung des Motorwirkungsgrades zu kombinieren. Um diesen Anforderungen gerecht zu werden, ist das Verständnis aller wesentlichen Merkmale des Verbrennungsprozesses von nöten. Der Prozess der Kraftstoffeinspritzung geht allen anderen vorraus und beeinflusst damit den gesamten Motor-Zyklus, von der Luft-Kraftstoff-Gemischbildung über die Verbrennung bis hin zum Emissionsverhalten. Die extremen Bedingungen innerhalb der Brennkammer macht die experimentelle Untersuchung komplex und teuer. Im Gegensatz dazu gibt eine CFD (Computational Fluid Dynamics) basierte Untersuchung umfassend Aufschluss über das Strömungsfeld und die Phänome der Verdampfung wie sie in Verbrennungskraftmaschinen auftreten.

In der vorliegenden Arbeit wird ein auf KIVA4-mpi aufbauendes CFD-Programm vorgestellt, das die Analyse des instationären Verhaltens von realistischen Motorkonfigurationen mittels Large Eddy Simulation (LES) und einem Spray Modul erlaubt. Das Programm beschreibt die Entwicklung des Spray über einen Euler-Lagrange Ansatz und berücksichtigt dabei den primären und sekundären Zerfall der Tropfen. Das Modell für den primären Tropfenzerfall basiert auf dem LISA Submodell (Linear Instability Sheet Atomization) wohingegen der sekundäre Tropfenzerfall über das TAB-Modell (Taylor Analogy Break-up) abgebildet wird. In Bereichen mit hoher Tropfenkonzentration hat die Tropfen-Tropfen-Interaktion einen starken Einfluss auf das dynamische Gesamtverhalten des Sprays. Die erste Neuerung der vorliegenden Arbeit ist die Beschreibung der Tropfen-Tropfen-Interaktion mittels eines Kollisions-Submodells, das unabhängig von Feinheit und Struktur des Rechennetzes arbeitet. Berücksichtigt werden dabei unter anderem elastischer Stoß, Zerfall, verformter Zerfall, reflektierter Zerfall und die Vereinigung von Tropfen (Koaleszenz). Die Bildung des Wandfilms an der heißen Zylinderoberfläche ist ein kritischer Prozess in einem Motor, da er dessen Leistung und Emissionsverhalten beeinflusst. Die zweite Neuerung bezieht sich auf ein verbessertes Wandfilm-Modell, das die kombinierten Effekte von kinetischer Energie der Tropfen und Wandtemperatur in den KIVA4-mpi Code berücksichtigt.

Bei der Durchführung von Simulationen in Verbrennungsmotoren ist es wichtig ein Rechennetz mit hoher Qualität zu erzeugen. Zur Netzgenerierung der Motorgeometrie wurde in der vorliegenden Arbeit das Programm ICEM-CFD verwendet. Da KIVA4-mpi nur mit block-strukturierten Netzen ohne “O-Grid” angewendet werden kann, ist eine Netzverfeinerung nur bis zu einem gewissen Grad möglich. Dieser Sachverhalt macht es schwierig ein ausreichend feines Netz zu erzeugen, dass die Anforderungen der LES erfüllt. In der vorliegenden Arbeit wird eine neue Vernetzungstrategie vorgeschlagen, die es erlaubt geeigente Netze für Verbrennungsmotoren zu erzeugen. Die neue Methode ermöglicht eine deutlich bessere Auflösung des Strömungsfeldes im Brennraum. Dies wird verdeutlicht an, erstens, dem Vergleich von Simulationsergebnissen für den Fall ohne Krafteinspritzung und ohne Verbrennung mit experimentellen Daten eines transparenten Brennraums vom Engine Combustion Network (ECN). Zweitens wird durch weitere Simulationen der Entwicklung von verdampfendem Kraftstoffspray und der Interaktion mit der Wand die Bedeutung des Einspritzvorgangs herausgestellt. Drittens wird mittels der neuen Vernetzungsstrategie ein realistischer Verbrennungsmotor mit vier Ventilen abgebildet. Die Simulationsergebnisse werden mit den zur Verfügung stehenden experimentellen Daten gut verglichen.

Contents

List of Figures

List of Tables

Nomenclature

Latin symbols

A_0	$-$	Dimensionless constant
B_M	$-$	Spalding mass transfer number
B_T	$-$	Spalding heat transfer number
C_c	$-$	Coefficient of contraction
C_d	$-$	Discharge coefficient
C_D	$-$	Drag coefficient
C_S	$-$	Smagorinsky model parameter
c	$-$	Arbitrary constant
c_p	$J/(KgK)$	Specific heat capacity by constant pressure
d	m	Droplet dimesion
D_D	m	Particle diameter
D_n	m	Nozzle dimesion
$\vec{F}$	m/s^2	Droplet acceleration term
$\vec{F}^s$	$kg/s^2\dot{m}^2$	Rate of change of unit volume due to spray
f	$-$	Probability distribution function
g	m/s^2	Gravity
h	$kg/s^2\dot{m}^2$	Enthalpy
$\mathbf{I}$	$-$	Unit tensor
$\vec{I}$	$kg/s^2\dot{m}^2$	Specific internal energy
$\vec{J}$	kg/s^3	Heat flux vector
J_w	kg/s^3	Wall heat flux
K	$-$	Wall impingement parameter
K_{cav}	$-$	Cavitation parameter
K_{th}	J/smK	Thermal conductivity
K_n	$-$	Knudsen number
k	m^2/s^2	Turbulent kinetic energy
L	m	Characteristic length scale
Oh	$-$	Ohnesorge number
Pr	$-$	Prandtl number
R	$J/(kg.K)$	Universal gas constant
$\Re$	m/s	Rate of change of droplet radius
Re	$-$	Reynolds number

Re_p	$-$	Reynolds number based on piston speed
Sh	$-$	Sherwood number
St	$-$	Stokes number
T	K	Temperature
t	s	Time
T_t	s	Turbulent time scale
u_p	m/s	Piston speed
u, v, w	m/s	Cartisian velocity components
V	m^3	Volume
W	kg/mol	Molecular weight
We	$-$	Weber number
$\vec{x}$	m	Position vector
x, y, z	m	Cartesian coordinates

Greek Symbols

σ	N/m	Surface tension
σ_{cav}	$-$	Cavitation number
σ_{icav}	$-$	Cavitation inception number
ρ	kg/m^3	Density
η_k	m	Kolmogorov length scale
μ	$Pa-s$	Dynamic viscosity
ν	m^2/s	Kinematic viscosity
λ_{free}	m	Mean free path
σ_{icav}	$-$	Cavitation inception number
ρ	kg/m^3	Density
ϵ	m^2/s^3	Turbulent kinetic energy dissipation rate
λ_{free}	m	Mean free path
τ	s	Time scale
τ_{ij}	m^2/s^2	Subgrid stress tensor

Operators

∞	Infinity
$\mathbf{J}$	Flux vector
$\mathbf{I}$	Unit dyadic
δ	Dirac delta function

Subscripts

l	Liquid
g	Gas
m	Species

i	Integral length scale
τ	Taylor length scale
k	Kolmogorov length scale
i, j, k	Coordinate directions
$coll$	Collision
$mean$	Averaged quantity
n	Normal component
vap	Vapor

Superscripts

s	Source term due to spray
c	Source term due to chemistry

Abbreviations

ALE	Arbitrary Lagrangian-Eulerian
$ATDC$	After top dead centre
BDC	Bottom dead centre
CA	Crank angle
CAD	Computer-aided design
CFD	Computational fluid dynamics
CFL	Courant-Friedrichs-Lewy
CO	Carbon mono-oxides
CO_2	Carbon di-oxides
CPU	Central processing unit/processor
CV	Control volume
DDB	Droplet deformation break-up
DDM	Descrete droplet method
DI	Diesel injection
$DISI$	Direct injection spark ignition
DNS	Direct numerical simulation
$DSMC$	Direct simulation monte carlo
$ETAB$	Enhanced Taylor anlogy break-up
GDI	Gasoline direct injection
HC	Hydrocarbon
IC	Internal combustion
ICE	Internal combustion engine
KH	Kelvin-Helmholtz
LCV	Laser correlation velocimetry
LDA	Laser doppler anemometry
LES	Large eddy simulation
$LISA$	Linear instability sheet atomization

NO_x	Nitrogen oxides
PDA	Phase doppler anemometry
PIV	Particle image velocimetry
$RANS$	Reynolds averaged Navier-Stokes
RMS	Root mean square
RNG	ReNormalised group
RPM	Revolution per minute
SGS	Subgrid-scale
TAB	Taylor anlogy break-up
TDC	Top dead centre
$URANS$	Unsteady RANS

1 Introduction

1.1 Motivation

In the recent time and near future, the ever increasing demand of internal combustion engine (ICE) for the transport carrier vehicles and continuously depleting fuel resources together with stringent regulation calls for environmentally compatible and economical engines. This requires a complex trade among the stringent regulations concerning pollutants, fuel consumption, engine thermal efficiency and wheel power output. The only ways forward would be either to look for the alternative fuels such as bio-diesel, bio-alcohol (methanol, ethanol, butanol), chemically stored electricity (batteries and fuel cells), hydrogen, non-fossil methane, non-fossil natural gas, vegetable oil, and other biomass sources or to make the automobile more energy efficient or to use hybrid vehicle. Figure 1.1 represents the current trend in vehicle demand suggesting the upward rise of vehicle demand in future, while Figure 1.2 displays the current and projected usage of transport fuel. It clearly appears that the conventional fuels such as diesel and gasoline contribute to maximum shares even in the future, although the recent advances are being made for alternative fuels. To minimize the fuel consumption, intensive research is being devoted to make the future automobile more fuel efficient (see Figure 1.3). All these trends and expectations require to develop innovative engine designs and investigations of IC-engine performance. To this purpose, the detail understanding of salient features of all possible engine operations and underlying physical phenomena are very essential. The experimental method is one of the fool-proof technique to carry out engineering analysis and subsequently design modifications on the engine. However, it often encounters challenges of high installation cost, overall design time line involved and sometime access limitations. An inhospitable condition such as high pressure, temperature, remnant of soot and combustion products inside engine make it sometime infeasible to carry out detail measurement on realistic IC-engine configurations. Therefore, a computational fluid dynamic (CFD) investigation is good candidate in tandem with experiment to provide very good insight of all physical phenomena occurring inside the engine [3]. Thereby, the experimental results are always necessary to provide good benchmark for validation of adopted CFD methodology. Once the CFD tool has been validated, it can be used as a very useful design tool that supports various parametric studies to achieve the optimum design parameters. This way considerably reduces the overall designing cost and time line while providing detailed early design information.

In internal combustion engine, considering all the physical phenomena involved such as valve and piston movements, transient intake and exhaust port opening, fuel injection, fuel evaporation, mixture formation, ignition, combustion and reaction makes a CFD simulation a highly complex and challenging task. To be able to represent the real behavior of an IC-engine all the relevant numerical models have to be capable enough to address real nature of all ongoing physical processes. In the case of gasoline direct injection (GDI) engines, mixture formation pattern varies from the lean to reach mixture and stratified to homogeneous mixture depending upon different engine status and loading conditions. However, the mixture formation is predominantly determined by the fuel injection. Therefore, fuel injection is a vital process for fuel-air mixture preparation under varied engine conditions. Very often during the intake charge of fresh air, fuel is injected, which gets evaporated and prepares fuel-air mixture for subsequent combustion in power stroke. In the case of diesel engine the fuel is directly injected into combustion chamber with elevated pressure and temperature. The injected fuel evaporates by picking up the heat from surrounding air and a heterogeneous fuel-air mixture forms which ultimately undergoes combustion due to self-ignition. Thus being the primitive process of engine operations, the fuel injection process influences the whole engine cycle via fuel-air mixture preparation along-with the combustion behavior and subsequently the emission performance of an IC-engine.

The fuel injection process is a multi-physic and multi-scale flow phenomena in nature. The high speed fuel injected in combustion chamber undergoes primary and secondary atomization. The movements of many individual fuel droplets and their interaction with the fluid flow is very vital for mixture formation and for ultimate combustion and emission results. The flow turbulence changes considerably the spray dynamics via the droplet dispersion, heat and mass transfer between fluid and particulate phase. The droplets can interact themselves as the fuel injection is generally a dense spray flow process. The situation becomes more complicated when the droplets that have not changed their physical state enters into the combustion zone. They are heated and ignited releasing hot combustible gases that burn in the gas phase. The rate of modification of physical state from liquid to gaseous phase (rate of droplet evaporation), as well as droplets spatial distribution and injection characteristics are key parameters for fuel-air mixture preparation and homogenization. Together they have particular importance for combustion.

In the context of a combustion chamber design, an accurate determination of droplet and vapor spatial distribution and a reliable control of the interaction between the spray with the surrounding turbulent gas flow are prerequisites. If the mixing of air and fuel is not perfect then there will be partially unburnt fuel. Obviously, the mixture greatly affects the efficiency of the energy extraction. If the mixture does not have enough oxygen present during combustion, it will not burn completely [3]. When combustion takes place in an oxygen starved environment, the present oxygen will be insufficient to fully oxidize the carbon atoms into carbon dioxide (CO_2), instead carbon monoxide (CO) will be formed. Controlling the mixture of fuel and air contributes to the reduction of the exhaust gaseous emission.

With respect to the design, an IC-engine has generally complex geometry with varying shape of cylinder head, piston crown, valve surface, intake and exhaust port. Since the engine geometry greatly influences the in-cylinder flow behavior, all shapes and contours are designed mainly to achieve optimum flow conditions (such as flow turbulence, in-cylinder tumble and swirl motion). The engine swirl is characterized by the formation of vortex along the cylinder axis, and it is important to prepare the homogeneous mixture fraction during the injection process. Similarly, the tumble motion is characterized by the flow vortex formation along the axis other than cylinder axis. It is very important for the ignition process, and subsequently for the flame propagation inside the combustion chamber. However, excess tumble motion can lead to mis-fire as a finite time is associated for reaction to take place.

The experimental investigation of fuel spray is generally carried out for stationary case (no moving piston and valves) with varying cylinder conditions due to the convenience in measurement technique [4]. In real configuration when the piston and valves are in motion, the spray dynamic changes considerably, while the high speed intake air interacts with the evolving spray jets, and often the experimental investigation becomes complex and expensive. On the contrary CFD based investigations provide comprehensive insight about in-cylinder flow field, spray injection phenomena and subsequent processes such as droplet dispersion, evaporation, mixture formation and combustion. It has been observed that the in-cylinder flow varies from one cycle to another, making the consideration of cycle-to-cycle variations very important in performing detail analysis of any IC-engine. These cyclic fluctuations can sometime lead to combustion failure caused by excessive tumble motion and results in total loss of energy in full load conditions and subsequently ejection of unburnt hydrocarbon to environments.

In order to understand the cycle-to-cycle variations, their nature, origin and their impact on the flow and mixing field within a combustion chamber, and to create a reliable basis for further studies including combustion, it is essential that the CFD code should be updated with spray sub-models that integrate an appropriate fuel injection description.

The present work is dedicated to develop and integrate an advanced fuel injection model into the KIVA4-mpi code. This code enables to perform simulations in multiple processors (parallel computations). Therefore it allows for performing multi-cycle engine simulations even for larger geometry with substantially refined mesh. However, generating mesh for a detailed IC-engine configuration for KIVA4-mpi code is a difficult task. Similar to KIVA-3V [5], the new version accepts only hexahedral mesh without O-grid for moving mesh. Hence the geometric flexibility is lost that makes it difficult to generate fine mesh. This limitation considerably reduces its applicability to perform CFD analysis in an engine with complex piston, cylinder head shape and ports with multiple canted valve and hence the extra feature of parallel computations is not fully exploited. Therefore, it is important to search for a new meshing strategy to generate fine mesh, which should be compatible with the KIVA4-mpi code. Furthermore, the original code only includes RANS-based flow description. Dealing with highly unsteady phenomena, the large eddy simulation (LES) method should be appropriate. Various research works have proven the potential of LES to deal with highly unsteady and complex phenomena accurately [5]-[9]. However, the integration of fuel injection model with IC-engine simulation in LES context in the framework of Euler-Lagrange method is new. To dwell on these issues motivates the present work.

1.2 Thesis outline and structure

In chapter two, fundamentals of all important physical phenomena relevant to fuel injection process in IC-engine applications are provided starting from the flow inside the nozzle to the spray impinging on the engine cylinder wall. These phenomena are namely the nozzle flow, cavitation, spray atomization (primary and secondary atomization), collision-coalescence, and spray wall interaction. The correlation parameters are described for each phenomena, from which various characterization and classification can be proposed to demarcate various regimes.

In third chapter, an overview of the relevant investigations that have been already carried out is highlighted. The mathematical models are reviewed with their merits and deficiencies, and the overall objective of the present work is outlined in this respect.

In chapter four, mathematical models adopted in this work are presented. The respective model improvements and novelties of this work are described in chapter five. In the context of KIVA4-mpi framework, to carry out LES analysis with real engine configuration necessitates the generation of requisite refined mesh. A detail description of new meshing strategy is provided in chapter six. This new technique is tested for two engine configurations that are described in the next chapters.

In chapter seven, the numerical configuration is described including all the relevant fuel injection sub-models. The improvements of individual models are validated for various spray parameters in terms of nozzle exit velocity, droplet size distribution, spray penetration depth and spray structures.

The ultimate scope of the present work is to integrate all the models for a real IC-engine description. In chapter eight, simulations are carried out for a real IC-engine configuration having relatively simple geometry with two-parallel valves and easy port shape. It features transparent combustion chamber (TCC) for visual access to perform various experimental measurements. Investigations are carried out for cold cases (with and without fuel injection) for relatively higher number of engine cycles. Thereby achievements are reported with respect to the adapted new meshing strategy, and results are shown in terms of in-cylinder flow behavior, fuel injection and fuel-air mixture formation.

To further demonstrate the applicability of the new meshing strategy and to perform CFD analysis in complex IC-engine configurations, an IC-engine configuration (Karlsruhe configuration) with 4-canted valve and complex port shape is studied in chapter nine. The results are compared with the experimental data available, and a detail analysis is performed providing more insight into the ongoing process.

Chapter ten summarizes the important and relevant findings of the present doctoral thesis, and provides an outlook outlining the scope of future work.

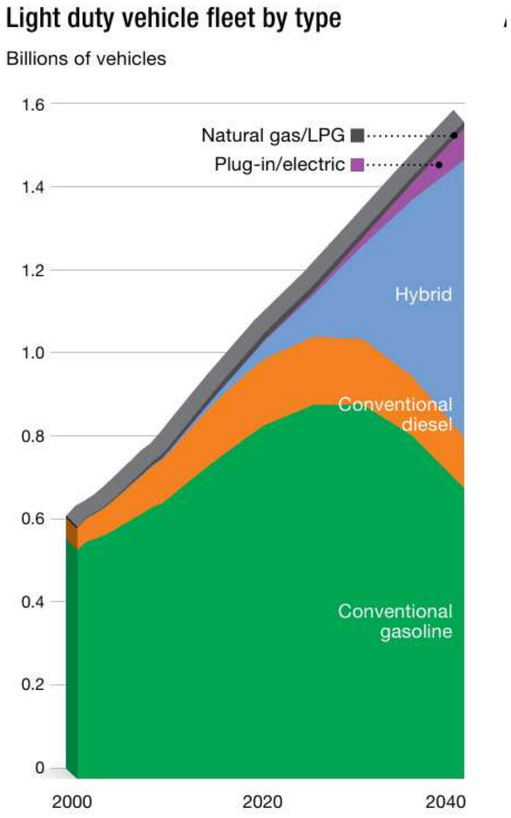

Figure 1.1: Projection of transport vehicle demand (The Outlook for Energy: A View to 2040 [1])

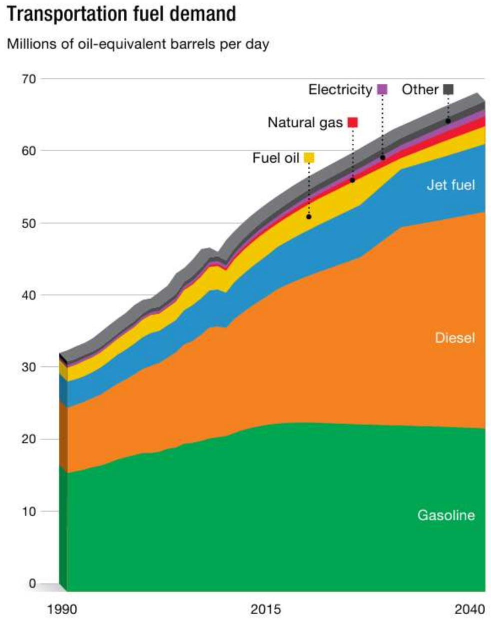

Figure 1.2: Projection of transport fuel demand (The Outlook for Energy: A View to 2040 [1])

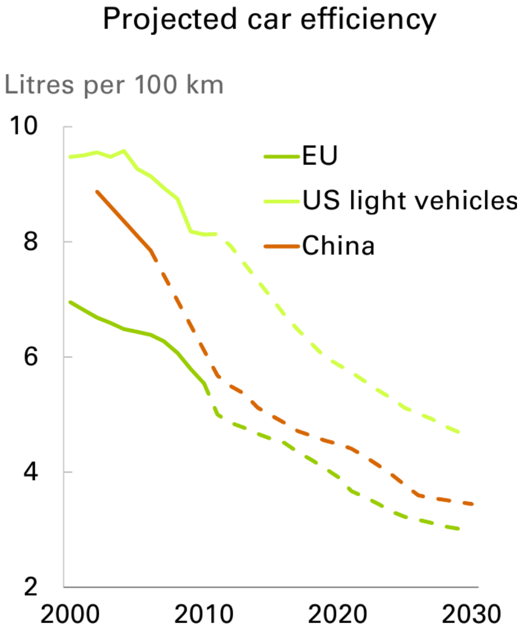

Figure 1.3: Passenger car fuel economy (source: Energy outlook 2030 ©BP 2012 [2])

2 Fundamentals of spray dynamic

2.1 Liquid spray and fuel injection

A spray is a cloud of dispersed droplets present in gas. The formation of droplets is generally termed as atomization process and the spray nozzle is a device used to generate spray. The main objective of the spray is to provide required distribution of liquid over given volume and cross-section by simultaneously increasing liquid surface area. In the present context of internal combustion engine, fuel injector is used to develop spray inside engine combustion chamber to form a required fuel-air mixture fraction, that will subsequently burn and generate power. The spray dynamic is very critical because the large surface area of a finely atomized spray enhances fuel evaporation rate, while dispersion of the fuel into the combustion chamber is critical for fuel distribution. In this way an optimum spray dynamic maximizes the efficiency of IC-engines and reduces the pollutants emission (soot, NOx, CO). Figure 2.1 is a pictorial depiction of a fuel spray. The complete injection process can be classified on the basis of spatial regime, such as flow inside the nozzle, primary atomization close to nozzle exit, further downward as a secondary atomization, and wall impingement. In mean time, based on the spray density, it can be also defined as dense and dilute spray. Inside the nozzle, the flow is highly transient in terms of velocity and mass discharge, where flow turbulence and cavitation is important. In the primary breakup region, the intact liquid core dis-integrate into ligaments of size comparable to nozzle diameter, these ligaments further breakup into droplets of similar order. Further downstream in secondary atomization, the already formed droplets further breakup into smaller droplets and in same time more and more surrounding gas/air entrain into spray area resulting in dispersion of the spray profile. In the dense spray the droplet-droplet interaction is vital parameter to consider, while in dilute region spray-gas interactions (drag, evaporation and fuel-air mixture formation) is essential. The length from the nozzle exit to the farthest droplet is called spray penetration depth, that signifies the ability of spray to reach in the required engine volume.

In this chapter, the fundamentals of the fuel spray will be provided, including the flow inside nozzle with susceptibility of cavitation. The dynamics of spray atomization with relevant break up regime will be discussed, then various possibilities of droplet-droplet interaction will be presented and finally the interaction of spray with heated wall and subsequent dynamics will be outlined.

2.1.1 Nozzle flow and cavitation

In general, the nozzle flow considerably affects the atomization behavior and thereby the complete spray dynamics. The fuel is injected in combustion chamber *(1-30 bar)* with injection pressure ranging from *50-200 bar*, in certain cases the injection pressure can go up to *2000 bar*. With such a huge pressure gradient across the fuel injector orifice, the fuel gains considerably high velocity

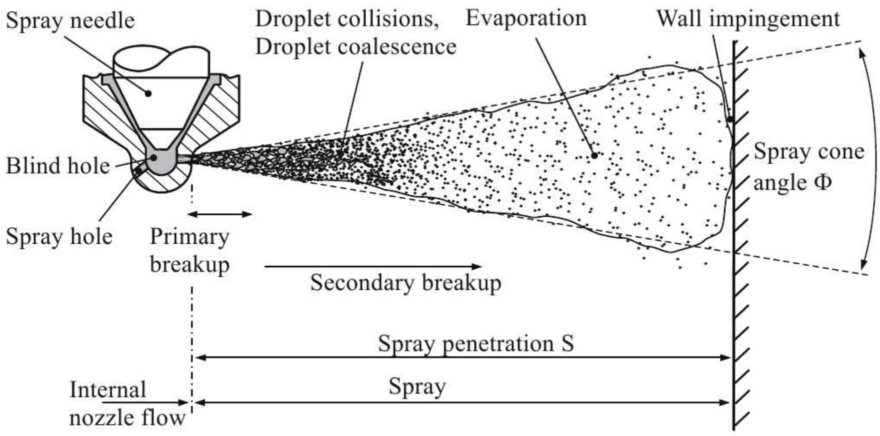

Figure 2.1: Schematic of fuel spray depicting relevant physical phenomena [3]

(hundreds of m/sec) in short distance (few millimeter) with large coefficient of contraction near the nozzle orifice. These lead to formation of the low pressure zone inside the nozzle hole. Depending on the fuel being used, fuel temperature and vapor pressure, gas pockets developed inside the nozzle cavity due to vaporization of the fuel. While many complicating factors are responsible for the formation cavitation, it is useful to adopt simplest correlation for the purpose of initial discussion. In practice, this can also provide a crude initial guideline. Traditionally, several special dimensionless parameters are utilized in evaluating the potential for cavitation. Perhaps the most fundamental of these is the cavitation number, σ_{cav}, defined as

$$\sigma_{cav} = \frac{(p - p_v)}{\frac{1}{2}\rho U^2} \tag{2.1}$$

Clearly, every flow has a value of σ_{cav} whether or not cavitation occurs. There is, however, a particular value of σ_{cav} corresponding to the particular inlet pressure, p_{CA}, at which cavitation first occurs as the pressure is decreased. This is called the cavitation inception number, and is denoted by σ_{icav}:

$$\sigma_{icav} = \frac{[(p)_{CA} - p_v]}{\frac{1}{2}\rho U^2} \tag{2.2}$$

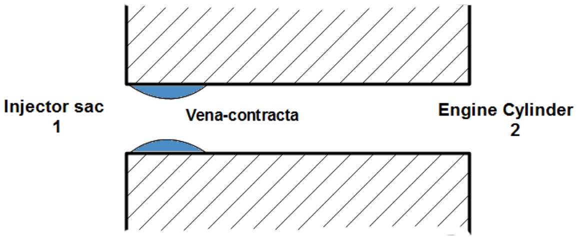

Figure 2.2: Schematic of nozzle flow with vena-contracta

Numerous experiments have been performed to correlate the cavitation parameter and coefficient of discharge. Figure 2.3 features a log-log plot of the coefficient of discharge versus the cavitation parameter.

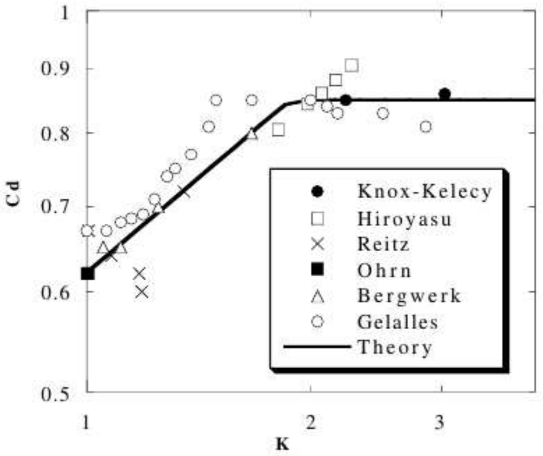

Figure 2.3: Experimental coefficient of discharge versus cavitation parameter (see the reference [10])

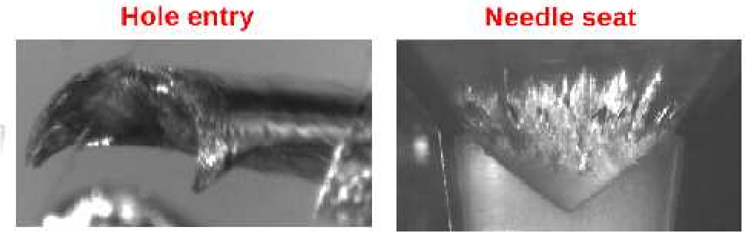

Figure 2.4: Experimental visualization of cavitation in transparent nozzle [11]

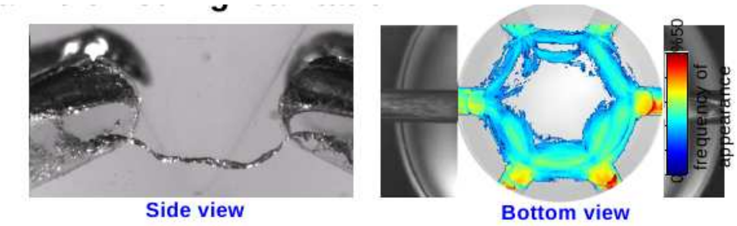

Figure 2.5: Cavitation probability: The transient nature of cavitation [11]

Several variations in the definition of cavitation number occur in the literature with respect to its application in different hydraulic appliances. In the case of injector nozzle the cavitation bubble forms because of the very low static pressure in high speed nozzle flow near a sharp orifice corner (e.g. a corner with a zero radius of curvature). The sharper the corner and the higher the velocity, the more likely cavitation is to occur. In the case of a sharp inlet, where the flow separates at the corner, the flow experiences a vena contracta. A diagram of the sharp entrance flow is shown in Figure 2.2. The formation of vena contracta reduces the effective flow area and thus the mass flow rate. The property C_d is called a coefficient of discharge and represents the efficiency of nozzle

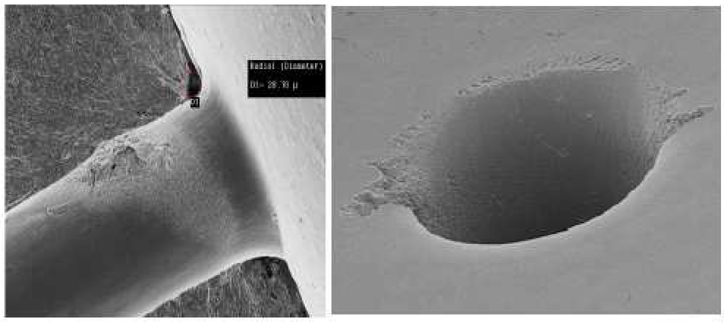

Figure 2.6: Cavitation damage at the nozzle orifice [12]

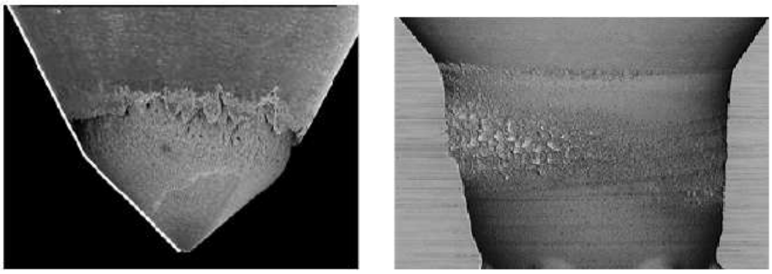

(a) **(b)**

Figure 2.7: Cavitation damage at the needle and sac wall [12]

between the points 1 and 2, and represented by:

$$C_d = \frac{\dot{m}}{A\sqrt{2\rho\left(P_1 - P_2\right)}} \tag{2.3}$$

In case of cavitating nozzle the pressure at contraction point can be fixed as vapor pressure P_v, therefore the mass flow rate becomes independent of the back pressure at point 2, and the mass flow rate can be written as:

$$\dot{m} = A_c\sqrt{2\rho\left(P_1 - Pv\right)} \tag{2.4}$$

By considering all the nozzle loss downstream from the vena contracta, the important correlation can be formulated for the coefficient of discharge and the cavitation number as follows:

$$C_d = C_c\left(\frac{P_1 - Pv}{P_1 - P_2}\right)^{\frac{1}{2}}, C_c = \frac{A_c}{A_1} \tag{2.5}$$

$$K_{cav} = \left(\frac{P_1 - Pv}{P_1 - P_2}\right) \tag{2.6}$$

Since the fuel injection is highly transient process and injection duration is generally very short (millisecond), the cavitation dynamics changes in the course of time and location. On one hand formation of the cavitation leads to restriction of the effective surface area of the fuel flow (see Figure 2.2) thus affecting the overall fuel mass delivery to cylinder. On the other hand it also promotes the atomization process by generating cavitation induced turbulence on the exiting fuel stream, which ultimately affects the subsequent spray dynamics by augmenting with the aerodynamics instability on fuel jet and subsequent primary atomization. However, the formation of cavitation makes injection process very much chaotic and unpredictable. Figure 2.4 depicts the location of cavitation in transparent injector, while Figure 2.5 shows the probability of cavitation generation over the time. The cavitation is also detrimental to the injector design as it leads to erosion of nozzle orifice (as shown in Figure 2.6) and nozzle needle/needle-sac (see Figure 2.7)) thus altering the size and shape of nozzle orifice, making it out of order. In practice, cavitation should always be avoided to have predictive injector behavior and longer injector life.

2.2 Liquid atomization

As stated before the atomization is the process of formation of cluster of droplets in gas. The high speed liquid jet with inherent turbulence is ejected from the injector nozzle, due to high relative velocity between the fuel jet and surrounding gas/air, the liquid jet experiences intense aerodynamic instability. These results in further amplification of surface instabilities leading to disintegration of smaller volume in the form of ligaments from liquid core, and these ligaments further fragment into droplets. In general, the surface instability is a combined effect of the momentum force (kinetic energy), pressure force (pressure energy), surface tension (surface energy) and drag force (viscous force). Therefore, atomization behavior is highly dependent on the in-flow conditions (nozzle geometry, injection velocity) and liquid fuel properties (density ρ, viscosity μ, and surface tension σ). For a given application, the fuel to be used is fixed, and by fixing the desired IC- engine configuration, the ambient condition for the injection is mostly defined. The remaining physical parameter, that governs the spray dynamic is the flow field inside the nozzle, that ultimately determines the onset of atomization process and droplet dispersion.

The mechanism of formation of initial droplets from the liquid core is called primary atomization. It is generally characterized by droplet size and breakup length. These droplets further experiences aerodynamics instability and breaks into more smaller droplets. This mechanism is termed as secondary atomization and characterized by droplet size distribution. The atomization process can be visualized by Figures (2.8 and 2.9). The snap shot is taken for the spray emerging in a cross air flow [13].

2.2.1 Primary atomization

In the context of complete spray dynamics, primary atomization is crucial physical phenomena to take into consideration. It triggers the formation of primary droplets from liquid core, hence therefore also determines evaporation behavior and on-set the droplets for further breakup. Altogether, the primary atomization is complex process to analyze both experimentally and numerically. However, the macroscopic parameters such as initial droplet size or break up length can be readily characterized by looking at the spray image. Based on the nozzle exit velocity Reitz and Bracco [14] have classified spray as shown in Figure 2.10.

Figure 2.8: Atomization of liquid jet in cross flow [13]

Figure 2.9: Snap-shot of spray profile [13]

1. Dripping regime (A) : In this regime droplet is directly ejected from the nozzle, the liquid mass is allowed to pass through the nozzle until it reaches the critical mass to be hold by the surface tension force, and subsequently droplet detached from the nozzle under gravitation. The nozzle discharge velocity is extremely low in this case.

2. Rayleigh regime (B) : At slightly higher jet velocity, breakup occur due to antisymmetric oscillations initiated by liquid inertia and surface tension force. At low jet velocities, the growth of long-wavelength, small-amplitude disturbances on the liquid surface promoted by the interaction between the liquid and ambient gas is believed to initiate the liquid breakup process. The driving force of this instability is that, liquid by virtue of their surface tension, always tend to minimize their surface area. If the amplitude is high enough the droplet detaches from the falling liquid columns. In this mechanism droplet diameter has larger scale than the liquid column diameter (nozzle diameter).

3. First wind-induced regime (C): As the jet velocity increases, the surface instability is amplified by the aerodynamics forces acting on the jet surface. This leads to early detachment of the droplet from the jet tip, and thereby decreasing breakup length and resulting droplet sizes in order of the nozzle diameter.

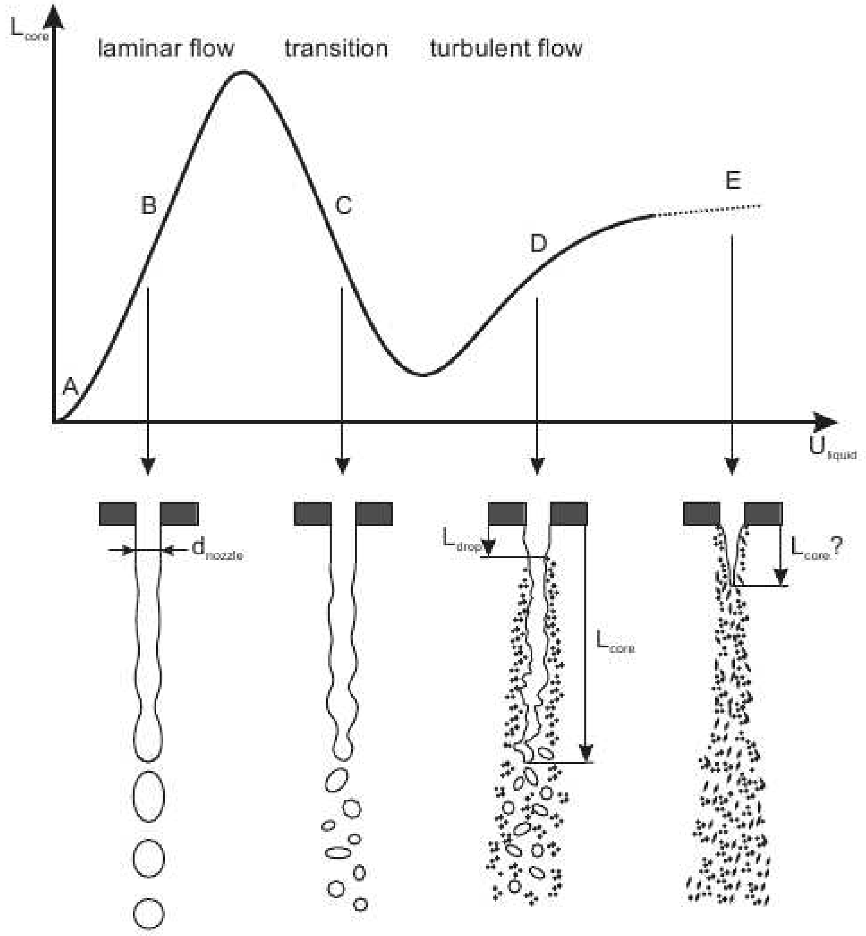

Figure 2.10: Jet stability curve and breakup regimes classified by Reitz and Bracco [14] and illustrated in [15]

4. Second wind-induced regime (D): In this case flow inside the nozzle is turbulent, unstable growth of short wave is further amplified by the aerodynamics forces on jet surface, resulting in stripping of liquid droplets not only in jet tip, but also at the jet surface. The breakup length is considerably reduced and droplet size becomes more finer.

5. Atomization regime (E): This regime is characterized by the formation of the droplet right from the nozzle exit; so the intact liquid core length goes to zero. The droplet diameters are much smaller than the nozzle diameter. The cavitation can be a driving factor in this kind of atomization behavior as it develops cavitation induced turbulence and breakup.

In order to make quantitative classification of different breakup regimes based on the flow parameters and boundary conditions, a relation between viscous force and surface tension force was established by Ohnesorge [16]:

$$Oh = \frac{\sqrt{We_l}}{Re_l}\,, Oh = \frac{\mu_l}{\sqrt{\sigma \rho_l D}} \tag{2.7}$$

The parameter Oh is known as Ohnesorge number, Re_l is Reynold's number, We_l is Weber number, and for given liquid droplet derived as:

$$We_l = \frac{\rho_l u^2 D_n}{\sigma}\,,\; Re_l = \frac{\rho_l u D_n}{\mu_l} \tag{2.8}$$

where u is the jet velocity D_n nozzle diameter. The quantities ρ_l, σ_l, and μ_l represent the liquid density, viscosity, and surface tension, respectively.

As we know from Eqn.(2.8), the Reynolds number is a ratio of the inertial to viscous forces, while Weber number is a ratio of inertial to surface tension forces. This makes the Ohnesorge number Eqn.(2.7) as ratio of the viscous forces and surface tension forces. Clearly all the relevant parameters have been incorporated, so that different breakup regimes can be categorized in a Ohnesorge diagram (see Figure 2.11 Ohnesorge number - Reynolds number). The different regimes are separated by the empirical lines defined by Reitz [16] in ascending order as follows.

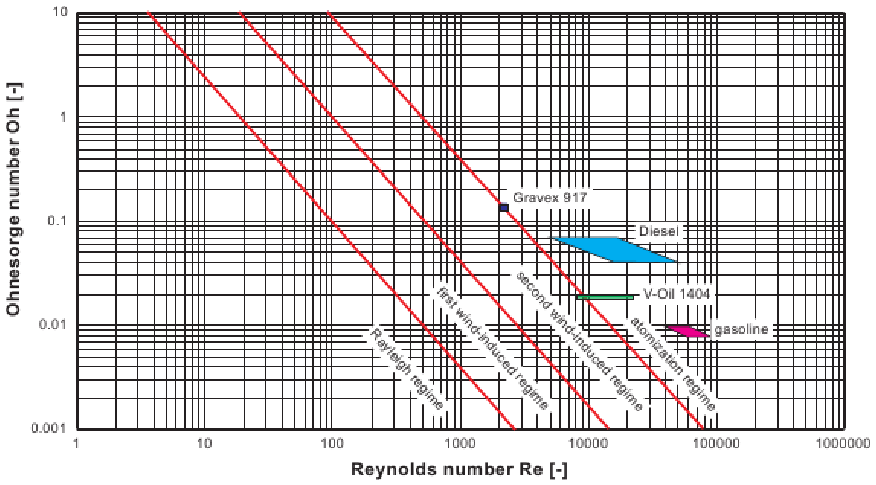

Figure 2.11: Ohnesorge diagram showing the breakup regimes and the operating points of Diesel and gasoline injection as well as for the Gravex-917 and V-Oil measurements [16]

$$Oh = 60{Re_l}^{-1.3971} \qquad Oh = 5750{Re_l}^{-1.3845} \qquad Oh = 4898{Re_l}^{-1.3653} \tag{2.9}$$

It should also be mentioned that, the Ohnesorge diagram does not consider the influence of the surrounding gas (ambient gas density ρ_g, viscosity μ_g) on the breakup process. It has been observed that, increasing the ambient pressure can lead to early onset of spray breakup. This effect can be included in the Ohnesorge diagram if the Ohnesorge number is replaced by following dimensionless number:

$$Z = Oh\sqrt{\frac{\mu_l}{\mu_g} We_g} \qquad We_g = \frac{\rho_g u^2 D_n}{\sigma} \tag{2.10}$$

The underlying physical phenomenon remains the same for atomization process, however in above classification the effect of different nozzles (geometry and shape) is not considered.

The primary atomization mechanism entirely depends upon the types of nozzle in consideration. For example, in case of the single/multi-hole nozzle the high speed fuel comes out as "solid" liquid jet. The large velocity gradient at interface between the liquid jet and surrounding gas/air enhances the surface instability. In case of the hollow-cone injector, the liquid comes out as a hollow thin-liquid sheet, and the thin sheet undergoes aerodynamic instability resulting in droplet formation.

2.2.2 Secondary atomization

The droplets generated from the primary atomization are not small enough to be stable, the secondary atomization is subsequent process, in which these droplets experience aerodynamic forces that are generated by the relative velocity between the droplets and the surrounding gas. This results in deformation of the droplets, while the surface tension forces will counteract to restore the droplets. When the deformation is sufficient enough these droplets fragment into smaller droplets. Similar to the primary breakup, in the case of secondary atomization the Weber number still hold the significance as a relevant dimensionless number for spray characterization. However, in this case, the gas Weber number will represent the real dynamics, with the length scale taken as droplet size d instead of the nozzle diameter D_n.

$$We_g = \frac{\rho_g u^2 d}{\sigma} \tag{2.11}$$

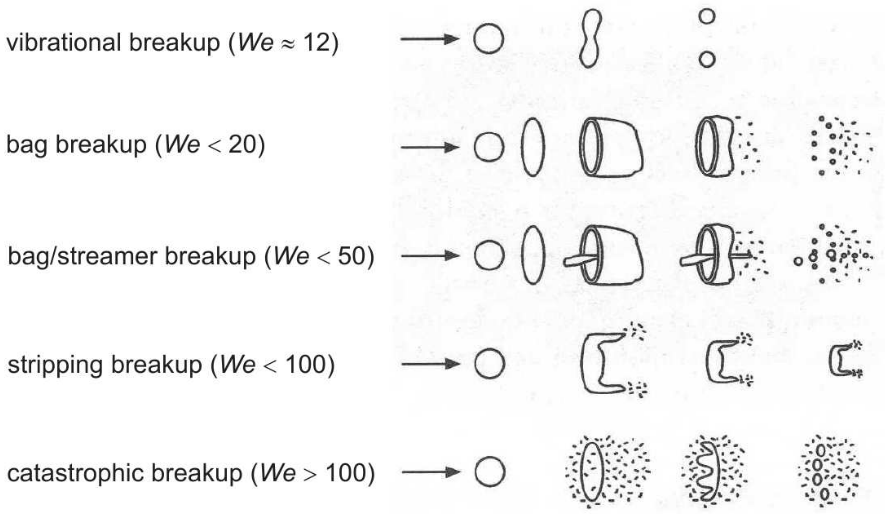

Figure 2.12: Secondary atomization regimes and corresponding transition Weber numbers [16]

Since the order of droplet size is small compared to the nozzle diameter, and the surface tension force will also be high for smaller droplets, a relatively higher velocity and correspondingly large Weber number is required for secondary atomization to take place. Therefore, with the help of the

Weber number We_g, it is possible to characterize the different regimes for the secondary atomization. A schematic representation of the breakup regime is illustrated in Figure 2.12 based on the Weber number, which is relevant to IC-engine application of spray.

2.3 Droplet-droplet interaction

The fuel injection for IC-engine application corresponds to the relatively dense spray phenomena, especially near the nozzle exit. Therefore, there are high probability for droplets to interact with each other. These interaction result in entirely different spray dynamics, as droplets after collision can experience different physical phenomena. It can be broadly classified by two parameters, the collision parameters (value B in Figure 2.13) represent the orientation of two droplets relative to each other, and the representative Weber number We_{coll} of the colliding droplets as described below.

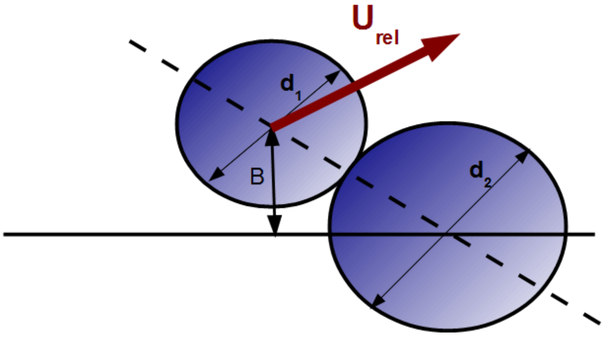

Figure 2.13: Collision parameters: Binary droplet collision

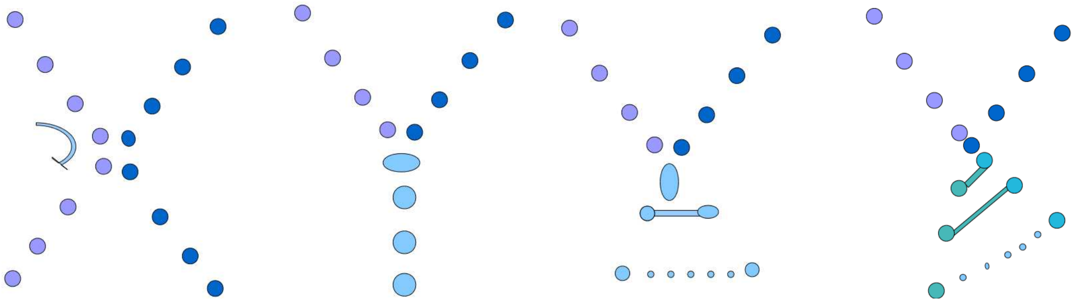

(a) (b) (c) (d)

Figure 2.14: Possible droplet interaction in binary collision (a) droplet rebound (b) coalescence (c) reflexive separation (d) stretching separation

$$We_{coll} = \frac{\rho_l {U^2}_{rel} d_{av}}{\sigma} \; , \; d_{av} = \frac{1}{2}\left(d_1 + d_2\right) \tag{2.12}$$

where U_{rel} is the relative velocity of the two droplets, and d_1 and d_2 are the droplet sizes.

Therefore, based on the various parameters such as diameter, velocity, surface tension and orientation of colliding droplets, different interactions are possible. The droplet-droplet interaction is very complex process, however it can be broadly classified by four mechanisms such as, rebound, coalescence, reflexive separation and stretching separation. In case of droplet rebound, the interacting droplets simply collide with each other and rebound in different directions without exchanging any mass, while in case of the coalescence droplets merge and form bigger droplet. In case of the reflective separation droplets collide head-on with each other and during the course of separation they form satellite droplets from the merged volume, while in case of stretching separation the droplet collide with angle and during separation it forms satellite droplets.

2.4 Spray wall interaction

Spray-wall interaction is considered to be an important physical phenomenon in many engineering applications. Based on the spray application, different dynamics for spray-wall interaction are required. For example, in the case of spray coating and spray painting, smooth and homogeneous thickness of wall film is very much important, while in case of IC-engine application the wall film formation is highly undesirable. The dynamics of spray-wall interaction are also highly dependent on the wall properties, such as rough or smooth wall, wall temperature and film thickness. In case of wall temperature between freezing and boiling temperature, heat transfer has minor influence on the spray impact, Therefore, affect of the temperature on the impact can be dis-regarded, and the possible interaction outcome in mainly droplet deposition and droplet splash. With certain droplet velocity, the droplet spread on the wall and form wall film by loosing part of its kinetic energy in to viscous dissipation and partly on surface tension effect. In case of increased impact velocity, the viscous dissipation in no longer able to absorb the kinetic energy and surface tension is not able to maintain the droplet cohesion and droplet get dis-integrated by splashing. However, depending upon the incident kinetic energy of droplets, spray mass may get partly deposited on surface. The dimensionless number such as Weber number and Reynolds number can be used to characterize spray wall interaction behavior for cold case, where wall temperature is between freezing and boiling point, however the velocity should be taken as normal component to the wall.

$$We_{ln} = \frac{\rho_l {U^2}_n d}{\sigma} \tag{2.13}$$

$$We_{ln} = \frac{\rho_l U_n d}{\mu_l} \tag{2.14}$$

To further characterize the spray wall interaction, the Ohnesorge number can be used to combine the effect of the Weber number and Reynolds number as follows:

$$Oh = \frac{\sqrt{We_{ln}}}{Re_{ln}} = \frac{\mu_l}{\sqrt{\rho_l \sigma_l d}} \tag{2.15}$$

The hot cylinder and piston surfaces are very common in IC-engine application. When the wall temperature is high, the Leiden-frost effect is observed: "the droplet surface in contact with significantly hot wall above Leiden-frost temperature produces an insulating and cushioning vapor layer which keeps off the droplet from being evaporated quickly". In such circumstances, when the impact velocity is low, the vapor cushion prevents the droplet from wetting the wall surface, thus preserving its cohesion, therefore the droplet rebound from the wall surfaces. However, when the impact velocity is sufficient high, it is no-longer case of only rebound, the droplets can splash, rebound and at the same time it can deposit on the wall surfaces.

The influence of wall temperature T_W can be represented by the dimensionless number, which is a function of the liquid boiling and Leiden-frost temperatures as:

$$T^{\star} = \frac{T_W - T_B}{T_L - T_B} \tag{2.16}$$

In general, boiling point temperature T_B and Leiden-frost temperature T_L depend upon the static air pressure, therefore effect of air pressure is inherently incorporated.

3 State of the art

The complete IC-engine operation consists of many stages and broadly classified as charge intake, fuel injection, fuel-air mixture formation, compression, ignition and expansion (power generation), and exhaust emission. There are extensive researches underway to address the real challenge to improve the engine performance by making it more efficient and at same time achieving low pollutants emission to comply with the modern environmental norms. Generally, both the experimental and numerical researches are carried out at individual stage of engine operation to address the specific physical phenomena involved. However, each individual process influences each other and has combined impact on the final performance and emission characteristics of the an IC-engine.

In this section, the detail discussion is carried out about all individual operations and corresponding research carried out so far. These are namely, spray dynamics that includes nozzle flow and cavitation, primary and secondary atomization, droplet-droplet interaction, spray wall interaction, and evaporation. We will also discuss the in-cylinder flow behavior of IC-engine together with the cyclic flow variations under fired/non-fired conditions.

3.1 Spray dynamics

In context of IC-engine, spray dynamics is vital and complex physical phenomena. The primary purpose of the spray formation during fuel injection is to prepare required fuel-air mixture for combustion to take place. Apart from the in-cylinder condition (gas pressure, temperature) and liquid fuel properties, the spray dynamics are greatly influenced by the nozzle flow condition (turbulence and cavitation). This changes the course of physical process during nozzle exit. There are number of experimental and computational/modeling studies that have been carried out focusing on the initiation of cavitation and the ensuing two-phase flow inside the diesel engine injector. A review of various modeling approaches can be found in [17]. Experimental studies using large size scaled and real size nozzle have shown the formation of complex structure inside the nozzle [18, 19]. They pointed out that the atomization behavior is significantly affected by the presence of cavitation, which in turn influences engine performance and exhaust emissions of the engine [20, 21]. Both experimental and computation studies were mainly concentrated primarily on understanding the cavitation phenomena and factors affecting the formation of cavitation. Effort was also devoted to the assessment of the injector life due to cavitation.

It is difficult task to carry out experimental study and real-time measurements on cavitation during the injection process. Most of the experimental studies reported refer to operations representing actual conditions inside actual engine. Due to rapid opening and closing of nozzle needle, the needle position greatly influences the flow inside a nozzle and in turn is responsible for transient evolution. Detail experimental and CFD studies are carried out with transparent nozzle with both large scale and real-size geometry [19, 22, 23]. In these study, the authors classified the cavitation phenomena in the terms of geometric and dynamic characteristics. The geometric cavitation is formed in particular location inside the nozzle (such as near needle sac, hole entry), while the dynamics cavitation is highly transient in terms of spatial and temporal evolution, and considerably influences the spray angle. The author also pointed out that the cavitation is major cause of injector failures as it leads to erosion of nozzle material, which is responsible for inconsistent nozzle performance. Since different scales are involved to address the nozzle flow and atomization process, it is big challenge to incorporate the entire phenomena (nozzle flow and atomization) in single CFD frame work.

To address two-phase flow phenomena in case of cavitation and atomization process, researchers have mainly try to solve it into two stages. First a detail CFD simulation is carried out for nozzle flow using either by volume of fluid (VOF) method or by the particle tracking approach to track the secondary phase formation due to cavitation. Then, the achieved results is further interpolated into boundary condition into second stage for atomization model [24]. The detail boundary condition could be in terms of transient velocity (mass flow rate), effective exit jet diameter, evaporated fuel mass and exit flow turbulence.

To resolve all the scales involved in the atomization process, the DNS is the only candidate that should be able to capture the entire physical process with surface tracking method similar to VOF [25, 26, 28], but it should also incorporate the transient needle movement to capture the unsteady behavior. However, its prohibitive computational costs restrict its usage primarily to academic applications. The DNS only for atomization process still requires input from nozzle flow in terms of turbulence intensity, velocity with respective injection time [29]. However, the fuel injection involves vast range of particle loading from dense to dilute spray, therefore it is difficult to justify the use of DNS in dilute region with detail description of surface phenomena for heat, mass and momentum exchange. The coupled VOF and particle tracking method is genuine effort to use the respective advantages of two methods. However, it is a complex method to represent parcel (Lagrange particle) from the small broken-off and near spherical chunk of VOF [27, 29]. The effort to reduce the computational cost is also tried to achieve by coupled large eddy simulation (LES)/DNS technique [30, 31, 32], although with slight reduction in computational cost, as it is still expensive as pointed out in [13]. Detail review on modeling of primary atomization in the context of LES/DNS is provided [13].

Alternatively, particle tracking approach is widely used to address the dispersed spray droplets in commercial and non-commercial CFD code, In this method cluster of droplets having the same properties (diameter, temperature, velocity etc.) are represented by a parcel so called numerical particle and tracked by Lagrangian method. This method is very good representative of multi-dimensionality of the spray and appears computationally economical in case of dilute spray. However, the accuracy of the method is highly depends up on the number of computational parcels used. Therefore large number of parcels are necessary to achieve reasonably acceptable results for dense spray.

To account for the fuel injection with this method, liquid is injected in the form of "blobs" that have a characteristic size equal to the nozzle orifice diameter, instead of assuming an intact liquid core at the nozzle exit. The basis of this model is the concept introduced by Reitz and Diwakar [33] that the atomization of the injected liquid and the subsequent breakup of drops are indistinguishable processes within a dense spray. Therefore, based on correlation parameters that should represent the exact primary atomization behavior of particular nozzle configuration, different atomization models were developed. In case of hollow gasoline direct injection (GDI), the jet comes out as hollow cone with thin liquid sheet. The nozzle flow generates surface wave, the aerodynamics forces at liquid-gas interface further amplify the instability until the sheet breaks into ligament and ligament further breaks into droplets. The first correlation was proposed for a hollow-cone spray Dorfner et al. [34]. The model was further improved by Han et al. [35]. The linearized instability sheet atomization (LISA) model was proposed by Schmidt et al. [50] and Senecal et al. [96]. All three approaches estimate the basic characteristics of the liquid fuel sheet formed in the vicinity of the injector and utilize these estimates for the prediction of spray features, such as the size of the resulting droplets, their velocity and the location. Contrary to hollow cone GDI, in the case of multi-hole GDI or diesel injector (DI), the circular orifice is used to inject fuel in the form of solid cylindrical jet. Due to the nozzle in-flow condition, the surface wave forms and further amplified by aerodynamic force generated by high relative velocity between ensuing jet and surrounding gas. Instability similar to Kelvin-Helmholtz develops and liquid droplets get stripped from the liquid core. The size of the newly formed droplets can be in the order of the wavelength of surface instability. The mostly adopted surface wave instability model was proposed by Reitz [105], Reitz and Diwakar [33], and Patterson and Reitz [37]. The model constant in primary breakup is largely dependent upon the individual nozzle and can vary up to order of 10 as suggested by Reitz and Brocco [14].

The droplets formed during primary atomization are somewhat larger in size and still carries enough momentum. The relative velocity between the droplet and surrounding gas results in droplet to deforms and oscillate from spherical shape and the droplets further breakup when the amplitude of oscillation reaches critical value, which is in the order of droplet diameter. In the context of Lagrange particle tracking, the main task of the primary atomization model is to provide initial conditions for droplets breakup in secondary atomization process. These initial conditions include droplet radius, droplet velocity, droplet dispersion etc. The Taylor analogy breakup (TAB) model is a classic method for calculating droplet breakup[38]. This method is based upon Taylor's analogy [39] between an oscillating and distorting droplet and a spring mass system. The ETAB (enhanced TAB) is the further improvement of TAB model by Tanner [40], in which the disintegration of the liquid jet is simulated as a cascade of drop breakups where each breakup event follows experimentally observed breakup mechanisms (stripping or bag breakup). Thus, the initially large droplets (parent droplets) undergo a series of breakups until the product droplets reach a stable condition. Within the break up length the stripped droplets can experience secondary atomization, therefore primary atomization together with the DDB (droplet deformation breakup) mechanism in a competing manner is chosen in order to predict the spray disintegration within the break-up length by Park and Lee [41].

Generally, the fuel injection processes involve dense flow of large number of fuel droplets with wide range of relative velocity among each other. Therefore, the probability for the droplet-droplet interactions is very high. This ultimately influences final droplet distribution and spray profile. Therefore, the droplet-droplet interaction must be accounted properly. The most of the spray models with Lagrange particle tracking are based on the statistical sampling, where each particle (also called computational parcel) represent numerous droplets from the larger populations [42]. This approach is able to capture the multi-dimensionality of the spray. Therefore the primitive collision model proposed by O'Rourke [43] is also based on stochastic approach. The method is based on control volume (CV) approach of binary collision model, in which droplets staying in the same CV will collide with each other. This way the increase in parcel number invariably increases the computational cost, with the number of parcels squared.

Schmidt and Rutland [46] proposed a NTC (no time counter) method, that has a linear cost. Both methods are cell-based. Like O'Rourke's collision algorithm, the NTC algorithm is first-order accurate in time and second-order accurate in space. Unlike O'Rourke's collision algorithm, in which all the possible collision pairs are considered, the NTC algorithm only considers a randomly chosen subset of candidate pairs after scaling up the collision probability by the estimated maximum probability, reducing the computational cost. The numerical issue associated with this new method is reported by Hieber [47], Nordin [48], Aneja and Abraham [49].

These collision models are still sensitive to grid size and its type. This issue also confirmed by Schmidt and Rutland [50] who pointed out that the mesh used for the gas phase solver is responsible. This widely used approach, established by O'Rourke [43] is sound when the droplet density variation is well-resolved. The grid dependency is more prominent in case of cartesian mesh, especially when injection point is defined as the common vortex of four cells. The spray becomes directional towards the individual 4-cartesian mesh as parcels residing in the same cell is allowed to collide. This way spray profiles adopt shape like four leaves, also called clover leaf collision artifacts. Schmidt and Rutland [46] tried to negate grid dependency incorporating additional mesh for spray calculation (also called collision mesh) other than regular mesh for gas phase solver. However, this becomes impracticable, when multiple injection points are defined, which is very common in modern IC engine applications. Hou and Schmidt [51] tried to make it independent of the mesh orientation by a continuous adaptive refining of the mesh in the region of dense spray using relative complex routine. Munnannur and Reitz [45] proposed a new approach by calculating the collision frequency based on the radius of influence. The radius of influence approach is evaluated by both a dynamic and a constant value.

Apart from the mesh dependency, the original collision model proposed by O'Rourke [43] only accounts for stretching separation and permanent coalescence. Due to this fact, it over predicts the droplet coalescence. It does not take care of other possible modes of droplet interaction such as bouncing and reflexive separation. A comprehensive collision model has been proposed by Munnannur et al. [44]. The model accounts for all relevant collision regimes (i.e. coalescence, stretching separation, reflexive separation and collision) and it is originally formulated by using detail experimental findings from Brazier-Smith et al.[52], Ashgriz and Poo [54], and Qian and Law [53]. It is comprehended into possible droplet interaction regimes using Weber number and impact parameter *(We-B diagram)* as shown in Figure (3.1). This model is further modified to take into account correctly the post-interaction momentum exchange [55]. However, the model is based on binary collisions of droplets in a given control volume (CV). Therefore, it still has dependency on control volume size and types (e.g. structure or unstructured mesh).

Spray-wall interaction is also considered as an important phenomenon in IC-engines. In the case of GDI the fuel is injected directly in the combustion chamber. The injected fuel must be vaporized and mixed properly with the charged air in order to have desirable combustion and engine power. In most of IC-engines, the fuel spray may impinge on engine surfaces (e.g. piston crown, cylinder

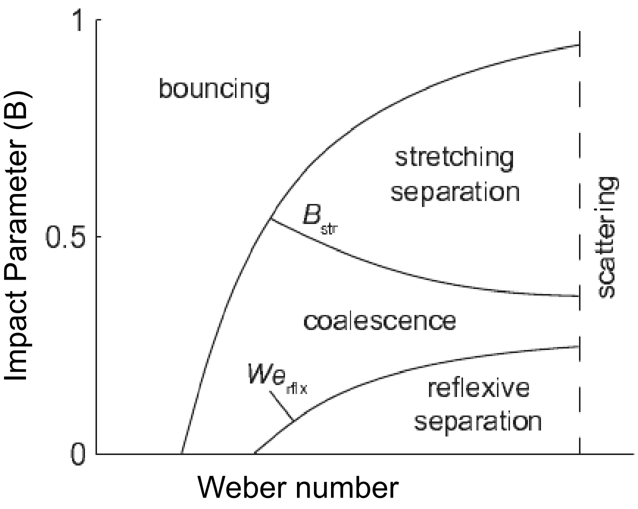

Figure 3.1: Collision regimes as described by Reitz and Munnannur [44] as illustrated in [55]

liner, valves) before vaporization and mixing are complete. Spray impingement has been shown to influence engine performance and emissions in both compression ignited (CI) and spark ignited (SI) engines [56]. The impingement mostly results in formation of wall film on engine surface, that influence the engine performance especially in transient control. It is a major factor affecting fuel-air ratio due to time lag resulting from a film of liquid fuel deposited on the piston surface to get evaporated [57]. The time lag results in decreased engine response, increased fuel consumption and increased unburnt hydrocarbon emissions. A general review is provided by Cossali et al. [60, 61] for droplet impact on solid wall.

Recently, Habchi [58] showed the effect of gas pressure in analogy with wall temperature, since the boiling point of the particular fuel will strongly depend upon the subjected gas pressure, therefore the time lag involved in film evaporation. Castanet et al. [59] showed that droplet can gain temperature, when it rebounds from the heated wall and they also showed influence of droplet incident velocity and wall temperature on wall impingement characteristics. However, above the Leiden-frost temperature, it only depends upon the incident velocity. Amiel [63] and Diwette et al. [64] performed numerous experiments on ethanol droplets. Impacts regimes (rebound, splashing, film deposition, etc.) were shown in a diagram of the wall temperature versus the Weber number. Mühlbauer et al. [65] studied spray behavior on wall/liquid film and quantified important parameters such as deposition rate of the liquid onto the wall and characteristics of the splashed fraction-velocity, size and flux of the drops in the secondary spray.

In KIVA4-mpi primitive wall film model suggested by O'Rourke et al. [67] is used , that includes droplet splash and wall deposition. The model only accounts for wall deposition and droplet splash, and later improved by O'Rourke and Amsden [68] to take into account the film motion due to impingement pressure and subsequent wall film spreading. However, the model doesn't take into account the influence of the wall temperature. Rosa et al. [66, 107] gave explicit expressions for the position of the limits between the different impact regime (see Figure 3.2) based on experimental observations made in [60, 63, 64].

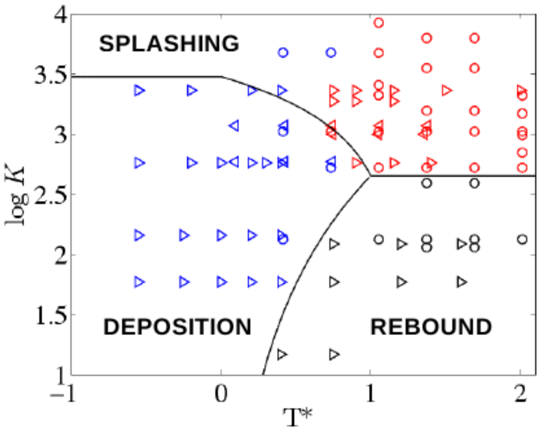

Figure 3.2: $\log K - T^{\star}$ diagram plotted by [107]: Experimental conditions from [60, 61] (left oriented triangles and circles) and [64] (right-oriented triangles) and observation: deposition (blue), splashing(red) and rebound(black) regimes. $T^{\star}$ is reduced temperature defined in Eqn.2.16 and K accounts for the flow parameters as function of droplet Reynolds number and Weber number (as defined in next chapter)

3.2 In-cylinder flow and cycle-to-cycle variations

The in-cylinder flow behavior is an important phenomenon that addresses the overall engine performances in terms of efficient combustion and pollutant emission [3, 69, 70]. It has been found that, the turbulence intensity and directional flow profile (tumble & swirl) just before the start of ignition dictates further course of combustion and flame propagation under different fuel-air ratios. There are numerous experimental and numerical studies reported on in-cylinder flow analysis [e.g. [71, 72] and cross references]. The experimental measurement carried out using PIV suggested that, to maximize turbulence intensity at the end of compression stroke, the tumble and swirl motion must be high [71]. A study carried out with increasing tumble and swirl motion also suggest the gain in turbulence intensity in respective directional velocity [73].

In addition, the swirl and tumble motion has greater influence on the direction of flame propagation than increase in the flame propagation speed with a stoichiometric fuel-air ratio as pointed out by Lee at al. [74], the tumble (with swirl motion) is more effective than pure tumble for rapid and stable combustion under lean mixture conditions [74]. The effect of engine speed on the tumble motion was analyzed with cold flow case (without combustion) in [75], that concluded that the tumble motion is relatively insensitive to engine speed, rather it is dependent on engine state (crank angle).

Moreover, the flow field varies from one cycle to another cycle resulting in cyclic variations of engine performance during consecutive cycles. Flow field analysis suggest that flow can be decomposes into its mean component and its fluctuating and turbulent part [76, 77]. These cyclic variations in engine flow field can sometime lead to unfavorable engine operation such as: misfire, incomplete combustion and HC emission. The engine design is a key parameter that may have a large influence on this variable part. It is therefore necessary to have engine design/geometry with reduced cyclic variations of the flow-field. However, it would be very difficult to adapt one geometry/design for the whole engine operating range. The possible way to control the in-cylinder flow field is through the modification of the flow field during the intake operation [78, 79, 80].

The in-cylinder aerodynamic behavior of an IC-engine has also been studied using numerical modeling and simulations. In context of a complex engine design, the numerical method can offer great support to carry out parametric study and suggest the design modifications. The recent availability of computational power permits to carry out detailed and comprehensive engine analysis. Therefore, the role of refined and updated computational fluid dynamic (CFD) models are becoming more and more significant. The detailed sub-models for the individual physical processes and use of relatively finer mesh together with dynamic mesh adaptability technique makes the IC-engine simulation more complete. In this perspective, many researchers have tried to address the in-cylinder flow behavior by using numerical simulation method [72]-[81]. As it is evident, the flow inside an IC-engine is highly turbulent with complex flow structure and three-dimensional in nature. It is consists of eddies with a wide spectrum of sizes. A CFD can offer good alternative to investigate such a complex flow in detail. The most widespread approaches from the practical point of view are the Reynolds averaged Navier- Stokes equations (RANS) methodology and LES. Previous studies [81, 82, 83] as well as detailed literature review [84] have shown that the commonly used RANS turbulence approach is not able to capture the highly unsteady flow field in an IC-engine. The classic RANS approach provides a good prediction of the mean flow structures inside the combustion chamber, but all information relative to the unsteady effects especially the cycle-to-cycle variations is lost in this process. The necessity of modeling the whole turbulent energy spectrum is the second severe restriction of this approach. Nevertheless, the RANS modeling approach based on different variations of the k-ϵ model has vast applications on various engineering turbulent flows to carry out quick design optimization with relatively coarser grid.

The unsteady RANS can be used for unsteady turbulent flows [85, 86]. Recent innovative concepts appear promising, even though they are not yet mature [86]. The LES has proven to be an appropriate technique to treat unsteady phenomena occurring in IC-engine by requiring less computational cost compared to DNS or DNS/LES. It is able to well capture intrinsically time and space dependent phenomena. It computes the large scale flow and mixing process accurately, thereby providing a valuable platform for small scale models that describe the micro-mixing and combustion process [87, 88]. A recent review is provided by Rutland [83] who presents comparative studies of the effect of different turbulence models on IC-engine applications. A number of research works, e.g. [82, 83, 110] confirms the possibility of using LES to investigate flow, mixing and combustion in reciprocating engines. Successful application of LES to engine flows has enhanced the understanding of in-cylinder turbulence generation including integral time and length scales evolution, heat and mass transfer, reaction progress and cycle-to-cycle variations [6]-[72].

Most of the LES studies reported are done either with cold flow (no-fuel injection and no combustion), or with homogeneous charged compression ignition (HCCI), while in case of GDI there are few literatures reported with fuel injection model [6]-[9]. However, the detail spray dynamics is being included in real engine simulation [89]-[91].

3.3 Objectives

In the present thesis, the effort is made towards integrating a comprehensive engine simulation tool that accounts for primary and secondary atomization, collision-coalescence, spray-wall interaction as reported in [92] in to KIVA4-mpi code in order to carry out detail IC-engine simulations. Thereby it is intended to include all possible physical phenomena taking place inside the engine cylinder beginning from the air-intake, fuel injection, evaporation, mixture formation, excluding ignition, combustion, reaction and subsequent exhaust gas discharge. In this study following aspects are addressed to be able to reach the targeted goal of developing a comprehensive engine simulation tool.

1. Integration of spray atomization models for hollow-cone and multi hole/pintle nozzle : primary atomization (linear instability sheet atomization for Hollow-cone and Kelvin Helmholtz for multi-hole pintle nozzle)
2. Improvement in the droplet-droplet (droplet collision-coalescence) model to make it independent of mesh size and mesh type.
3. Coupling of the fuel injection model with spray-wall interaction model by taking into account the cylinder and piston wall temperature
4. Development of a new meshing strategy, that is compatible with the current KIVA4-mpi version having possibilities to improve the grid resolution and at the same time able to perform parallel computations in multiple processors while achieving multi-cycle calculation in quick time.
5. Characterization of the cycle-to-cycle variations of in-cylinder flow behavior in conjunction with the fuel injection for two different engine configurations.

For this purpose, the KIVA4-mpi code [42, 95] is used as platform. It is presented in detail in the subsequent chapter.

4 Mathematical models for engine simulation in KIVA4-mpi code

In present thesis a CFD code KIVA4-mpi is used to simulate such wide ranging phenomena. Moreover, the KIVA4-mpi code is designed for engine simulation with adaptive mesh technique for the piston and valve movements. In this chapter, a general description of the flow is provided in section 4.1, that has significant role in the current study, then detail mathematical model/sub-models adopted to represent the individual process in IC-engine are described in section 4.2. How these models are improved or adapted in KIVA4-mpi is highlighted in chapter 5.

4.1 Characteristics of flow problem

In the development of a CFD numerical method, the description of continuous phase is based on law of continuum mechanics. They are the conservation of mass, conservation of momentum, and conservation of energy. In many engineering applications, the flow can be characterized by their nature, such as smooth or chaotic flow. In particular, it is classified with regimes namely laminar, transient and turbulent. The state of fluid motion is often characterized by the dimensionless Reynolds numbers [120], which gives measure of the ratio of inertial forces to viscous forces:

$$Re = \frac{UL\rho}{\mu} = \frac{UL}{\nu} \tag{4.1}$$

where U is the characteristic velocity, L the characteristic length, ρ the fluid density, μ and ν are the dynamic and kinematic fluid viscosity, respectively. The characteristic length scale L depends mostly on the flow-configuration under consideration. The flow is said to be laminar, when Reynolds number is low and viscous forces are dominant. In such as case the fluid flow is very smooth and each fluid particle follows well defined pattern and it does not changes with time similar in the case of steady state. While at high Reynold number the flow is considered to be turbulent flow, it is dominated by the inertial forces, which results in intense chaotic eddies, vortices and other flow instabilities.

4.1.1 Turbulent flow

Generally, flow is considered laminar, when the Reynolds number defined by Eqn.(4.1) is close to unity. The transition from laminar to turbulence is considered when the Reynolds number reaches to critical value Re_{crit}, although laminar region can still exist at higher Reynolds number as suggested by Schlichting [121] under certain conditions such as flow free from the disturbance. For example of pipe flow, Re_{crit} is in order of 2.10^3, where, U is the mean axial velocity and length scale L is given by pipe diameter. The fully turbulence is achieved at Reynolds number somewhere between $2\text{x}10^3$ and $2\text{x}10^5$ depending upon the specific case. It can go as high as $2\text{x}10^8$ in case of jet airplane or even much higher for atmospheric flow. Therefore, Reynolds number provides indication of flow instability and possible occurrence of turbulence. Additionally, the flow turbulence can be defined by parameter called turbulence intensity I, which is ratio of maximum amplitude of velocity fluctuation to the mean large scale velocity. Thus, flow can have less turbulence even with higher Reynolds number.

In more generic way, Bradshaw [122] gave the following formulation of turbulence: "Turbulence is a three-dimensional time-space dependent motion in which vortex stretching causes velocity fluctuations to spread to all wavelengths between a minimum determined by viscous forces and a maximum determined by the boundary conditions of the flow". However, Turbulent flows enclose a wide spectrum of features, where the most important are listed as below:

- irregular nature (with time and space);
- three-dimensional and rotational;
- diffusivity (key feature of turbulent flow that helps in enhanced mixing property);
- high Reynolds number;
- dissipative in nature (can cause increased drag force in particular flow);
- wide range of scales of motion (large/small eddies)

A detail description of turbulent flow, various computational models for turbulent flows and their respective difficulties are highlighted in [123].

4.1.2 Turbulent scales

Turbulent flows, generally consist of the rotational flow structure, so called turbulent eddies with wide range of scales. Most of the turbulence energy production is associated with large eddies because they breakup and exchange their energy with the smaller eddies. The energy of the smaller eddies is further transferred to even more smaller eddies. This energy cascade process ends at the smallest eddies. The size of these smallest eddies is predominately determined by the molecular process of viscous dissipation and the energy associated with the motion is finally dissipated and converted into internal thermal energy. It is known that the smallest scales of turbulence are the Kolmogorov micro-scales of length, time and velocity [124, 125] as defined as:

$$l_k = \left(\frac{\nu^3}{\epsilon}\right)^{1/4}, \quad \tau_k = \left(\frac{\nu}{\epsilon}\right)^{1/2}, \quad u_k = (\nu\epsilon)^{1/4} \tag{4.2}$$

where ϵ is the dissipation rate. Another widely used length scale from statistical turbulence theory is the Taylor micro-scale. The definition is given by

$$l_\tau{}^2 = \frac{\overline{u'^2}}{(\partial u'/\partial x)^2} \tag{4.3}$$

In most experiments the length scales are also defined using a characteristic scale l_i which is the proper length of the domain and is called integral length scales. l_i can be defined as the distance after which the self correlation of the velocity components vanishes. An estimation of integral length scales can be given by the following equation:

$$l_i \sim \frac{k^{3/2}}{\epsilon} \tag{4.4}$$

where the proportionality constant is of the order of unity. Taylor scales l_τ characterize the range of scales that are very small compared to integral scales l_i and at the same time very large compared to Kolmogorov micro-scales l_k. Therefore, there is the following relation between their quantities: $l_k << l_\tau << l_i$. The turbulent kinetic energy spectrum $E_w(k_w)$ in dependence of the wave number k_w is schematically plotted in Figure 4.1, where $k_w = 2\pi/l$. More detailed information can be found in [123].

Turbulent in-cylinder flows are characterized by a wide spectrum of time and length scales which change from the largest eddies down to the Kolmogorov micro-scales. The largest eddies are characterized by the integral length scale l_i which is comparable to the largest flow structures determined by the geometry of the flow, e.g. intake jet. The largest eddies transfer their energy sequentially to smaller eddies (it is a so-called energy cascade) until the inertia forces are sufficiently small compared to the effects of dissipation, therefore all length scales, including integral l_i as well as the smaller Taylor and Kolmogorov length scales are important and have to be considered.

An assessment of turbulent scales which are relevant to the engine geometry and speed, the resulting turbulent flow field and the effect of compression ratio on turbulent scales are very important. An extensive review concerning turbulence modeling in IC-engines focused on evaluation of turbulence intensity and length scales for in-cylinder flows has been reported by Yavuz [127]. The summary concerning the turbulent length and time scales is shown in Table 4.1. The relevant length and time scales pertaining to both geometry and turbulence are reviewed in the works by Heywood [69], Reynolds [120] and computed in [126]. Results and conclusions obtained in [127] can be summarized in the following way:

- The turbulence intensity is found to scale with the mean engine speed. The maximum turbulent intensity at TDC is approximately equal to 50% of the mean piston speed.
- The turbulence intensity is naturally correlated with intake flow parameters near TDC.
- The temporal length scales increase with crank angle during the intake and compression strokes.
- The in-cylinder turbulence near TDC of compression is nearly isotropic in the absence of intake generated swirling flow. During intake the turbulent flow is neither homogeneous nor isotropic.

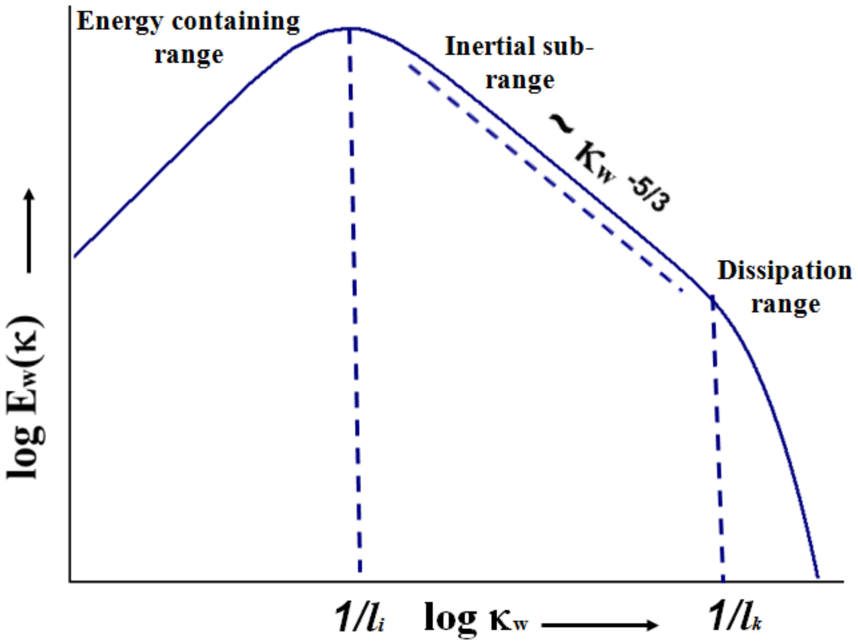

Figure 4.1: Schematic of turbulent kinetic energy spectrum

- The flow regimes inside the boundary layer as well as the main vortex motion inside the cylinder can be characterized by a Reynolds number defined as

$$Re = \frac{u_p L}{\nu} \tag{4.5}$$

where u_p is the mean piston speed, L is the stroke, ν is the kinematic viscosity.

Table 4.1: Estimated length scale for an automotive-size engines (rpm 1000)

Scale	Estimated value	Engine stroke
l_i	10.0 mm	intake stroke
l_i	2.0-5.0 mm	compression, near TDC
l_τ	1.0 mm	
l_k	0.01 mm	
τ_i	1.0 ms	
τ_τ	0.1 ms	

4.1.3 Gas phase governing equations

As already pointed out above, it is assumed that the theory of continuum mechanics is valid. The unsteady equations of motion of turbulent, chemically reactive mixture of ideal gases, coupled to the equations for a single-component vaporizing fuel spray are given in this section. The governing equations can be used to solve both laminar and turbulent flows. The mass, momentum and energy equations for three-dimensional chemically reacting fluid flow [42] can be written in the following way. The transport equation of mass for each species m of a multi-component mixture yields:

$$\frac{\partial \rho_m}{\partial t} + \nabla \cdot (\rho_m \mathbf{u}) = \nabla \cdot \left[\rho D \nabla \left(\frac{\rho_m}{\rho} \right) \right] + \dot{\rho}_m^c + \dot{\rho}^s \delta_{m1} \tag{4.6}$$

where t is the time, ρ_m mass density of species m, ρ total mass density, u fluid velocity vector and D diffusion coefficient. The terms $\dot{\rho}_m^c$ and $\dot{\rho}^s \delta_{m1}$ represent source terms due to chemistry and spray, respectively. δ is the Dirac delta function. A definition $\dot{\rho}_m^c$ will be given in later section of this chapter. The conservation of momentum is given in the following form:

$$\frac{\partial \rho \mathbf{u}}{\partial t} + \nabla \cdot (\rho \mathbf{u}\mathbf{u}) = -\nabla p - A_0 \nabla \left(\frac{2}{3} \rho k \right) + \nabla \cdot \sigma + \mathbf{F}^s + \rho g \tag{4.7}$$

where p is the fluid pressure, k turbulent kinetic energy, σ viscous stress tensor, $\mathbf{F}_s$ rate of gain per unit volume due to the spray and g the specific body force. The dimensionless quantity A_0 is equal to zero in laminar and to unity in the turbulent case. The viscous stress is defined by:

$$\sigma = \mu \left[\nabla \mathbf{u} + (\nabla \mathbf{u})^T \right] - \frac{2}{3} \mu \nabla \cdot \mathbf{u} \mathbf{I} \tag{4.8}$$

where μ is the dynamic viscosity and $\mathbf{I}$ unit dyadic. The transport equation for the specific internal energy is:

$$\frac{\partial \rho I}{\partial t} + \nabla \cdot (\rho \mathbf{u} I) = -p \nabla \cdot \mathbf{u} + (1 - A_0)\, \sigma : \nabla \mathbf{u} - \nabla \cdot \mathbf{J} + A_0 \rho \epsilon + \dot{Q}^c + \dot{Q}^s \tag{4.9}$$

where I is the specific internal energy, exclusive of chemical energy, ϵ the dissipation rate of turbulent kinetic energy $\dot{Q}^c$ and $\dot{Q}^s$ are the source terms due to the chemical heat release and spray interactions, respectively. $\mathbf{J}$ is the heat flux vector which is the sum of contributions due to heat conduction and enthalpy diffusion given by:

$$\mathbf{J} = -K_{th} \nabla T - \rho D \sum_m h_m \nabla \left(\frac{\rho_m}{\rho} \right) \tag{4.10}$$

where T is the fluid temperature, h_m specific enthalpy of species m and K_{th} thermal conductivity. The equations of state are assumed to be of an ideal gas, giving equations for pressure, internal energy, specific heat of mixture and specific enthalpy, respectively, as

$$\begin{aligned} & p = R_0 T \textstyle\sum_m \left(\frac{\rho_m}{W_m} \right) \\ & I(T) = \textstyle\sum_m \left(\frac{\rho_m}{W_m} \right) I_m(T) \\ & C_p(T) = \textstyle\sum_m \left(\frac{\rho_m}{W_m} \right) C_{pm}(T) \\ & h_m(T) = I_m(T) + R_0 T / W_m \end{aligned} \tag{4.11}$$

where R_0 is the universal gas constant, W_m and $I_m(T)$ are molecular weight and specific internal energy of species m , respectively. The coefficient $C_{pm}(T)$ refers to the specific heat at constant pressure. Finally, it should be mentioned that no chemical reactions will be considered in this work and therefore, the terms $\dot{\rho}_m^c$ and $\dot{Q}^c$ are neglected.

Dealing with turbulent flows, modeling methods have to be used as DNS is computationally prohibitive, the two well known modeling strategies, RANS and LES, will be shortly outlined.

4.1.4 Reynolds averaged Navier-Stokes equation

The RANS method is based on time or ensemble-averaging the Navier-Stokes equation coupled with appropriate turbulence models. The averaging procedure obviously results in a loss of information contained in the instantaneous equations. Different procedures which are used to handle the closure problem lead to different RANS turbulent models. The first limitation of RANS is that the approach provides information about the mean flow while all information relative to the instantaneous processes, e.g. cyclic variability is lost. The second one is that the effects of all scales of motion have to be modeled which makes modeling a challenging task. Grid or time step refinement improves the numerical accuracy but does not inherently increases the dynamic range of scales that are resolved. The most widely used model of turbulence in IC-engine applications is the k-ϵ model. The standard k-ϵ model which is included in the KIVA4-mpi code solves the equations for the turbulent kinetic energy k and its dissipation rate ϵ :

$$\frac{\partial \rho k}{\partial t} + \nabla \cdot (\rho u k) = -\frac{2}{3}\rho k \nabla \cdot u + \sigma : \nabla u + \nabla \cdot \left[\left(\frac{\mu}{Pr_k} \right) \nabla k \right] - \rho \epsilon + \dot{W}^s \tag{4.12}$$

$$\frac{\partial \rho \epsilon}{\partial t} + \nabla \cdot (\rho u \epsilon) = -\left(\frac{2}{3} C_{\epsilon 1} - C_{\epsilon 3} \right) \rho \epsilon \nabla \cdot u + \nabla \cdot \left[\left(\frac{\mu}{Pr_\epsilon} \right) \nabla \epsilon \right] - \frac{\epsilon}{k} \left[C_{\epsilon 1} \sigma : \nabla u - C_{\epsilon 2} \rho \epsilon + C_s \dot{W}^s \right] \tag{4.13}$$

The quantities $C_{\epsilon 1}$, $C_{\epsilon 2}$, $C_{\epsilon 3}$, Pr_k and Pr_ϵ are constants whose values are determined from experiments and with some theoretical consideration. Standard values of these constants are given in Table 4.2. Source terms involving the quantity W_s arise due to interaction with the spray.

Table 4.2: Standard values of $k - \epsilon$ turbulence model constants.

Model Constant	$C_{\epsilon 1}$	$C_\epsilon 2$	$C_\epsilon 3$	Pr_k	Pr_ϵ
Value	1.44	1.92	-1.0	0.1	1.3

4.1.5 Direct numerical simulation

Direct numerical simulation means the solution of the unsteady three dimensional Navier-Stokes equation and the state relations for all scales of turbulence without introduction of any models.

The whole spectrum of motion from large energy carrying eddies down to the Kolmogorov microscales must be resolved on the computational mesh. By taking in to account the Kolmogorov scales given by Eqn.((4.14)) an estimation of the required grid size can be given. Consideration of the Courant-Friedrichs-Lewy (CFL) criterion yields in addition a restriction for the time step. The scaling for the number of grid points required for DNS is given by the following expression:

$$N_{DNS} = \left(\frac{L}{l_k}\right)^3 \cdot {Re_t}^{-9/4} \tag{4.14}$$

Direct numerical simulation is one of the most accurate numerical methods. However, since the computational costs are very high, DNS can only be realized at low Reynolds number and serves mainly as a tool for fundamental research in turbulence [25, 28] as well as a development tool for new turbulence models. A DNS application to the in-cylinder flow in an internal combustion engine has so far not been reported in the literature due to its expensive computational cost for flow with higher Reynolds number [123].

4.1.6 Large eddy simulation

Since both spatial and temporal scales must be resolved, the method of direct numerical simulation (DNS) imposes strict limitations on the grid resolution as well as the time step. Large eddy simulation is a multi-scale technique with a complexity intermediate between DNS and RANS approaches. The fundamental idea of LES is based on the separation of turbulent scales [123], where energy containing large eddies are directly computed while small scale turbulent structures are modeled. LES can be more accurate than the RANS approach because the small scales tend to be more isotropic and homogeneous than the larger ones, and thus are more amenable to universal modeling.

The separation between the large and small scales is based on a filtering operation with a filtering function G. The filter removes all finer fluctuations and the governing equations only describe the space-filtered fields. The instantaneous flow field is split into the resolved large scales (φ) and the modeled small scales $(\varphi^{'})$, see equation (4.15). The extraction of the resolved large scale part from the original variables is mathematically defined by the convolution of the original variables with a filter function G as

$$\overline{\varphi}\left(x_i, t\right) = \iiint_{+\infty}^{-\infty} \left(G\left(x_i^{`}\varphi\left(x_i - x_i^{`}\right)\right)\right) \text{ with } \varphi = \overline{\varphi} + \varphi^{'} \tag{4.15}$$

The most commonly used filter functions are the sharp Fourier cut-off, the Gaussian and the top-hat filter [128]. Usually, the non-resolved small scales are determined by the computational grid, causing the resolved scales to be partly affected by the numerical scheme used to describe the governing equations.

4.1.7 Sub-grid-scale models

The filtering operation of the governing equations results in additional sub-grid-scale (SGS) terms, that need to be closed. The SGS terms represent the interaction between the resolved large scale and unresolved small scale part of the flow [128]. The problem of turbulent closure is the expression of these unknown SGS contributions in terms of the resolved large scale quantities. They are

$$\tau_{ij} = \overline{u_i u_j} - \tilde{u_i}\tilde{u_j} \tag{4.16}$$

4.1.8 Smagorinsky model

Most of the current sub-grid-scale models are based on the eddy viscosity approach, which assumes that small scale turbulence affects the flow in the same way as the molecular viscosity. Therefore, the fine structure term τ_{ij} may be modeled by adding a turbulent viscosity ν_t to the molecular viscosity ν_{mol} , resulting in an effective viscosity $\nu_{eff} = \nu_t + \nu_{mol}$. Thereby, the concept of eddy viscosity relates the sub-grid-scale stresses τ_{ij} to the large scale strain-rate tensor S_{ij} :

$$\tau_{ij} - \frac{1}{3}\tau_{kk}\delta_{ij} = -2\nu_t \overline{S}_{ij} \tag{4.17}$$

where

$$\overline{S}_{ij} = \frac{1}{2}\left(\frac{\partial \overline{u}_i}{\partial x_j} + \frac{\partial \overline{u}_j}{\partial x_i}\right) \tag{4.18}$$

In addition to the concept of eddy viscosity, a second major assumption is equilibrium between production and dissipation of small scale kinetic energy. Although the large scales are generally not in equilibrium, the equilibrium hypothesis is likely to be realistic at the level of the small scales which tend to become equilibrium much faster. Considering a transport equation similar for the SGS kinetic energy, the equilibrium assumption leads to the following simplified formulation:

$$-\tau_{ij}\overline{S}_{ij} = \epsilon_\nu \tag{4.19}$$

where ϵ_ν is the viscous dissipation of the SGS energy. Equation (4.19) illustrates the assumption that the small scales of motion adjust instantaneously to the perturbations of the large scales and implies the existence of an inertial sub-range, where viscous effects are negligible and inertial effects dominate [128]. In the inertial sub-range, the energy follows the universal Kolmogorov spectrum, where the kinetic energy is transferred from the large scales to increasingly smaller scales until it is finally dissipated.

Smagorinsky [129] based his model on the equilibrium hypothesis (4.19) and propose that the eddy viscosity is proportional to the local strain-rate tensor:

$$\nu_t = l^2|\overline{S}| \tag{4.20}$$

where

$$|\overline{S}| = \sqrt{2\overline{S}_{ij}\overline{S}_{ij}} \tag{4.21}$$

The length scale l characterizes the small eddies and is chosen proportional to the local length scale associated with the filtering procedure through the coefficient C :

$$l = C^{1/2}\Delta \tag{4.22}$$

The coefficient $C_S = C^{1/2}$ is called the Smagorinsky constant and used in the frame of the Smagorinsky model to yield

$$\nu_t = (C_s\Delta)\,|\overline{S}| \tag{4.23}$$

where for non-uniform grid the filter width is defined by the grid size Δ in the following way:

$$\Delta = (\Delta_x\Delta_y\Delta_z)^{1/3} \tag{4.24}$$

Here Δ_x, Δ_y and Δ_z are the grid size in x, y and z directions, respectively. The theoretical values for the Smagorinsky constant, assuming a Kolmogorov spectrum [128] is $C_S = 0.18 - 0.23$, but often a value of $C_S = 0.1$ is used. Nevertheless, the coefficient has to be tuned for the specific applications. This leads to dynamic determination of C_S by so called Germano procedure [130]. That is not applied in this work for simplicity.

4.2 Spray dynamics

In generic term, the spray can be defined as a cloud of dispersed droplets present in gas. It has vast engineering and industrial applications. Based on the desired application, entirely different spray dynamics are required. Therefore, it is necessary to develop detailed understanding of all sub-processes involved in a complete spray dynamics. The trajectories and spray profile are governed by initial kinetic energy of droplets, drag forces and interactions between the drops and the surrounding gas. An adequate accurate modeling of these and other spray processes can lead to significant improvements in performance of CFD model, its applications. The spray sub-process in the context of IC-engine simulations are namely, spray atomization (primary and secondary), droplet-droplet interaction (collision-coalescence), turbulence dispersion, flow drag, evaporation (multi-component droplet evaporation), turbulence dispersion, droplet wall interaction, spray ignition, combustion , soot and pollutant formation.

4.2.1 Basic spray equation

The typical spray system exhibits high degree of randomness in terms of its location, droplet dimension, velocity, droplet internal energy. An analogy can be made with gas as a large number of small particles (atoms or molecules), all of which are in constant, random motion. Based on the kinetic theory of gases, the mathematical description of a spray can be made by following the evolution of the droplet number density function (NDF) f via the Williams spray equation (Eqn. 4.25)

[132]. In KIVA [42], f has eleven independent variables including three droplet position coordinates $\mathbf{x}$, three velocity components $\mathbf{v}$, the drop radius coordinate r, the drop temperature T_d (assumed to be uniform within the drop), and the droplet distortion from sphericity y, the time rate of change $dy/dt = \dot{y}$, and time t. Therefore,

$$f\left(\mathbf{x}, \mathbf{v}, r, T_d, y, \dot{y}, t\right) \mathrm{d}\mathbf{v}\mathrm{d}r\mathrm{d}T_d\mathrm{d}y\mathrm{d}\dot{y} \tag{4.25}$$

is the probable number of droplets per unit volume at position $\mathbf{x}$ and time t with velocities in the interval $(\mathbf{v}, \mathbf{v} + d\mathbf{v})$, radii in the interval $(r, r + dr)$, temperatures in the interval $(T_d, T_d + dT_d)$ and displacement parameters in the intervals $(y, y + dy)$ and $(\dot{y}, \dot{y} + d\dot{y})$. The time evolution of f is obtained by solving the following spray equation,

$$\frac{\partial f}{\partial t}+\nabla_{\mathbf{x}}\cdot(f(v))+\nabla_{\mathbf{v}}\cdot(f\mathbf{F})+\frac{\partial}{\partial r}(fR)+\frac{\partial}{\partial T_d}\left(f\dot{T}_d\right)+\frac{\partial}{\partial y}(f\dot{y})+\frac{\partial}{\partial \dot{y}}(f\ddot{y}) = \dot{f}_{coll}+\dot{f}_{break} \tag{4.26}$$

The quantities $\mathbf{F}$, R, $\dot{T}_d$ and $\ddot{y}$ are the time rates of change for an individual droplet of its velocity, radius, temperature, and oscillation velocity $\dot{y}$, respectively. $\dot{f}_{coll}$ and $\dot{f}_{break}$ represent the probability source terms due to droplet collisions and breakups. All these spray droplet parameters must be provided by the spray model.

By solving the spray equation in combination with gas phase equations (described in section 4.1.3) exchange of mass, momentum and energy have to be incorporated properly, $\dot{\rho}^s$ is the exchange functions such as mass exchange due to evaporation, $\mathbf{F}^s$ is the drag force due to surrounding gas, $\dot{Q}^s$ is the energy exchange by evaporation droplet to gas and $\dot{W}^s$ is the negative of the rate at which turbulent eddies are doing work in dispersing the droplets as described in Eqn. (4.30). These are obtained by summing the rate of change of mass, momentum, and energy of all droplets at position $\mathbf{x}$ and time t as.

$$\dot{\rho}^s = \int f\rho_d 4\pi r^2 R d\mathbf{v} dT_d dy d\dot{y} \tag{4.27}$$

$$\mathbf{F}^s = \int f\rho_d \left(4/3\pi r^3 \mathbf{F}' + 4\pi r^2 R\right) d\mathbf{v} dT_d dy d\dot{y} \tag{4.28}$$

$$\mathbf{Q}^s = \int f\rho_d \left(4/3\pi r^2 R \left[I_l + \frac{1}{2}\left(\mathbf{v} - \mathbf{u}\right)\right] + 4/3\pi r^3 \left[C_l \dot{T}_d + \mathbf{F}'\left(\mathbf{v} - \mathbf{u}\right)\right]\right) d\mathbf{v} dT_d dy d\dot{y} \tag{4.29}$$

$$\dot{W}^s = \int f\rho_d 4/3\pi r^3 \mathbf{F}' \cdot \mathbf{u}' d\mathbf{v} dT_d dy d\dot{y} \tag{4.30}$$

where $F' = (\mathbf{F} - \mathbf{g})$ and $(\mathbf{v} - \mathbf{u})$ is the relative velocity between the drop and the gas, u' the gas-phase turbulence velocity I_l and C_l are the internal energy and specific heat of liquid drops, respectively.

The spray equation, Eqn. (4.26) has been solved by some researchers using an Eulerian finite difference method (e.g., Gupta and Bracco [133]). However, this method has been found to be impractical since each independent variable has to be discretized on a grid, and with the 11 independent variables of Eqn. 4.26 the computer storage required becomes excessive (e.g., with a coarse mesh of 10 mesh points in each dimension, 10^{11} grid points would be needed). Recently many developments are reported that intend to reduce the complexity of solving the kinetic spray equation by moment transformations of droplet velocity and its size. These moments are closed by appropriate method known as direct quadrature method of moments (DQMOM) (see references in [134]). Although some improvement in modeling of sub-processes are reported [134, 135, 136], this is still in nascent phase, and requires substantial effort to incorporate all sub-models necessary to be used in real engineering applications.

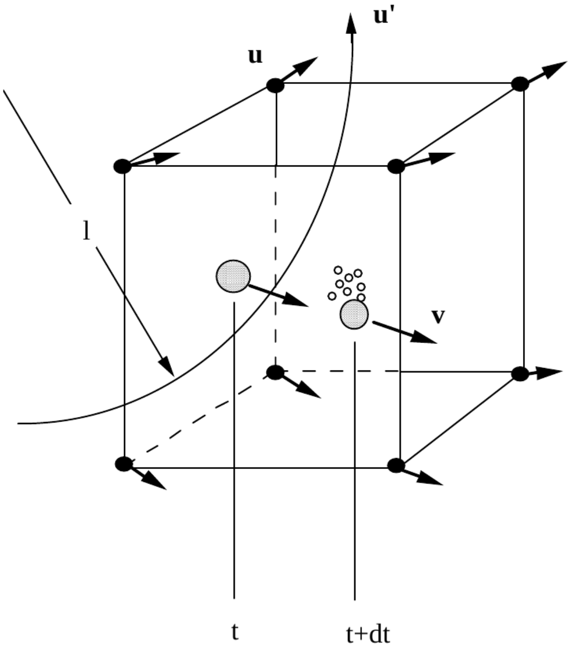

Figure 4.2: Schematic diagram of spray drop history in a computational cell during time dt [138]

The alternative to the above mentioned technique and a more practical solution is the Lagrangian Monte Carlo approach proposed by Dukowicz [137], and implemented in the KIVA code (Amsden et al.[42], Reitz [138]). In this method the paths of stochastic parcel of droplets are followed in physical, velocity, radius and temperature space (together with the drop distortion parameters). Mathematically, the spray Eqn. (4.26) is a hyperbolic equation, and the path represents characteristic in the solution space. As depicted in Figure 4.2, a drop is moved to its new location in physical space after a time interval, dt as given by:

$$\frac{d\mathbf{x}}{dt} = \mathbf{v} \tag{4.31}$$

The droplet velocity vector is determined by the relation

$$\frac{d\mathbf{v}}{dt} = \mathbf{F} \tag{4.32}$$

were the force per unit mass **F**, on the droplets (see Eqn. 4.26) depends upon the drag and body force. The drag depends upon the droplet relative velocity in gas. For the evaporating spray, the rate of change of droplet radius is determined as:

$$\frac{dr}{dt} = \Re \tag{4.33}$$

where, the quantity $\Re$ is derived from the vaporization correlations, which will be further discuss in detail in next chapter. The spray breakup and droplet-droplet interaction is also key parameter that influences the spray profile, this effect can be expressed as:

$$df = \left(\dot{f}_{coll} + \dot{f}_{break}\right) dt \tag{4.34}$$

Modeling the droplet-droplet interaction requires to take into account relevant interaction regimes to allow for resolving all possible interactions, more detail description will be provided in next chapter for adopted methodology.

In the stochastic particle model of Dukowicz [137], each parcel represents a number of identical drops, each with the same values of droplet velocity, radius, temperature, and droplet distortion and turbulent eddy parameters. Since it is an stochastic model, the collection of parcels in the computational domain represents the real spray droplet number distribution, and with sufficient large number of parcels the statistics are improved.

4.2.2 Spray atomization model

The atomization is very primitive and vital process, that has a strong influence on spray vaporization rates as it determines the final droplet size and hence it increases the total surface area of liquid fuel. This help to achieve relatively faster vaporization, that is desirable for most of the IC-engine applications. Thereby atomization is described as consisting of primary and secondary atomization mechanisms, that are described by standard models, namely the linear instability sheet atomization (LISA) model [96] for primary atomization for hollow cone GDI, Kelvin-Helmholtz instability (KH) model for cylindrical-orifice nozzle, while for the secondary atomization Taylor-analogy breakup (TAB) model [38].

4.2.2.1 Primary atomization

The original KIVA4-mpi code does not have any primary atomization model. It includes only secondary atomization model as described in the next section. However, considering the importance of the primary atomization model (1) to provide initial conditions to the secondary atomization model, (2) to avoid unnecessary model tuning exercise for each nozzle applications and (3) to improve the better predictive capability of the injection model, it is highly recommended to integrate a primary atomization in KIVA4-mpi code. The complete description and implementation of the primary atomization model for different sets of nozzle applications are discussed in the next chapter.

4.2.2.2 Secondary atomization

The Taylor-analogy breakup (TAB) suggested by O'Rourke et al. [38] is used in KIVA4-mpi code for secondary atomization of droplets formed during primary atomization. The model is based on the assumption of competitive contribution from viscous, surface tension, and aerodynamics forces. The droplet undergoes deformation similar to linear spring mass-damped system. When the deformation is sufficiently high, it results in droplet breakup. The motion of equation for the droplet deformation is given by

$$\ddot{y} = \frac{C_F}{C_b}\frac{\rho_g}{\rho_l}\frac{U^2}{r^2} - C_k\frac{\sigma}{\rho_l r^3}y - C_d\frac{\mu_l}{\rho_l r^2}\dot{y} \tag{4.35}$$

where ρ_g, ρ_l, μ_l and σ are the gas density, liquid density, liquid viscosity and surface tension, respectively. The described Eqn. (4.35) is very similar to that of a damped and forced harmonic oscillator. In this Equation, $y = x/C_b r$, where x is the displacement of the equator of the droplets from its equilibrium position. The breakup occurs if $y > 1$. After the breakup the Sauter mean diameter (SMD) of the new droplets is obtained by the law of energy balance.

$$SMD = \frac{D_D}{1 + 2C_k C^2{}_b/3 + (4C^2{}_b - C^2{}_v C^2{}_b)\,(\rho_l r^3/6\sigma)} \tag{4.36}$$

where D_D is described in Eqn. (5.11), the dimensionless constants in TAB model are $C_b = 0.5$, $C_d = 0.5$, $C_k = 0.5$, $C_F = 1/3$, and $C_v = 1.0$. This model is already available in KIVA4-mpi code and has been validated in [90]. In the TAB model, the droplet deformation is expressed by the dimensionless deformation $\mathbf{y} = 2\mathbf{x}/\mathbf{r_n}$, where $\mathbf{x}$ describes the deviation of the droplet equator from its underformed position (see Figure 4.3) and r_n is the initial droplet radius. In the following r_n will be noted r as in Figure 4.3. Droplet breakup occurs if the quantity y exceed the unity.

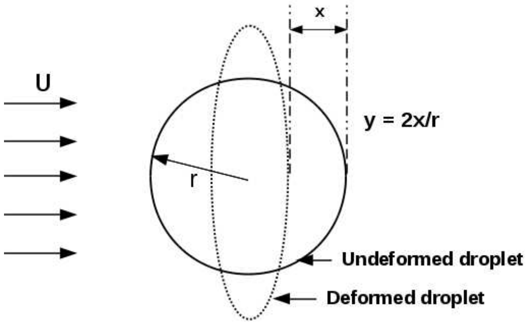

Figure 4.3: Schematic of particle distortion for the TAB model

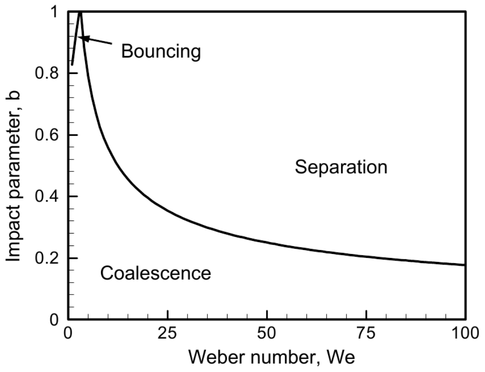

Figure 4.4: A basic collision regimes as described by O'Rourke [43]

$$m\ddot{y} + d_s\dot{y} + ky = \mathbf{F_s} \tag{4.37}$$

$$\frac{\mathbf{F_s}}{m} = C_F \frac{\rho_\mathbf{g} \mathbf{U}_{rel}{}^2 r}{\rho_\mathbf{l}} \ , \quad \frac{d_s}{m} = C_D \frac{\mu_l}{\rho_l r^2} \ , \quad \frac{k}{m} = C_k \frac{\sigma}{\rho_l r^2} \tag{4.38}$$

The analytical solution of the ODE (4.37) can be expressed as :

$$y\left(t\right) = \frac{\mathbf{We_g}}{12} e^{(t/\mathbf{t_d})} \left[\left(y_0 - \frac{\mathbf{We_g}}{12} \right) \mathbf{cos}\omega\mathbf{t} \left(\frac{y_0}{\omega} - \frac{\left(y - \frac{\mathbf{We}_g}{12} \right)}{\omega \mathbf{t_d}} \right) \mathbf{sin}\omega\mathbf{t} \right] \tag{4.39}$$

$$\mathbf{t}_d = \frac{2}{5} \frac{\rho_l r^2}{\mu_l} \ , \quad \omega = \frac{\mathbf{C}_k \sigma}{\rho_l \mathbf{r}^3} - \frac{1}{\mathbf{t_d}} \ , \quad \mathbf{A}^2 = \left(y - \frac{\mathbf{We_g}}{12} \right)^2 - \left(\frac{\dot{y}}{\omega} \right)^2 \tag{4.40}$$

where ω, $\mathbf{t}_d$ and $\mathbf{A}$ represent the frequency of oscillation, breakup time and amplitude of oscillation, respectively.

From the energy and mass balance, the new droplet can be calculated using the following relation

$$\frac{\mathbf{r}_{parent}}{\mathbf{r}_{child}} = \frac{7}{8} + \frac{1}{8} \frac{\rho_l \mathbf{r}_{Parent}{}^3}{\sigma} \dot{y}^2 \tag{4.41}$$

where the subscript "parent" represents the droplet radius before breakup, while the subscript "child" represents the new born or new calculated droplet radius.

4.2.3 Droplet collision model

In general, the fuel injection processes involve dense flow of large number of fuel droplets with wide range of relative velocity among each other. Therefore, the probability for the droplet-droplet interactions is very high. This ultimately influences final droplet distribution and spray profile. The collision model in KIVA4-mpi code is commonly based on the model proposed by O'Rourke [43], a two regimes binary collision model. It accounts for stretching separation and permanent coalescence as shown in Figure 4.4. Due to this fact, it over-predicts the droplet coalescence process, since it does not take care of other possible modes of droplet interactions, such as bouncing and reflexive separation. A comprehensive collision model has been proposed by Munnannur et al. [44]. This was further modified to take into account the exact momentum exchange during the collision by Pischke et. al. [55]. The resulting model accounts for all relevant collision regimes (i.e. coalescence, stretching separation, reflexive separation and collision).

However, the model is based on binary collision of droplets in given control volume (CV). Therefore it becomes highly sensitive to control volume size and types (e.g. structure/unstructured). This grid dependency has been reduced by incorporating additional mesh for spray calculation other than regular mesh for gas phase solver [46]. When multiple injection points are defined, as it is very common in modern IC engine applications this becomes impracticable. A suitable improvement is necessary and will be realized in section 5.2.

4.2.4 Spray evaporation model

In the KIVA4-mpi code the evaporation behavior of the fuel spray is described by a detailed multi-component evaporation model [95] with possibility to solve for 100 fuel components. As the fuel used in iso-octane, a multi component model is not necessary. To reduce the complexity of the calculations in the present work, a single component evaporation model based on the lumped-body theory is chosen [42]. The application of the complex model is work in progress. In the model used, the energy balance on the droplet surface due to heat transfer from the surrounding and latent heat evolution due to evaporation, can be formulated as Eqn. (4.42).

$$Q_t = \dot{m}_f L + \dot{Q}_i \tag{4.42}$$

In Eqn. (4.42), the quantity L is the latent heat of liquid droplets. The heat conduction rate from the droplet surface into the droplet interior is expressed as

$$\dot{Q}_i = 4\pi r^2 h_c (T_\infty - T_s) \tag{4.43}$$

where, r is the droplet radius, T_∞ and T_s are the ambient and droplet surface temperature, respectively. The heat transfer coefficient h_c depends on the Nusselt number given by

$$Nu = \left(2.0 + 0.6 Re^{\frac{1}{2}} Pr^{\frac{1}{2}}\right) \frac{ln\,(1 + B_T)}{B_T} \tag{4.44}$$

where the Reynold's number $Re = 2\rho_g U r / \mu_g$ and Prandtl number $Pr = \mu_g C_p / K_g$, and ρ_g, μ_g, C_p, K_g being the air density, viscosity, heat capacity and heat conductivity, respectively. B_T is the Spalding heat transfer number $B_T = C_p\,(T_\infty - T_s)/L_{eff}$. The mass transfer from the droplet in Eqn. (4.42) is given by the correlation suggested by the Frossling correlation [42].

$$\dot{m}_f = 2\pi r (\rho D)_g B_m Sh_d \tag{4.45}$$

where $(\rho D)_g$ is the fuel vapor diffusivity in the air, and Sh_d is the Sherwood number that accounts in the presently used convection model for boundary layer effects. It was determined by the following expression

$$Sh_d = \left(2.0 + 0.6 Re^{\frac{1}{2}} Sc^{\frac{1}{2}}\right) \frac{ln\,(1 + B_m)}{B_m} \tag{4.46}$$

where the Schmidt number $Sc = \mu_g/(\rho D)_g$, and the Spalding mass transfer number $B_m = (Y_s - Y_\infty)/(1 - Y_s)$. More details about the evaporation model used are provided in [95]. The evaporated mass fraction is transported with an appropriate transport equation in which the SGS scalar flux vector is modeled by a simple gradient assumption [95].

5 Model improvement in KIVA4-mpi code

In the fuel injection process, both the primary and secondary atomization mechanisms involve entirely different dynamics for droplet formation and breakup. It is very difficult to incorporate both mechanisms in a single atomization model, therefore separate models are required for individual mechanism. Moreover the primary atomization mechanism is highly dependent on the kind of nozzle used for specific application. These limitations lead to distinguish primary atomization model for specific nozzle and to couple with a general secondary atomization model. In the present study, two nozzle configurations are considered: a multi-hole cylindrical orifice nozzle and second an outward opening hollow cone injector. The secondary atomization mechanism is described in both cases by the TAB model discussed in previous section, the adopted primary atomization model is discussed in next sections for both the nozzle applications.

5.1 Primary atomization model

5.1.1 Multi-hole GDI spray

The primary breakup model considered for multi-hole GDI is based on the Kelvin-Helmholtz (KH) instability approach (see Figure 5.1). Such instabilities can occur, when velocity shear is present within a continuous fluid, or when there is sufficient velocity difference across the interface between two fluids. One example is wind blowing over a water surface, where the wind causes the relative motion between the stratified layers (i.e., water and air). The instability will manifest itself in the form of waves being generated on the water surface. Similarly in the case of fuel injection there is large difference in the interface velocity between the high speed fuel jet and the surrounding air. The Kelvin-Helmholtz (KH) instability breakup model assumes a circular liquid column of infinite extent in axial direction emanating into a stationary incompressible gas. The maximum growth rate and the corresponding wavelength is determined from the numerical solution of the dispersion relation equation [37].

$$\frac{\Lambda_{KH}}{r} = 9.02\frac{\left(1+0.45Z^{0.5}\right)\left(1+0.45T^{0.7}\right)}{\left(1+0.87{We_g}^{1.67}\right)^{0.6}} \tag{5.1}$$

$$\Omega_{KH}\left[\frac{\rho_f r^3}{\sigma}\right] = \frac{\left(0.34+0.38{We_g}^{1.5}\right)}{\left(1+0.4T^{0.67}\right)\left(1+Z\right)} \tag{5.2}$$

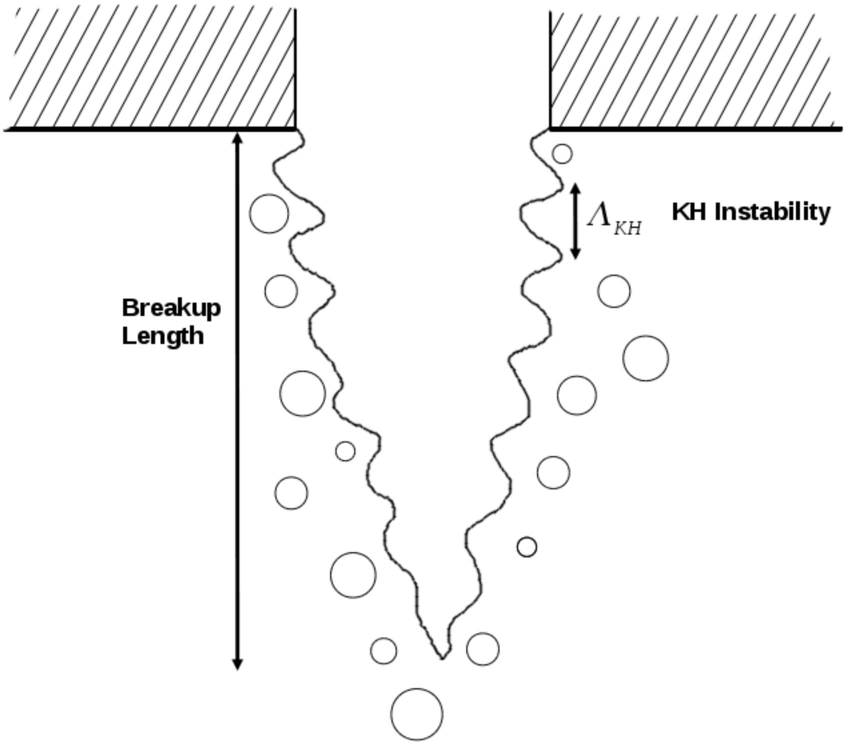

Figure 5.1: Schematic of primary atomization with Kelvin-Helmholtz (KH) model

$$Z = \sqrt{\frac{We_f}{Re_f}}\ , \quad T = Z\sqrt{We_g} \tag{5.3}$$

$$We_l = \frac{\rho_l \mathbf{U}_{rel}^2 r}{\sigma}\ , \quad We_g = \frac{\rho_g {\mathbf{U}_{rel}}^2 \mathbf{r}}{\sigma}\ , \quad Re_l = \frac{\rho_l \mathbf{U}_{rel} \mathbf{r}}{\mu}\ , \quad Re_g = \frac{\rho_g \mathbf{U}_{rel} r}{\mu} \tag{5.4}$$

where r is the radius of droplets and U_{rel} is the relative velocity between droplet and air. The subscript l and g represent the parameters for liquid and gas, respectively. In the model, the critical radius r_c is the radius of droplets after breakup time τ_{KH} as given below [98].

$$r_c = 0.67\Lambda_{KH} \tag{5.5}$$

$$\tau_{KH} = \frac{0.726 B_1 r}{\Omega_{KH}\Lambda_{KH}} \tag{5.6}$$

where B_1 is the KH breakup rate coefficient. It is determined from some phenomenological models [98]. Under the assumption that the droplet radius reduces to the critical radius r_c during the breakup process, the radius of the droplet after breakup r_{new} can be calculated by using the relation

$$\frac{r - r_{new}}{dt} = \frac{r - r_c}{\tau_{KH}} \tag{5.7}$$

To couple this primary breakup model to a secondary droplet breakup one, it is important to determine the breakup length. Once the fuel is injected from the nozzle giving rise to high relative velocity between the jet and surrounding air, the primary breakup process undergoes within so called breakup length. On the other hand the relative velocity beyond the breakup length is considerably low and overall effect will be cumulative to all forces. Therefore the subsequent breakup of droplets will be governed only by the secondary breakup model. The breakup length defines obviously a clear switch parameter. The breakup length is calculated based on nozzle diameter d_0 and density ratio by using the equation proposed by Beale and Reitz [98],

$$L_b = \frac{1}{2}\mathbf{B}_1 d_0 \sqrt{\frac{\rho_f}{\rho_g}} \tag{5.8}$$

5.1.2 Hollow cone GDI spray

The injector modeled is a continental piezoinjector with outwardly opening nozzle, which represents one of the available GDI piezoinjector. In the Lagrangian particle tracking framework as stated before, there is not a universally applicable model available for primary atomization process. For hollow cone GDI, the primary atomization is modeled with the linear instability sheet atomization (LISA) model suggested by Senecal et al. [96]. The model is based on the assumption that, hollow liquid sheet is formed near the nozzle exit; the unstable liquid sheet breaks into ligaments, and ligament breaks to form primary droplets (see Figure 5.2). Thereby the characteristic breakup length of the sheet atomization is given by

$$L = U\delta = \frac{U}{\Omega} ln\left(\frac{\eta_b}{\eta o}\right) \tag{5.9}$$

where the quantity U is the droplet velocity, and $ln\left(\frac{\eta_b}{\eta o}\right)$ is given by the value 12 in the present study based on the work of Dombrowski and Johns [97]. After the ligament breakup, the diameter of ligaments is given by

$$d_L = \sqrt{\frac{16h}{K_{max}}} \tag{5.10}$$

where K_{max} is the wave number corresponding to the maximum growth rate Ω, and h is the film half thickness. Based on the assumption made by Dombrowski and Johns [97], the breakup will occur when amplitude of the unstable waves is equal to the radius of ligaments, and subsequently one drop will form according to the mass balance relation given by

$$D^3{}_D = \frac{3\pi d^2{}_l}{K_L} \tag{5.11}$$

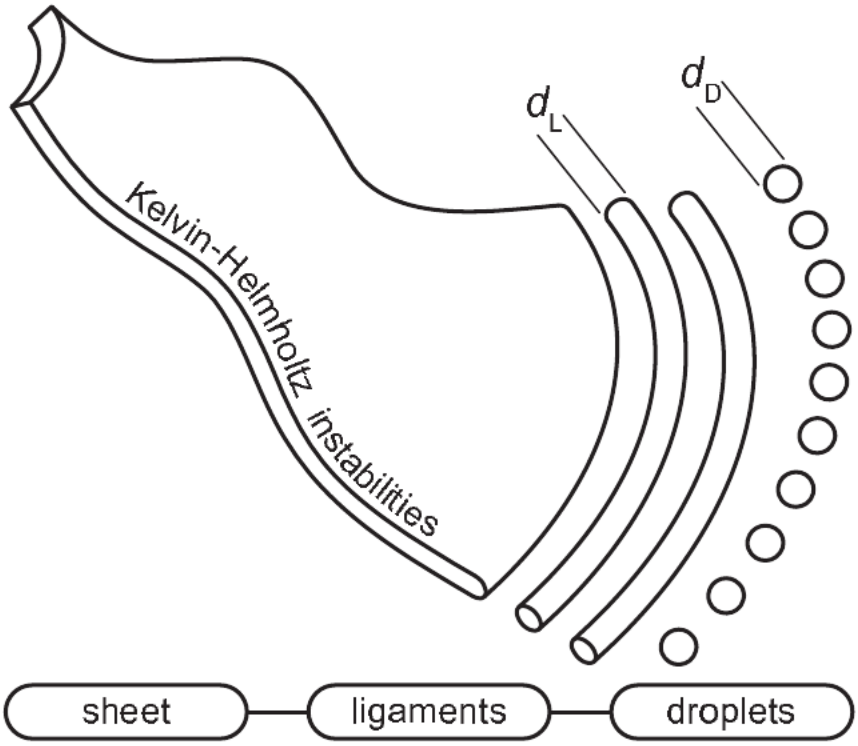

Figure 5.2: Schematic of LISA primary atomization model [55]

where the K_L is most unstable wavelength on the ligament and is given by

$$K_L d_l = \left[\frac{1}{2} + \frac{3\mu_l}{2(\rho_l d_l \sigma)^{1/2}} \right]^{1/2} \tag{5.12}$$

In Eqn. (5.12) ρ_l, μ_l and σ are the liquid density, viscosity and surface tension, respectively. The above expression in Eqn. (5.12) is the Weber's results for the wave number corresponding to the maximum growth rate for the breakup of a cylindrical viscous liquid column. This model has been integrated in KIVA4-mpi code and validated as reported in [90].

5.2 Improved droplet collision-coalescence model

As pointed out earlier, the collision models in KIVA4-mpi code are commonly based on the model proposed by O'Rourke [43], that accounts only for stretching separation and permanent coalescence. Due to this fact, it over predict the droplet coalescence. A comprehensive collision model has been proposed by Munnannur et al. [44], which accounts for all relevant collision regimes (i.e. coalescence, stretching separation, reflexive separation and collision). However, the model is based on binary collision of droplets in given control volume (CV). Therefore the model becomes highly sensitive to control volume size and types (e.g. structure or unstructured). The grid dependency can be reduced by incorporating additional mesh for spray calculation other than regular mesh for gas phase solver [46]. However, it becomes impracticable, when multiple injection points are defined, as it is very common in modern IC engine applications. The present work suggests a collision model based on the Munnannur et al. [44] model, while being independent of mesh size and type.

5.2.1 Reference collision model

The collision model suggested by Munnannur et al.[44] is used as reference model, without considering collision induced droplet breakup. The possible collision outcomes are shown in Figure 5.3. The collision regimes are represented by combined function of the collision Weber number We_{coll} and impact parameter B. In the present study, the impact parameter B is calculated statistically from the random number generated with uniform distribution of ζ by following the relation.

$$B = \sqrt{\zeta} \tag{5.13}$$

Four distinct regimes of collision (e.g. bouncing, stretching separation, reflexive separation, and coalescence) are defined in the shown Figure 5.3. The velocity interaction after the collision is given by the relation as described in Eqn.(5.14), where z is the ratio of relative velocity before and after collisions calculated for different collision regimes [55].

$$U_{i,k} = \frac{m_i u_{i.k} + m_j u_{j,k} + m_j u_{i,k} - u_{j,k} z}{m_i + m_j} \tag{5.14}$$

$$z = \frac{U_{i,k} - U_{j,k}}{u_{i,k} - u_{j,k}} \tag{5.15}$$

$$z_{coalescence} = 0.0 \tag{5.16}$$

$$z_{stretching} = \sqrt{\frac{B - B_{str}}{u_{i,k} - B_{str}}} \tag{5.17}$$

$$z_{reflexive} = \sqrt{1 - \frac{We_{rflx}}{We_{coll}}} \tag{5.18}$$

$$z_{bouncing} = 1.0 \tag{5.19}$$

where m is mass of droplets, U and u are the velocities of droplets before and after collision, indices i and j represent two interacting droplets, and k expresses velocity components (k = 1,2,3). The boundary for the stretching separation and reflective separation are defined as B_{str} and We_{rflx} as clearly shown in Figure 5.3.

5.2.2 Collision modification

In the new approach, droplet collision is made independent of CV, while improving the modified approach in [45]. Figure 5.4.a shows the possibility of the collision event in CV based approach. In this approach, even if the droplets are located in the extreme end in a control volume, collision

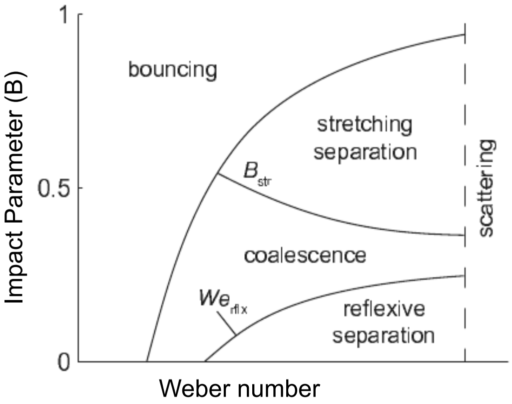

Figure 5.3: Collision regimes as described by Reitz and Munnannur [44] illustrated in [55]

will likely take place, irrespective of mesh size. Figure 5.4.b represents the no-collision case, even though droplets are very near to each other but in different CV. In the case of structured mesh, another form of artifact arises known as Clover leaf artifact as observed by Schmidt et al.[46]. This artifact has been attributed both due to mesh orientation and collision scheme used. Figure 5.4.c shows the recent approach for collision to take place, instead of considering the CV a spherical kernel is chosen at the geometric centre of each droplet. For the case, droplets falling inside the same kernel, the collision will take place irrespective of CV. This way the collision model becomes insensitive to the mesh size and type. The collision frequency from the new scheme with kernel radius of R_{ker} is described as:

$$\lambda = \frac{n_{max}\pi \left(r_{max} + r_{min}\right)^2 U_{rel}}{V_{ker}} \tag{5.20}$$

where n_{max} represents the number of droplets in a populous parcel, r_{max}, and r_{min} the droplet radius in populous and less populous parcel, U_{rel} the relative velocity between droplets and the V_{ker} is the kernel volume calculated as

$$V_{ker} = \frac{4}{3}\pi {R^3}_{ker} \tag{5.21}$$

It has already been observed [45] that the collision model is highly sensitive to the value of V_{ker}. If V_{ker} is calculated with semi-deterministic approach as stated [45], it becomes highly computational intensive and results further deteriorate if the mesh is fine. While, in case of constant V_{ker}, it is difficult to obtain generalized value of R_{ker}. In the present simplified approach the R_{ker} is chosen dynamically so that the value V_{ker} is equal to four times of the control volume where droplets exist. In this way the equivalent value of R_{ker} becomes twice and collision model can search for potential collision partners in the neighboring CVs. To avoid large value of R_{ker} in coarser mesh region, the maximum value is set to be 10 times of the nozzle slit diameter (in present case *0.25 mm*). In this way the mesh dependency of collision model is suppressed and is computationally cheaper to calculate R_{ker}, Furthermore the higher limit of R_{ker} restricts value of V_{ker} so that the collision model does not search excessively for large number of potential collision partners. The

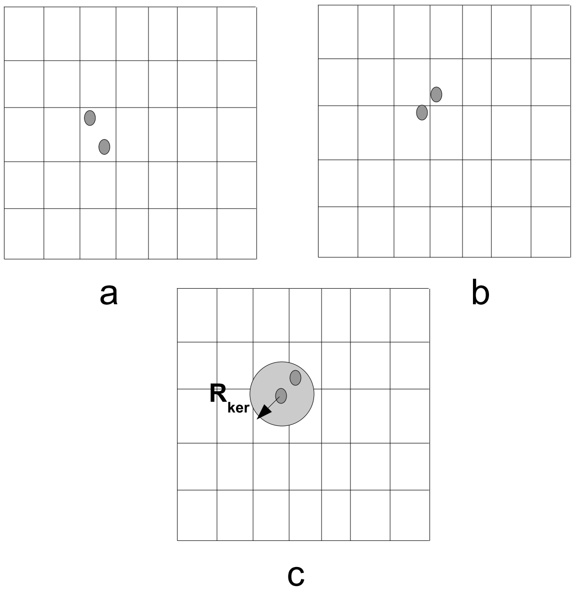

Figure 5.4: Schematic of collision possibilities with (a) classical control volume based approach (collision possible) [44] (b) no collision possible [44] (c) kernel based new approach

model improvements is highlighted in the result section.

5.3 Wall film formation

The importance of the spray-wall interactions has been largely pointed out in section 3.1. In case of wall temperature between freezing and boiling temperature, heat transfer has minor effect on the spray impact, Therefore, affect of the temperature on the impact can be dis-regarded, and the possible interaction outcome in mainly droplet deposition and droplet splash. With certain droplet velocity below critical value the droplet spread on the wall and form wall film by loosing part of its kinetic energy in to viscous dissipation and partly in to surface tension effect. while in case of increased impact velocity, the viscous dissipation in no longer able to absorb the kinetic energy and surface tension is not able to maintain the droplet cohesion. Thus droplet get dis-integrated to smaller droplets, partly get splashed out from the wall surfaces and the amount of remained droplets on wall mainly depends on the impact velocity. In case of high wall temperature, the Leiden-frost effect is observed: the droplet surface in contact with significantly hot wall above Leiden-frost temperature, produces an insulating and cushioning vapor layer which keeps off the droplet from being evaporated quickly, in such scenario with low impact velocity, the vapor cushion prevents the droplet from wetting the wall surface, thus preserving its cohesion, therefore the droplet rebound from the wall surfaces. Another scenario which is not relevant to present study is when the wall temperature is below freezing temperature, the impinged droplet stick and freeze on the surface and form layers of icing wall.

In the present section, the spray application is solely for the IC-engine configurations under study. In the case of GDI the fuel is injected directly in the combustion chamber. The injected fuels must be vaporized and mixed properly with the air charge in order to have desirable combustion and engine power. In most of IC-engine designs, the fuel spray may impinge on engine surfaces (e.g. piston crown, cylinder liner, valves) before vaporization and mixing are complete. Spray impingement has been shown to influence engine performance and emissions in both compression ignited (CI) and spark ignited engines (SI) [56]. The impingement mostly results in formation of wall film on engine surface, that influence the engine performance especially in transient control. It is a major factor affecting fuel-air ratio due to time lag resulting from a film of liquid fuel deposited on the piston surface. The time lag results in decreased engine response, increased fuel consumption and increased HC emissions. In order to improve the engine performance, it is essential to avoid the formation of liquid film on/inside the engine cylinder by design and parametric optimization. The original KIVA4-mpi code has wall film model suggested by O'Rouke et al. [67], that includes droplet splash, film spreading due to impingement forces, and motion due to film inertia. It does not take into account the effect of high wall temperature, which is very common in case of IC-engine configurations.

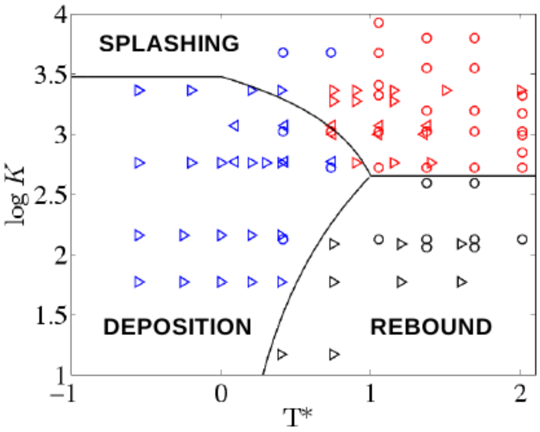

Figure 5.5: $\log K - T^{\star}$ diagram plotted by [66]: Experimental conditions from [60] (left oriented triangles and circles) and [64] (right-oriented triangles) and observation:deposition (blue), splashing(red) and rebound(black) regimes [see also Figure 3.2]

In the case of spray wall interaction, it is commonly observed that the Weber number is known to be representative of the impact regime. Moreover, viscous dissipation plays crucial role in attenuation of the surface instabilities, and that effect can be represented by the Reynold's number.

$$We_n = \frac{\rho_l {U_n}^2 d}{\sigma_l}, \quad Re_n = \frac{\rho_l U_n d}{\mu_l} \tag{5.22}$$

The combined effect of the droplet kinetic force, viscous force and surface tension can be described by single dimensionless parameter K to demarcate the regime of impact in case of normal wall temperature as expressed in following equations.

$$K = We_n.Oh^{-\beta}, \quad Oh = \frac{\sqrt{We_n}}{Re_n} = \frac{\mu_l}{\sqrt{\rho_l d \sigma_l}} \tag{5.23}$$

where the exponent parameter β has several values in literature. However in the present study it is taken as 0.25, which is in agreement with the observation made by Mundo et al. [139] and

Marengo et al. [140].

Finally, the influence of the wall temperature is represented by dimensionless number $T^\star$, which is a function of the liquid boiling and Leiden-frost temperatures and wall temperature. The wall temperature above the Leiden-frost temperature changes the evaporation dynamics considerably, because the formation of the thin vapor film between the liquid droplets and the heated wall, which decreases the the rate of droplet evaporation. As discussed in the section 3.1, it act as a cushion between the impinging droplets and wall surface ultimately resulting in droplets to bounce back.

$$T^\star = \frac{T_W - T_B}{T_L - T_B} \tag{5.24}$$

Boiling and Leiden-frost temperatures generally depend on the static air pressure. Therefore, $T^\star$ also represents the effects of air pressure, in turn takes care of the influence of the static pressure.

The combined effect of droplet parameters and wall temperature is depicted in Figure 5.5 as a spray impact regime with combined function of $\log K - T^\star$. For the wall temperature below the Leiden-frost temperature ($T \leq {T^\star}_1$), the relations $K_r(T^\star)$ and $K_s(T^\star)$ determine all three impact regimes for range of $0 < T^\star < {T^\star}_1$ as below:

1. if $K < K_r(T^\star)$ then the drop will bounce of solid surface with slight amount gets evaporated.
2. if $K_r(T^\star) < K < K_s(T^\star)$ then the drop will be deposited on the wall by coalescence with other droplets or wall-film and subsequently gets evaporated after picking up heat from the wall surface.
3. if $K_s(T^\star) < K$ then droplet will be splashed out into cloud of smaller droplets.

For the wall temperature ($T > {T^\star}_1$), the Leiden-frost effect will be prominent, only two modes of impact are observed as below,

1. $K < K_r(T^\star)$ then the droplet will bounce and partially evaporates.
2. $K > K_r(T^\star)$ then the droplet splashes and partially evaporates.

The regime plot (see Figure 5.5) is derived from the least square fit of the experimental data with the following expressions:

$$K_s\left(T^\star\right) = \begin{cases} K_0 & \text{if } T^\star < 0 \\ K_0 + \frac{T^\star}{T_1^\star}\left(K_1 - K_0\right) & \text{if } T^\star < 0 \\ K_1 & T_1^\star < T^\star \end{cases} \tag{5.25}$$

where $T_1^\star = 1.0$, $K_0 = 3000$ and $K_1 = 450$ and

$$K_r\left(T^\star\right) = \begin{cases} 0 & \text{if } T^\star < 0 \\ K_1\left[\frac{T^\star}{T_1^\star}\right]^\gamma & \text{if } 0 < T^\star < 0 \\ K_s\left(T^\star\right) = K_1 & T_1^\star < T^\star \end{cases} \tag{5.26}$$

where, with the value $\gamma = 3$, Eqn.(5.25) and Eqn.(5.26) together define the comprehensive spray impact regimes for all the value of the K and $T^\star$.

6 Engine geometry and new meshing strategy

In the CFD calculation and analysis, grid generation is one of the vital, primitive and complex task. Most of the time, it is difficult to generate mesh conforming to exact geometry, therefore the modification on the shape of the geometry to certain degree of assumption is permitted until it does not adversely affect the essential feature of the fluid flow during CFD analysis for given engineering configuration. There are numerous tools to generate mesh for a given geometry. However, the mesh file format depends mostly on the CFD software being used for particular application. Sometime the meshing itself is difficult and very much time consuming. In that case, it becomes vital consideration for overall time line of any CFD analysis. The modern IC-engines inherently features complex geometry, which generally consists of moving piston and canted valves, intricate shape of cylinder head, valves, piston crown and bowl, etc. For such an engine geometry, the grid generation for KIVA code is one of the most complex and difficult task. Only few meshing tool conform to the KIVA mesh output or it has interface to generate the grid for KIVA. Since our focus is not to modify the KIVA code, which requires extensive modification inside the KIVA code, a different strategy is rather adopted for grid generation with as little as modification in the current form of KIVA code. In this chapter, an overview of traditional mesh generation technique or KIVA code is provided, then a new meshing strategy is presented and demonstrated.

6.1 Engine simulation features

While carrying out CFD simulation of an IC-engine, following engine parameters should be considered

1. Squish: It is the region inside engine cylinder which varies due to piston movement along the stroke length with respect to engine crank angle
2. Intake/exhaust valves: The transient movement of intake/exhaust valve opens and closes gas path to/from the cylinder
3. Bowl: It is the volume on the piston surface due to the shape of the piston crown provided to achieve required flow profile and compression volume
4. Dome: It is the region between the top dead centre (TDC) of piston position and and cylinder head

The first two parameters are the important to be considered while setting up mesh for the CFD simulation of an IC-engine configuration. To represent real IC-engine behavior, an appropriate subroutine is required to be incorporated in the CFD code for the piston, and valve surface movement with respect to engine crank angle. Although KIVA has its own mesh movement routine for piston and valve surfaces, a particular consideration is required for good quality mesh during mesh generation.

6.1.1 Grid generation with K3PREP

The KIVA preprocessor known as KIVA-PREP is generally used to generate mesh. It is based on the text input to generate the required mesh for given geometry, in which the whole geometry is divided in multiple block. Therefore, it is difficult to provide input for individual block on text to generate mesh for intricate shaped engine geometry with complicate shape of piston, cylinder head, valve, ports. Therefore , it becomes redundant to use KIVA-PREP to generate mesh for modern engine geometry. However, Ansys ICEM-CFD provides another alternatives for mesh generation, which has user friendly graphic user interface (GUI), which is necessary to generate good quality mesh for complex geometry. Its relevant advantages and drawbacks are described in next section.

6.1.2 Ansys ICEM-CFD: A meshing tool

The ICEM-CFD is a commercial software package from Ansys. It is a comprehensive meshing tool able to create complex geometry with intricate details. It allow to generate mesh for given geometry with both hexahedral and tetra mesh, with feasibility to export mesh file for varieties of CFD softwares. It supports import of CAD surfaces and then automatically generates a mesh around the geometry. The ICEM-CFD has an interface for KIVA-code which includes different versions (KIVA3, KIVA-3V, KIVA4 and KIVA4-mpi) for setting up the boundary conditions and preparation of the grid file in required format for KIVA. The important and salient features of the ICEM-CFD can be summarized as follows (a) capability to import/export CAD geometries with various format; (b) very easy geometrical modification having possibility to add, delete and modify existing geometry or its parts; (c) blocking module has option to generate, delete/edit blocks conforming intricate geometry with possibility to generate O-grid/L-gird/V-grid required for respective geometrical shape; (d) grid refinement can be easily managed with control on mesh distribution for important region on geometry; (e) features to check and improve the quality of the mesh with a variety of criteria, that assists to specify and fix possible problems. The main drawback in the context of KIVA code is that, meshing with the ICEM-CFD is still a time-consuming task and depends mainly on the user's past experience.

In the next section, an overview is provided for both versions of KIVA (KIVA-3V and KIVA4-MPI) with their respective benefits and limitations with ICEM-CFD, then a new meshing strategy is demonstrated in real engine configurations.

6.2 Overview of KIVA-3V

KIVA-3V code is based on cartesian co-ordinate especially designed for the engine simulation. Appropriate subroutine is defined for the injection and ignition timing/duration together with routines for mesh movement for piston and valve surfaces. To be able to achieve adequate mesh quality during mesh movement, in each computational time-step a complex mesh snapping (layers of mesh deactivated and activated whenever required) and rezoning (node re-arrangement for good mesh orthogonality/distribution) techniques are required. All these require proper indexing of all the neighboring nodes and control volume. In the context of KIVA-3V, this can be only achieved with the block structured hexahedral mesh without any O-grid by using even Ansys ICEM-CFD. Figure 6.1 represents the projected mesh on the piston of an engine with 2 valves, since it is generated without O-grid, the mesh orthogonality is lost at the corner of the each block (see the 4-corners of valves and piston marked with red circles). It becomes worse when the mesh is refined further. Figure 6.2 clearly shows, the elements are not orthogonal in the corner region marked with red circles, thus it limits the maximum number of control volume to be used. This way the meshing flexibility and mesh quality is considerably compromised for the relatively complex engine geometry, that may ultimately influence the simulation speed and quality of results even with the use of refined CFD models.

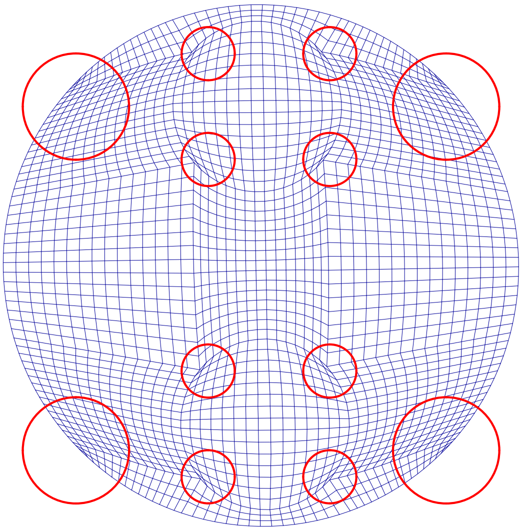

Figure 6.1: Projection of mesh on piston for engine with 2-valve (coaser mesh)

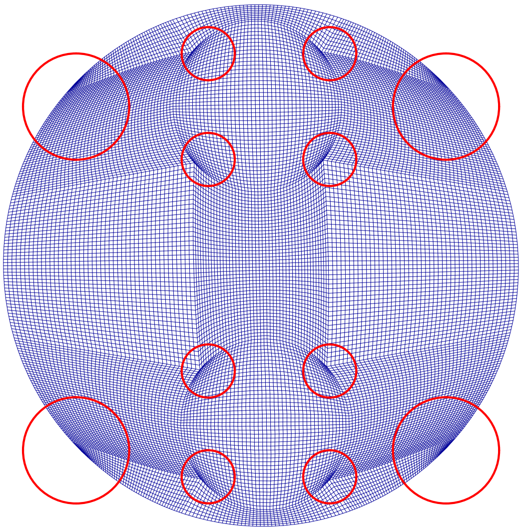

Figure 6.2: Projection of mesh on piston for engine with 2-valve (finer mesh)

6.3 Overview of KIVA4-mpi

The KIVA4-mpi retains all the features of KIVA3V, and in addition it allows mesh generation with O-grid and to a certain degree an unstructured mesh using ICEM-CFD, this way it provides very good flexibility to generate mesh for a complex geometry. The most prominent feature of the KIVA4-mpi is to be able to perform parallel computations, making it highly suitable to carry out multi-cycle engine simulation relatively quick. However, it accepts O-grid and unstructured mesh only when moving mesh problem is not being solved. Therefore, in the context of generating mesh for a engine simulation with moving piston and valve surface, there is no improvement in KIVA4-mpi and hence the essential feature for the KIVA4-mpi to run in parallel processor mode can not be exploited properly for larger and refined IC-engine configurations.

The above mentioned meshing problem arises mainly because the ICEM-CFD is unable to transport a variable that is required to identify all the immediate neighboring nodes when O-grid is used. It can not resolve the indices (top, bottom, left, right, front and back) for neighbor in corner of O-grid which will have only 3-neighbors instead of required 4-neighbors. This variable is very important while solving the moving mesh problem in KIVA code, as it helps to re-refine the mesh by adjusting the given node in all three co-ordinate directions based on its neighboring node positions and this way it preserve the mesh orthogonality while mesh movements.

6.4 Grid generation with ICEM-CFD

To rectify the difficulty mentioned in the above section, a considerable amount of effort is required to modify the KIVA4-mpi code to work in compatible way with the limitations of ICEM-CFD. In the present work, instead of modifying the complete code, a new strategy is devised to generate mesh in ICEM-CFD which retains all the important and enhanced features of the KIVA4-mpi. However, this has only limitation of mesh rezoning along the mesh movement direction, while being sufficient to simulate the moving piston and valve geometry in the case of IC-engine simulation.

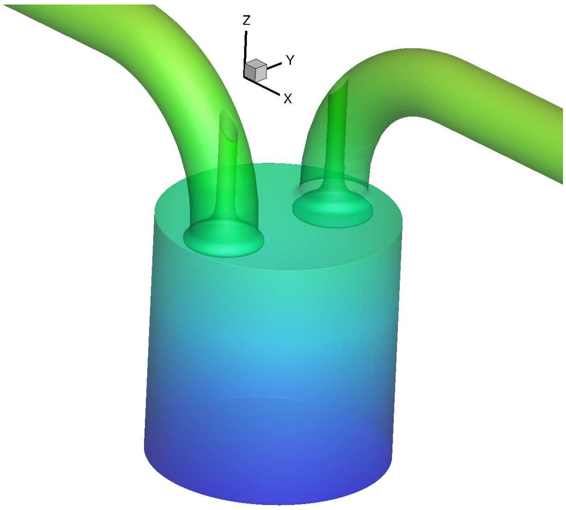

Figure 6.3: Example engine geometry; with cylinder squish, intake/exhaust valves and ports [141].

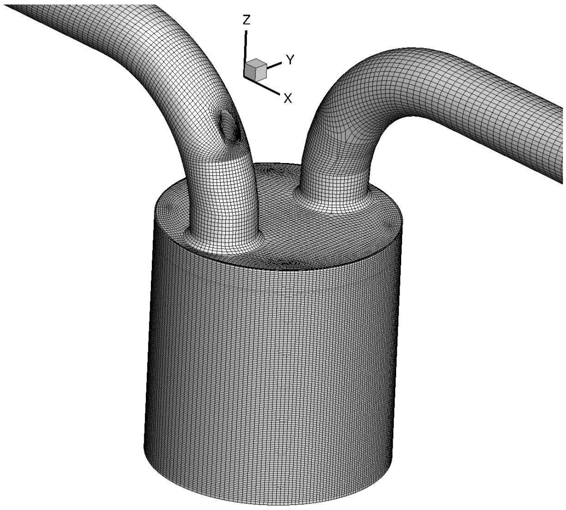

Figure 6.4: Final mesh (Hexahedral mesh) generated in ICEM-CFD [141].

The real engine geometry chosen to demonstrate the new method is shown in Figure 6.3 and the corresponding final mesh is shown in Figure 6.4. Figure 6.5 displays the detail engine parts. It has flat circular piston with two parallel valves representing the intake valve and exhaust valve, respectively. In the following section, all individual steps for the new meshing technique are described in details. In the new approach, the meshing strategy is adopted by considering in advance all the geometric features of the engine such as valves (number, size & its position), piston crown and cylinder head shape, squish and clearance length.

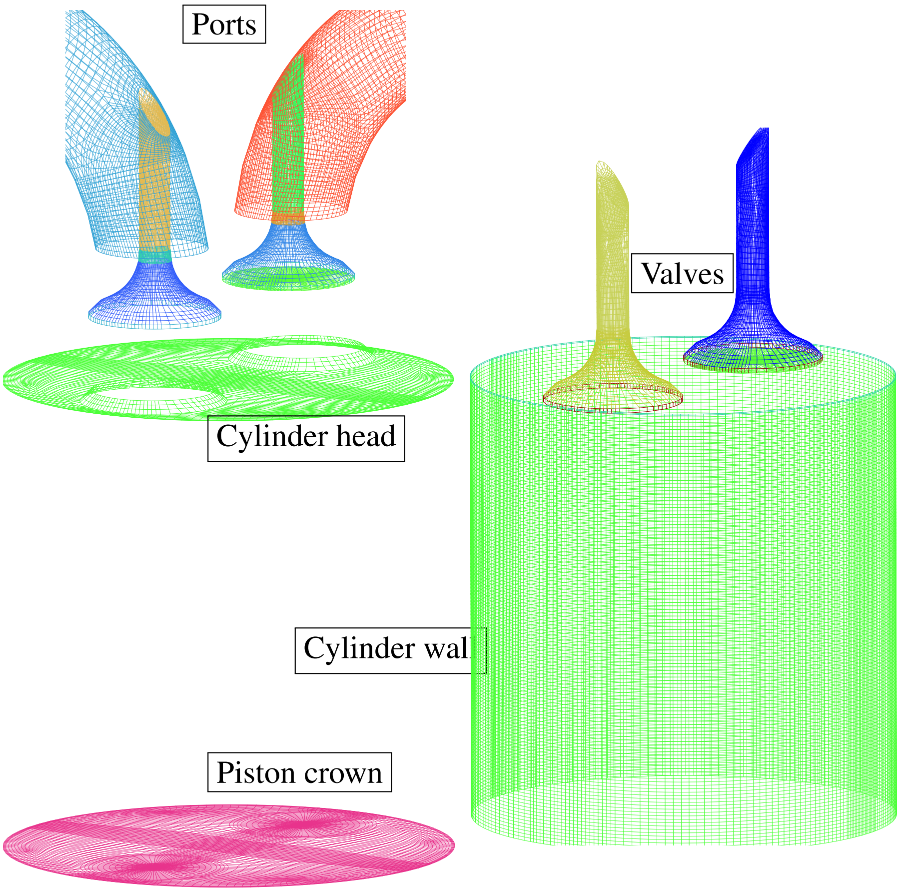

Figure 6.5: Details of the engine geometry with two parallel valves

6.4.1 Piston meshing

Figure 6.6 shows the piston surface and project valve curves (green curves) on the piston surfaces. As stated in previous section, to generate mesh for the two valves and corresponding ports in later stages, a prior consideration of valve geometry is required while meshing the piston surface. The big yellow curve in Figure 6.6 represents the dimension of the circular piston. For the two valves, the inner most curve is required to mesh the valve stem, while the other two curves are required to develop the valve surfaces (valve top and valve bottom surface) for setting up proper boundary conditions.

In the very first stage we require to generate a planner mesh for piston surface. We are not providing here a detail explanation of every individual steps taken in ICEM-CFD, rather we expect reader has basic understanding of all the tools available for geometry, blocking and meshing in ICEM-CFD. Figure 6.7 shows the final associated 2-D blocking of the piston surface. The initial single block is split in many small blocks to conform the relevant geometry. Appropriate O-grids are generated for all circular sections and all the edges are properly associated to respective curves, so that it retains the original dimension and shape of the curves. For the purpose of comparison, the adjacent Figure 6.8 represents the traditional KIVA engine blocking method without any O-grid.

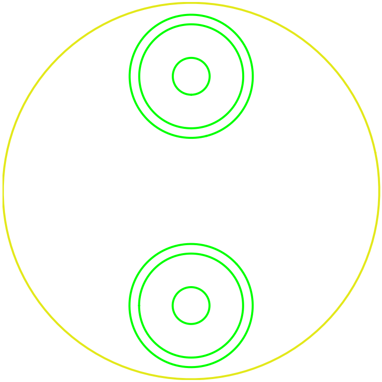

Figure 6.6: Curves for the piston and projected valve edges on piston surface (engine with 2-valve)

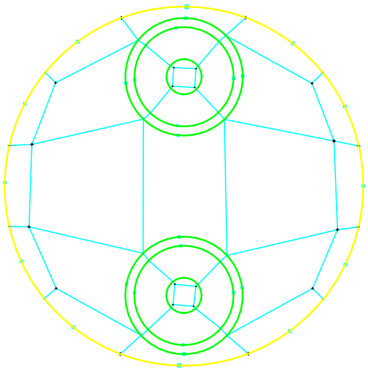

Figure 6.7: O-grid blocking (light blue color) to generate mesh for piston (engine with 2-valve)

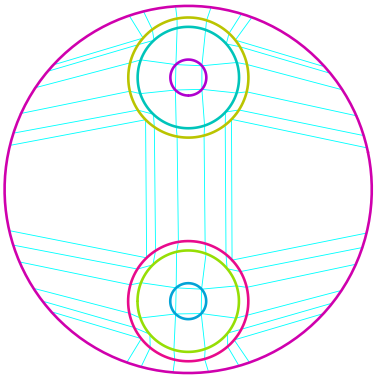

Figure 6.8: Traditional structured blocking (light blue color) to generate mesh for piston (engine with 2-valve)

Once the blocking is over, it is required to provide sufficient number of nodes for each edges to have desired mesh quality (fine/coarse mesh). Figure 6.9 represents the final mesh for the piston surfaces after relevant mesh smoothening. In the adjacent (see Figure 6.10), mesh is shown without O-grid to compare the final mesh quality. It is clearly visible that, the current meshing approach preserve the orthogonality near the corner of the circles and considerably improve the mesh quality with marked green circle in zone where the mesh orthogonality was lost with traditional method. The comparison shown in Figures 6.11& 6.11 suggests that with the current approach, mesh can be further refined without compromising its quality, which is not the case in traditional approach.

6.4.2 Engine squish meshing

To carry out CFD simulation in the 3-dimensional mesh with moving piston boundary condition, a volume mesh is required from the 2-D planer mesh generated for the piston surface. This can be achieved by extruding the planer mesh in required direction (Z-direction in case of KIVA) up to desired squish length with sufficient number of mesh layers in between. Figure 6.13b shows the extruded mesh in Z-direction. For the better visualization, extruded coarse mesh is shown. During mesh extrusion, it is necessary to put required flag or part name to provide appropriate boundary conditions while setting up the simulation later on.

6.4.3 Valve and cylinder head meshing

The mesh is extruded for the cylinder squish region in the previous section till the valve bottom surface. During the extrusion, only one name can be assigned to the top face, therefore, separate names should be assigned to the mesh that should represents the bottom of two valves (see Figure 6.13b). The separate name required mainly to define the proper boundary condition for valve face movement. The next step is to generate the volume mesh for valves from the existing top-layer of the mesh. This can be achieved by again extruding the mesh in Z-direction to the distance equal to the valve skirt thickness (see Figure 6.13c). After extrusion, the next set of mesh boundary gets generated together with volume elements. It is again required to separate the mesh for top surface of the valves and assigned appropriate names to them. The different set of names are also required for respective volume elements to the valves. After extrusion, valve surfaces are still flat, now it is necessary to provide exact shape to the mesh to represent the valves top surface (see Figure 6.13d). The Figure 6.14 represents one of the flat mesh for valve top to be projected in adjacent actual valve top surface. This can be done by selecting mesh for valve top and projecting it to the geometrical surface of valve top. This way it will resemble exact valve geometry, and the mesh elements automatically conform the valve volume (see Figure 6.15).

The engine geometry in consideration has flat circular cylinder head, therefore it is relatively easier to assign the top face of extruded mesh layer to the circular cylinder head. The Figure 6.16 display the extruded mesh to generate the cylinder head with mesh layer separated for the port meshing. In general engine can have canted valves (2 to 4 valves) with non-flat cylinder head. In such a scenario, extra effort may required to associate the extruded mesh over the entire cylinder head with requisite mesh quality maintained.

Once the mesh has been assigned to cylinder head, it is now require to further extrude mesh separated (red color mesh in Figure 6.16) for port. Figure 6.17 represents the mesh for initial length of intake/exhaust ports.

6.4.4 Intake-exhaust port meshing

With present approach, it is always feasible to generate mesh for the port and valve-stem region mesh by mesh extrusion. However, it is very easy for straight geometric feature. Considering the possible complex shape of the inlet and exhaust port with valve-stem, it requires considerable effort. Therefore it consume lot of time and hence it is not advisable. Since, port mesh does not require any moving elements, complete mesh can achieved in two stages. First to generate mesh only for ports with the traditional way using 3-D geometry and blocking with O-grids. Secondly, merge the interface of ports with the interface of mesh achieved till previous section. The top inset picture in Figure 6.18 shows part of the 3-D geometry and blocking of the inlet port alongside with generated mesh. The similar technique is adopted for another ports.

The next step is to assemble the engine mesh generated through the extrusion technique and port mesh with normal 3-D blocking with O-grid as shown in Figure 6.18. The mesh interface is highlighted and zoomed for better visualization (shown in inset). In order to merge interfaces properly, number of nodes and its locations must be same in both sides. The completed mesh for the given engine geometry is already displayed in earlier Figure 6.4.

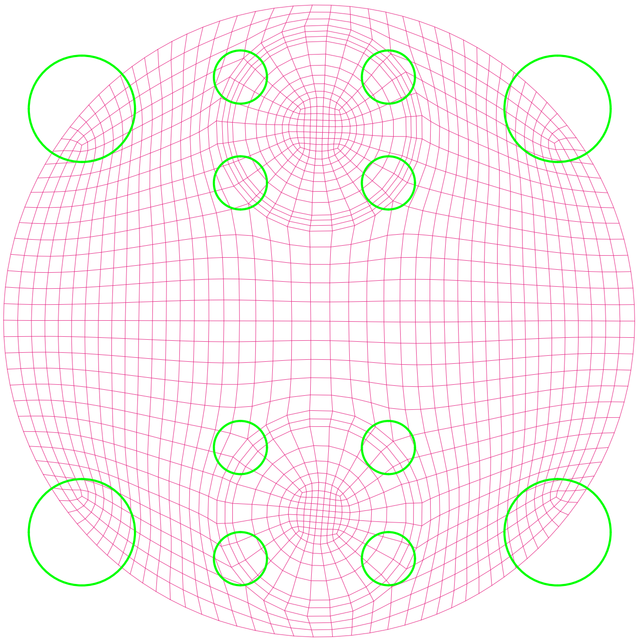

Figure 6.9: Generated mesh for piston surface (present approach)

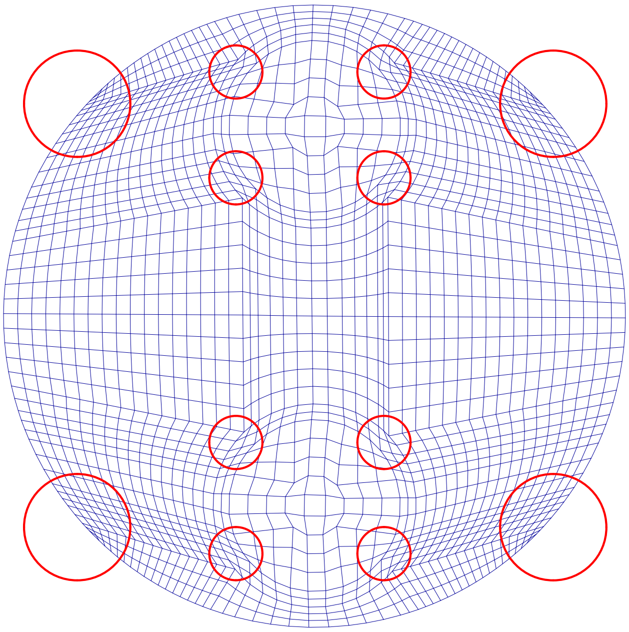

Figure 6.10: Generated mesh for piston surface (traditional blocking for KIVA)

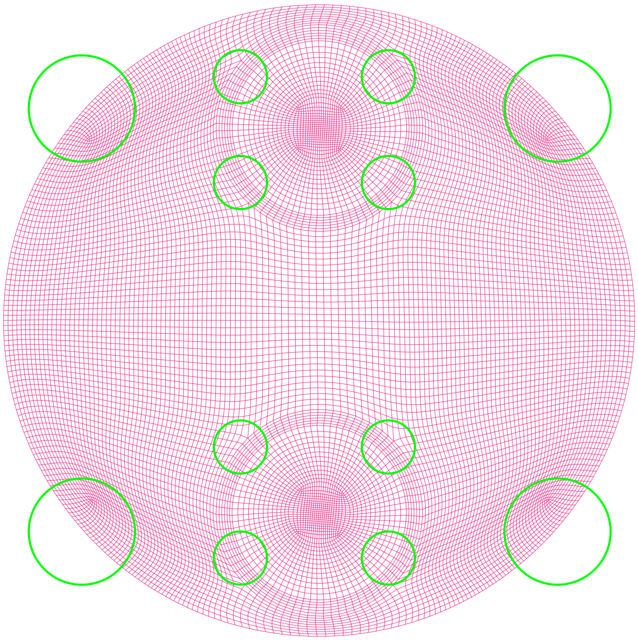

Figure 6.11: Refined mesh for piston surface (present approach)

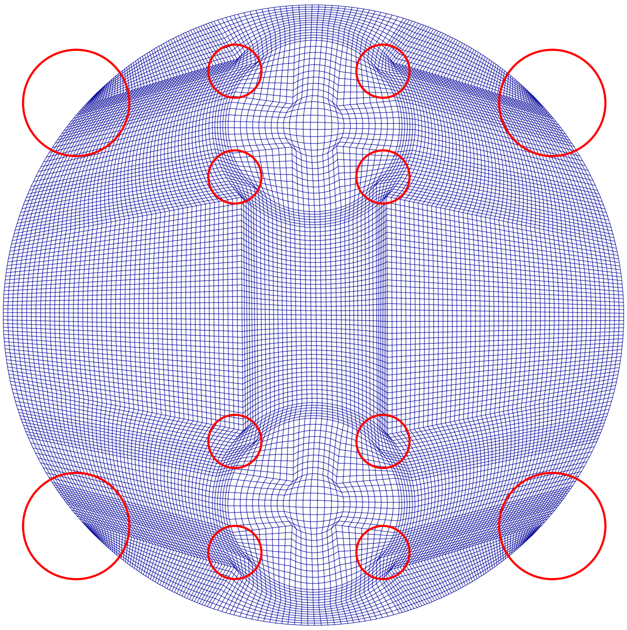

Figure 6.12: Refined mesh for piston surface (traditional blocking for KIVA)

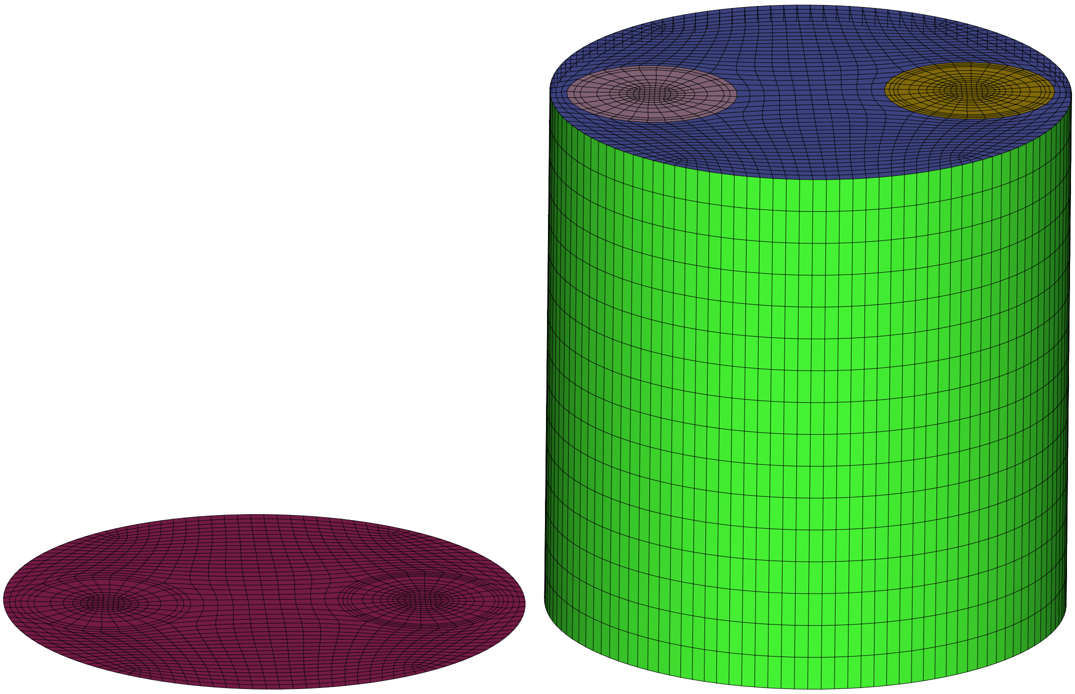

(a) Piston surface meshing

(b) Mesh extrusion to generate squish and mesh layer for valve bottom

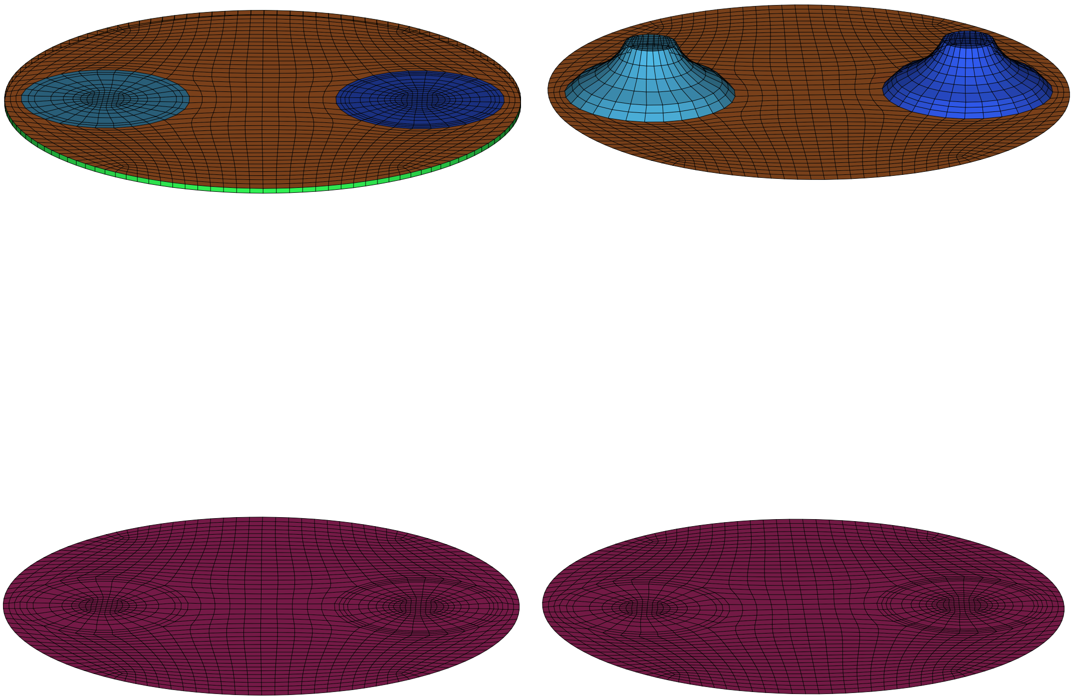

(c) Mesh extrusion to generate mesh layer for valve top

(d) Projection of the mesh to the valve top surface

Figure 6.13: Steps to generate engine mesh with ICEM-CFD

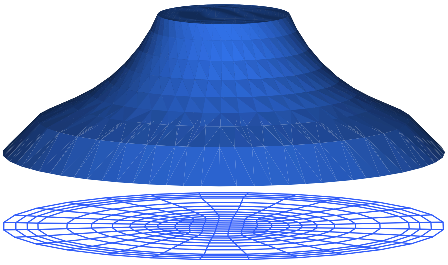

Figure 6.14: Nodes need to be projected on actual valve surface

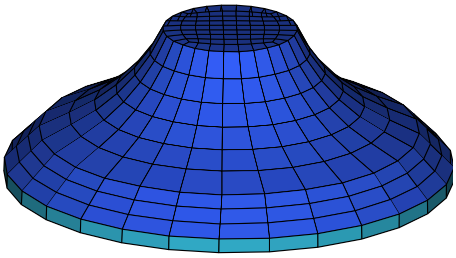

Figure 6.15: Nodes are moved and projected to conform the actual valve shape and dimension

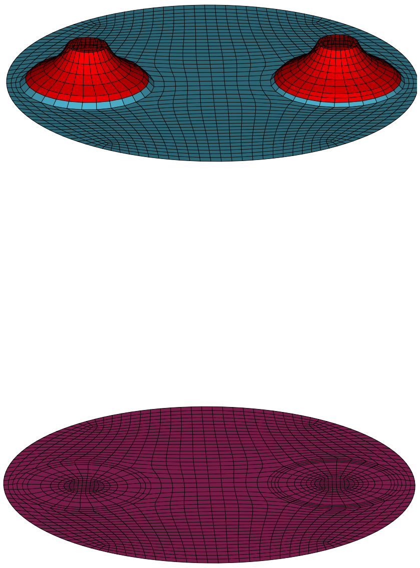

Figure 6.16: Projected mesh to the valve top surfaces

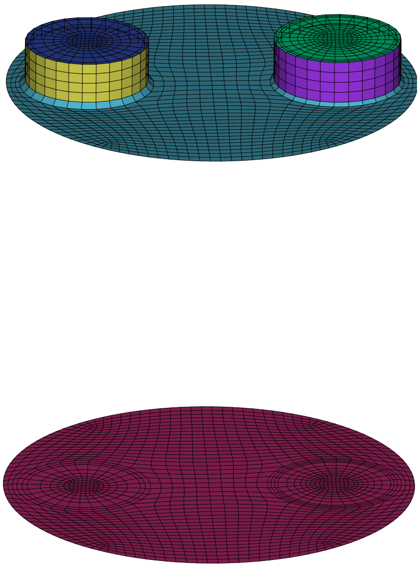

Figure 6.17: Mesh extruded for initial length of the ports

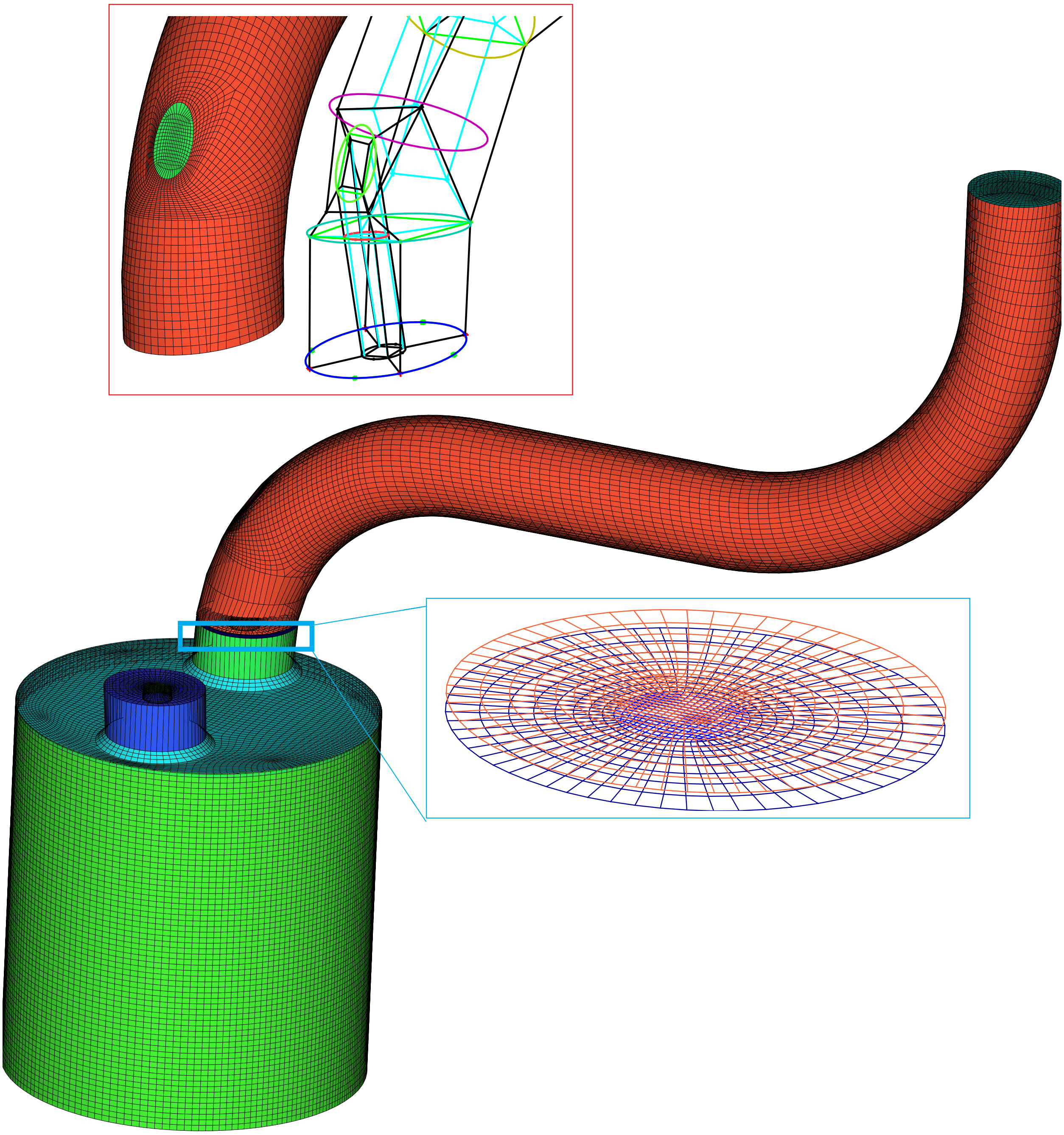

Figure 6.18: Port mesh to be merged in the mesh for engine geometry generated through extrusion (inset picture shows the interface between these two meshes)

7 Validation of the fuel injection module

The spray dynamic is greatly influenced by the types of nozzle used, especially the primary atomization mechanism. As already discussed, this requires separate formulation for the primary atomization model in the Lagrange particle tracking framework. In the present study, two types of nozzles are in consideration. The first one represents the latest outward opening hollow cone gasoline direct injector (GDI), while another is 6-hole gasoline direct injector similar to diesel injector. The fuel injection model includes, primary atomization model, secondary atomization, collision-coalescence model, evaporation model. For the quantitative and qualitative assessment, simulations are also performed with three turbulence models k-ϵ, RNG k-ϵ, and LES based on smagorinsky model. In the case of the real engine configuration, spray wall interaction is important phenomena to consider as the injected fuel droplets can impinge on cylinder wall and form wall film, which is highly detrimental in terms of engine performance and pollutant emissions.

Spray wall impingement

The implemented wall impingement model is validated against the experimental configuration outlined in reference [62]. The measurements were performed for different combination of K number and $T^{\star}$ values with iso-octane fuel. In the numerical configuration, the fuel property data are taken from the library originally implemented in KIVA4-mpi code. Figure 7.1 shows the qualitative comparison of the bouncing effect on the heated wall. Since the droplet incidence velocity is relatively lower, the effect of hot wall is predominate as compared to the droplet kinetic energy. This way droplets get bounced off from the surface without dis-integrating. With higher velocity (K = 1020) and wall temperature ($T^{\star}$ =1.96) (see Figure 7.2), the impact momentum is high enough to dis-integrate the droplet, however the droplet still bounced off from the surface due to considerably heated wall. A further quantative comparison of droplet splashing in shown in Figure 7.3. The obtained experimental data on splashed droplet diameter is plotted against the simulated results. Considering the highly stochastic phenomena, the compared results show that the model is able to predict the wall impingement phenomena well.

Experimental and numerical configuration for hollow-cone GDI

The validation data are taken from the experiments performed with various combinations of cylinder pressure and temperature [4, 55]. The velocity measurement was carried out close to nozzle exit to verify the injection velocity boundary conditions. PDA measurement was performed for the droplet distribution at specified locations at 20 mm and 15 mm below injector tip for the 5 bar and 10 bar cylinder pressure, respectively. The spray visualization technique was used to capture the spray structure and profile, together with the spray penetration depth provided to analyze the spray evolution. The key experimental details are listed in Table 8.1. The fuel is injected for the duration of 0.4 ms with the injection profile shown in Figure 7.4. More experimental details are available in [4, 55].

In the CFD simulations, the combustion chamber is represented by a cylindrical computation domain as shown in Figure 7.5 (diameter 7 cm, height 3.5 cm) using 3-dimensional hexa-hedral grid with total mesh counts of ca. 1.5 $millions$. The control volumes are made finer in the middle region, where most of the Lagrange particles are expected to be solved. The initial conditions of air at pressure of 5 bar and temperature of 300 K for the non-evaporating case are used, while for the evaporating spray cylinder pressure of 5 and 10 bar and temperature of 600 K are applied. The injection boundary condition that replicates the experiment is defined at the bottom centre (see arrow marked in Figure 7.5) of the cylinder in z-direction with an initial spray cone angle of $95°$. Since there is finite time associated with the opening and closing of the injector needle, the injection boundary condition is taken as variable injection velocity as shown in Figure 7.4 for a total injection duration of 0.4 ms [55]. A total of 150,000 parcels are sufficient for these simulation cases. The computations were performed in Linux OpenSUSEx64 11.2, Intel© Core™ 2 Duo, 4GB, 3.16 GHz workstation and the total computational time taken with all fuel injection models included is estimated to approximately 11 hours.

At first the spray simulation is performed with three different turbulence models namely, k-ϵ, RNG k-ϵ, and LES smagorinsky model for non-evaporating spray only (chamber pressure 5 bar, temperature 300 K). The influence of turbulence models on spray dynamic is compared for droplet velocity, droplet distribution, spray penetration depth and spray profile. Then the LES simulation is performed for evaporating spray at 600 K chamber temperature with pressure 5 bar and 10 bar.

7.1 Results and discussion

To properly assess the influence of the modified collision model, a simulation is performed for the spray evolution without switching on the atomization and evaporation model. In the case of control volume based binary collision model, the clover leaf collision artifact is clearly visible. Figure 7.6a shows the spray profile taken on the z-$plane$. Such an artifact arises mainly with structured mesh. The droplets profile becomes preferential to directional due to the orientation of the cartesian mesh. The artifact becomes more prominent in two scenarios: first, when the injection point is defined at the common vertex of four CVs; secondly, when the hollow cone spray is being solved. The improvement in spray results with the modified collision approach in [90] is shown in Figure 7.6b. Instead of CV based approach, a spherical kernel is used to calculate the droplet collisions. Note that kernel dimension is made dynamic to take care varying mesh distribution as described in [90]. Since it is independent of mesh size and type, the clover leaf collision artifact is considerably removed

In case of hollow-cone GDI simulation, to confirm the applied boundary conditions for the nozzle exit velocity, a comparison is made with LCV measurement carried out at ambient pressure at

$1\ mm$ above the nozzle exit (see Figure 7.7). The measurement data is available only for initial injection duration, due to difficulty in measurement of dense spray. The prediction shows reasonably good agreement with the available LCV data. From compared results, it is clearly visible that k-ϵ model under-predicts the spray velocity near nozzle exit, while other two models (RNG k-ϵ model and Smorinsky LES model) predict reasonably good the near nozzle flow. These effects are also visible in Figure 7.14 displaying a comparison of the calculated spray penetration depth with experimental data. The spray length generally varies along the circumferential direction. A high speed spray generally comes out from the nozzle as combination of many strings, and each string has its own penetration depth [4]. Therefore the experimental data are marked with range representing minimum and maximum spray length. As expected the k-ϵ model under estimates, and the RNG k-ϵ model also slightly under-predicts, while the Smagorinsky LES predicts reasonably well the spray penetration depth. These discrepancies can be understood in Figure 7.9 illustrated for the half section, It shows the effective viscosity profile at the end of injection $(0.4\ ms)$. It is clearly visible that k-ϵ calculates the effective viscosity comparatively higher than the other two models. The higher effective viscosity increases the drag force on the spray. The increased drag force also results in the higher dispersion of the spray profile, as pointed out later. This effect is also important for the turbulence mixing in case of evaporating sprays in the context of fuel-air mixture preparation. The droplet size distribution is compared in Figure 7.15a with the PDA measurement for the time duration $0.71\ ms$ to $1.11\ ms$ after the start of injection. The measurement is carried out at $20\ mm$ above the nozzle exit. The results show, that the RNG k-ϵ model over-predicts slightly more than the LES model, but overall reasonably good agreement is achieved. The results from the k-ϵ is not included in this plot since the quality of the results is not comparable. Figure 7.11 shows comparison of the complete spray profile between LES and experiment only, the toroidal vortex are clearly evident in both simulated (Smagorinsky model) and experimental results. Figure 7.12 provide a comparison of spray structure for all three models (k-ϵ, RNG k-ϵ, Smagorinsky LES). Figure 7.12.a clearly shows a bigger toroidal vortex for k-ϵ compared to other two models. This is mainly because of the increased effective viscosity and subsequent higher spray dispersion. These phenomena are also observed in Figure 7.15, showing the half sectional view of velocity streamlines. The two vortex in both sides of GDI spray are clearly visible in all cases, however a larger vortex is predicted in the case of k-ϵ.

Figures 7.14a, 7.14b, 7.14c display the comparison of spray penetration depth after start of injection for all three cases investigated here with conditions *5 bar/300 K*, *5 bar/600 K*, and *10 bar/600 K*. The effect of evaporation process on the spray dynamic is obviously included for evaporating spray. The experimental data is represented by bar with lower and higher penetration range, while gray solid line represents the computed spray penetration depth. Due to higher chamber pressure in case of $10\ bar$, as expected the overall penetration depth is considerably reduced. However, the simulation results show good agreement with experiments with all three cases. The droplet size distribution for all three cases are compared in Figures 7.15a, 7.15b, 7.15c with the PDA measurement for the time duration $0.71\ ms$ to $1.11\ ms$ after the start of injection. The measurement is carried out at $20\ mm$ above the nozzle exit for cylinder pressure of $5\ bar$, and $15\ mm$ for cylinder pressure of $10\ bar$, respectively. In non-evaporating case, distribution profile is slightly shifted towards bigger diameter, while in evaporating case this occurs towards smaller diameter. However, considering the stochastic nature of spray, the model is able to capture the distribution trend reasonably well.

7.2 Conclusion: Hollow-cone GDI

In the present work an upgraded injection spray model, which includes models relevant for fuel injection process (atomization, collision, turbulence, evaporation) is demonstrated to be able of capturing the main features of spray once LES is used. The effect of different turbulence models (k-ϵ, RNG k-ϵ, Smagorinsky LES) is especially compared for the non evaporating GDI spray case. Using the light scattering visual image, LCV and PDA measurement data for validation and comparison of spray data for non-evaporating and evaporating case from RWTH Aachen University [55], it appears that, the simple Smagorinsky model achieved good agreement in predicting the spray penetration depth, droplet size distributions as well as important flow properties such as nozzle exit velocity, turbulence level & effective viscosity and formation of toroidal vortex.

The collision model is updated to take care of all the possible interactions between the droplets while being independent of mesh size and mesh type. The model validation performed both with non-evaporating and evaporating spray. In both cases, the LES together with the spray module is able to predict the spray penetration depth, droplet size distributions and the important flow properties such as nozzle exit velocity, with good accuracy. This LES model will then be used for further investigations in combination with the IC-engine modules.

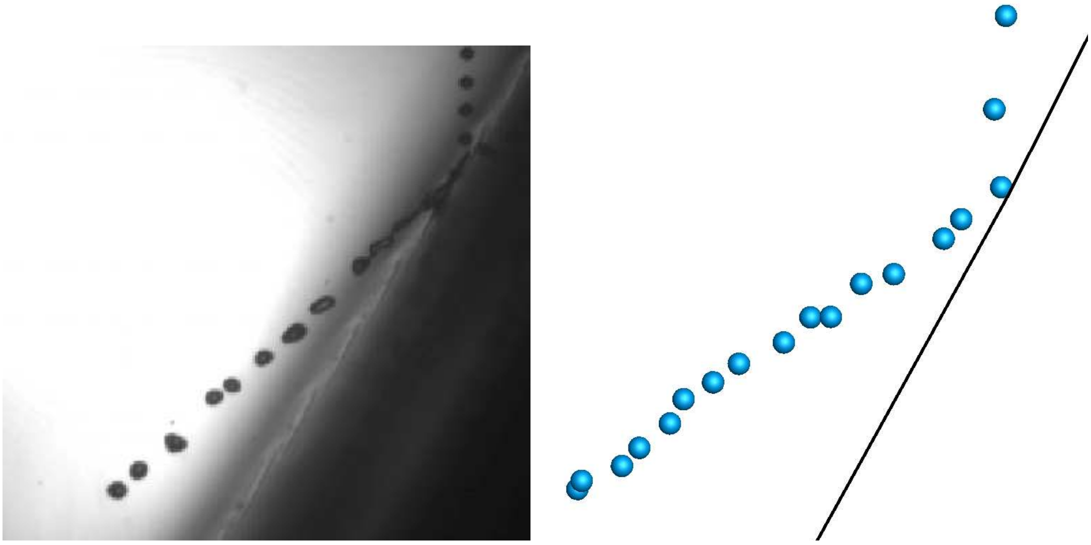

(a) Experiment **(b)** Simulation

Figure 7.1: Bouncing of iso-octane droplets on a hot wall [K = 382, $T^{\star}$ =1.44]

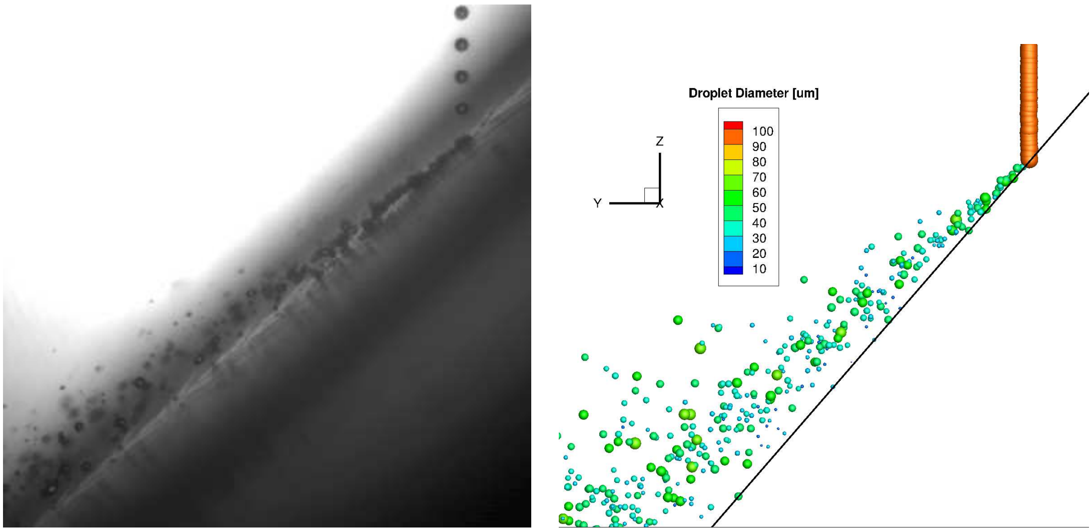

(a) Experiment **(b)** Simulation

Figure 7.2: Splashing of iso-octane droplets on a hot wall [K = 1020, $T^{\star}$ =1.96]

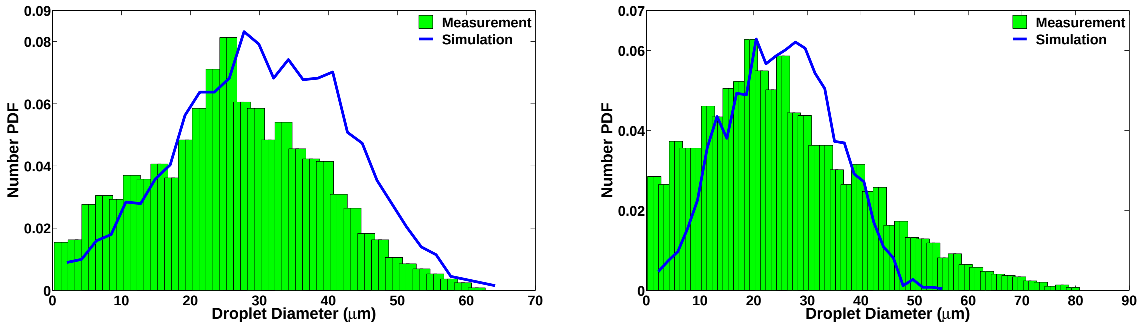

(a) log(K) = 3.33, $T^{\star}$ =1.7, d_0=100 μm **(b)** log(K) = 3.62, $T^{\star}$ =2.03, d_0=100 μm

Figure 7.3: Number probability density functions of droplet size after splashing impact experimental measurements [62] against simulation

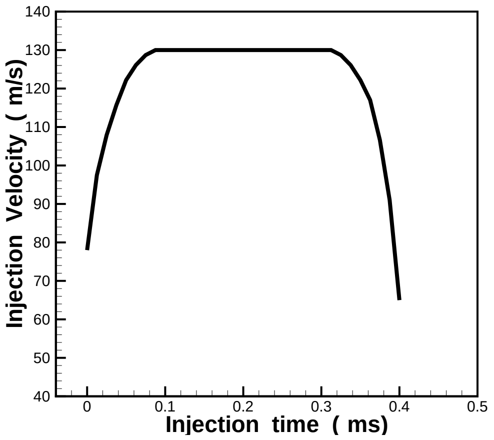

Figure 7.4: Injection profile with respect to time, Pischke et. al,[55]

Parameter	Value
Fuel	Iso-octane
Fuel mass injected	7.8 mg
Injection time	0.4 ms
Injection temperature	300 K
Injection pressure	100 bar
Nozzle slit thickness	25 μm
Cylinder pressure	5 bar
Cylinder temperature	300 K

Table 7.1: Experimental operating conditions, Pischke et. al.[55]

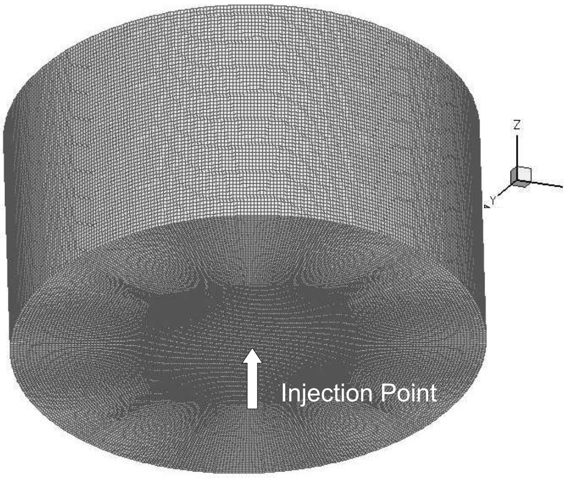

Figure 7.5: Computational domain, representing the chamber geometry with total CVs of approx. 1.5 millions and injector location at bottom centre (see white arrow)

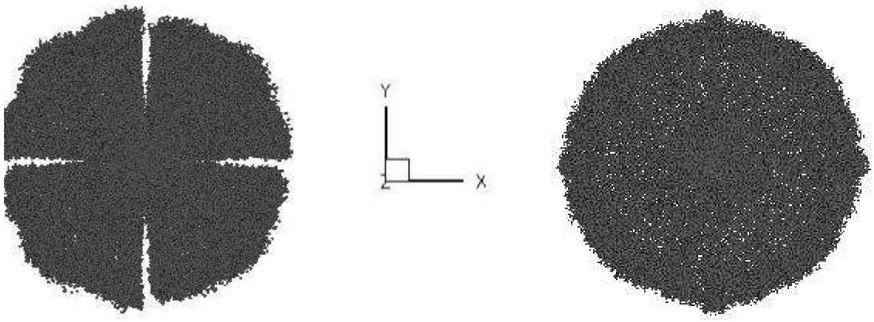

(a) **(b)**

Figure 7.6: Comparison spray profile (non-evaporating case): (a) clover leaf collision artifact due to control volume approach in structured mesh (b) collision artifact rectified with the new scheme

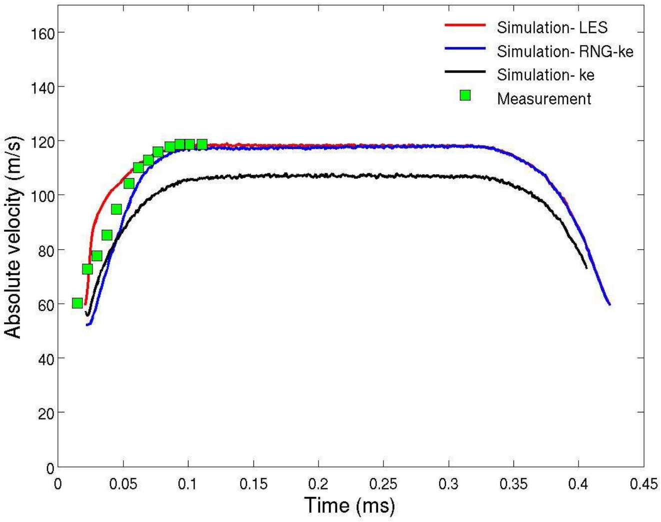

Figure 7.7: Comparison of simulated (three turbulence models) and LCV measurement of injector exit velocity 1 mm above injection point, Pischke et. al.[55]

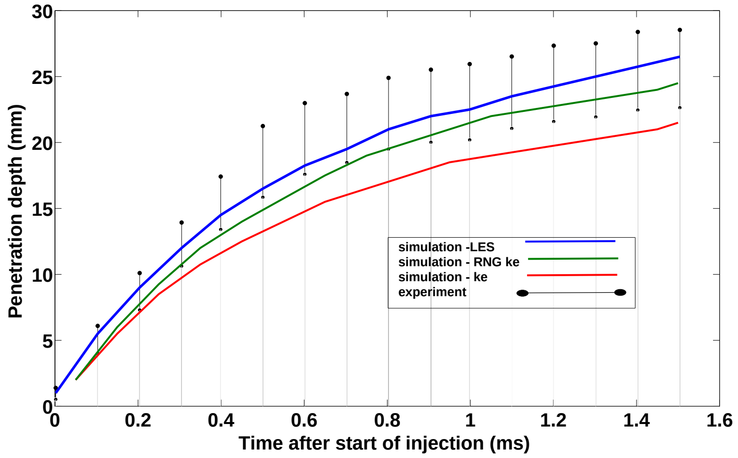

Figure 7.8: Comparison of model predictions with measurement (max. and min. depth) for spray penetration depth

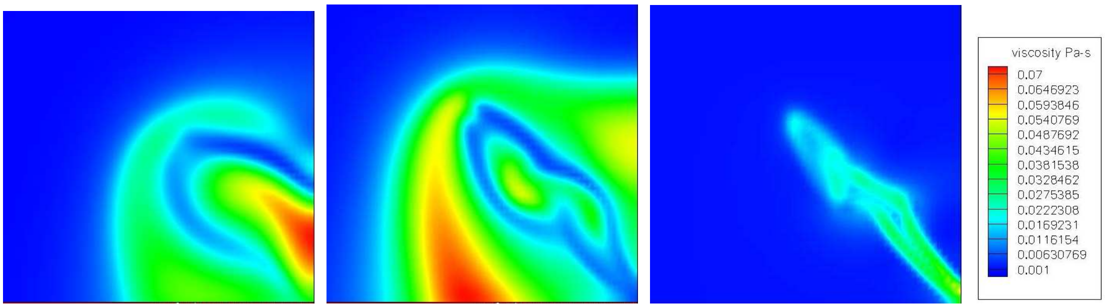

(a) k-ϵ **(b)** RNG k-ϵ model **(c)** Smagorinsky LES

Figure 7.9: Comparison of the effective viscosity (Pa-s) at the end of injection (0.4 ms)

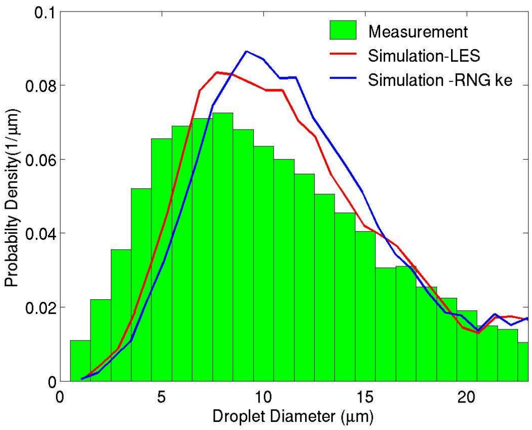

Figure 7.10: Comparison of simulated and PDA measurement of the drop size distribution sampled from t = 0.71 -1.11 ms, 20mm from injection point

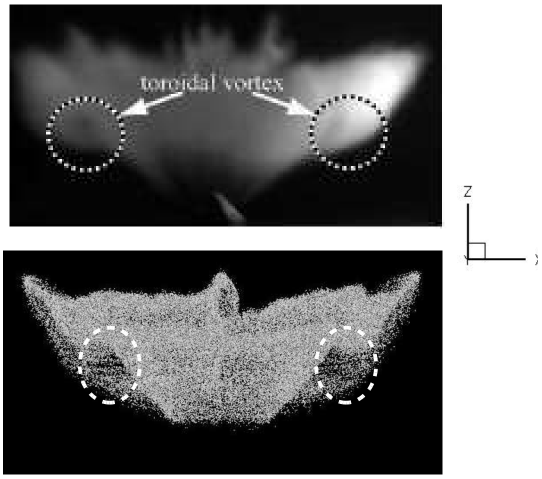

Figure 7.11: Comparison of toroidal vortex formation on spray surface (at 0.8 ms) [top- experiment, bottom-LES simulation]

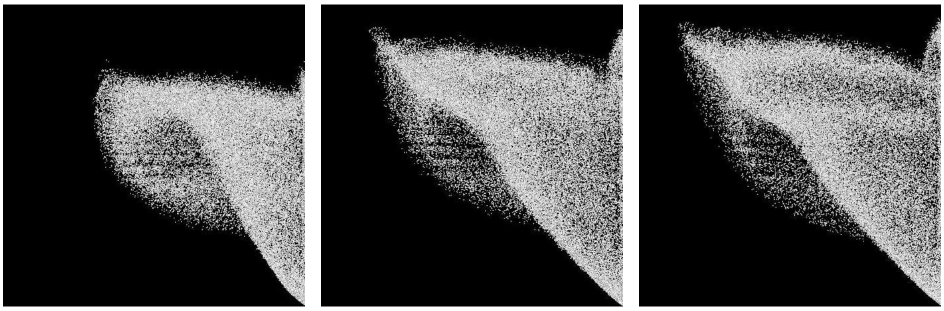

(a) k-ϵ model **(b)** RNG k-ϵ model **(c)** Smagorinsky LES

Figure 7.12: Comparison of the spray profile at the end of injection (0.4 ms)

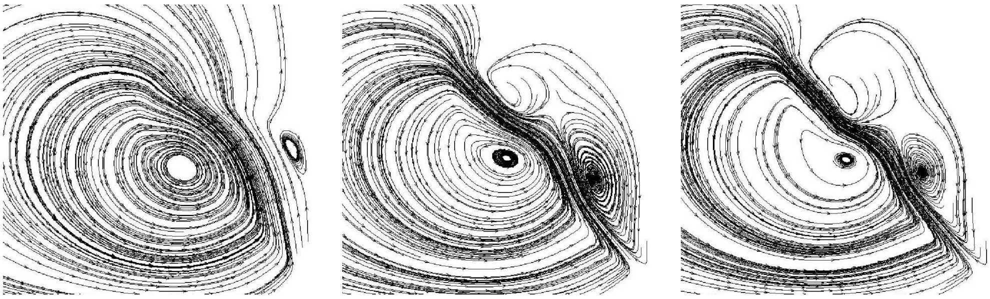

(a) k-ϵ model **(b)** RNG k-ϵ model **(c)** Smagorinsky LES

Figure 7.13: Comparison of streamlines at the end of injection (0.4 ms)

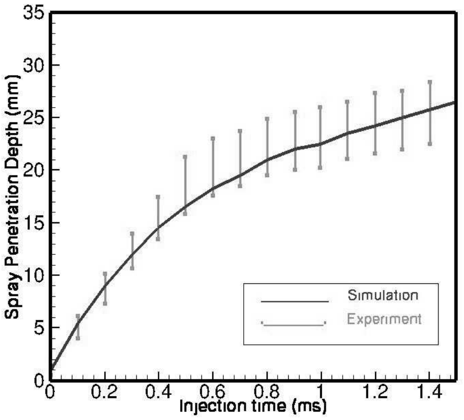

(a) Non-evaporating case: *5 bar* and *300 K*

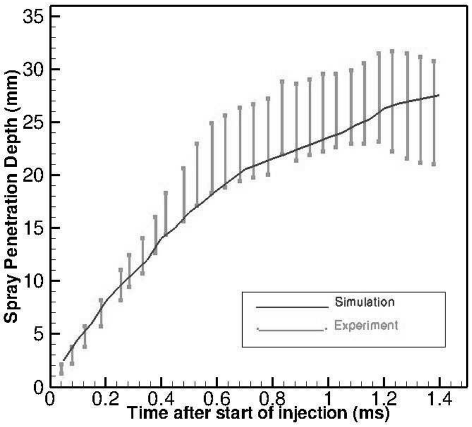

(b) Evaporating case: *5 bar* and *300 K*

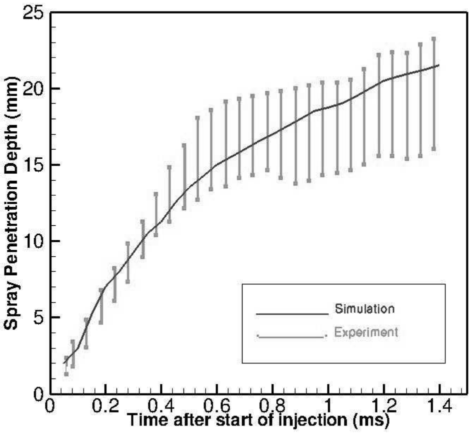

(c) Evaporating case: *10 bar* and *600 K*

Figure 7.14: Comparison of model prediction and spray visualization measurement (max. and min. depth) for spray penetration depth [55]

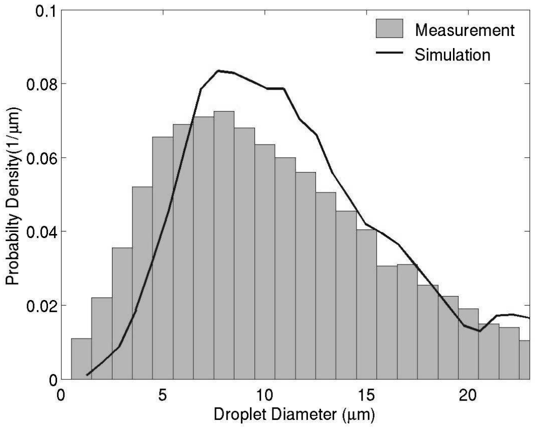

(a) Non-evaporating case: *5 bar* and *300 K*

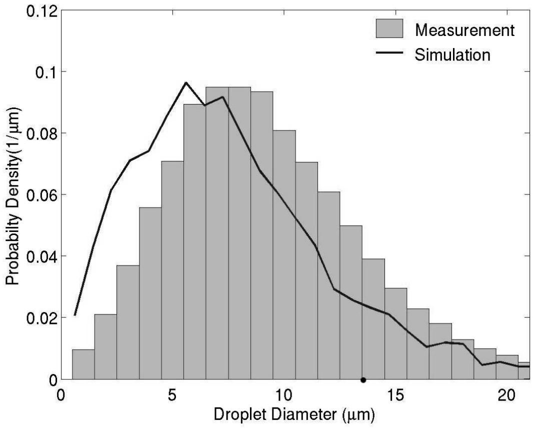

(b) Evaporating case: *5 bar* and *600 K*

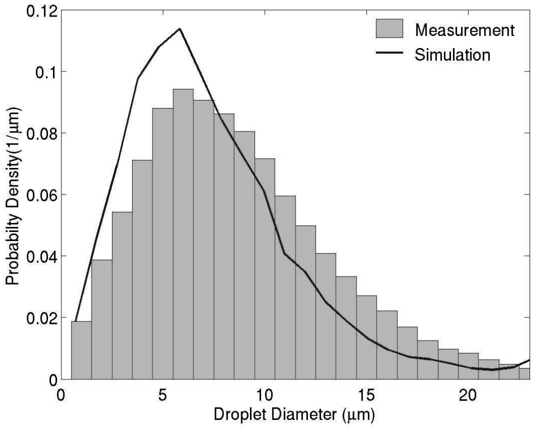

(c) Evaporating case: *10 bar* and *600 K*

Figure 7.15: Comparison of simulated and PDA measurement of the drop size distribution sampled from t = 0.71 -1.11 ms [55]

8 IC-engine simulation for TCC configuration

In this section, results of multi-cycle numerical investigation of a TCC (transparent combustion chamber) engine configuration are presented and discussed. Firstly the engine specification and parameters are listed, then the results obtained by using a standard k-ϵ and adopted LES turbulence model are compared. The influence of the present meshing technique and its quality is compared with the traditional blocking method for KIVA code. Then statistical analysis are performed for the flow field inside the combustion chamber in terms of cycle-to-cycle variations using LES. Finally, the validated fuel injection module is integrated into the flow-solver to investigate the fuel spray evolution inside the combustion chamber and subsequent fuel-air mixture formation.

8.1 Engine configuration and numerical setup

In order to demonstrate and evaluate the adopted engine simulation technique, an engine configuration with relatively less complex geometry (simple piston crown , cylinder head and valve shape) is highly desirable. At the same time the configuration should be able to demonstrate experimentally all the essential features of engine operations and relevant flow dynamics. In the present study, an optical gasoline engine, so called ”Transparent Combustion Chamber” (TCC) [141] designed to support the development and validation activities for the CFD software is used. The details of the engine configuration is made online in Engine Combustion Network, Sandia (ECN) to provide easy access to CFD researcher for their model validations. The engine geometry is shown in Figure 8.1. It features parallel two valves with simple intake and exhaust port geometry and a pancake-shaped combustion chamber [141]. To validate the engine simulation, measurement data are available for the cylinder pressure curve with respect to the engine crank angle, and PIV data are available for the velocity field inside the engine cylinder.

The engine has bore and stroke dimension of $92\ mm$ and $86\ mm$ respectively, with variable engine speed. However, in present case the engine speed is *800 rpm*. The valve lift diagram is provided in Figure 8.4. The intake valve is remained open for crank angle at (18^o) BTDC to 240^o ATDC and the exhaust valve for crank angle duration of 148^o BTDC to 28^o ATDC. The complete engine parameters are listed in Table 8.1. The fuel injection parameters are listed in the Table 8.2 to carry out LES simulation with fuel spray. In the CFD configuration total of ca. *0.9 million* control volumes (CVs) are used to represent the cylinder squish, valves and ports geometry (see Figure 8.3) for the simulation using KIVA4-mpi code with new meshing technique discussed in earlier section. The two classes of grid distribution is used one by using traditional meshing approach having coarser mesh, while another refined mesh with new meshing technique for KIVA4-mpi. However, for engine simulation with coarse mesh, only approx. *39,000 CVs* are used due to meshing limitation with traditional blocking method for KIVA code (see Figure 8.2). The final distribution of control volumes for various engine parts are listed in Table 8.3.

Table 8.1: Engine parameters: GM TCC (ECN)

Parameter	Value
Bore	92 mm
Stroke	86 mm
Engine RPM	800
Compression ratio	10
Intake valve open	Intake-BTDC 18^o
Intake valve close	Intake-ATDC 240^o
Exhaust valve open	Intake-BTDC 148^o
Exhaust valve close	Intake-ATDC 28^o

Table 8.2: Injection parameters: GM TCC (ECN)

Parameter	Value
Fuel	Gasoline
Fuel mass	8.0 mg
P_{inj}	100 bar
T_{inj}	333 K
Start of Injection	53^o ATDC
Duration of Injection	10^o CA
Injector slit thickness	25 μm
Spray cone angle	95^o

Table 8.3: Computational grids distribution for engine: GM TCC (ECN)

Region	Fine mesh	Coarse mesh
Combustion chamber	698,220	32116
Intake port (1) + Exhaust port (1)	216,376	5900
Intake valve (1) + Exhaust valve (1)	7020	700
Total control volumes	**921,616**	**38716**

8.2 Multi-cycle engine simulation

To carry out statistical analysis for in-cylinder flow and to assess the cyclic fluctuations of given engine configuration, sufficient large number of simulated engine cycles are required. In the present case, cold flow simulation is performed over 50 engine cycles using LES and 10 cycles using RANS approach in KIVA4-mpi code with fine grid . However, in case of coarse mesh, LES simulation of 14 cycles are sufficient to assess the model predictability on cycle-to-cycle variations. The integrated fuel injection model is used to carry out simulation of spray evolution inside engine cylinder with fine grid only.

8.2.1 Validation of in-cylinder flow field

The experimental data for multiple engine cycles are used for validation. In experiment, the in-cylinder pressure measurements are performed for complete engine cycle. The PIV data for the flow field is available for more than 3000 engine cycles at crank angle of 100^o and 300^o. The PIV measurements are taken in the $x - plane$ close to the cylinder head between the intake and exhaust valve. Figure 8.5 shows the comparison of in-cylinder pressure profile plotted against engine crank for one cycle. The calculated result show very good agreement with obtained experimental pressure profile. Figure 8.6 depicts the comparison of the flow profile during intake stroke for the engine crank angle of 100^o. The LES result is averaged flow profile over 50 engine cycles. The result shows good agreement in term of velocity magnitude and flow structure. The two vortex profiles are clearly visible along with the main intake stream in both experiment and simulated result. The flow field during the compression stroke is plotted in Figure 8.7 for engine crank angle of 300^o. Both in the experiment and simulated results, the reduced velocity magnitude with organized flow structure can be observed. These results shows that presented LES is able to capture well the flow profile.

8.2.2 Comparison of LES and RANS simulation

The RANS simulation is performed to evaluate its predictive capability in resolving the in-cylinder flow field and compared with LES results. The standard k-ϵ model available in KIVA4-mpi code is used for RANS simulation using fine grid with approx. *0.9 million* control volumes. The results are obtained at 95^o-ATDC for 10 consecutive engine cycles. Figures 8.9, represents the comparison of instantaneous flow profile obtained for RANS and LES simulations for initial engine cycles. The result clearly shows the RANS model is able to predict nicely the mean flow structure. However, it is unable to resolve the important aspect of cycle-to-cycle variations of in-cylinder flow field (see Figure 8.8a-8.8c). Contrary to that (see Figure 8.9a-8.9c), the LES model is able to capture the transient in-cylinder flow field by showing the evidence of distinct in-cylinder flow profile at same crank angle for many consecutive engine cycles.

8.2.3 Influence of grid size

The LES are also performed to demonstrate the viability of the mesh refinement required to resolve the in-cylinder flow structure. As mentioned before, generating mesh with traditional KIVA approach is complex task due to fact that the O-grid blocking is not possible, after certain level further refinement of mesh is not possible. Therefore, the most achievable mesh quality having relatively coarse mesh is used to simulate the engine flow. Figure 8.10 depicts the instantaneous velocity plotted for 14 cycles along the x-centre line for engine crank angle 120^o using coarse mesh. It is clearly visible that the LES model is unable to resolve the unsteady flow structure which was inevitable with such a coarse mesh. Also the important information about the unsteady cyclic variability of in-cylinder flow is lost, hence the simulation is not carried out for further engine cycles. The instantaneous velocity profile obtained using LES model with fine grid for initial 20 cycles is plotted in Figure 8.11, showing the LES model is now able to resolve the cycle-to-cycle variations of in-cylinder flow field.

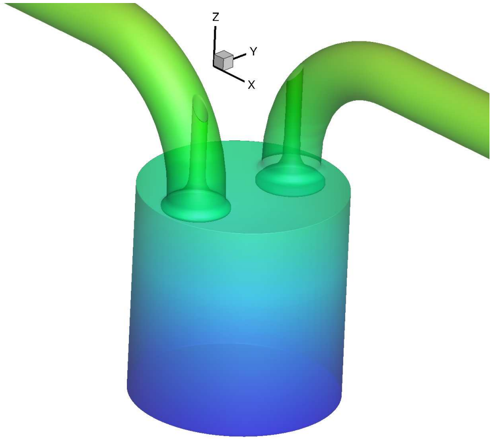

Figure 8.1: Engine geometry showing cylinder squish, intake/exhaust valves and ports [141].

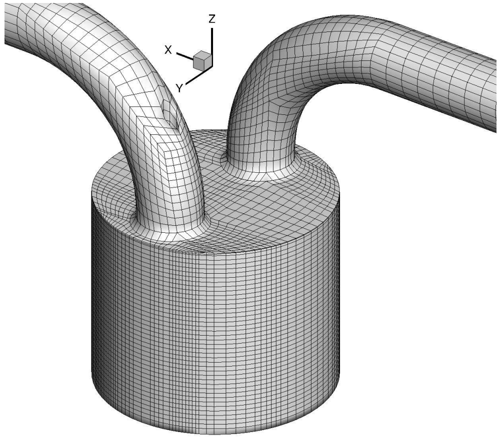

Figure 8.2: Hexahedral coarse mesh for engine geometry generated in ICEM-CFD [141].

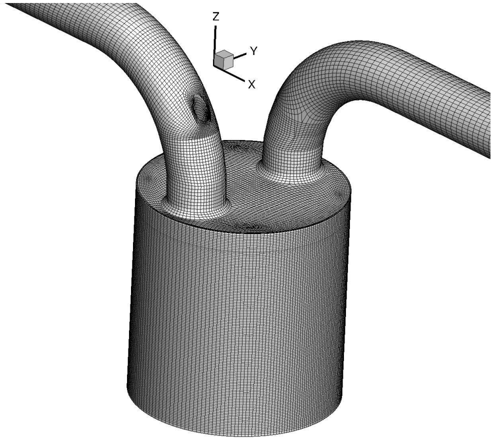

Figure 8.3: Hexahedral fine mesh for engine geometry generated in ICEM-CFD [141].

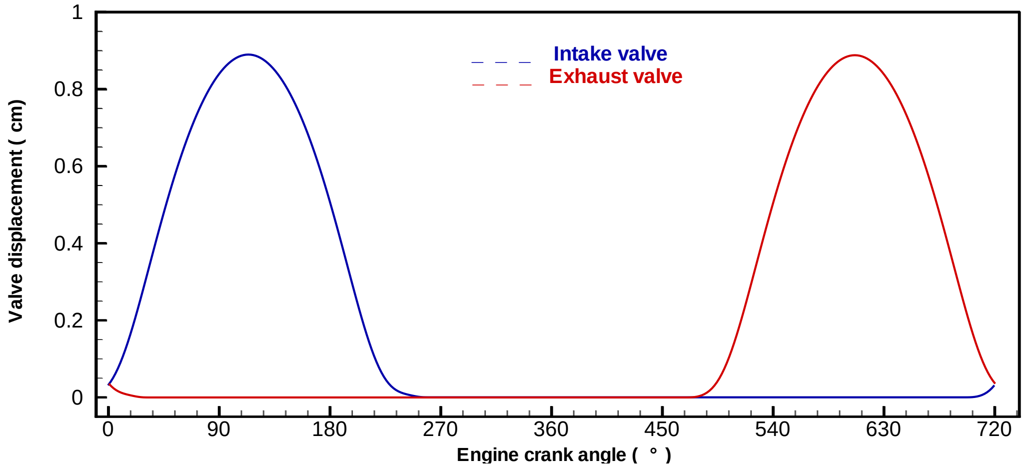

Figure 8.4: Intake/exhaust valve displacement profile at various engine crank angle

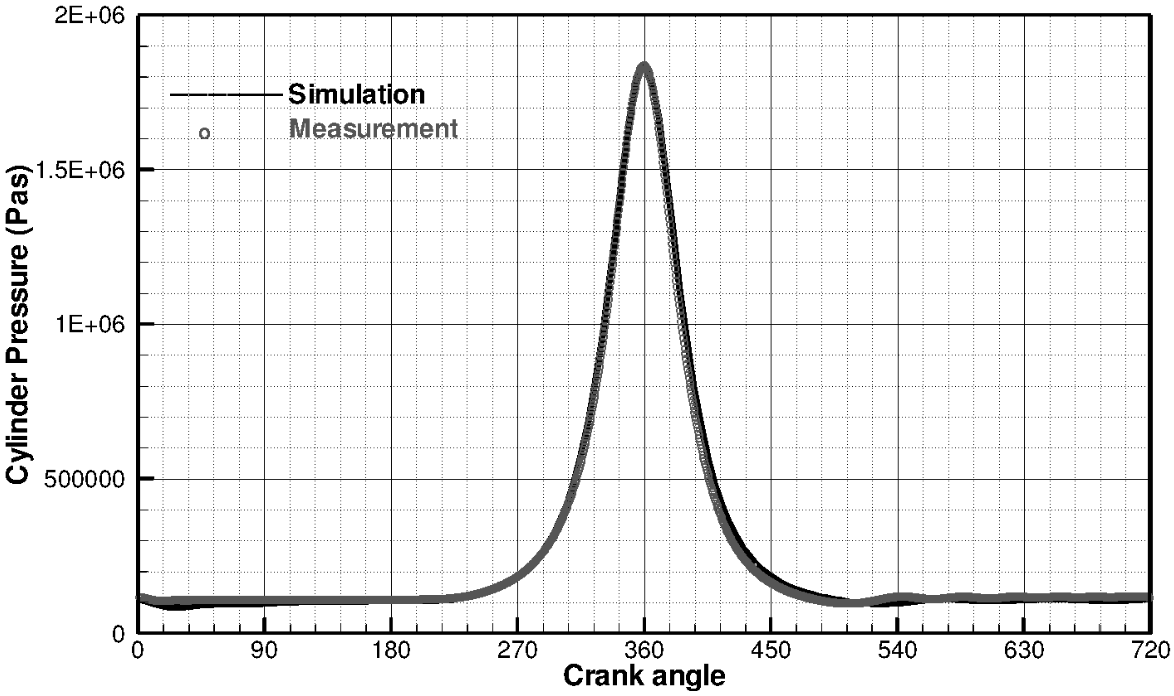

Figure 8.5: Comparison of in-cylinder pressure curve: simulated (black line), experimental (gray circle [141])

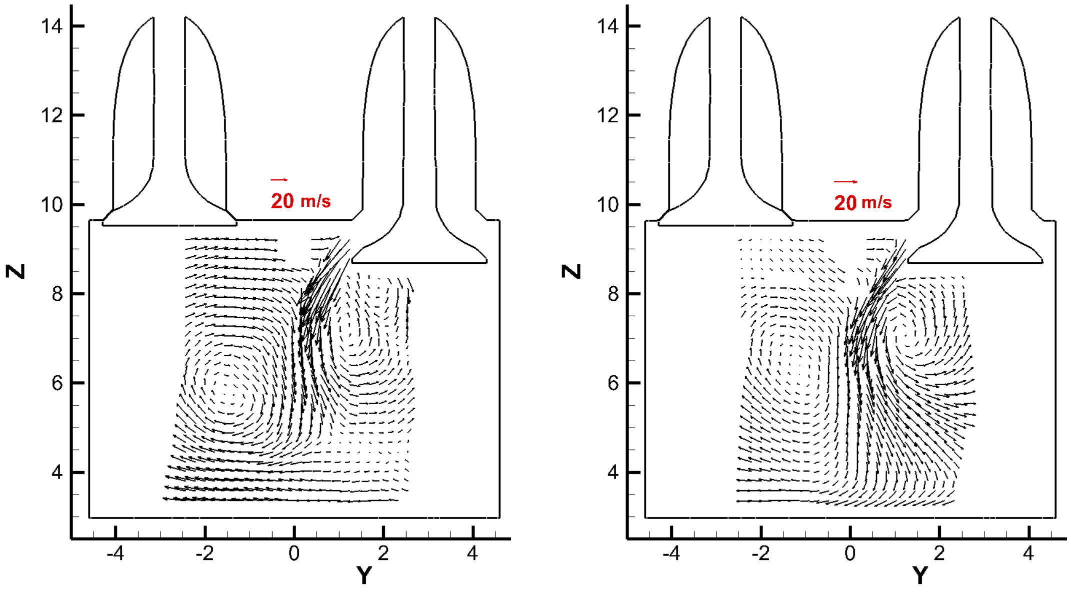

(a) LES (50 cycles) **(b)** PIV (3000 cycles)

Figure 8.6: Velocity flow field at 100^o ATDC for (a) LES, (b) experiment

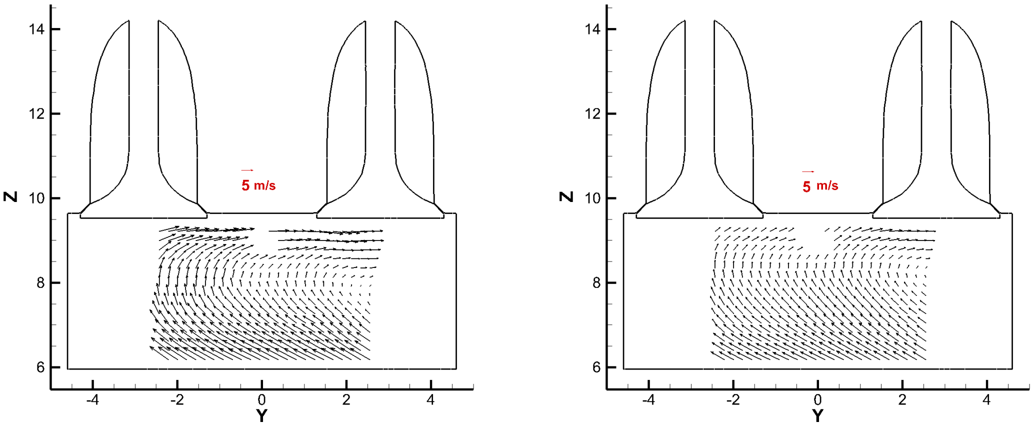

(a) LES (50 cycles) **(b)** PIV (3000 cycles)

Figure 8.7: Velocity flow field at 300^o ATDC for (a) LES, (b) experiment

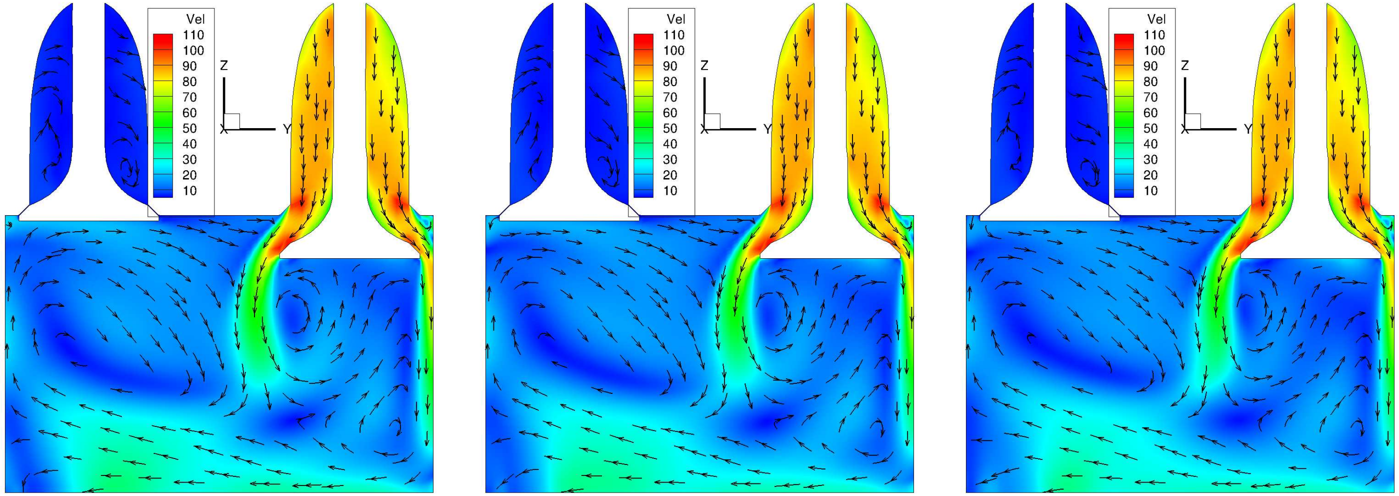

(a) **(b)** **(c)**

Figure 8.8: RANS results for velocity profile at 90^o ATDC for (a) 2^{nd} engine cycle, (b) 3^{rd} engine cycle (c) 4^{th} engine cycle

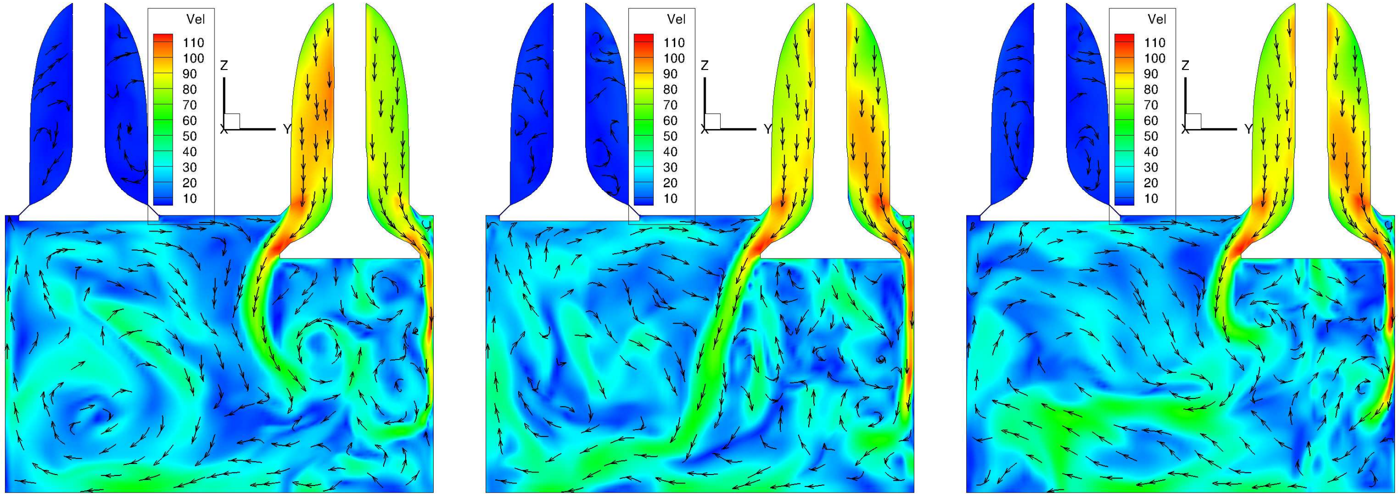

(a) **(b)** **(c)**

Figure 8.9: LES results for velocity profile at 90^o ATDC for (a) 2^{nd} engine cycle, (b) 3^{rd} engine cycle (c) 4^{th} engine cycle

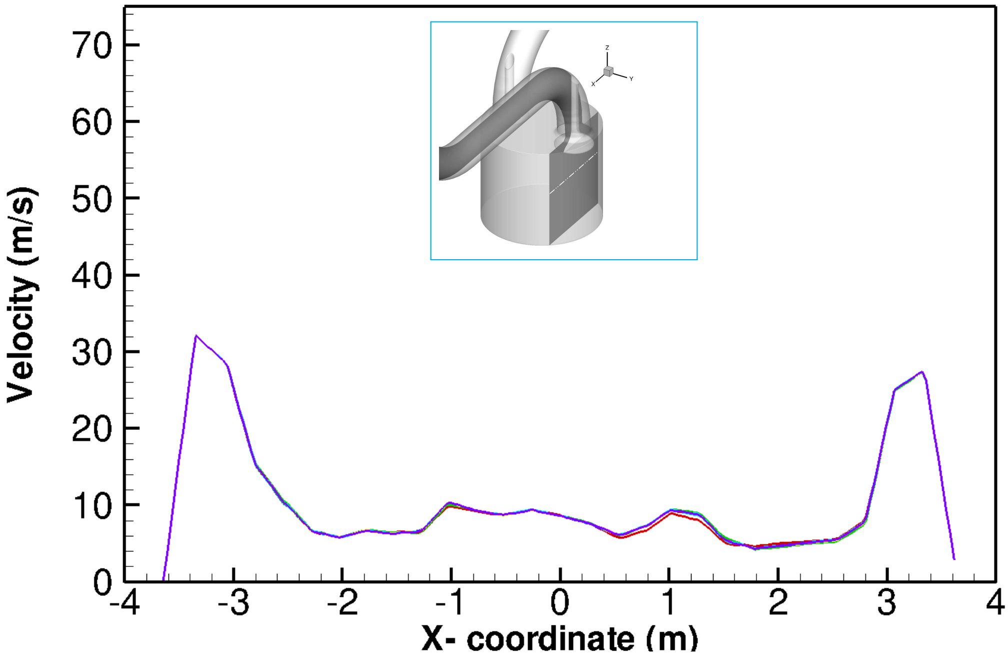

Figure 8.10: Coarse mesh : Simulated instantaneous veloity profile along y-centre line for 14 engine cycles at 120^o ATDC

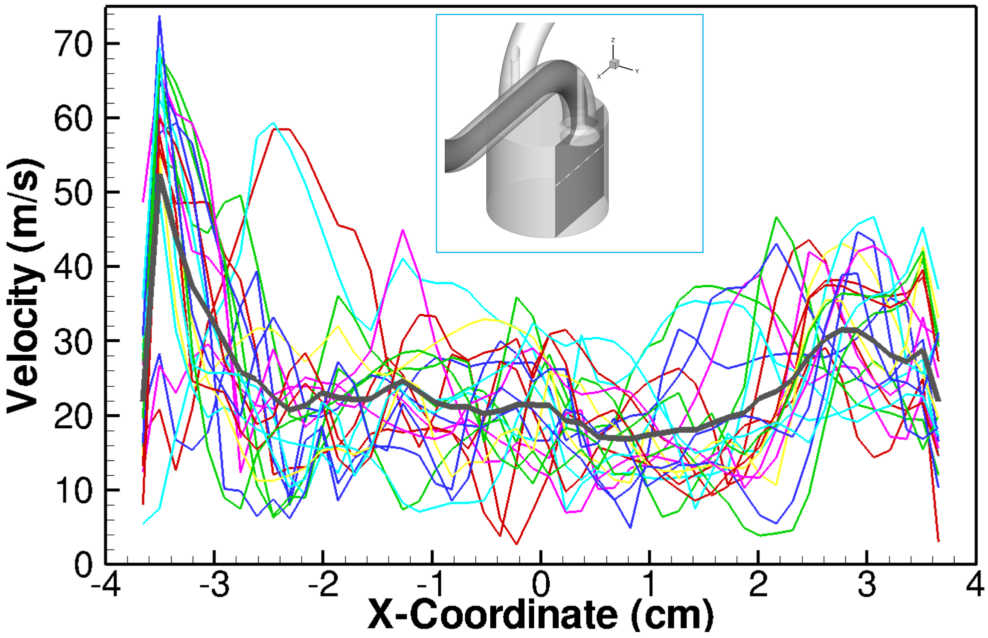

Figure 8.11: Fine mesh : Simulated instantaneous velocity profile along y-centre line for 20 engine cycles at 120^o ATDC

8.2.4 Cycle-to-cycle variations

In order to carry out study on cycle-to-cycle variations for in-cylinder engine flow, a sufficient large number of engine cycles are required for the mean flow to be statistical independent. In this section results are produced for velocity mean, and fluctuation at various engine crank angle representing different stages of engine operations.

8.2.4.1 Intake stroke

The strong low pressure generated due to expansion of the squish volume by downward piston movement draw fresh air with relatively high speed through the thin passage around the valve sheets with sufficient high turbulence. The shape of intake-valve and valve sheet generally guide and influence greatly the flow structures inside the engine cylinder. It also helps to develop the swirl and tumble motion. In the present study the flow structures developed during the intake stroke is depicted in the Figure 8.12. The high speed intake charge strikes piston top and generates complicated 3-dimensional vortex structures as shown in Figure 8.12. The intensity of the swirl flow is important during the fuel injection process for proper dispersion and efficient fuel-air mixture formation. While intensity of the tumble flow is required for effective flame propagation during the ignition. The excessive tumble motion may also lead a flame to extinguish and complete loss of engine power.

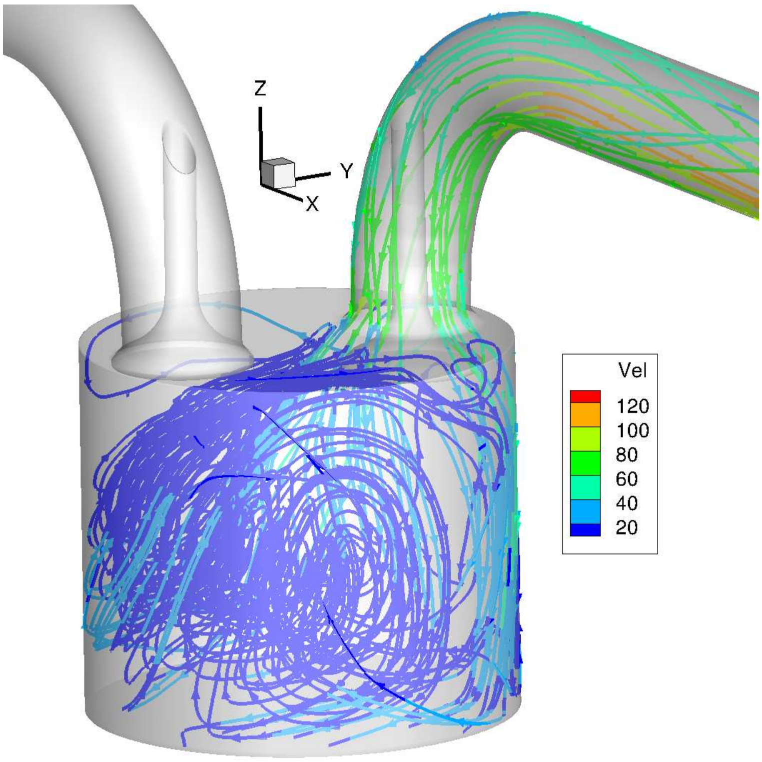

Figure 8.12: 3D streamline profile when intake valve is opened CA = 120^o ATDC

The highest achieved intake charge velocity during the suction stroke is 170 m/s, when intake valve opening and pressure drop across the valve is optimum. In the present engine configuration the maximum velocity is achieved at around 40^o engine crank angle when the valve lift is around $4.2\,mm$. The averaged velocity (for 50 cycles) profile in the $X-plane$ is provided in Figure 8.13a depicting a sectional view including both the intake and exhaust valves at the engine crank angle of 120^o ATDC. The valve guided air-charge stream strikes the piston top and bend along the piston surface in clockwise direction, thus forcing the ensuing charge motion from the intake valve to tilt towards the right hand side. This way the charge motion creates a tumble motion in the X-$plane$ (see the vector plot in Figure 8.13a). The high intake charge motion also carries high degree of turbulence when it passes through the valve openings and therefore the high intensity velocity fluctuations are inevitable during the intake stroke. The RMS averaged value of velocity fluctuations over the 50 cycles is depicted in Figure 8.13b. The high intensity fluctuations are clearly visible in both side of intake valves. The RMS averaged velocity fluctuations profile suggests the frequent lateral movements (both side) of the charge stream along the averaged velocity profile. The velocity fluctuations for 50 cycles in the X-$plane$ along a horizontal line is shown in Figure 8.14. Figure 8.14a represents the instantaneous velocity profile for various engine cycles with superimposed average velocity (thick-black line). The two velocity peak is clearly visible for high intake charge around the intake valve. The peak velocity zone is seen to be varying along average velocity corroborating observation in the previous figure. The observed velocity fluctuations over the mean velocity is as high as $\pm 40\ m/s$.

The mean velocity profile at various sections in the $Z-plane$ is shown in Figure 8.15 in descending order from the cylinder head together with the respective RMS averaged velocity profile over 50 cycles. The high velocity is clearly visible in the region around the intake valve in Figure 8.15a close to valve bottom with maximum fluctuations near the cylinder wall. The vector plot of velocity field does not show any evidence of swirl motion at this stage, although small vortex clearly visible in the few sections. The intensity of velocity fluctuation is seen to gradually diffused over the cross section along the downward stroke length.

A further illustration of cycle-to-cycle variations on in-cylinder flow is provided in Figure 8.16 with mean velocity, and RMS averaged velocity plot at various z-location (in central X-$plane$). It is arranged in descending order from the cylinder head towards the piston surface. The top left figure shows the velocity plot at Z = *8 cm* very close to cylinder head. The obvious velocity peak can be observed near the wall in the right hand side located slightly off-center. The corresponding plot on the velocity variation (see Figure 8.16 top-middle) clearly shows the velocity fluctuations in the region of higher mean velocity. The intensity of the central location tends to diminish with further downwards, however the finite fluctuation is still visible near the cylinder wall. The results at further downward locations Z = *1 cm*, and Z = *2 cm* (bottom two row) illustrate homogeneous mean velocity and turbulence. This trend is also visible in the normalized RMS velocity profile shown in the third columns.

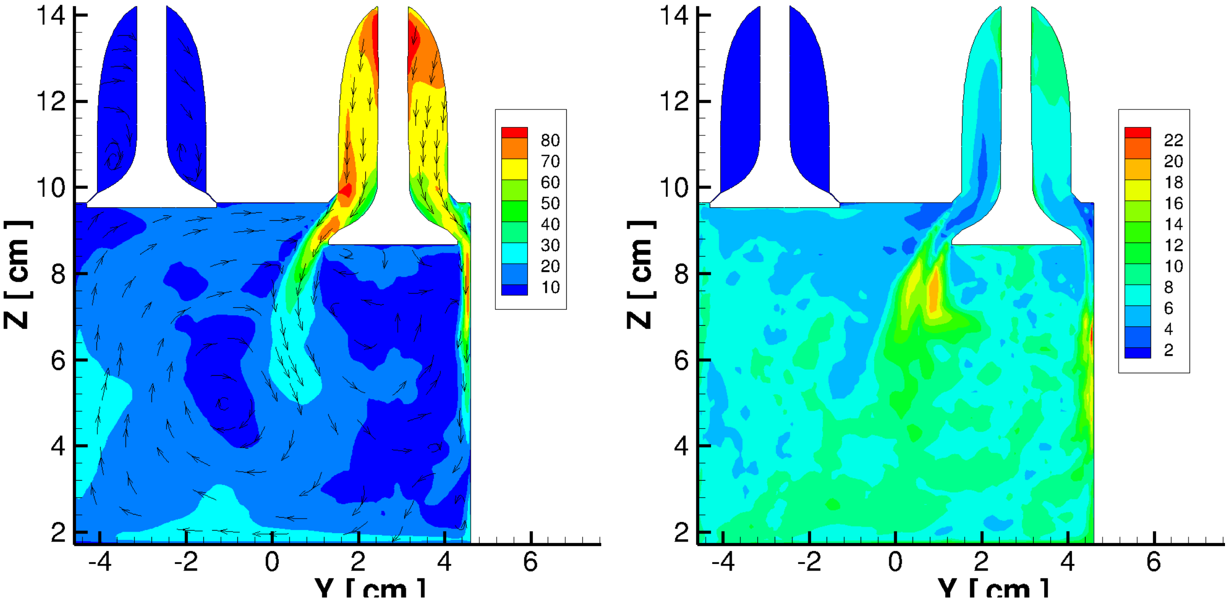

(a) (b)

Figure 8.13: Plotted profile for 50 cycles CA = 120^o ATDC (a) average velocity profile and (b) velocity variance

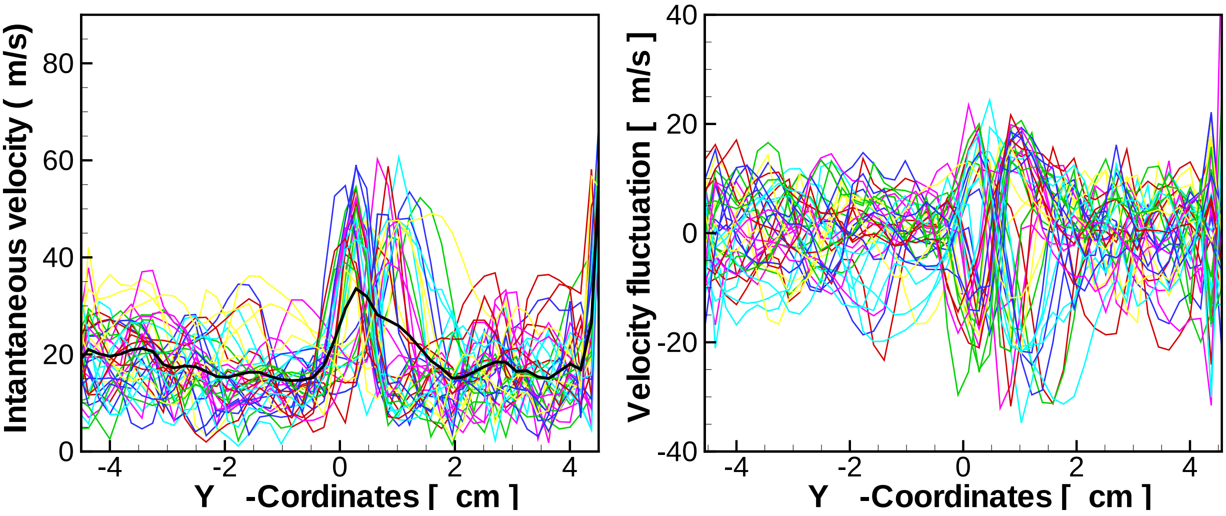

(a) (b)

Figure 8.14: Plotted profile for 50 cycles CA = 120^o ATDC (a) instantaneous velocity profile and (b) fluctuating velocity

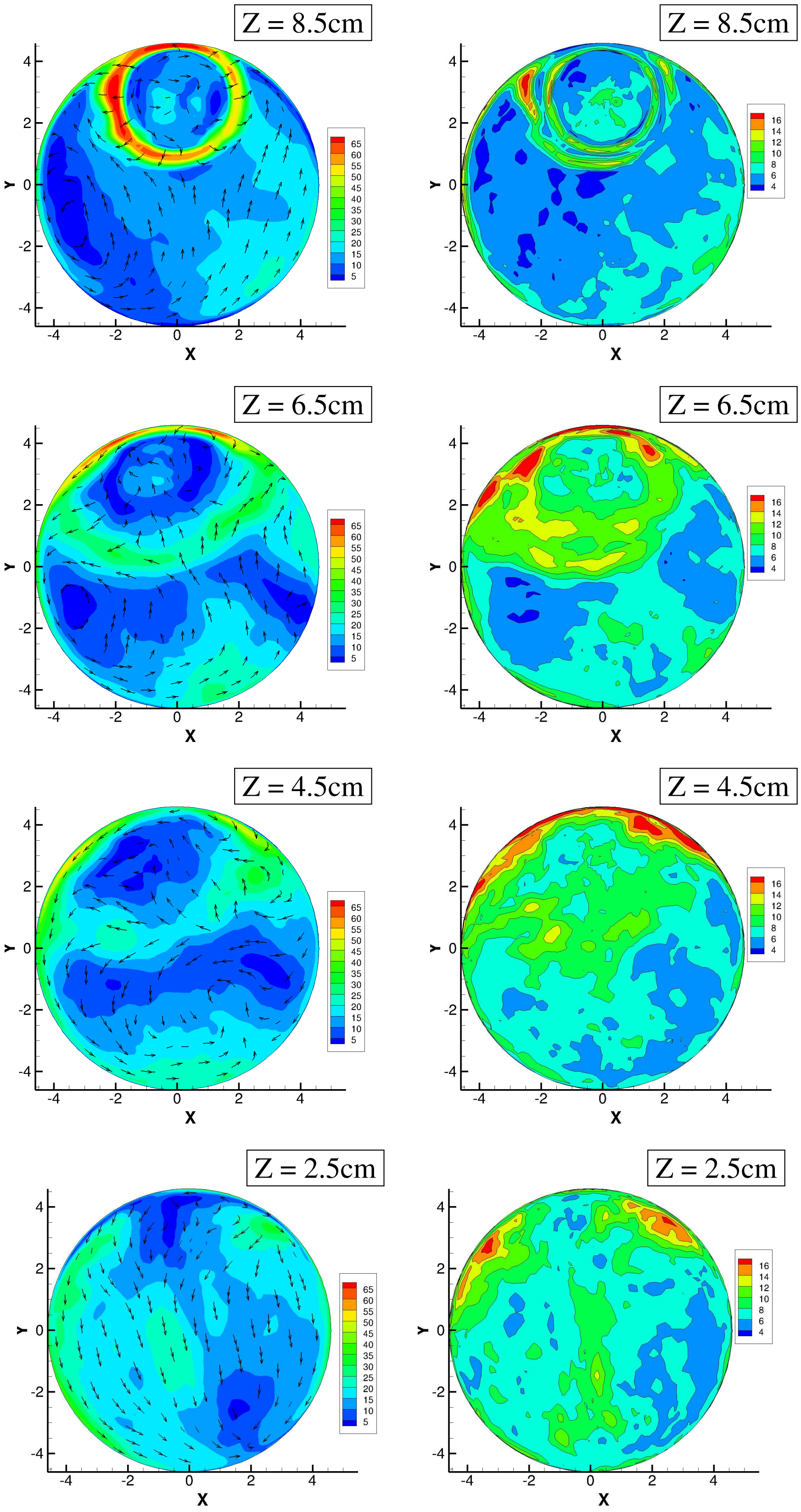

Figure 8.15: Mean velocity profiles (left column) and rms averaged velocity profiles (right column) at selected z-positions during intake stroke CA = 120^o

8.2.4.2 Compression stroke

In general, the upward piston movement after intake stroke is considered as a compression stroke, however the pressure start to build up only when the intake valve is completely closed (in the present case till CA = 252^o). The velocity profile after the closure of intake valve is illustrated in Figure 8.17a with corresponding RMS profile of velocity fluctuation in right hand side (see Figure 8.17b). It can be observed that, overall flow dynamics during the intake stroke has helped to generate the vortex which centered towards the right-middle region (intake valve side). The RMS profile of the velocity fluctuation clearly shows the turbulence generated during the charge intake is still persist in the compression stroke, however the degree of turbulence is greatly reduced. The Figure 8.18a depicts plot of the instantaneous velocity at section Z = *8.0 cm* at engine CA of 260^o ATDC showing peak velocity has shifted opposite side (exhaust valve side) of the vortex centre, however the intensity of the velocity fluctuation is relatively homogeneous with fluctuating velocity in the range of $\pm$*3 m/s*.

The velocity vectors and corresponding contours are plotted to visualize and analyze the flow profile in the various Z-$planes$ (see Figure 8.19) with respective RMS velocity fluctuations in the right hand side. Since, at this stage the intake valve is closed the peak velocity is considerably small in all the sections, which is seen to be convected towards the exhaust valve region. The velocity structure at various section does not represent any formation of the 3-dimensional swirl formation. However, in the middle regions (see Figure 8.19) does show vortex structures, but the vortex centre is considerably offset with each other. This could be mainly due to the effect of complex tumble motion generated during the suction stroke. The RMS profile of velocity fluctuation broadly shows a homogeneous in all the sections with velocity variance of around $\pm$*5 m/s*. The obtained profile for mean velocity at various section (see Figure 8.20) also suggest that the higher velocity in the lower left region, while the velocity variance is almost homogeneous in all the section. The normalized velocity variance is of same order as during intake stroke.

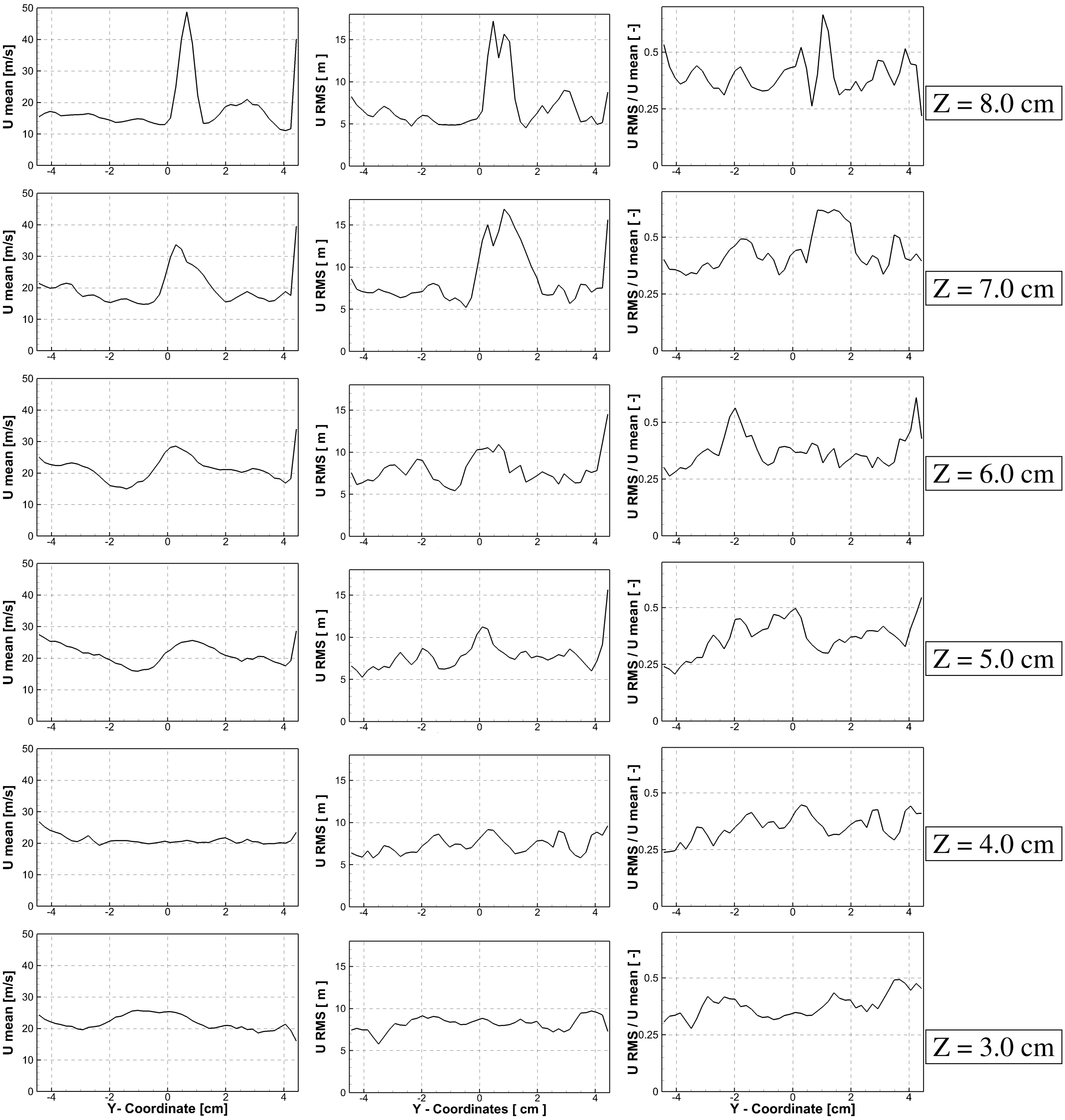

Figure 8.16: Mean velocity profiles (left column), standard velocity deviation (middle column) and rms of velocity normalized with local mean velocity (right columns) at selected z-positions during intake stroke, CA = 120^o

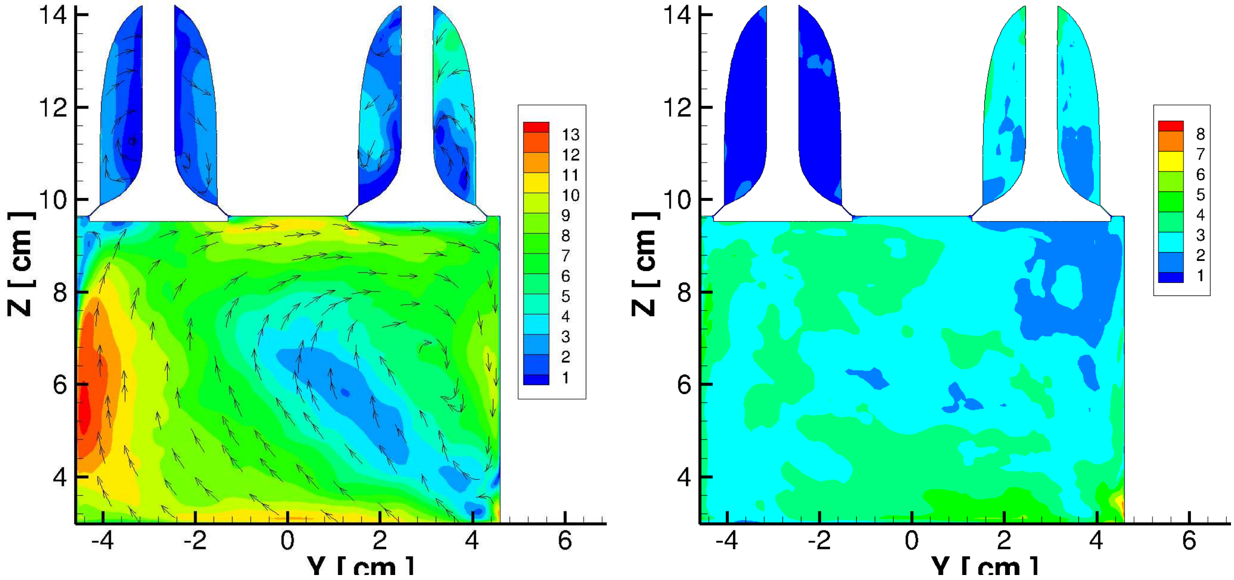

(a) (b)

Figure 8.17: Plotted profile for 50 cycles CA = 260^o ATDC (a) average velocity profile and (b) velocity variance

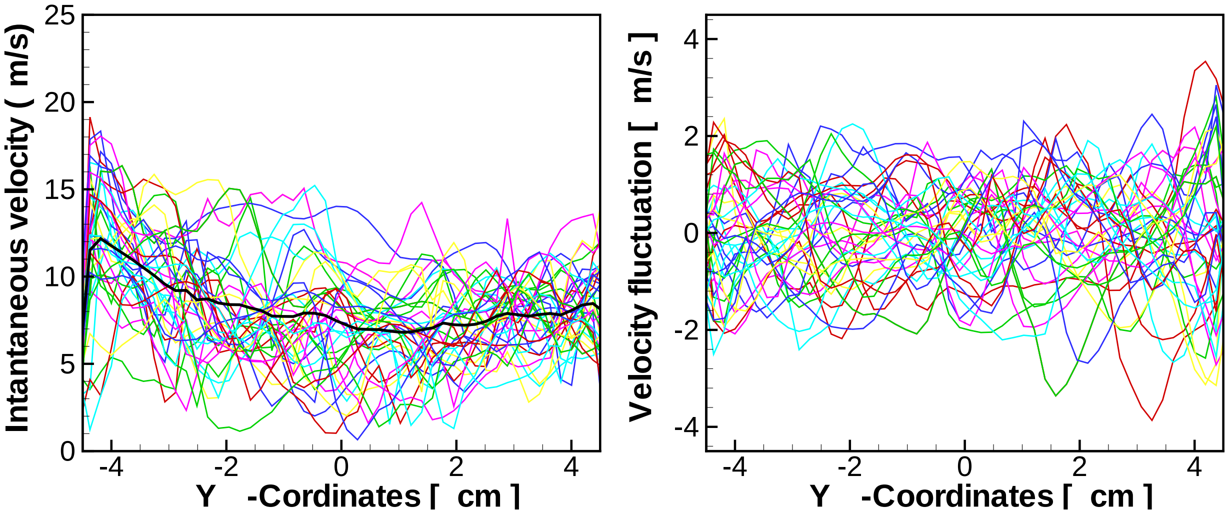

(a) (b)

Figure 8.18: Plotted profile for 50 cycles CA = 260^o ATDC (a) instantaneous velocity profile and (b) fluctuating velocity

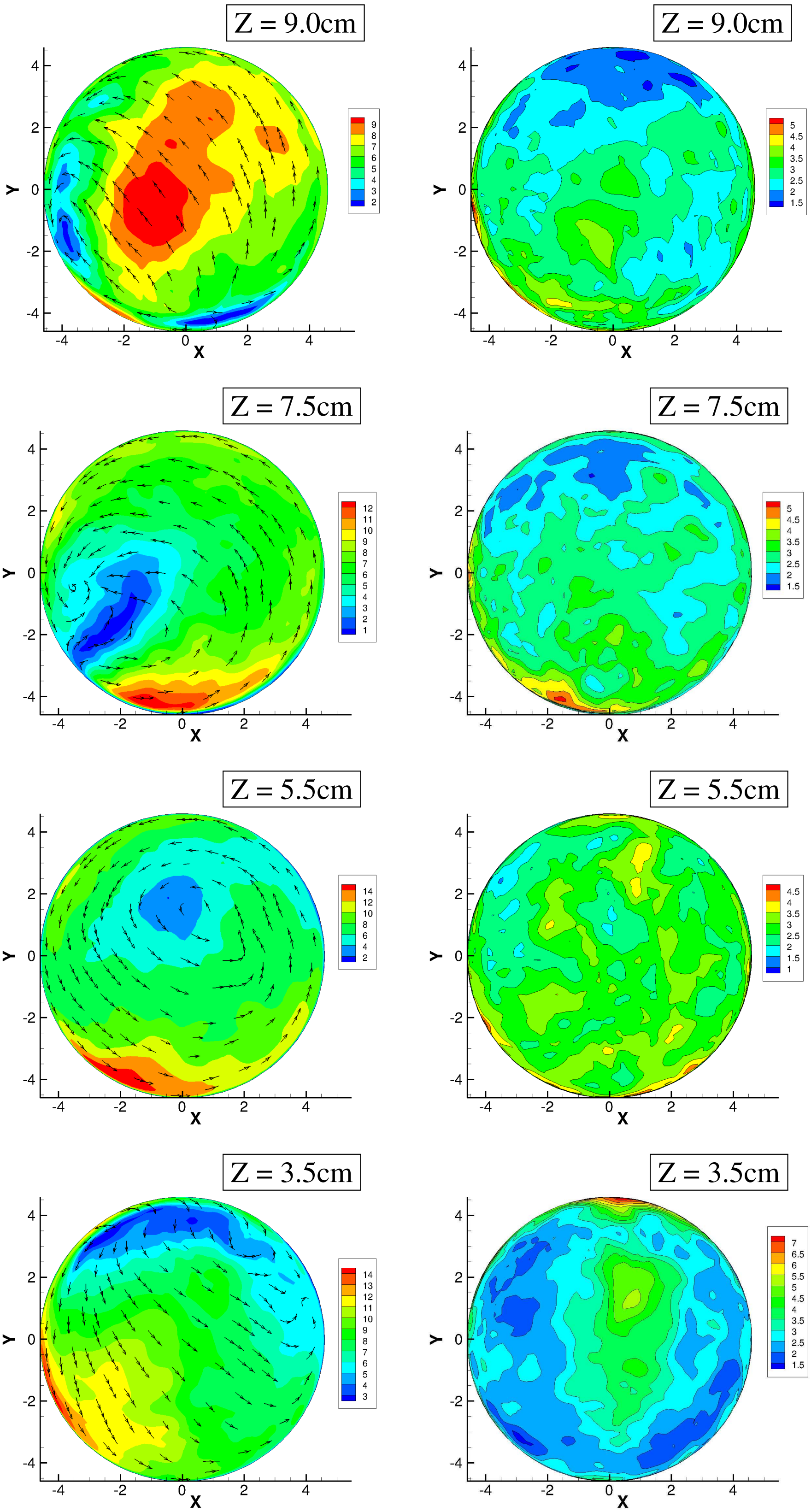

Figure 8.19: Mean velocity profiles (left column) and rms averaged velocity profiles (right column) at selected z-positions, for CA = 260^o

8.2.4.3 Expansion stroke

The expansion stroke is characterized by the downward motion of the piston surface and expansion of the product gas after combustion. In the present study, the cold flow is simulated without consideration of the combustion and reaction. Therefore, the actual flow condition differs in terms of the pressure, temperature, and final velocity profile. However, the cold flow analysis is still useful and it can be able to address and analyze the basic feature of a given engine configuration to recommend relevant design changes.

The velocity profile is illustrated in the Figure 8.21a for engine crank angle of 450^o. The maximum velocity magnitude is observed in the order of piston speed, which is relatively smaller than in the case of intake and compression stroke. The velocity magnitude gradually decreases from the piston surface to the cylinder head. The plotted velocity vector is representing mainly the downward motion of the piston surface. The corresponding RMS velocity profile is shown in the adjacent Figure 8.21b representing homogeneous turbulence. The obtained instantaneous velocity profile in X-$plane$ along the line at *Z = 8.0 cm* is plotted in Figure 8.22 along with the velocity fluctuation. The result shows a noticeable cycle-to-cycle variations on velocity field, but the degree of fluctuation is very small in the range of the $\pm 2\ m/s$.

An illustration is also made for velocity contour and respective RMS value at various sections along the Z-direction in Figure 8.23. In all the sections, vortex located in central region with vortex radius equivalent to cylinder radius is clearly visible suggesting the formation of swirl motion. The RMS velocity contour suggests even velocity fluctuations over the plane with exception near the wall region. Figure 8.24 is the line plot for mean velocity , variance and normalized variance showing similar trends. Although the magnitude of the velocity variance is of similar range for all the sections, the normalized velocity is higher near to cylinder head due to smaller mean velocity.

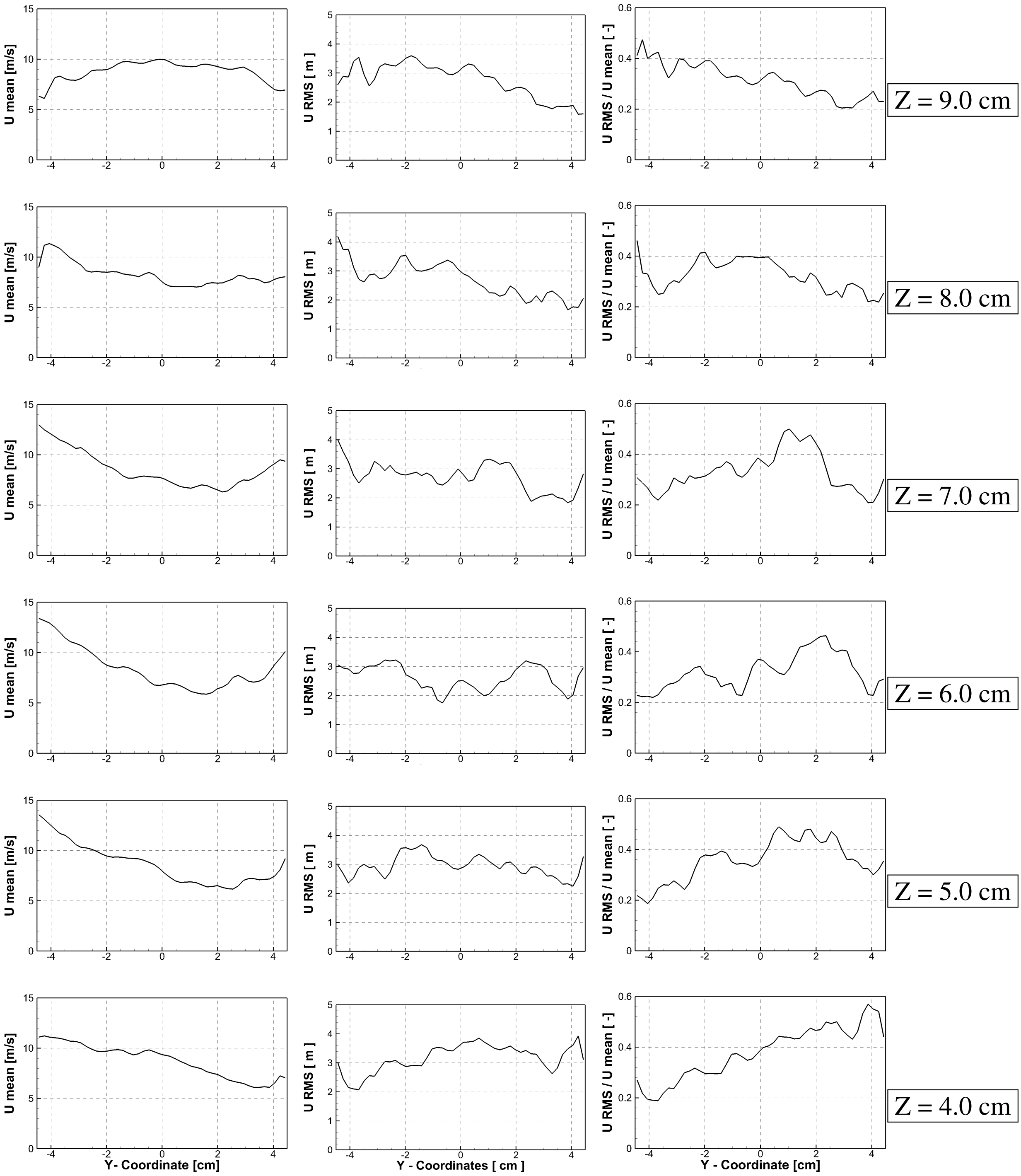

Figure 8.20: Mean velocity profiles (left column), standard velocity deviation (middle column) and rms of velocity normalized with local mean velocity (right columns) at selected z-positions during intake stroke, CA = 260^o

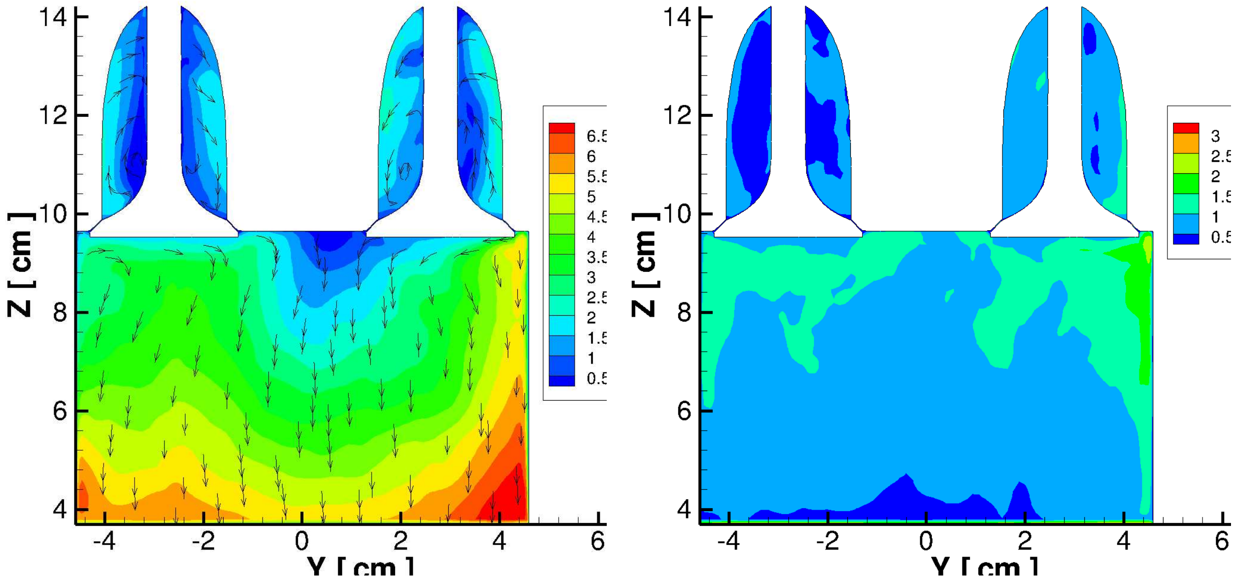

(a) **(b)**

Figure 8.21: Plotted profile for 50 cycles CA = 450^o ATDC (a) average velocity profile and (b) velocity variance

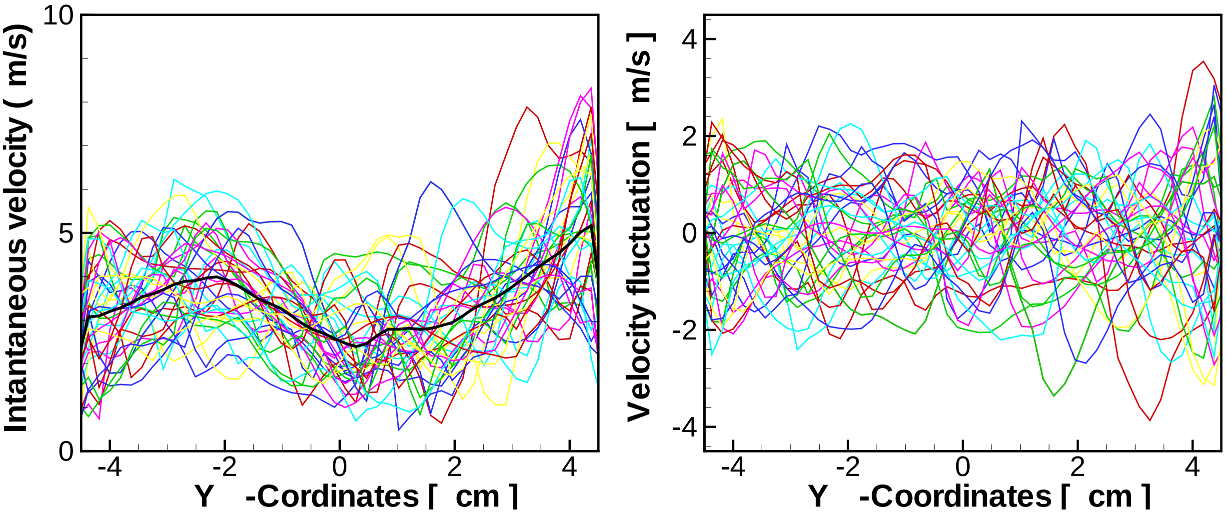

(a) **(b)**

Figure 8.22: Plotted profile for 50 cycles CA = 450^o ATDC (a) instantaneous velocity profile and (b) fluctuating velocity

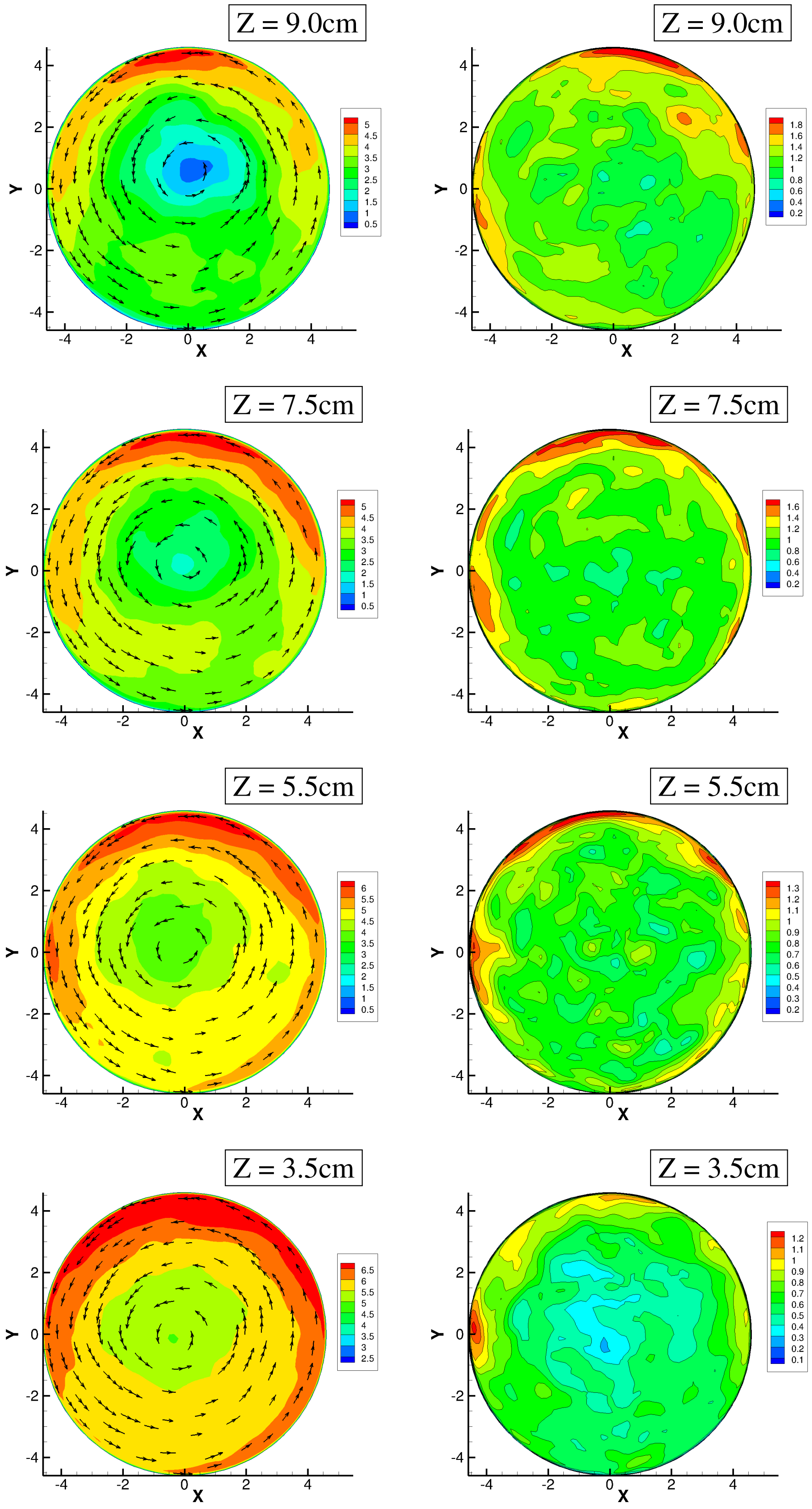

Figure 8.23: Mean velocity profiles (left column) and rms averaged velocity profiles (right column) at selected z-positions for CA = 450^o

8.2.4.4 Exhaust stroke

The exhaust stroke is characterized by an expunction of the burnt gas from the cylinder volume after power stroke to make the engine ready for the new engine cycle. In general the exhaust stroke is considered from the (bottom dead centre) BDC (CA 540^o) to TDC (CA 720^o). However, this process can start at any crank angle before/after once exhaust valve is opened, which depends on the requirement of particular engine configuration. In the present configuration, the exhaust valve opens at engine CA 250^o BTDC (CA 470^o) and closes at CA 28^o ATDC. It means the exhaust valve is opened well within the power stroke and remained opened until CA 28^o in the initial stage of intake stroke of next engine cycle. The early opening and late closure of the intake stroke is designed mostly to achieve the required pressure curve in the engine cycle and better scavenging of the burnt gas. Sometime the valve lift profile for exhaust valve is designed to retain some amount of burnt gas for next cycle to avoid NOx formation due to high temperature.

The mean velocity is plotted together with RMS velocity profile in Figure 8.27. In the exhaust stroke, the flow is driven mainly by the pressure difference across the exhaust valve. The region for high velocity can be seen in the area of valve passage and exhaust port (see Figure 8.25a) with velocity fluctuation is also maximum in this zone. The instantaneous velocity is plotted with mean velocity averaged over 50 engine cycles for the section $Z = 8.0\,cm$. The results clearly indicates the peak velocity towards the exhaust valve region. The velocity fluctuation is high in this region with value ranging between $\pm$ $5.5\,m/s$.

The velocity and RMS velocity contours are shown in Figure 8.27. The high velocity zone can be seen around the exhaust valve with magnitude higher towards the wall due to restricted passage. The velocity magnitude diminishes in the downward section and gradually diffuse across the plane. The maximum intensity of velocity fluctuation is also visible in the region of higher velocity, while homogeneous in elsewhere. The vortex formation in lower sections can be implied to the uneven flow distribution around the exhaust valve.

A further quantitative analysis is shown in Figure 8.28 with mean velocity, RMS velocity and normalized RMS velocity profile. In proximity to the valve edge, the mean velocity shows two velocity peaks with corresponding peak in the RMS and normalized RMS profile. Even-though the absolute velocity variance is quiet small. The normalized RMS value is nearly 0.4 in most of the sections indicating the relative intensity of the fluctuation with mean velocity. The mean velocity and RMS gradually die down away from the piston head.

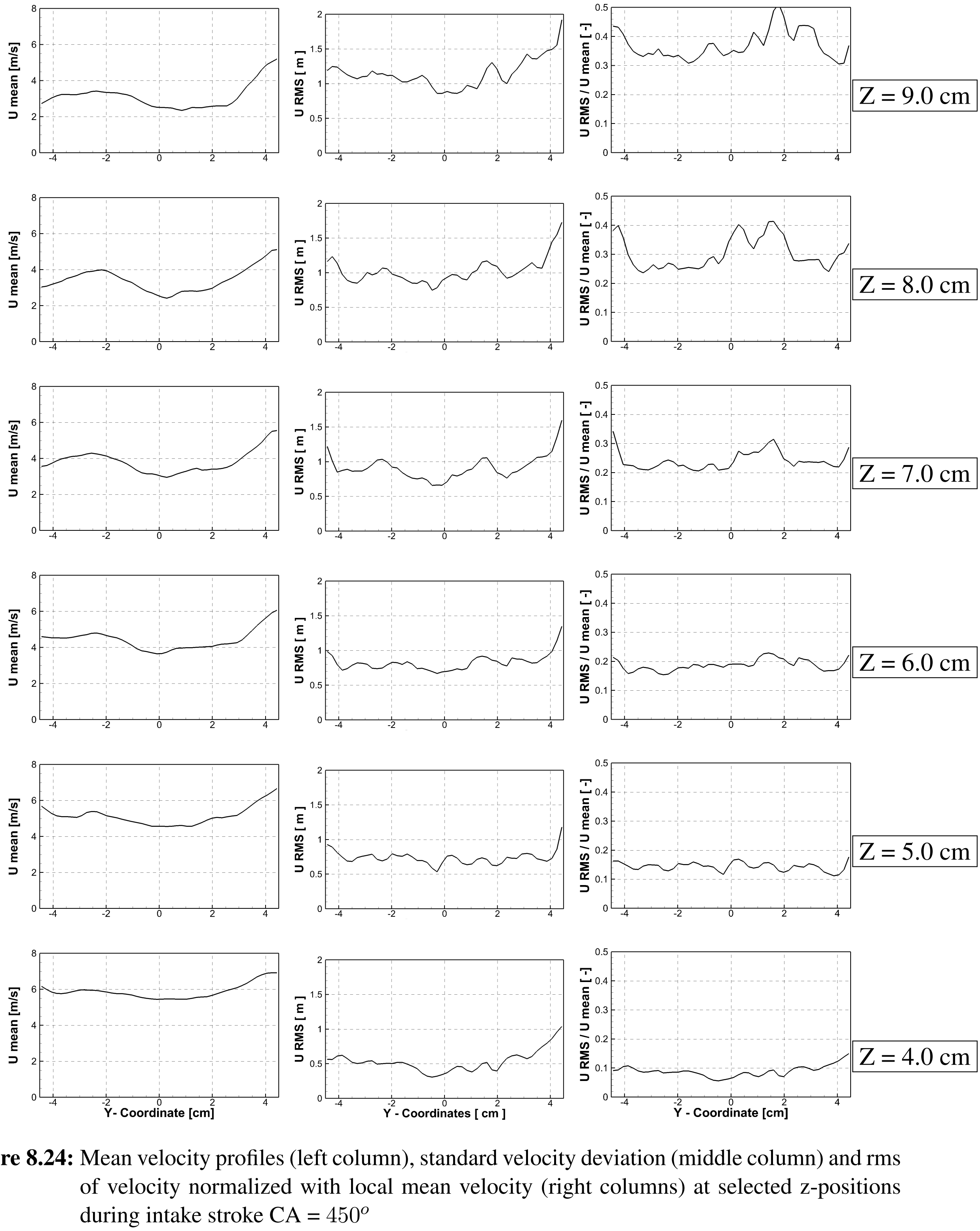

Figure 8.24: Mean velocity profiles (left column), standard velocity deviation (middle column) and rms of velocity normalized with local mean velocity (right columns) at selected z-positions during intake stroke CA = 450^o

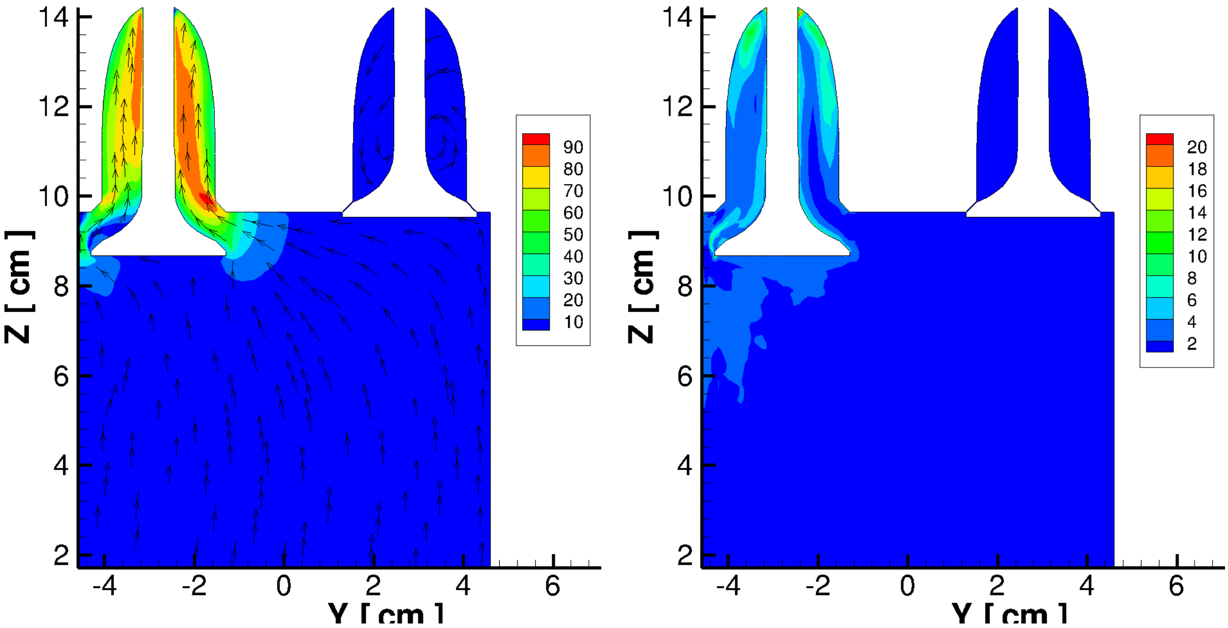

(a) (b)

Figure 8.25: Plotted profile for 50 cycles CA = 600^o ATDC (a) average velocity profile and (b) velocity variance

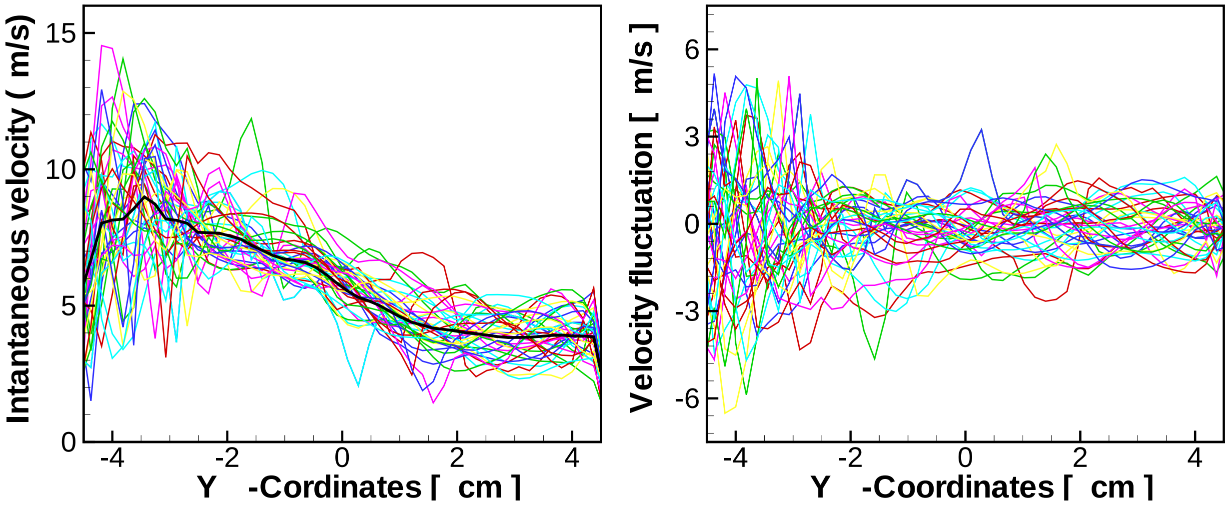

(a) (b)

Figure 8.26: Plotted profile for 50 cycles CA = 600^o ATDC(a) instantaneous velocity profile and (b) fluctuating velocity

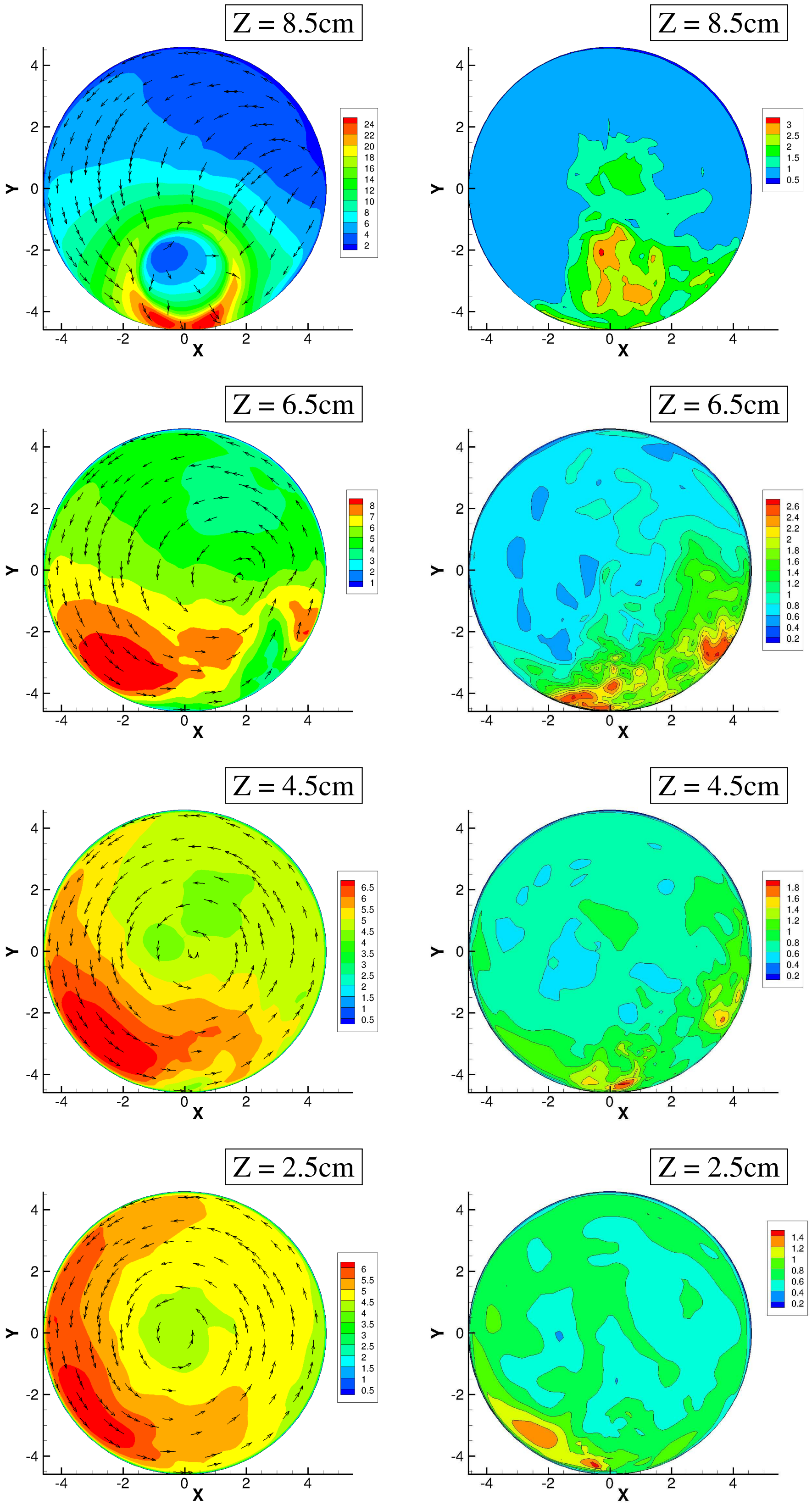

Figure 8.27: Mean velocity profiles (left column) and rms averaged velocity profiles (right column) at selected z-positions for CA = 600^o

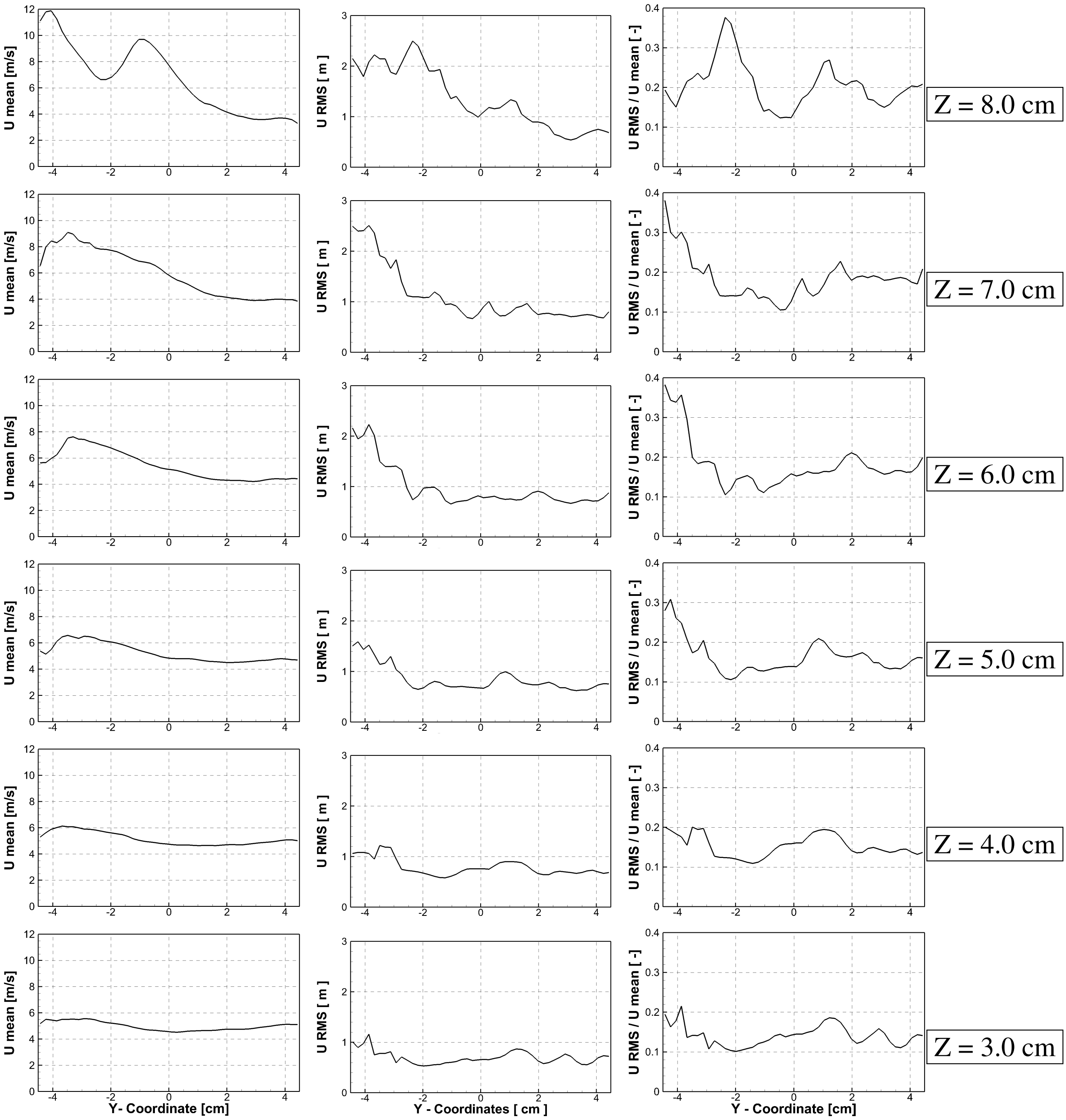

Figure 8.28: Mean velocity profiles (left column), standard velocity deviation (middle column) and rms of velocity normalized with local mean velocity (right columns) at selected z-positions during intake stroke, CA = 600^o

8.3 Influence of fuel injection in the in-cylinder flow field

In order to analyze the evolution of the GDI spray in real engine configuration, the present TCC engine is selected. The flow profile has been already validated with cold flow simulation with averaged cylinder pressure profile with respect to the engine crank angle and the velocity profile against the PIV measurement inside the engine cylinder. To investigate the fuel spray dynamics, a continental piezoinjector with outwardly opening nozzle, which represents one of the available GDI piezoinjector is used [4, 55]. The injector is validated with experimental results comprehensively in terms of the nozzle exit velocity, spray profile, and droplet distribution. The more details about the injector configuration and numerical set up are provided in previous chapter and references [89, 90, 91]. Based on the successful assessment of the fuel injection module and due to the lack of experimental data for the real engine configuration under study, focus is on the numerical analysis of the interaction of high speed intake air with evolving fuel spray and mixture formation. LES has been performed only for one engine cycle, and the spray evolution properties are evaluated at various stage of engine crank angles.

The results are presented in Figures 8.29-8.33 at various stage of engine crank angles for velocity vector, spray profile, velocity contour and evaporated fuel mass fraction. In Figure 8.29, it is clearly visible that the high speed intake air at CA 53^o strikes the GDI spray and deform it considerably. In this process the overall gas phase velocity profile changes considerably. The high velocity region can also be seen along the GDI spray and formation of the inward and outwards vortex is clearly visible below the hollow cone spray and in the vicinity of the intake fuel-air spray interaction. Thereby, it also influences the mass fraction profile (see Figure 8.29c). The process of the fuel-air mixture preparation, that is vital for the IC-engine operation, is then tracked and its evolution is displayed in further Figures at crank angle of 57^o, 59^o, 61^o, 63^o and 66^o, respectively (see Figures 8.30c-8.34c). In case of GDI, there are maximum possibilities of the high speed non-evaporated fuel getting deposited on the piston surface and forms wall liquid film. The deposited fuel then picks up heat from the piston surface and subsequently gets evaporated as visible in Figure 8.33c. This behavior is more pronounced in later stage of fuel injection as shown in Figure 8.34 for CA 66^o ATDC, where relatively large amount of fuel is deposited on the piston surface leading to a large amount of evaporated fuel mass fraction coming out from the surface (see Figure 8.34c). In ideal case, the injected fuel should evaporate completely and form proper fuel-air mixture to have desirable engine performance. The formation of the liquid film directly affects the engine performance especially in transient control. It is a major factor affecting fuel-air ratio due to evaporation time lag resulting from a liquid film deposited. This time lag results in decreased engine response, increased fuel consumption and increased emissions.

8.4 Summary and conclusions

A detail numerical analysis was carried out for the IC-engine configuration with two parallel valves. The hexahedral grid is used to represent the engine geometry, the grid is generated using the new meshing strategy. The LES turbulence model is first validated by comparison with the experimental results obtained for cylinder pressure curve along the engine crank angle, while the velocity profile is compared with PIV results. The compared results show reasonably good agreement between the simulated and the experimental results. Then the LES turbulence model is compared with the RANS (k-ϵ) turbulence model for the multi-cycle simulation to evaluate the turbulence model and its viability to address the important aspect of the cycle-to-cycle variations of the in-cylinder flow. The LES model provides promising results in resolving the flow structure and cycle-to-cycle variations, while the RANS model is able to nicely capture mean flow profile only. The importance of a good quality grid is demonstrated by comparing the results for the traditional meshing strategy against the adopted strategy in the present work. The limitation to achieve quality results due to inability to generate quality mesh is now sorted out with the new technique. While the results from the traditional meshing does not show any sign of the cycle-to-cycle variations, the current approach greatly improve the results quality.

In order to carry out statistical analysis on the in-cylinder flow, LES was further carried out up to 50 engine cycles for the present engine configuration. The mean and RMS averaged velocity profiles are used to analyze the different features of the in-cylinder flow, such as tumble motion, swirl motion, velocity magnitude and turbulence intensity. The maximum velocity with highest achieved turbulence is obtained during intake stroke near the thin passage of the valve and the flow dynamics at this stage is greatly responsible to generate the tumble motion in compression stroke. However, with this engine configuration, the swirl motion is missing during the intake and compression stroke. This can be attributed to the simple shape of the engine geometry. The turbulence intensity is mostly homogeneous in the later parts of the engine operation (compression, expansion, exhaust stroke) with exception of the near wall region exhibiting comparative high degree of velocity variance.

In order to outline the impact of fuel injection module on the IC-engine simulation, LES was carried out for the cold flow coupled to the fuel injection model already validated previously. The injection model includes all relevant sub-models essential for the engine applications. Note that, it is difficult to carry out experiment with fuel injection in such adverse engine condition. Thus only qualitative study was carried out using LES.

The CFD model was able to capture the transient behavior of evolving spray. It could also show, how intake charge motion considerably influences spray dynamics and vice versa, thereby fuel-air mixture formation and its distribution over the entire engine volume. The simulation results demonstrate the evidence of the formation of liquid film on the piston wall which is undesirable for the optimum engine performance.

The integrated improved spray wall interaction model was able to address the wall-impingement phenomena quiet nicely. The presented result can be used as a basis for further analysis of unsteady effects along with cycle-to-cycle variations in real engine configurations including combustion during the power stroke and subsequently a step forwards toward the development of comprehensive engine simulation tool that includes all the required models to address and analyze modern IC-engines.

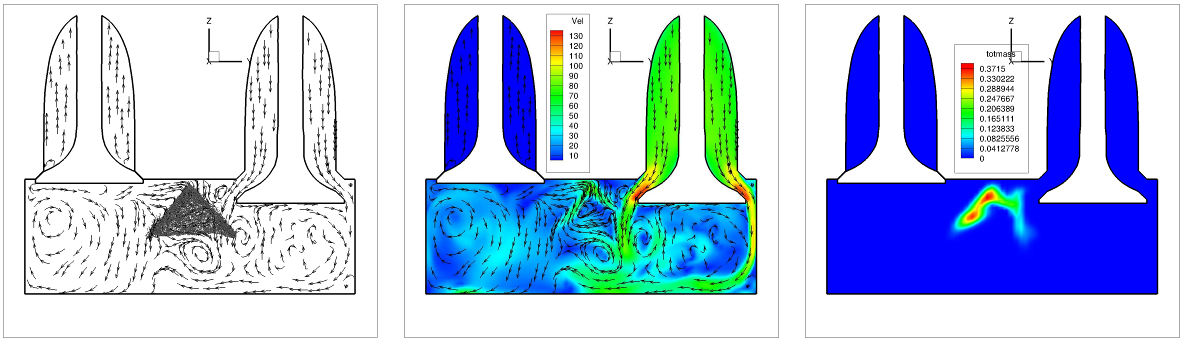

(a) **(b)** **(c)**

Figure 8.29: Sectional view (x-plane) at CA plot 55^o ATDC for (a) Velocity vector and spray droplet (b) Velocity vector and absolute velocity (c) Evaporated fuel mass fraction

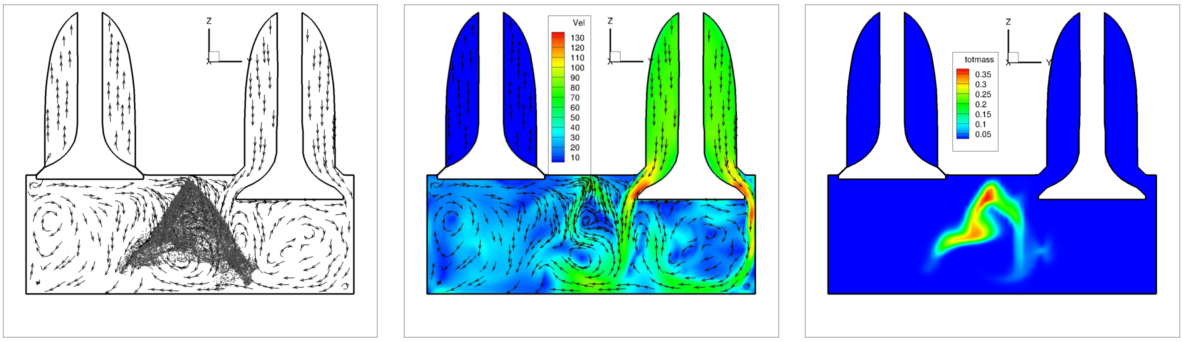

(a) **(b)** **(c)**

Figure 8.30: Sectional view (x-plane) at CA plot 57^o ATDC for (a) Velocity vector and spray droplet (b) Velocity vector and absolute velocity (c) Evaporated fuel mass fraction

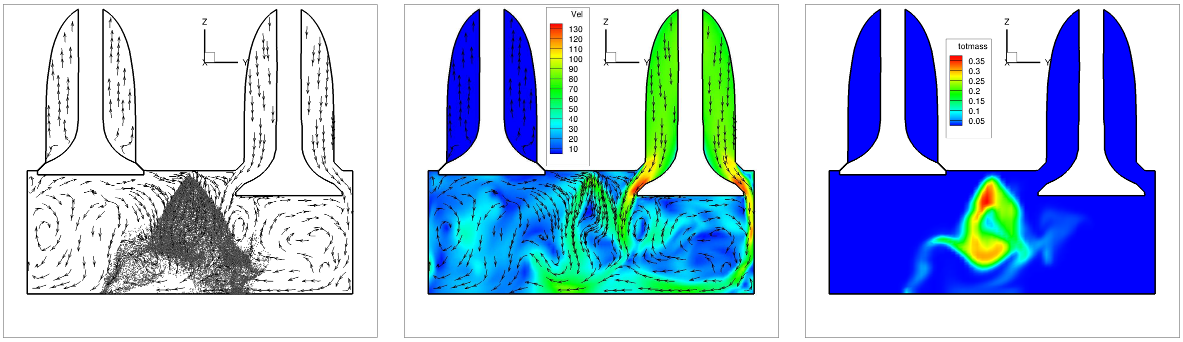

(a) **(b)** **(c)**

Figure 8.31: Sectional view (x-plane) at CA plot 59^o ATDC for (a) Velocity vector and spray droplet (b) Velocity vector and absolute velocity (c) Evaporated fuel mass fraction

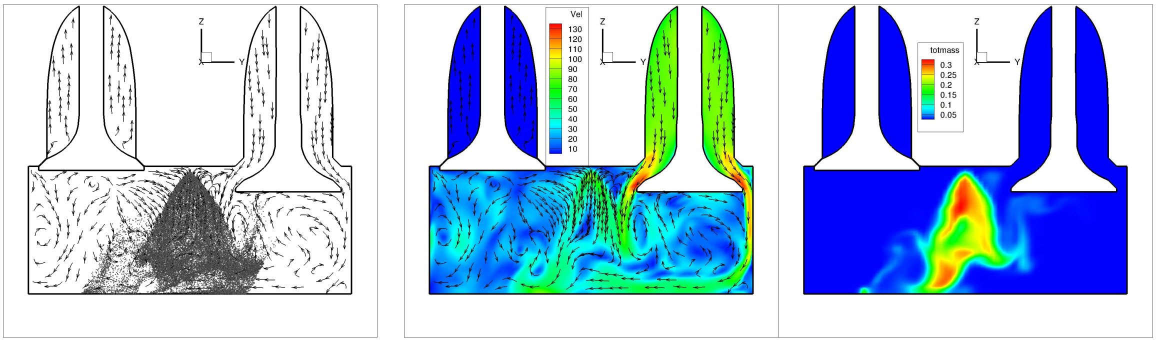

(a) **(b)** **(c)**

Figure 8.32: Sectional view (x-plane) at CA plot 61^o ATDC for (a) Velocity vector and spray droplet (b) Velocity vector and absolute velocity (c) Evaporated fuel mass fraction

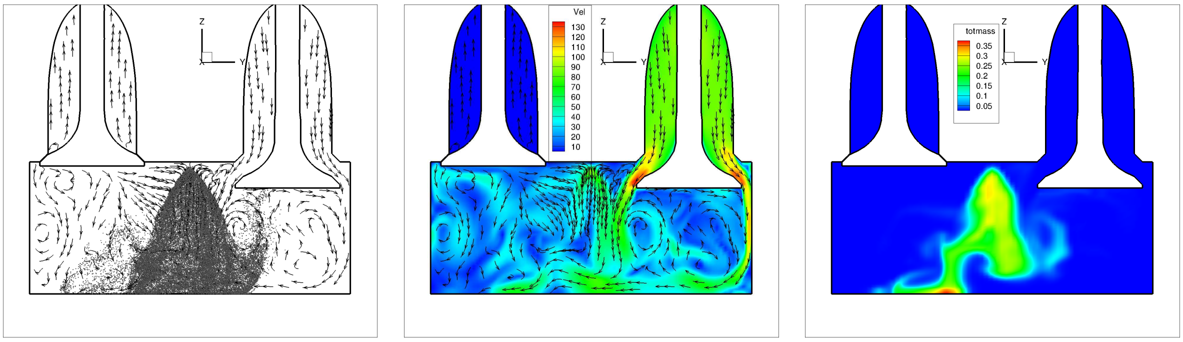

(a) **(b)** **(c)**

Figure 8.33: Sectional view (x-plane) at CA plot 63^o ATDC for (a) Velocity vector and spray droplet (b) Velocity vector and absolute velocity (c) Evaporated fuel mass fraction

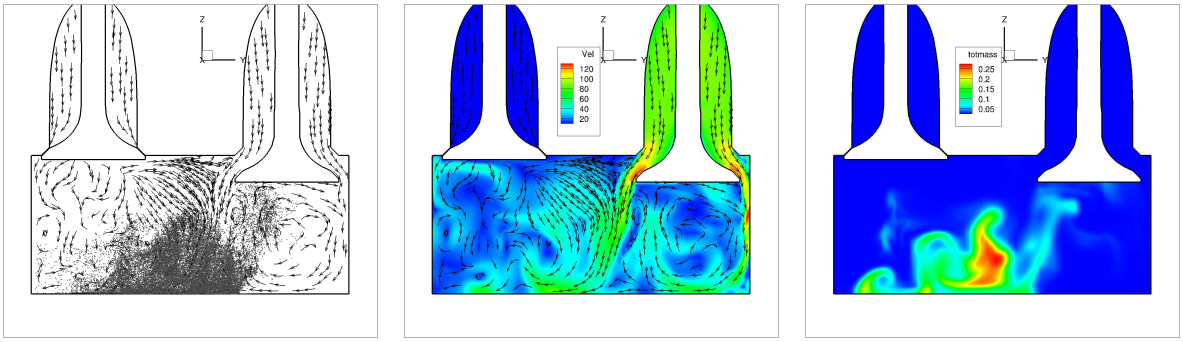

(a) **(b)** **(c)**

Figure 8.34: Sectional view (x-plane) at CA plot 66^o ATDC for (a) Velocity vector and spray droplet (b) Velocity vector and absolute velocity (c) Evaporated fuel mass fraction

9 IC-engine simulation with canted 4-valves

In this section a complex engine configuration with canted 4-valves is investigated. The important and peculiar operating features of the engine are first presented. Then, a statistical analysis is performed for the flow field inside the combustion chamber in terms of cycle-to-cycle variations for multiple cycles using LES technique.

9.1 Engine configuration and numerical Setup

The engine configuration is taken from the Karlsruhe Institute of Technology. The complete geometry and mesh are illustrated in Figure 9.1, the zoomed and closure view of the engine design and respective mesh are provided in Figure 9.2, 9.3. It represents a complex engine design in the context of mesh generation for setting up numerical simulations. The engine has 4-canted valves, 2 valves for intake and 2 valves for exhaust. The individual exhaust port is used for 2 valves, while for the intake a single port is splited into two towards the valve end. Considering the shape of the cylinder head and intake/exhaust port, the engine features are highly complex configuration than one discussed in the previous chapter. Therefore it needed considerable time to achieve the required mesh quality, needless to say it could be only possible with the new meshing strategy used to generate mesh for geometry discussed in previous chapter.

For the numerical setup approximately $1.4\ millions$ hexahedral control volumes are used to represent the engine geometry (see Table 9.1). The engine has bore diameter of $100\ mm$ and stroke length $86.7\ mm$ with engine speed of $2000\ rpm$. More details about the engine configuration is provided in Table 9.2. The current engine configuration has peculiar valve displacement diagram as shown in Figure 9.4. The intake valve opens at engine crank angle 89^o ATDC, contrary to conventional valve opening around the top dead centre (TDC) and it closes around at CA 208^o ATDC. The exhaust valve opens at CA 523^o and closes at CA 631^o, that is again contrary to traditional method in which the exhaust valve closes at the end of exhaust stroke or even some crank angle in the next engine cycle. It will be interesting to see the influence of such a variation on the overall in-cylinder flow dynamics with the help of present CFD simulation and its analysis.

For the present engine configuration, there are not sufficient experimental data available to verify the predictive capability of the adopted numerical approach. The experimental results on the cylinder pressure curve are compared with computed results in Figure 9.5. The results show good agreement with experiment. However the computed results under-estimate the peak pressure value by $2.0\ bar$, which could be attributed to the pressure boundary condition provided at the inlet of the intake port. The pressure curve shown in Figure 9.5 clearly shows unusual but expected two peaks in the cylinder pressure curve, such behavior is mainly because of the unique valve displacement profile adopted for present engine configuration. The intake valve closes at crank angle of 207^o ATDC. Then pressure starts to build-up during compression stroke till it reaches to value of 28.0 bar at top dead centre (TDC). Then pressure starts to descend in the expansion stroke till the exhaust valve is opened (at 523^o CA) and piston reaches bottom dead centre with pressure value of around atmospheric pressure and remains near this value till exhaust valve is closed at CA 631^o, although the exhaust stroke is considered to be till engine crank angle of 720^o. However, due to the early closure of the exhaust valve at CA 631^o, pressure again starts to built up in the so called exhaust stroke till it reaches TDC and the beginning of next engine cycle. Therefore, from the start of next cycle, the cylinder pressure has already built-up to approximately value of 22.5 bar.

9.2 Multi-cycle LES engine simulation: non-reacting

The numerical simulation for in-cylinder flow is performed using the Smagorinsky SGS turbulence model in KIVA4-mpi code with parallel computation for multiple number of engine cycles. Considering the fact that, the engine simulation required complicated Arbitrary Lagrangian-Eulerian (ALE) approach for moving mesh problem to take care of the piston and valve movement, it is relatively more computationally expensive to get results for sufficiently large number of engine cycles to carry out good statistical analysis. In this section the results are produced for mean, and fluctuation flow at various engine crank angle representing different engine operations. In the next few sections, a detail analysis is carried out for in-cylinder flow behavior at various crank angle representing the main engine operations such as intake, compression, expansion and exhaust stroke.

Table 9.1: Computational grids distribution for engine: Karlsruhe engine

Region	**KIVA4-mpi CVs**
Combustion chamber	872,066
Exhaust port	231,368
Intake port	228,508
Intake valve	24,960
Exhaust valve	22,912
Total control volumes	**1379,814**

Table 9.2: Engine parameters: Karlsruhe engine

Parameter	Value
Bore	100 mm
Stroke	86.7 mm
Engine RPM	2000
Compression ratio	10.84
Intake valve open	Crank angle 89^o
Intake valve close	Crank angle 208^o
Exhaust valve open	Crank angle 523^o
Exhaust valve close	Crank angle 631^o

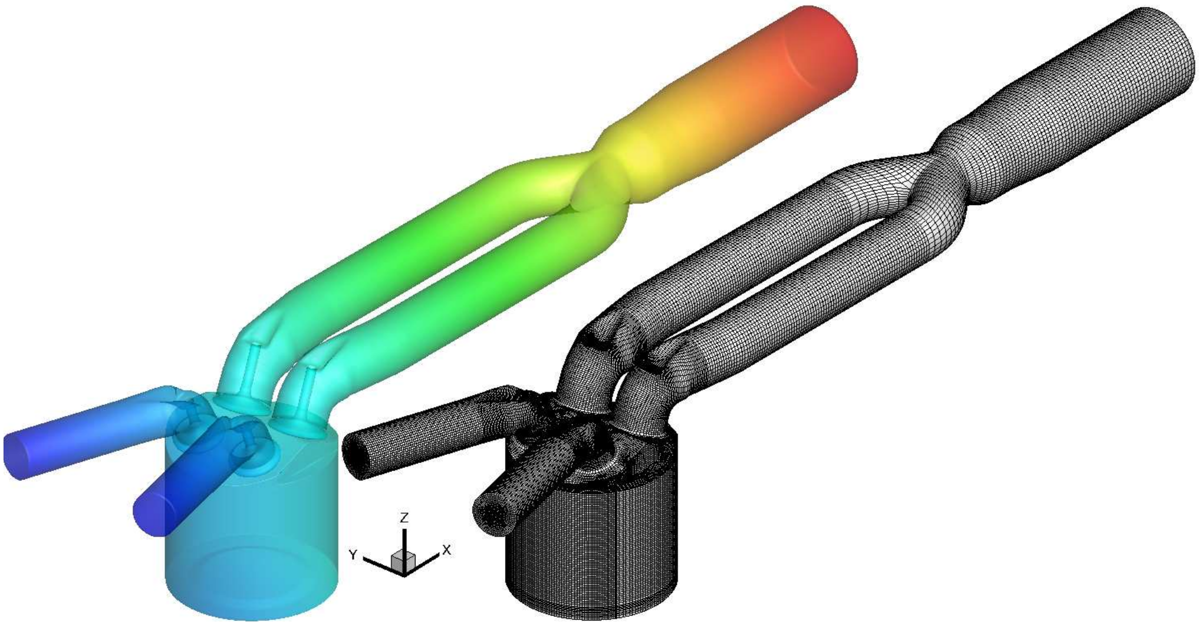

Figure 9.1: Karlsruhe engine geometry and mesh showing cylinder squish, intake/exhaust valves and ports

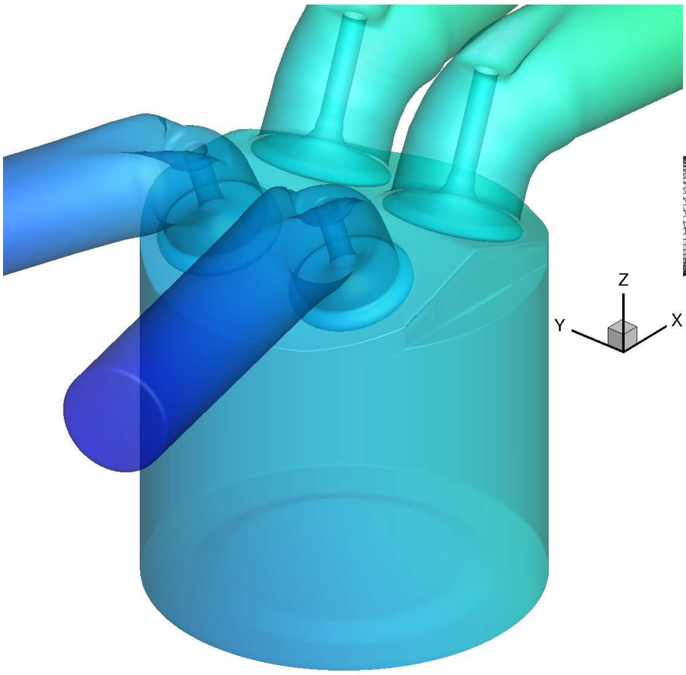

Figure 9.2: Engine geometry (zoomed view) showing cylinder squish, intake/exhaust valves and ports.

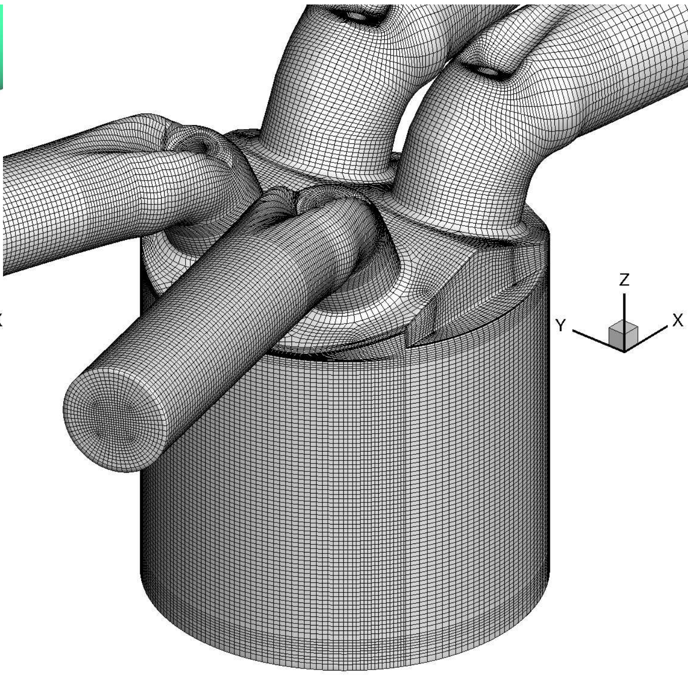

Figure 9.3: Hexahedral mesh (zoomed view) for engine geometry generated in ICEM-CFD.

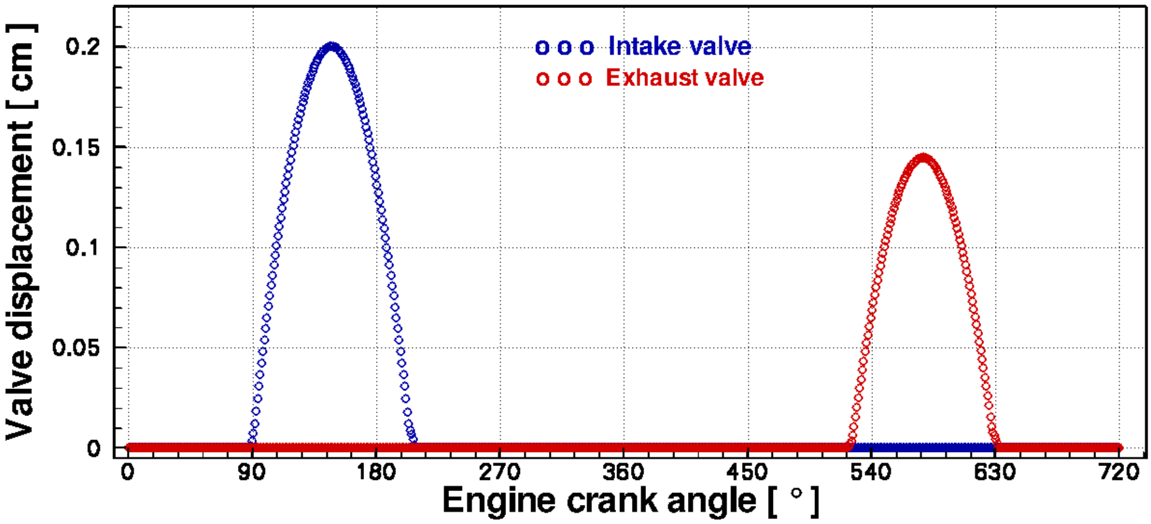

Figure 9.4: Valve diplacement profile for Karlsruhe engine with respect to engine crank angle

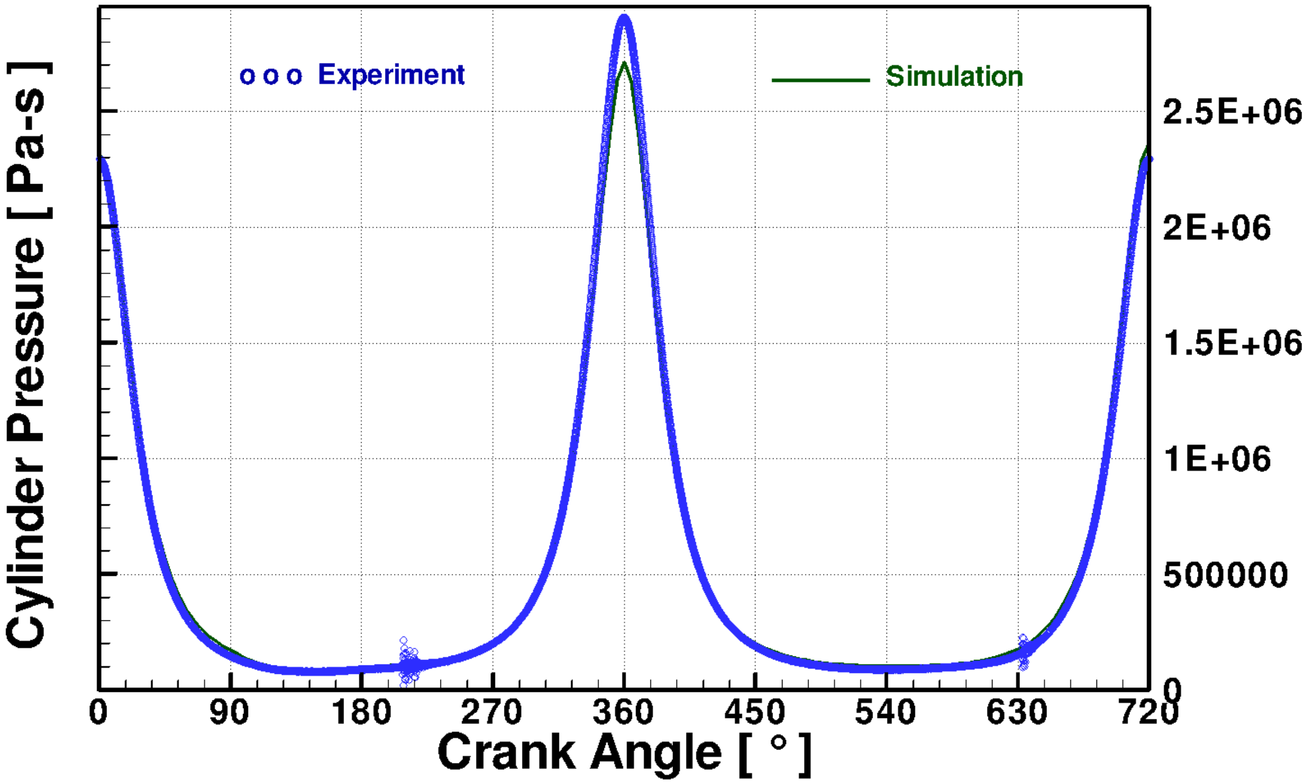

Figure 9.5: In-cylinder pressure curve with respect to engine crank angle: Karlsruhe engine

9.2.1 Intake stroke

In general, during the intake stroke engine draws fresh air due low pressure generated by expansion of the squish volume due to downward piston movement. In this engine configuration, even-though the intake valve is opened at crank angle 89^o, there is little evidence of flow being developed in the squish region. The velocity of intake stream has not peaked up even at crank angle of 150^o (see Figure 9.6a). The primary reason for such a flow behavior is the already built-up cylinder pressure before beginning of intake stroke as discussed in previous section. At engine CA 89^o the pressure inside the cylinder is around $1.7\ bar$ higher than the atmospheric pressure $(1.0\ atm)$ (see Figure9.5). Hence, there is higher chances of the flow reversal, i.e. instead of gas/air flowing inside the cylinder, it starts flowing out through intake port (also known as back flow). The cylinder pressure reaches to atmospheric pressure only around CA of 125^o and pressure becomes equilibrium across the intake valves. Then further downward movement of piston creates low pressure inside the cylinder and the inward flow commence. At engine CA of 150^o the averaged cylinder pressure is around $0.82\ bar$, therefore at this stage flow field inside the squish region has not yet developed (see Figure 9.6a). The sectional view is taken along the X-$plane$ covering an intake and an exhaust valve. With such an under-developed flow, the turbulence intensity will inevitably low as illustrated in Figure 9.6b with higher value only near the constricted region of valve passage. The more quantitative comparison of the velocity profile along a line near the valve region is shown in Figure 9.7a for 35 engine cycles. Although, the flow field has yet to developed, but results clearly showing evidence of cyclic variations. The velocity peak visible in the right hand side corresponds to the velocity near the intake valve. The fluctuations is depicted in Figure 9.7b with little variation of the fields.

The results are further analyzed in Figure 9.8 showing the mean velocity profile at engine crank angle of 150^o for various Z-$plane$ in descending order close to cylinder head towards the piston crown. The region of high velocity field for two intake valves are clearly visible in the section near the cylinder head (at Z = *-2.0 mm*), due to canted valves velocity field is developed only from one side (see Figure 9.8a). In further down and towards the piston crown, the strength of the velocity field gradually decreases (see Figure 9.10) with slightly higher velocity in the right hand side representing the influence of opened intake valves with negligible influences on the lowest plane at Z =*-7.5 cm*. The corresponding plot on the velocity variations are illustrated in Figure 9.9, showing the maximum value close to the intake valve region for Z = *0.0 cm*. The turbulence intensities are very much homogeneous and small for the rest of the planes (see Figure 9.10)

A further quantitative statistical analysis is provided in Figure 9.10, at CA 150^o while intake valve is opened. The profiles are taken in X-$plane$ covering both the intake valves along the Y-$line$ at various Z locations and arranged in descending order from the cylinder head to piston surface. Figure 9.10a represents the mean velocity profile, the 3 peaks location is clearly visible in the plot representing velocity of incoming charge near the intake region, the profile is not symmetric due to uneven shape of the cylinder dome, the corresponding velocity variations that are plotted in Figure 9.10b shows similar trend. However, the normalized variance shows more or less even profile except right hand side with small peak due to the higher variations. The mean velocity profiles in further downwards show evenly distributed with low velocity both side due to wall influence with homogeneous velocity variation (see Figure 9.10g- 9.10o). The intensity of velocity variations are gradually decreasing along the downward Z-section.

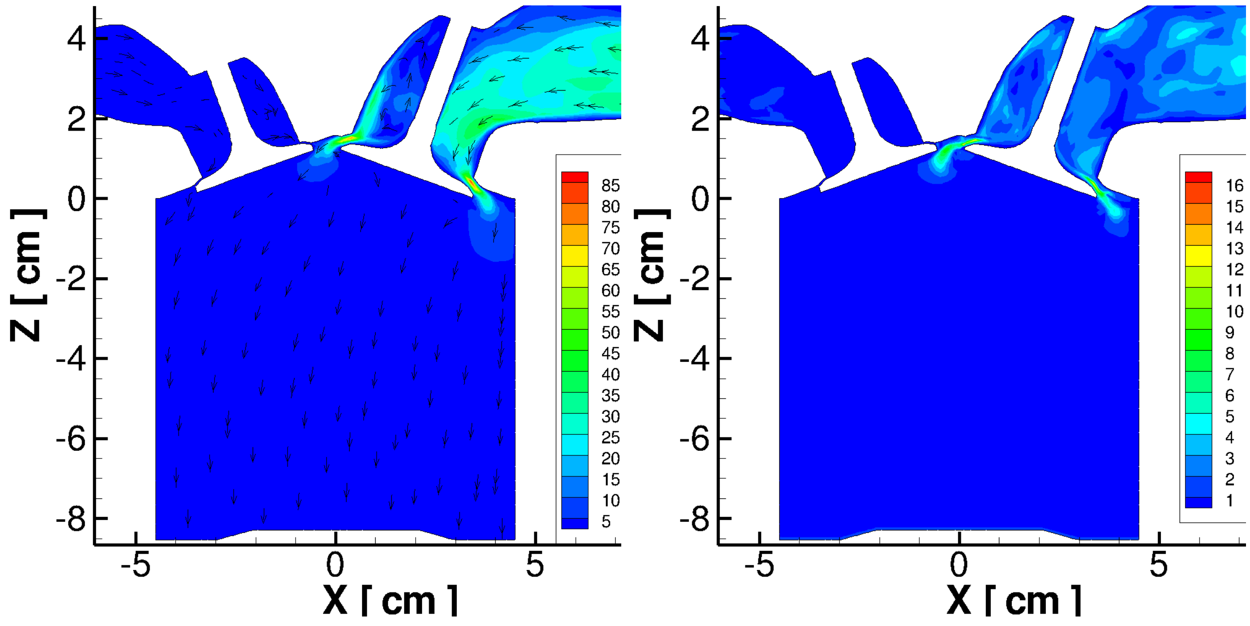

(a)

(b)

Figure 9.6: Karlsruhe engine: Plotted averaged profile for 35 cycles CA = 150^o ATDC (a) averaged velocity profile and (b) velocity variance

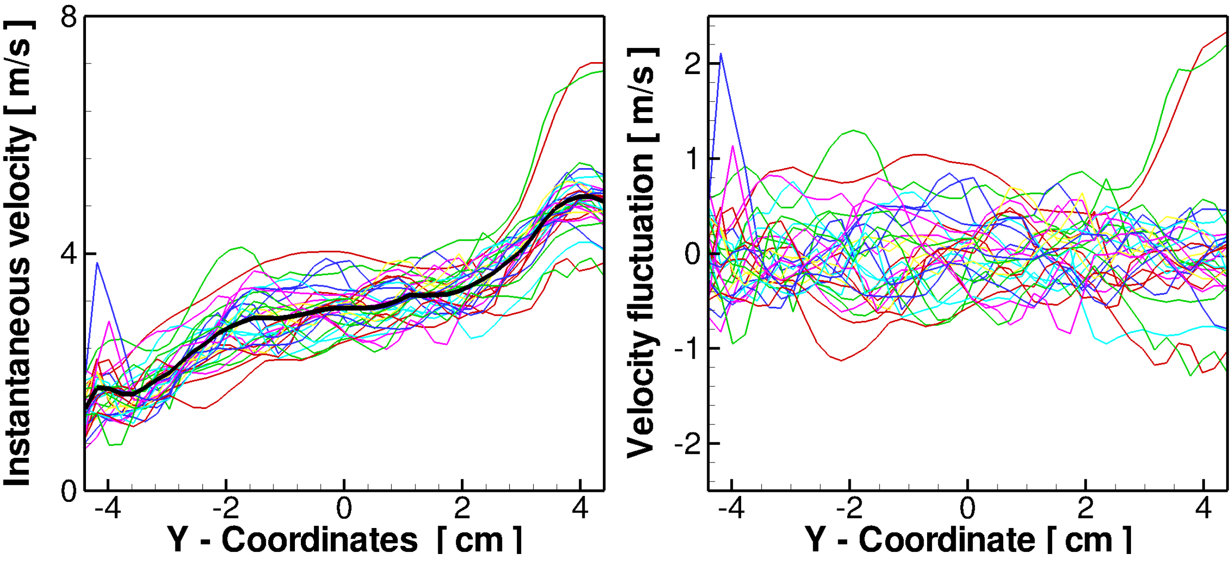

(a)

(b)

Figure 9.7: Karlsruhe engine: Plotted profile for 35 cycles at Y-$plnae$ at Z = *-2.0 cm* CA = 150^o ATDC (a) instantaneous velocity profile and (b) fluctuating velocity

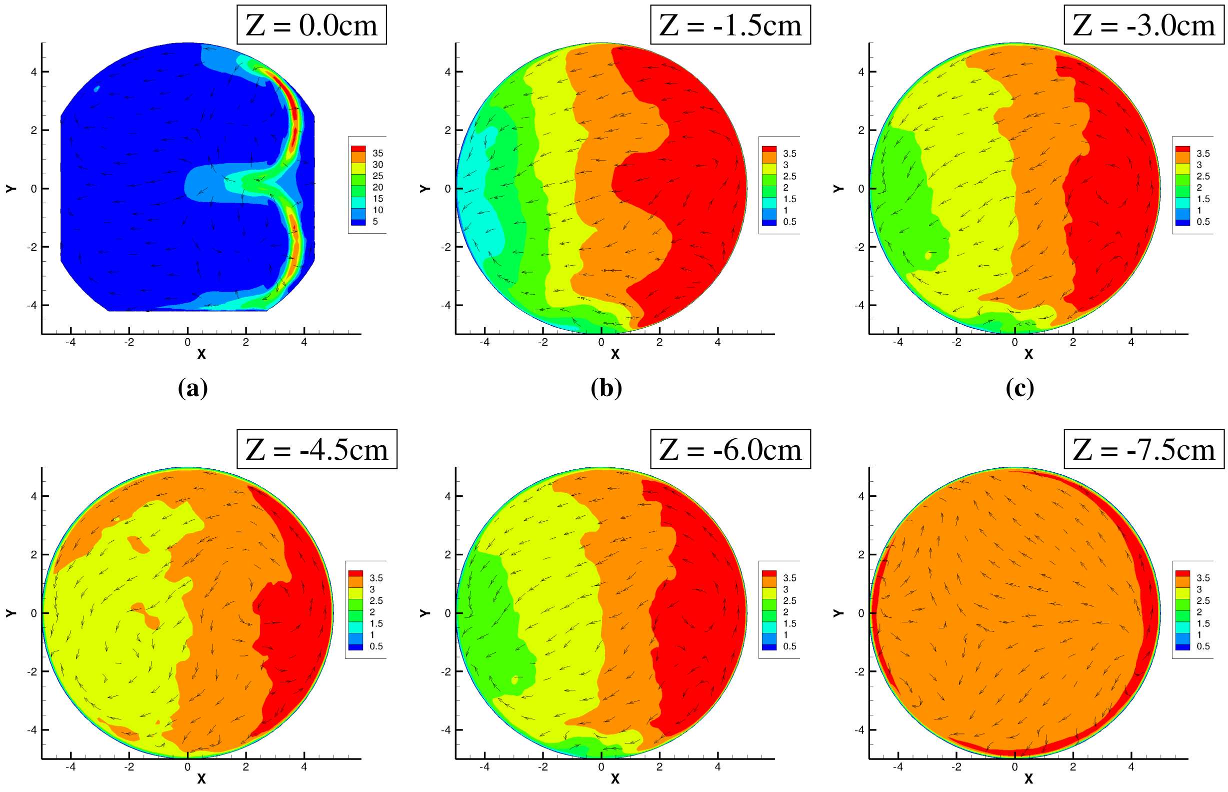

(a) (b) (c)

(d) (e) (f)

Figure 9.8: Karlsruhe engine: Mean velocity profiles on *xy-plane* at selected z positions during intake stroke, CA = 150^o

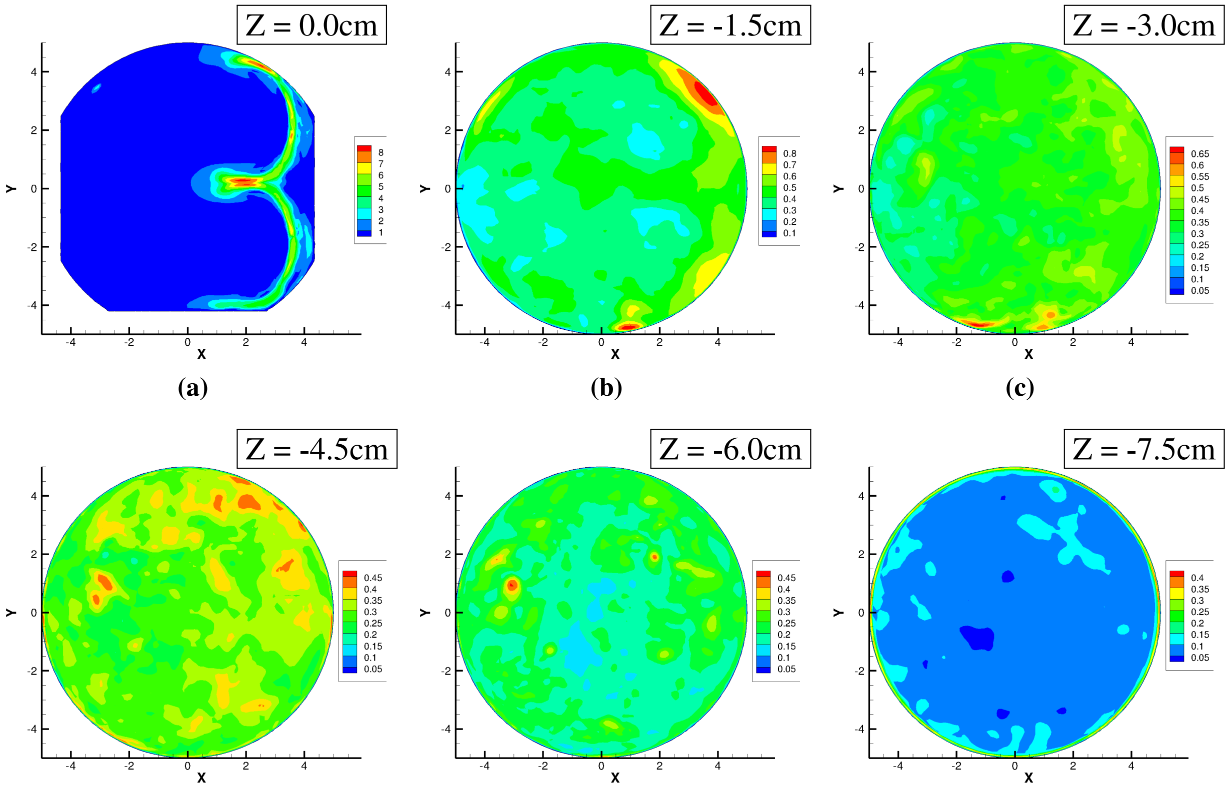

(a) (b) (c)

(d) (e) (f)

Figure 9.9: Karlsruhe engine: RMS velocity profiles on *xy-plane* at selected z positions during intake stroke, CA = 150^o

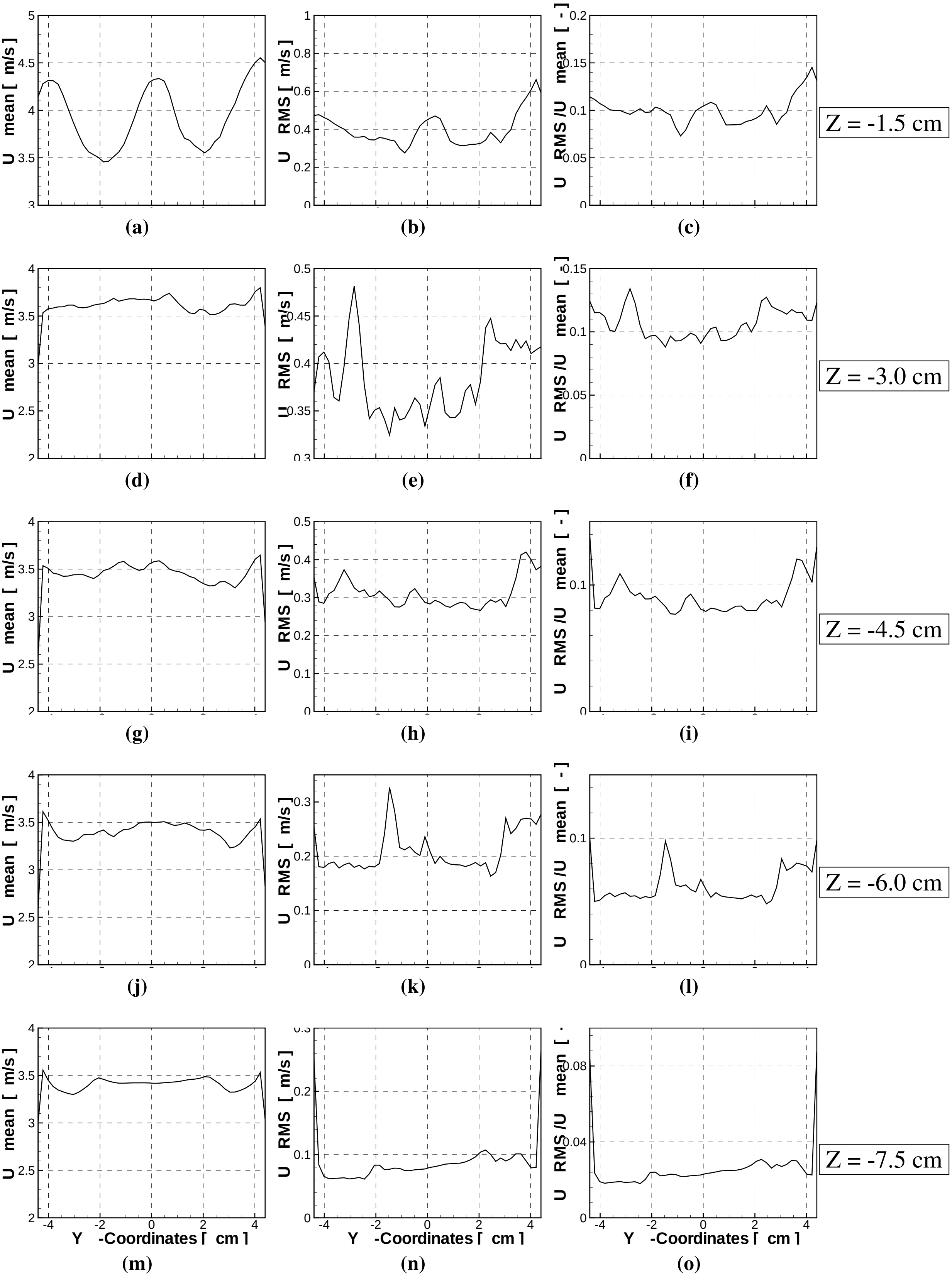

Figure 9.10: Karlsruhe engine: Mean velocity profiles (left column), standard velocity deviation (middle column) and rms of velocity normalized with local mean velocity (right column) at selected z positions during intake stroke, CA = 150^o

9.2.2 Compression stroke

In the compression stroke the upward movement of the piston squeezes the trapped charge inside the cylinder. In this engine configuration, the intake valves remain opened in the compression stroke till CA 207^o, then the cylinder pressure starts to build up. Figure 9.11a shows the mean cylinder flow profile at engine crank angle 240^o ATDC. The flow structures are not well defined (such as swirl or tumble motion) and it is distributed every where inside the cylinder, there is also no signature of tumble motion in this plane. The velocity variation depicted in Figure 9.11b also represent more or less even distribution with lower value towards the piston region. The instantaneous velocities plotted for multiple cycles show evidence of cyclic variations (see Figure 9.12a), however the averaged velocity shows little variations along the Y-direction, with homogeneous fluctuations ranging between $\pm\ 5m/s$ (see Figure 9.12b).

The mean velocity profiles are extracted at the various value of z on xy-$plane$ along the stroke length (see Figure 9.13). The velocity does not represent any odered flow structures as the multiple pockets of low and high velocity can be seen all over the plane for all the sections. The evidence of any swirl motions are also not visible for this engine configuration. Although, some kind of vortex structures can be seen at the sections *z = -3.0 cm* and *z = -4.5 cm*, but the vortex locations does not in-line with each other suggesting the localized vortex formation. The visible higher velocity magnitude in the right hand side in the lower sections at *z = -3.0 cm* , *z = -4.5 cm*, and *z = -6.0 cm* can be attributed to the velocity field reflected from the piston bottom during the charge intake. Figure 9.14 represents the velocity variation profile for 35 engine cycles shown at corresponding z location in the xy-$plane$. The velocity fluctuation profile seems more homogeneous on the planes near the cylinder head, while it becomes more heterogeneous towards the piston surface as shown in Figure 9.13. This could be attributed to the reflected velocity structure from the piston wall that carry low turbulence.

The plots of mean velocity profile and respective variation are illustrated in Figure 9.15. The value of the mean velocity can be seen lower in the region of left intake valve and the value gradually increases and becomes near homogeneous towards the downward sections. However the value of velocity variance and normalized velocity variance seems to lie in the same range over various sections in the xy-$plane$.

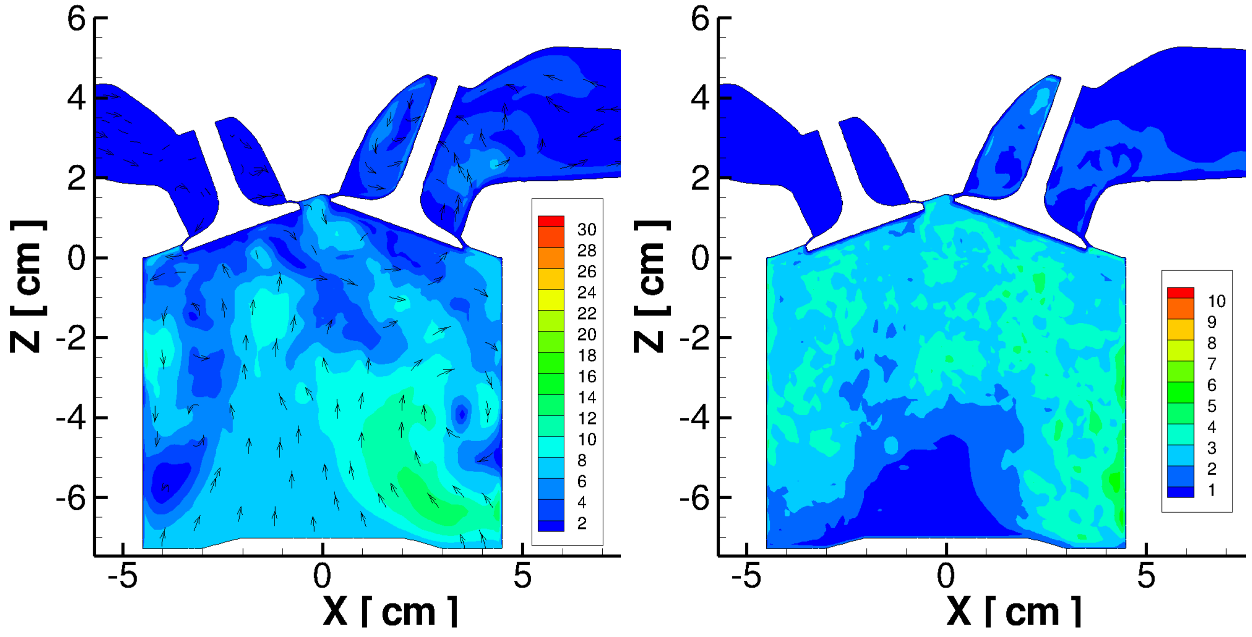

(a) **(b)**

Figure 9.11: Karlsruhe engine: Plotted averaged profile for 35 cycles CA = 240^o ATDC (a) averaged velocity profile and (b) velocity variance

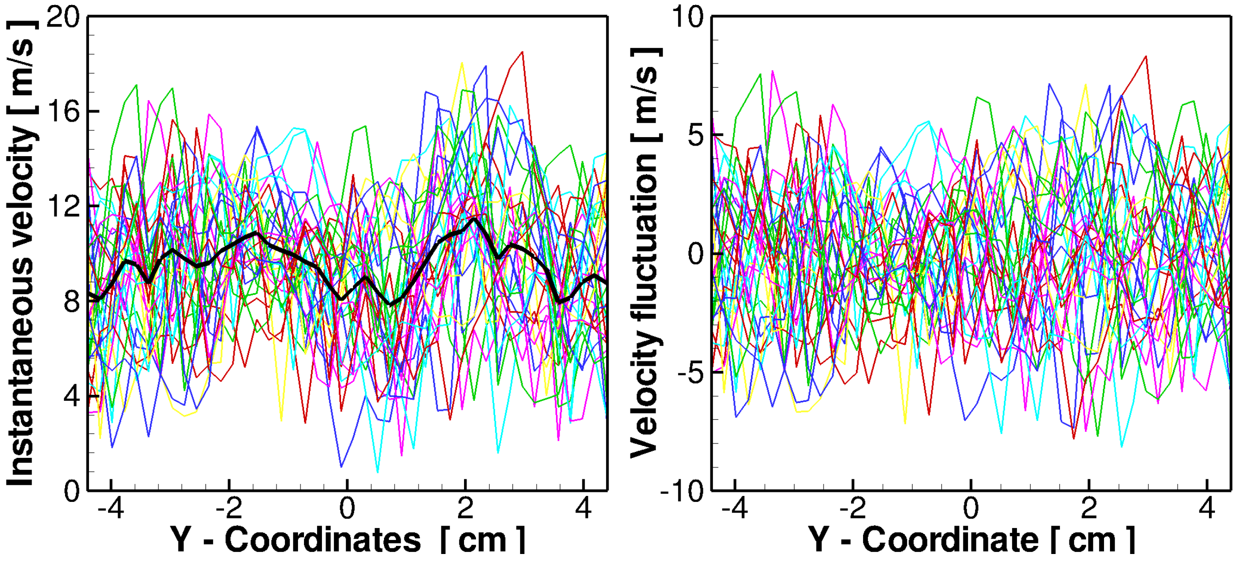

(a) **(b)**

Figure 9.12: Karlsruhe engine: Plotted profile for 35 cycles at Y-plnae at $Z = -2.0cm$ CA = 240^o ATDC (a) instantaneous velocity profile and (b) fluctuating velocity

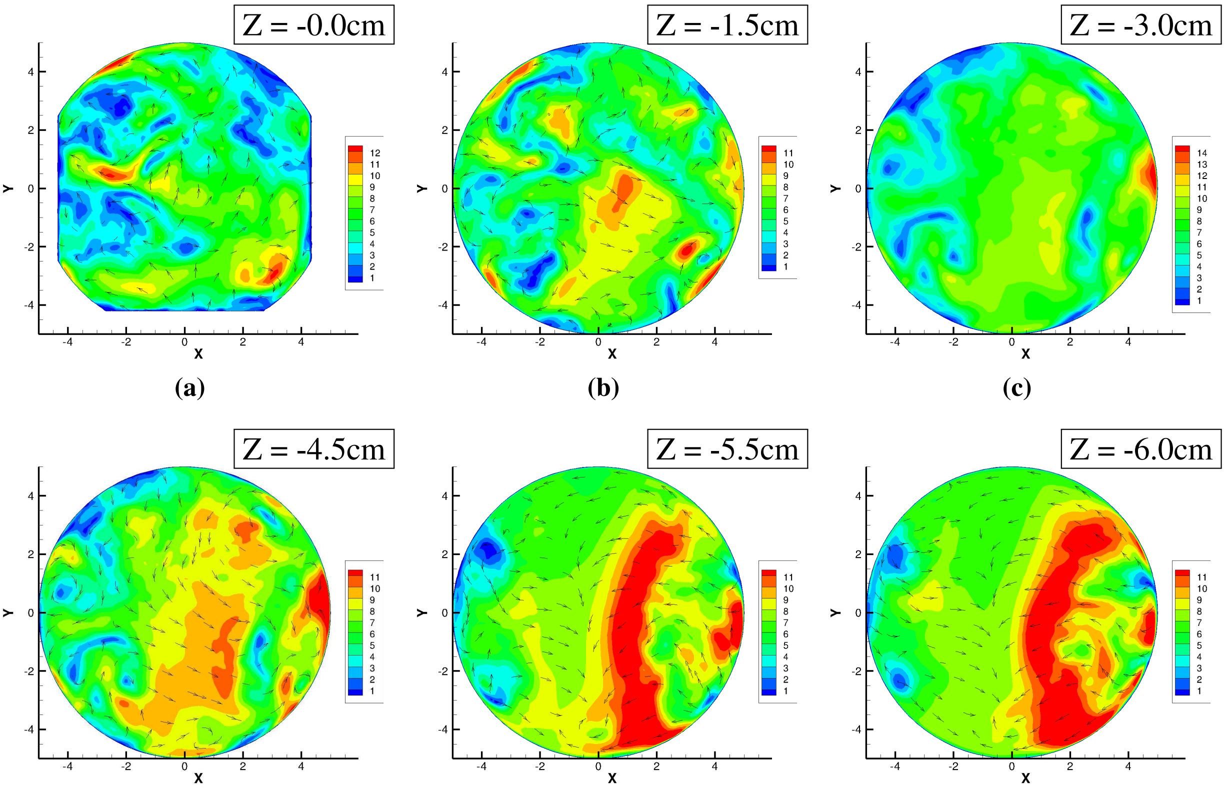

(a) **(b)** **(c)** **(d)** **(e)** **(f)**

Figure 9.13: Karlsruhe engine: Mean velocity profiles on xy-$plane$ at selected z positions during intake stroke, CA = 240^o

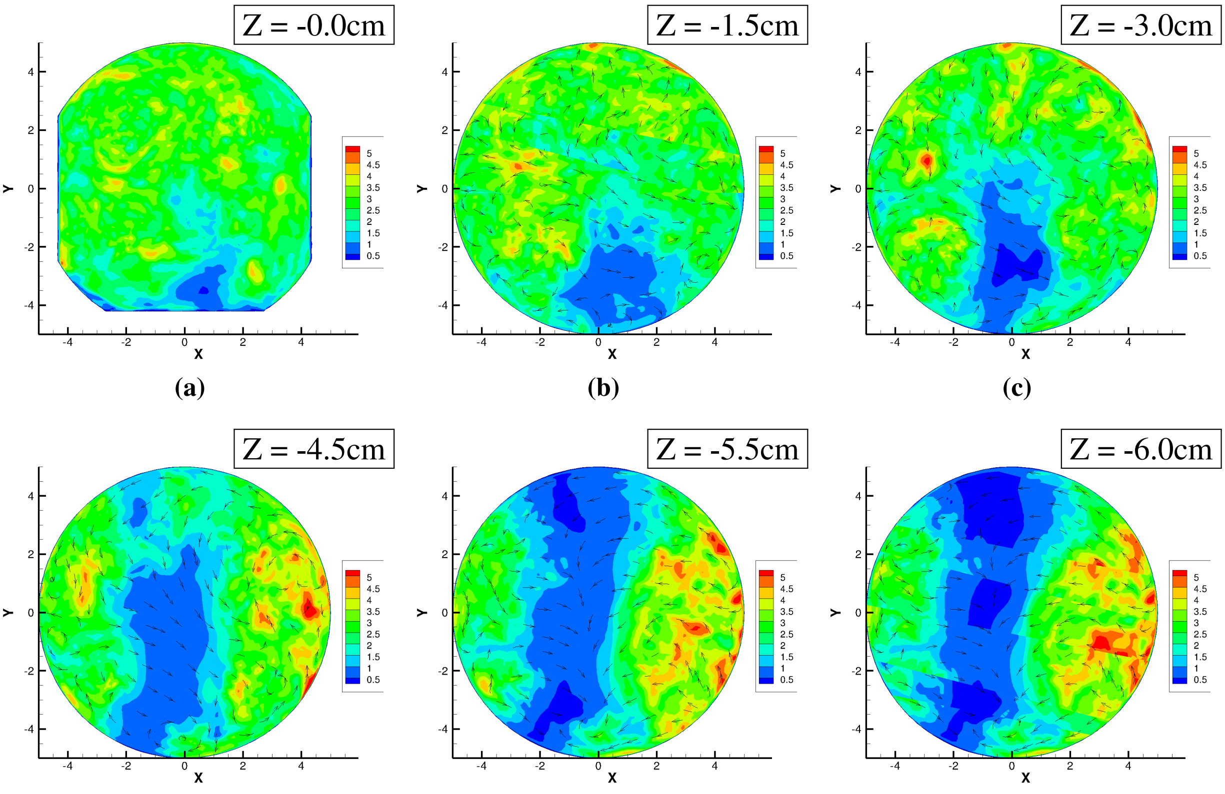

(a) **(b)** **(c)** **(d)** **(e)** **(f)**

Figure 9.14: Karlsruhe engine: RMS velocity profiles on xy-$plane$ at selected z positions during intake stroke, CA = 240^o

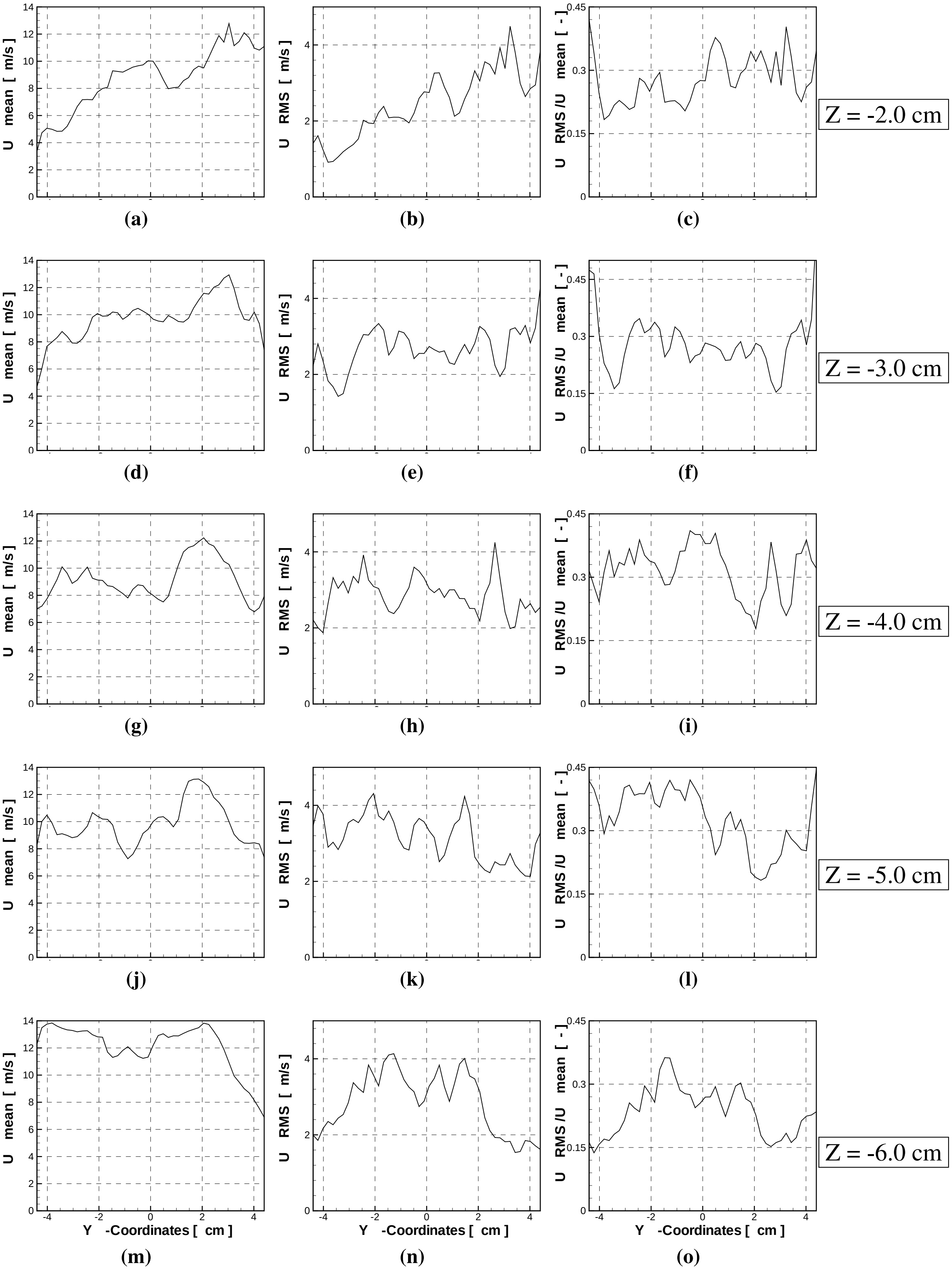

(a) **(b)** **(c)**

(d) **(e)** **(f)**

(g) **(h)** **(i)**

(j) **(k)** **(l)**

(m) **(n)** **(o)**

Figure 9.15: Karlsruhe engine: Mean velocity profiles (left column), standard velocity deviation (middle column) and rms of velocity normalized with local mean velocity (right column) at selected z positions during intake stroke, CA = 240^o

9.2.3 Expansion stroke

In general, the expansion stroke is characterized by the ignition and subsequent expansion of fuel-air mixture as a burnt gas by rising temperature due to heat evolution of combustion. The increased cylinder pressure exerts push on the piston surface providing power to crank shaft and whole engine assembly. In the motored case (no combustion), sharp rise in pressure due to ignition is not expected, instead pressure follows path similar to compression stroke as shown in Figure 9.5. In the expansion stroke, compressed charge relieved due to downwards movement of piston and cylinder pressure gradually decreases. Since most of the flow turbulence gets dissipated and damped down during the compression stroke, turbulence intensity is relatively low before the start of the expansion stroke. Therefore, velocity will be in the order of piston speed and velocity fluctuation will be comparatively lower than that of during the compression stroke as shown in Figure 9.16b for crank angle of 480^o. The quantitative comparison of instantaneous velocity for many cycles are depicted in Figure 9.17a showing homogeneous distribution of mean velocity, and corresponding velocity fluctuation around $\pm 1.5\ m/s$.

The in-cylinder mean velocity is plotted at various z locations in the xy-$plane$ in Figure 9.18. In case of expansion stroke, velocity profile does not represent any preferred flow (such as swirl and tumble motion) instead profile have localized structures. The overall velocity magnitude shows decreasing trends towards the piston surface. The gas close to the piston surface tries to readjust themselves with new piston position and achieve velocity in the range of the piston speed. The RMS velocity depicted in Figure 9.19 shows very slight variations with low and homogeneous turbulence intensity.

To carry out the statistical analysis, mean and velocity variance are plotted along the y-$axis$ for various z locations in Figure 9.20. The gradual increment of overall velocity magnitude is clearly visible as pointed out in the previous paragraph with very little fluctuations as the velocity variance is relatively small value around *0.5-1.0 m/s*. The normalized value of RMS shows the variation in the range of 0.15 to the mean value.

9.2.4 Exhaust stroke

In the exhaust stroke the "burnt" gas are pushed out from the engine cylinder. In some cases the exhaust gas is recirculated back to the engine cylinder to reduce maximum temperature inside the cylinder and subsequently NO_x formation, this process is termed as exhaust gas recirculation (EGR). However in the present motored case, the expanded air is purged out from the engine cylinder. For this engine configuration, the exhaust valve opens at engine crank angle of 523^o slightly before the end of expansion stroke and closes at CA 631^o well before the end of exhaust stroke. Therefore, it retains much of the exhaust gas for next cycle and may not be necessity of EGR. Due to early closure of exhaust valve, the retained gas again get compressed till the piston reaches to top dead centre (TDC) increasing the cylinder pressure up to $22.5\ bar$ as shown in Figure 9.5.

The results for the mean and velocity variance are plotted in Figure 9.21 for engine crank angle of 570^o ATDC. The sectional view is taken along the xz-$plane$ to shows one intake and one exhaust valve. The velocity profile clearly shows the region of high velocity in the exhaust port and valve passage. The velocity variance shows increased value near the exhaust port only (see Figure 9.21b). In the rest of the region turbulence seems rather homogeneous. The instantaneous velocity profile for multiple cycles are plotted in Figure 9.22a taken at z location of *2 cm*. The profile shows gradual increment of velocity towards left hand side representing the exhaust gas flow through the ports. The velocity variance seem to be uniform over the length with value $\pm$*2 m/s* (see Figure 9.22b).

The mean velocity contour at different z locations on the xy-$lane$ is shown in Figure 9.23. The velocity profile close to cylinder head *(z = 0.0 cm)* shows increased velocity near the exhaust valve representing the exhaust gas flow. The flow profile for the rest of the sections look similar in trend with comparatively higher velocity towards the exhaust port side. However, the velocity profile close to the piston surface is slightly higher and more uniform than that of middle section. The higher velocity can be attributed to the upward piston movement and the magnitude is in the range of the piston speed. The velocity variance is plotted in Figure 9.24 for the respective sections. The results for section *(z = 0.0cm)* shows decreased velocity variance near the exhaust valve region representing more directional and well organized flow near the exhaust port. The overall turbulence intensity seems to be uniform over all the sections with small patches of higher variance due to localized flow structured shown in the mean velocity profile.

The plot of mean velocity profile and respective velocity variance is illustrated in Figure 9.25 along the y-$axis$ at various z location on the yz-$plane$. The section is created on yz-$plane$ with *x = -2.19 cm* covering both opened exhaust valves. Although the exhaust valve is opened, the higher mean velocity can be observed in the sections towards the piston surface. This can be attributed to the less pressure gradient across the exhaust valve and therefore the exhaust valve opening has not yet influenced the flow field in downward regions. This way the mean flow profile increases towards the piston surface with maximum velocity in the range of piston speed. The velocity profile is also slightly higher towards the right hand side and are more homogeneous in downwards direction due to uneven shape of the cylinder bowl with left hand side having extra section restricting the flow profile. The velocity variance and normalized variance are higher near the cylinder head and gradually damped down towards the piston surface, however the normalized variance shows slightly rapid declination.

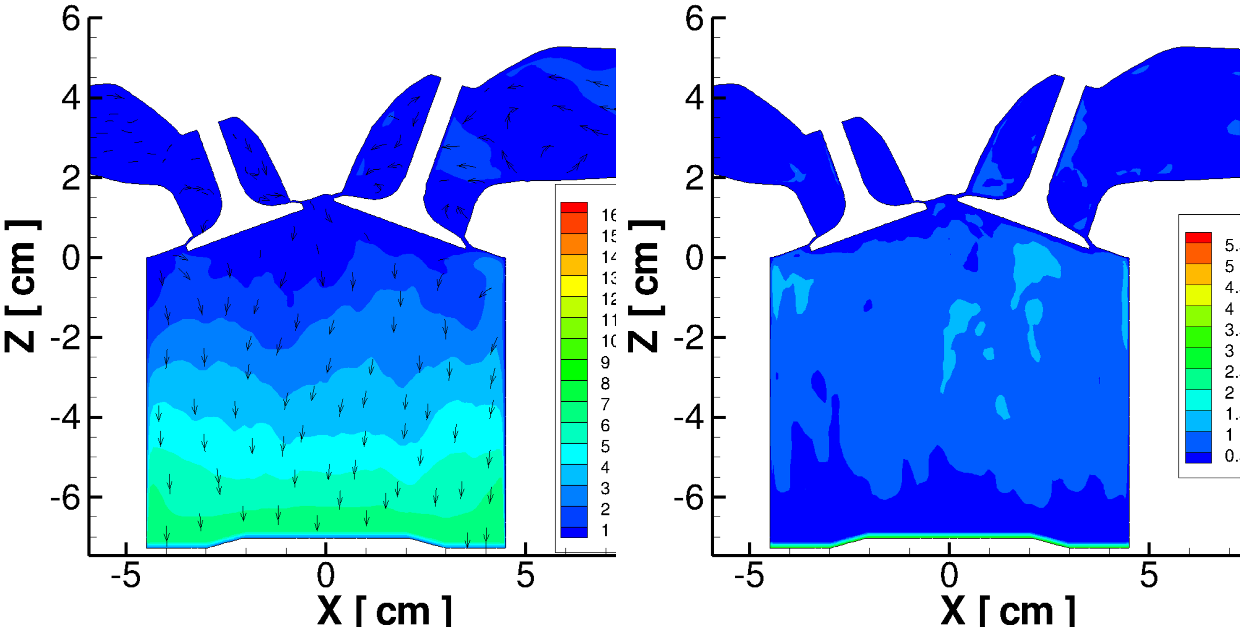

(a)

(b)

Figure 9.16: Karlsruhe engine: Plotted averaged profile for 35 cycles CA = 480^o ATDC (a) averaged velocity profile and (b) velocity variance

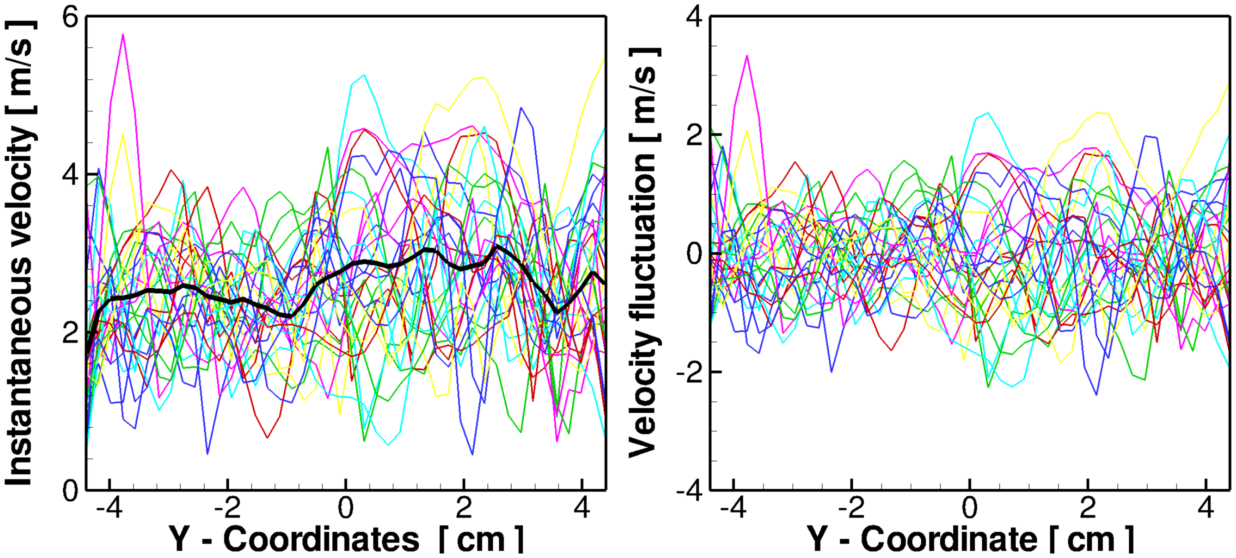

(a)

(b)

Figure 9.17: Karlsruhe engine: Plotted profile for 35 cycles CA = 480^o ATDC (a) instantaneous velocity profile and (b) fluctuating velocity

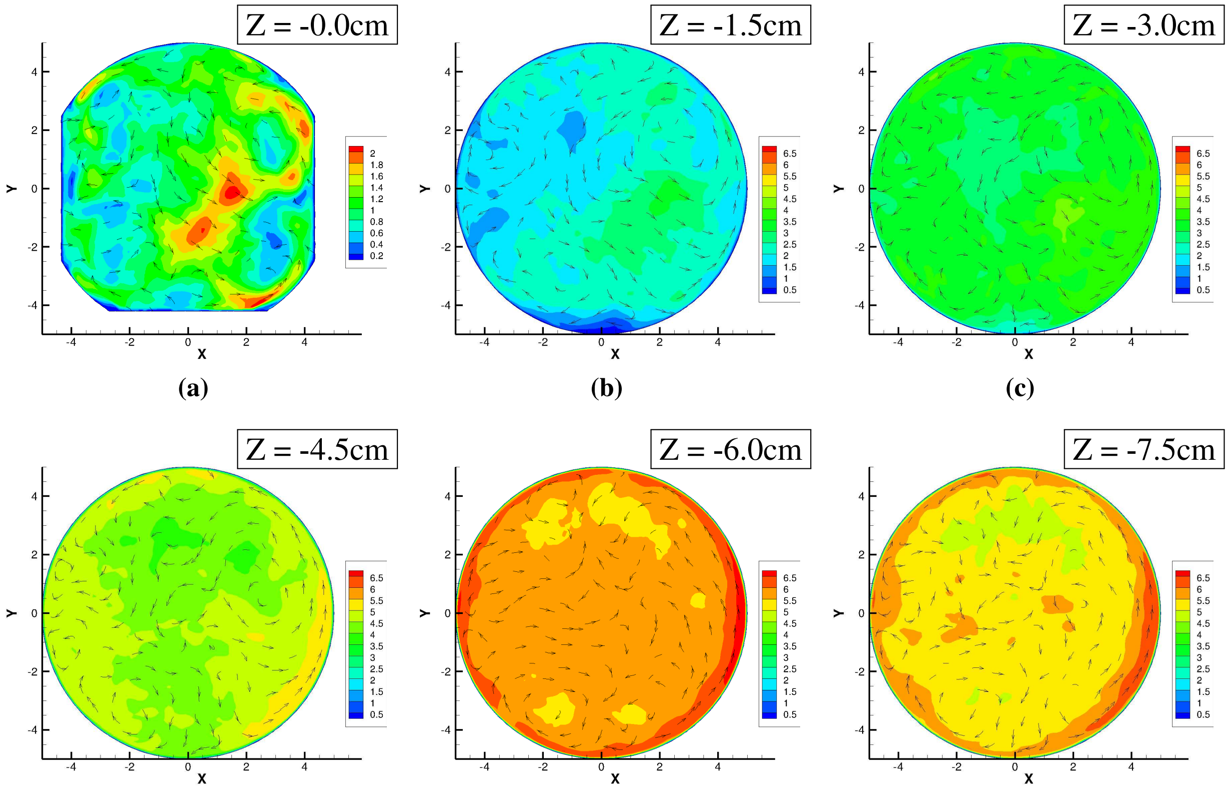

(a) (b) (c)

(d) (e) (f)

Figure 9.18: Karlsruhe engine: Mean velocity profiles on xy-$plane$ at selected z positions during intake stroke, CA = 480^o

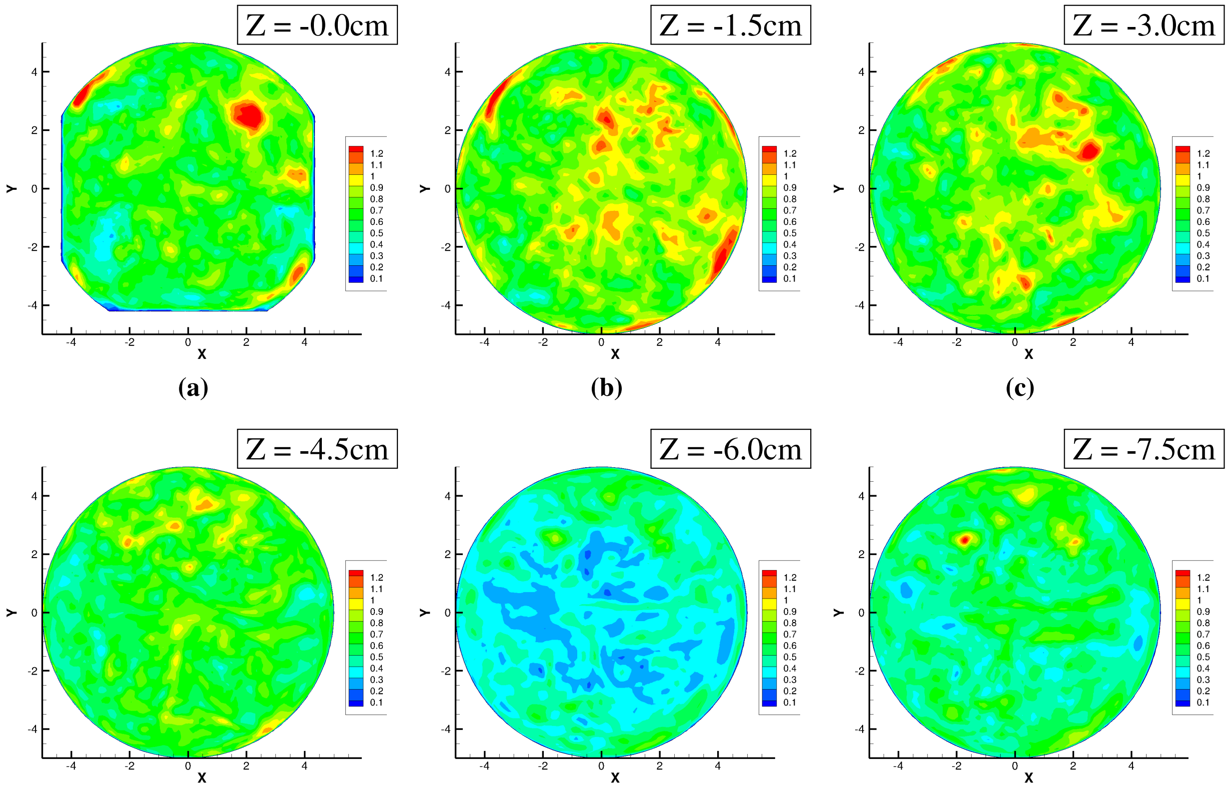

(a) (b) (c)

(d) (e) (f)

Figure 9.19: Karlsruhe engine: RMS velocity profiles on xy-$plane$ at selected z positions during intake stroke, CA = 480^o

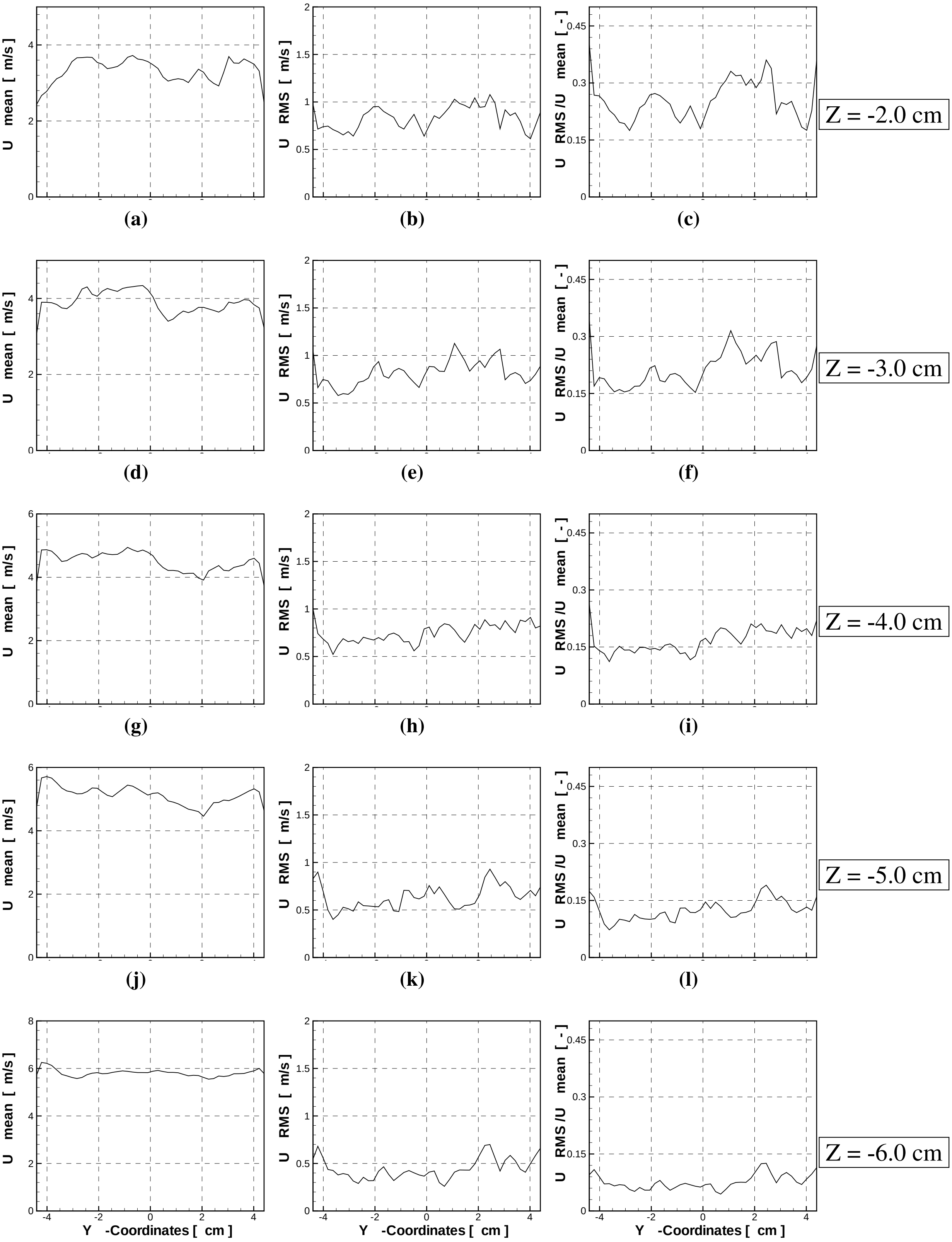

(a) **(b)** **(c)**

(d) **(e)** **(f)**

(g) **(h)** **(i)**

(j) **(k)** **(l)**

(m) **(n)** **(o)**

Figure 9.20: Karlsruhe engine: Mean velocity profiles (left column), standard velocity deviation (middle column) and rms of velocity normalized with local mean velocity (right column) at selected z positions during intake stroke, CA = 480^o

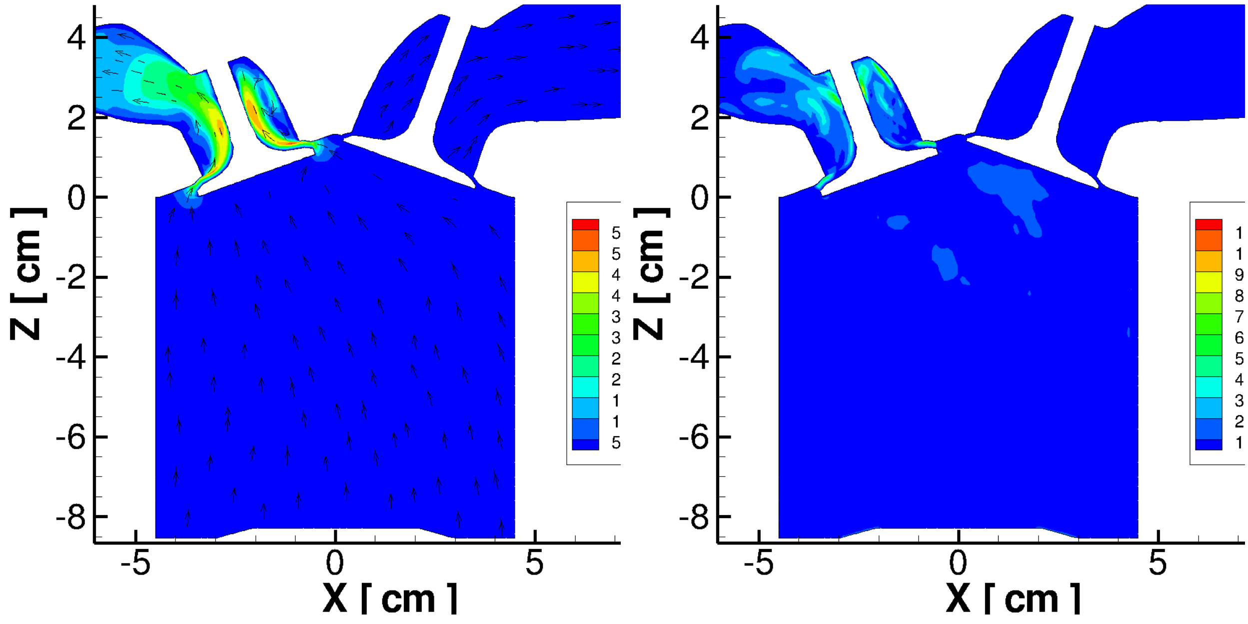

(a) (b)

Figure 9.21: Karlsruhe engine: Plotted averaged profile for 35 cycles CA = 570^o ATDC (a) averaged velocity profile and (b) velocity variance

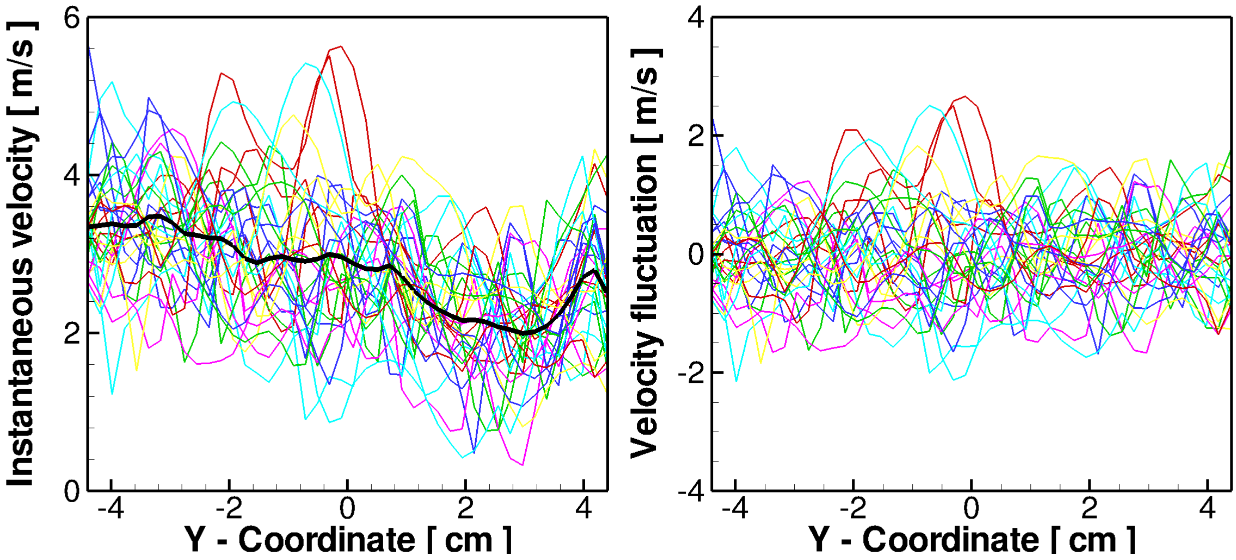

(a) (b)

Figure 9.22: Karlsruhe engine: Plotted profile for 35 cycles CA = 570^o ATDC (a) instantaneous velocity profile and (b) fluctuating velocity

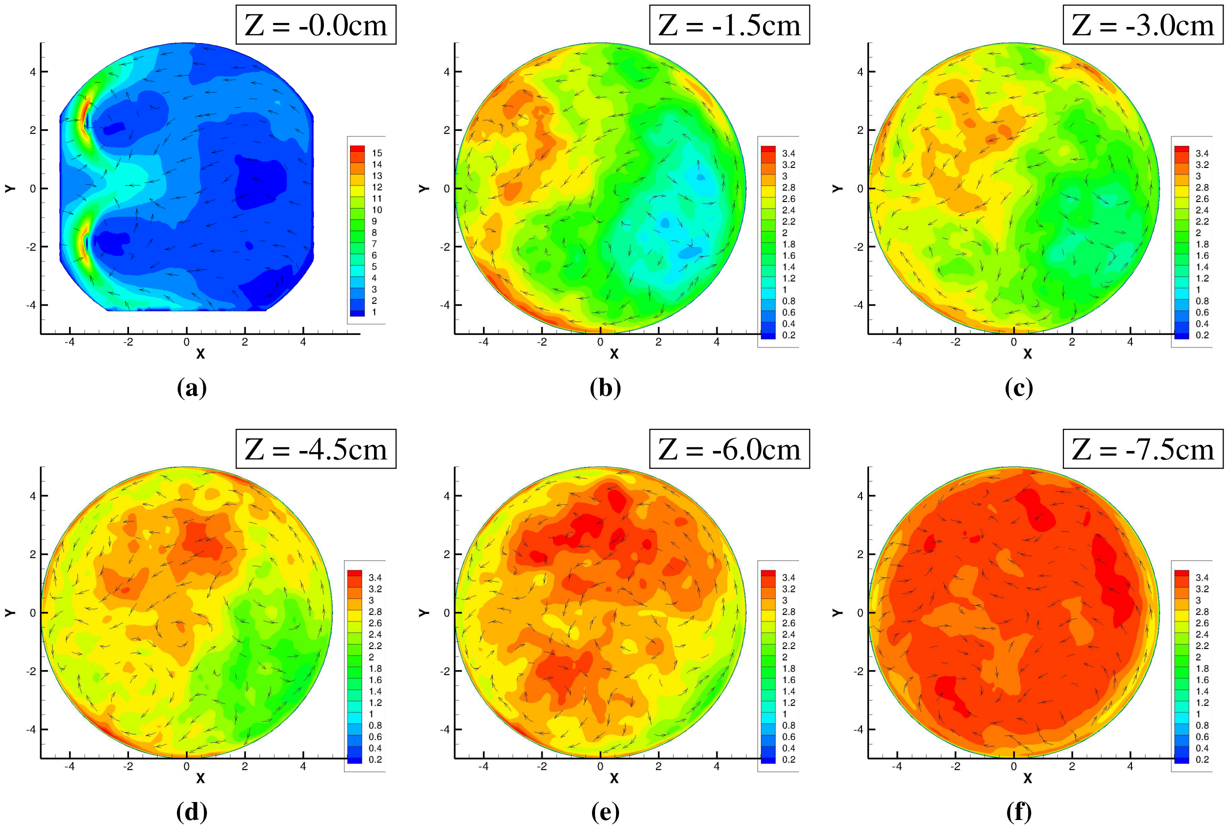

(a) **(b)** **(c)**

(d) **(e)** **(f)**

Figure 9.23: Karlsruhe engine: Mean velocity profiles on $xy\text{-}plane$ at selected z positions during intake stroke, CA = 570^o

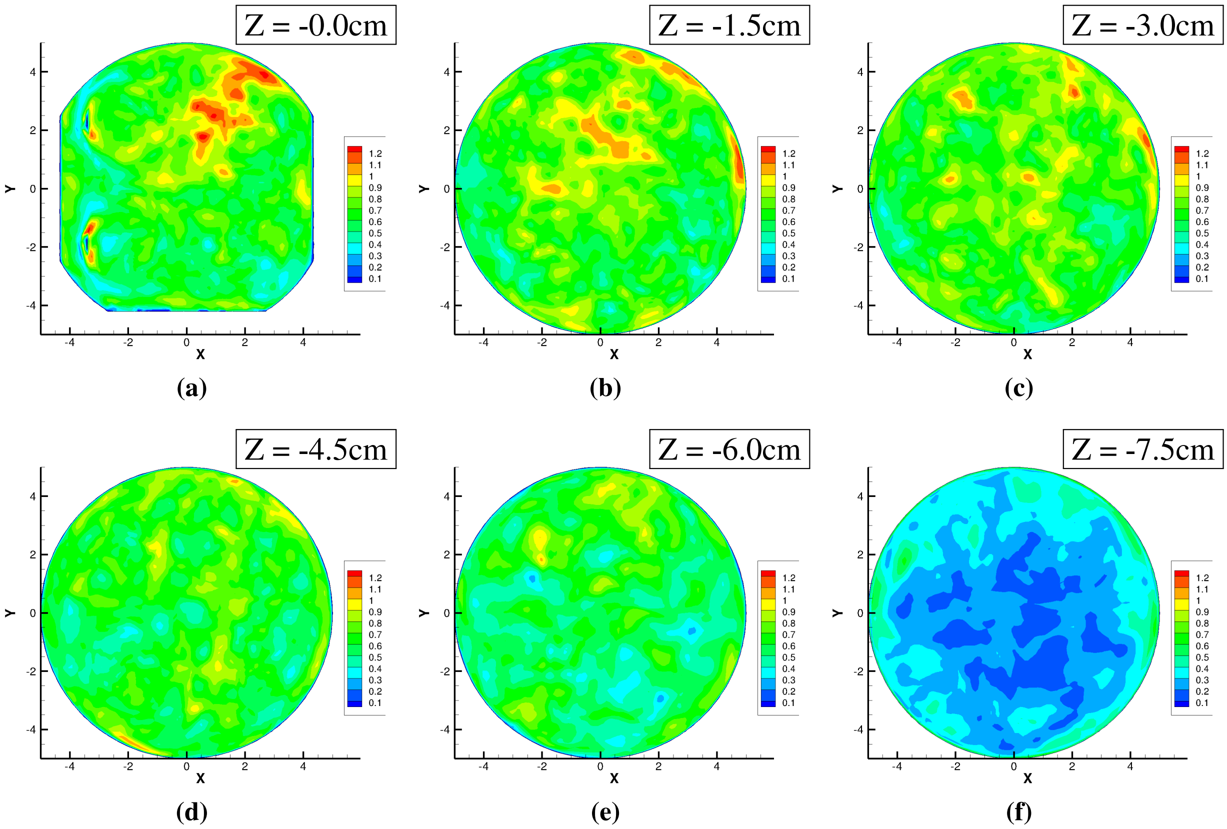

(a) **(b)** **(c)**

(d) **(e)** **(f)**

Figure 9.24: Karlsruhe engine: RMS velocity profiles on $xy\text{-}plane$ at selected z positions during intake stroke, CA = 570^o

9.3 Summary and conclusions

A numerical analysis was carried out for a more complex engine configuration with 4-canted valves and complex intake and exhaust port using large eddy simulation (LES). The mesh generation was performed with ICEM-CFD using hexahedral grids by adopting the new mesh technique introduced in the present work. The relatively fine grid was used to perform the engine simulation with approximately *1.4 millions* control volumes and around *0.9 million* control volumes for the engine combustion chamber.

The present simulation demonstrates the applicability of the new meshing technique for the KIVA4-mpi code to carry out numerical analysis in real complex engine configurations. This particular engine has peculiar intake/exhaust valve profiles for opening and closing. In contrary to traditional engines, the intake valve opens at engine crank angle of 89^o and closes at CA 207^o with maximum lift of approx. of $2.0\ mm$. The exhaust valves opens at 527^o angle and closes at CA 631^o well before the end of exhaust stroke. Therefore, the unique profile for in-cylinder pressure curve is observed with two peak pressures, one during the end of compression stroke and second during the end of exhaust stroke. The computed pressure curve also shows similar trend in in-cylinder pressure curve, and comparable to the experimental findings. However, due to lack of measurement data, the flow fields computed using LES method could not be validated. The author relies on the prediction capability of KIVA4-mpi demonstrated through the validation in previous chapters. The in-cylinder flow does not represent any kind of global flow structures such swirl and tumble motion as observed in typical engine configuration. However, it shows the evidence of scattered and localized structures throughout the engine geometry. That could be of interest for the fuel-air mixture preparation. The numerical simulation also provides information about the back flow during the initial stage of intake opening.

The simulation was performed for multiple cycles. The turbulence intensity was evaluated and analyzed for different engine processes. The numerical analysis shows the cyclic variations at different engine crank angles. The turbulence intensity is maximum during the intake stroke, that helps to maintain sufficient homogeneous turbulence level in the compression stroke. Considering the motored case in expansion stroke, the mean flow pattern is largely influenced by the piston speed and turbulence level is relatively homogeneous but low as compared to compression stroke due to the dissipation of kinetic energy during compression stroke. In the exhaust stoke, the velocity field is guided first by the upward piston motion and then by the fully opened exhaust valve.

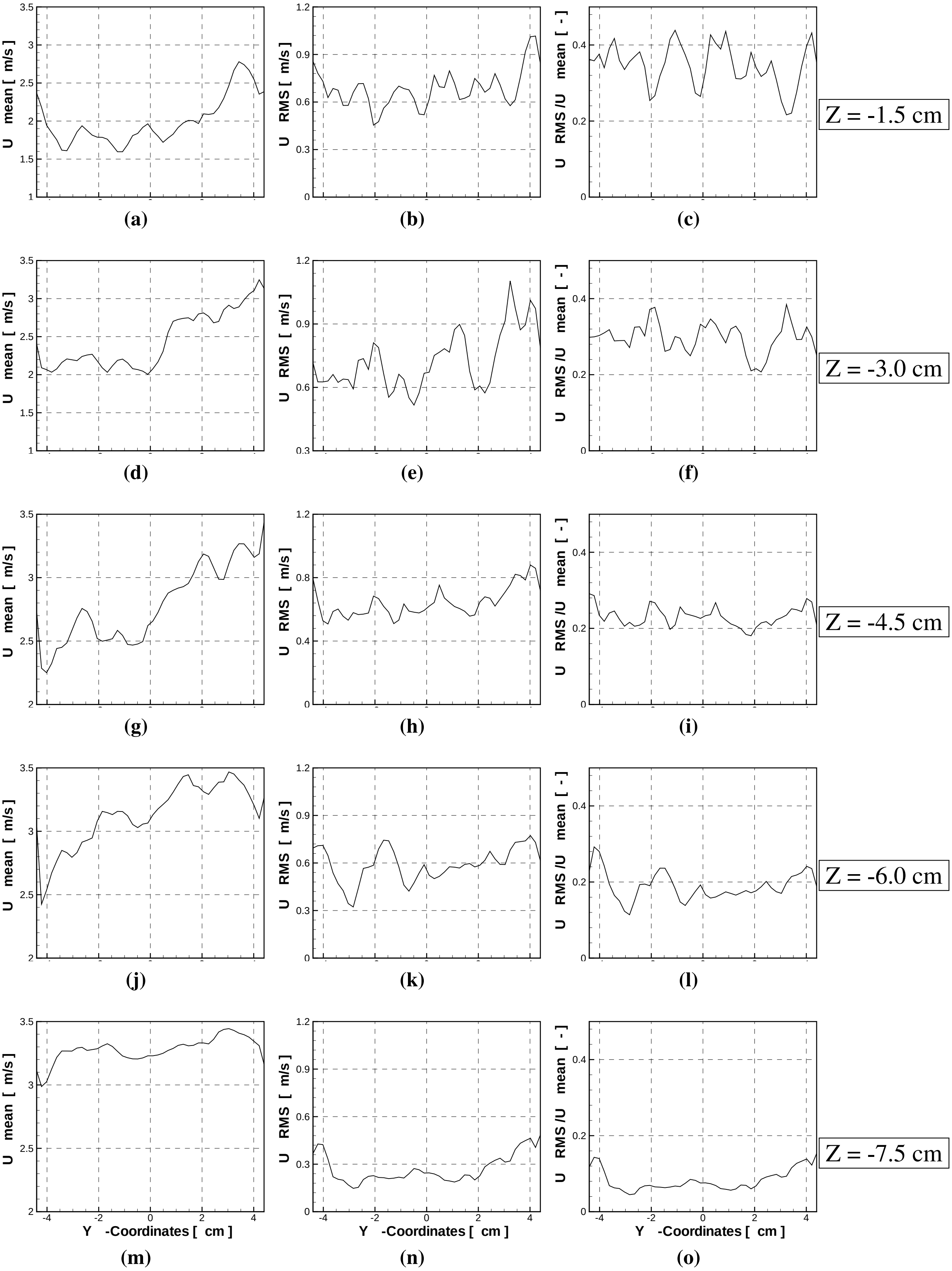

Figure 9.25: Karlsruhe engine: Mean velocity profiles (left column), standard velocity deviation (middle column) and rms of velocity normalized with local mean velocity (right column) at selected z positions during intake stroke, CA = 570^o

10 Summary and outlook

The presented work was dedicated towards the development of a comprehensive IC-engine simulation tool that is intended to resolve mathematically all the important physical phenomena relevant to IC-engine applications. These are mainly the intake charge motion, fuel injection, spray dynamics (collision , coalescence, drag, evaporation, wall impingement), fuel-air mixture formation. Combustion processes were not included in the present study. This model development was based on large eddy simulations (LES) to enable investigations of highly unsteady cycle-to-cycle variations in IC-engine configurations.

Following results could be achieved:

- A complete fuel injection module was devised based on a Lagrange particle tracking framework that includes following sub-models:
  - Since, it is difficult to adopt universal atomization model for all kind of nozzle configurations, a separate model for primary atomization is required for specific nozzle. In the present study, the LISA model is integrated to represent the primary atomization for outward hollow cone GDI, while the KH-model is used for multi-hole cylindrical orifice nozzle. The secondary atomization in all nozzle configurations is described using TAB-model already available in KIVA4-mpi.
  - Since the injection process involves a dense flow of large number of fuel droplets, resulting high probability of droplet-droplet interactions influences considerably the spray evolution. An advanced droplet-droplet interaction model was integrated. This includes rebound, coalescence, reflexive separation, stretching separation. Based on binary interactions, it is especially modified to be independent of mesh size and mesh type. The new updated collision scheme showed improvement in rectifying the collision artifacts.
  - As the wall impingement is one of the important and very common physical phenomena encountered in the IC-engine applications, the formation of the wall film inside the engine cylinder is highly undesirable as it leads to uneven engine performance, HC emission and soot formations. A modified wall-impingement model was incorporated and successfully tested. It includes the effect of wall temperature on the impingement outcomes.

  The developed fuel injection module was validated comprehensively under various conditions.

- Comparative studies were then performed using different turbulence models (k-ϵ, RNG k-ϵ, LES). The LES model demonstrated good performance in predicting various spray dynamics, also including evaporating spray by using single component evaporation model. The results showed good agreement in terms of droplet distribution, spray profile and penetration depth for various combinations of cylinder pressure and temperatures.

- The mesh generation to carry out simulation using KIVA code for real and complex IC-engine configuration is a challenging task. It is virtually impossible to generate mesh for the real engine with requisite refined mesh. Therefore, in the present study a new meshing technique was devised using ICEM-CFD for real engine geometry. With the present approach, a good quality mesh could be achieved with desired mesh refinements. The meshing technique was tested for two engine configurations. The first geometry has two parallel valves with simple cylinder head and port shape. The second features 4-canted valves with complex shape of the cylinder head, intake and exhaust ports.

- Multi-cycle LES investigations were then carried out in these two engine configurations.
  (a) For the engine TCC-ECN configuration, the simulation results showed good agreement with the reported experimental data. Comparative studies were performed: (1) to assess the simulation capability of RANS and LES turbulence models in terms of resolving the flow structures. LES could resolve nicely the flow structures and showed evidence of flow cyclic variability. RANS could only provide mean flow information while being unable to predict the cycle-to-cycle variations, (2) to evaluate the mesh sensitivity using coarse and fine mesh, the results clearly showed the viability of mesh refinement necessary to resolve the flow structure with LES. (3) to capture the impact of fuel injection including the wall film formation. The results for hollow-cone GDI showed the influence of in-cylinder flow on spray dynamics and vice versa. The liquid film formation on the piston surface was also observed. Its effect was pointed out justifying the importance of the improved wall film model.

  (b) For the complex engine configuration, that has unconventional valve displacement profile and influences in-cylinder pressure curve for an engine cycle, the simulated results compared well with available experimental data. The two pressure peaks were observed in both experiment and simulation. The build up pressure at the start of intake stroke signifies the residual burnt gas similar to exhaust gas recirculation. The in-cylinder flow analysis was also performed for various stages of engine operation. This did not show any evidence of global flow structures (swirl and tumble motion), in contrary small localized structures could be seen at various section.

To fully complete this work, some remaining tasks that could not be achieved, have to be performed in the future. The issues that should be addressed must include:

1. A detailed validation of the injection module under various operating conditions of real engine configuration.
2. A comprehensive validation of LES including the injection module for in-cylinder flow dynamics for both the engines mentioned in this study.
3. Incorporation of ignition and combustion models to be able to simulate and assess the combustion and emission behavior of the adopted IC-engine configurations including fuel injection.

Bibliography

[1] 2012 The Outlook for Energy: A View to 2040, exxonmobil.com/energyoutlook, 2012. xi, 5

[2] BP Energy Outlook 2030, London, January 2012. xi, 5

[3] Merker, G.M., Schwarz, C., Stiesch, G., and Otto, F., (2005): *Simulating Combustion : Simulation of combustion and pollutant formation for engine-development*, Springer-Verlag Berlin Heidelberg, 2005. xi, 1, 2, 8, 24

[4] Martin D., Pischke P., Kneer R., (2010): *Investigation of the influence of multiple gasoline direct injections on macroscopic spray quantities at different boundary conditions by means of visualization techniques*, International Journal of Engine Research, 2010, Vol. 11(6), pp. 439-454. 3, 65, 66, 67, 100

[5] Goryntsev, D., (2007):*Large Eddy Simulation of the Flow and Mixing Field in an Internal Combustion Engine*, PhD. Thesis, Technical University Darmstadt, Germany, 2007. 3

[6] Goryntsev, D., Sadiki, A., Klein, M., and Janicka, J., (2009) *Large eddy simulation based analysis of the effects of cycle-to-cycle variations on air-fuel mixing in realistic DISI IC-engines*, Proceedings of Combustion Institute, 32, 2009. 25

[7] Goryntsev, D., Sadiki, A., and Janicka, J., (2012): *Cycle-to-Cycle Variations Based Unsteady Effects on Spray Combustion in Internal Combustion Engines by Using LES*, SAE Technical Paper 2012-01-0399, 2012.

[8] Goryntsev, D., Sadiki, A., and Janicka, J., (2011): *Towards large eddy simulation of spray combustion in direct injection spark ignition engine*, SAE Technical Paper 2011-01-1884, 2011.

[9] Goryntsev, D., Sadiki, A., and Janicka, J., (2011): *Investigation of Fuel-Air Mixing in DISI Engine using LES*, SAE Technical Paper 2011-01-1886, 2011. 3, 25

[10] Schmidt, D., (1997): *Cavitation in Diesel Fuel Injector Nozzles*, PhD. Thesis, Mechanical Engineering, University of Wisconsin-Madison, 1997. xi, 9

[11] Gavaises, M., Andriotis, A., Papoulias, D., Mitroglou, N., and Theodorakakos, A., (2009): *Characterization of string cavitation in large-scale Diesel nozzles with tapered holes*, Physics of Fluids 21, pp. 052107(1-9), 2009. xi, 9

[12] Gavaises, M., Papoulias, D., Andriotis, A., Giannadakis, E., and Theodorakakos, A., (2007): *Link between cavitation development and erosion damage of diesel fuel injector nozzles*, SAE Technical Paper No. 2007-01-0246, 2007. xi, 10

[13] Herrmann, M., (2010): *Detailed numerical simulations of the primary atomization of a turbulent liquid jet in cross-flow*, Journal of Engineering for Gas Turbine and Power, 2010, 132(6), pp. 061506- 061515. xi, 11, 12, 20

[14] Reitz, R.D., and Bracco, F.V., (1986): *Mechanisms of breakup of round liquid jets*, Book Chapter - The Encyclopedia of Fluid Mechanics, N. Cheremisnoff, Ed., Gulf Publishing, Houston, Texas, Vol. 3, Chapter 10, 233-249, 1986. xi, 11, 13, 21

[15] Balewski, B. S., (2009): *Experimental investigation of the influence of nozzle-flow properties on the primary spray breakup*, PhD Dissertation, Technical University Darmstadt, Germany, (2009). xi, 13

[16] Reitz., R., (1978): *Atomization and other breakup regimes of a liquid jet*. Ph.d. thesis, Princeton University, 1978. xi, 13, 14, 15

[17] Giannadakis, E., (2005): *Modeling of cavitation in automotive fuel injector nozzles*, Ph.D. thesis, 2005, Imperial College, London, UK. 19

[18] Soteriou, C., Andrews R.J., and Smith M., (1995): *Direct injection diesel sprays and the effect of cavitation and hydraulic flip on atomization*, SAE Paper 950080, 1995. 19

[19] Giannadakis, E., Papoulias, D., Gavaises, M., and Arcoumanis, C., (2007): *Evaluation of the predictive capability of diesel nozzle cavitation models* SAE Papers, 2007-01-0245. 19, 20

[20] Payri, F., Benajes, J., Pastor, J. V., and Molina, S., (2002): *Influence of the post-injection pattern on performance, soot and NOx emissions in a HD diesel engine*, SAE paper 2002-01-0502. 19

[21] Tamaki, N., Shimizu, M., Nishida, K., and Hiroyasu, H., (1998): *Effects of cavitation and internal flow on atomization of a liquid jet*, Atomization Sprays, vol 8(2), pp. 179-197, 1998. 19

[22] Andriotis, A., Gavaises, M., and Arcoumanis, C., (2008): *Vortex flow and cavitation on diesel injector nozzles*, Journal of Fluid Mechanics, vol 610, pp. 195-215, 2008. 20

[23] Mitroglou, N., Gavaises, M., Nouri, J.M., and Arcoumanis, C., (2011): *Cavitation inside enlarged and real-size fully transient injector nozzle and its effect on near nozzle spray formation*, DIPSI Workshop 2011 on Droplet Impact Phenomena & Spray Investigation, May 27th, 2011, Bergamo, Italy 20

[24] Som, S., Aggarwal, S.K., EI-Hannouny E.M., and Longman, D.E., (2010): *Investigation of Nozzle Flow and Cavitation Characteristics in a Diesel Injector*, Journal of Engineering for Gas Turbines and Power, Vol 132(4), pp. 042802-042813, 2010. 20

[25] Klein, M., Sadiki, A., and Janicka, J., (2003):*A digital filter based generation of inflow data for spatially developing direct numerical or large eddy simulations*, Journal of Computational Physics, Vol 186(2), pp. 652-665, 2003. 20, 33

[26] Sander, W., and Weigand, B., (2008): *Direct numerical simulation and analysis of instability enhancing parameters in liquid sheets at moderate Reynolds numbers* , Physics of Fluids vol. 20, pp. 053301-053318, 2008. 20

[27] Kim D, Desjardins O, Herrmann M, and Moin P., (2007): *The primary breakup of a round liquid jet by a coaxial flow of gas*, Proceedings of Annual Conference on Institute of Liquid Atomization and Spray System, 20th, ILASS Toronto. 20

[28] Klein M. (2005): *Direct numerical simulation of a spatially developing water sheet at moderate Reynolds number*, International Journal of Heat Transfer and Fluid Flow 26, pp. 722-731, 2005. 20, 33

[29] Zeng, P., Binninger, B., Peters, N., Herrmann, M., (2010): *Direct Numerical Simulation of Spray Primary Breakup with Phase Transition*; Spray 2010. 20

[30] Herrmann M., and Gorokhovski M., (2008): *Modeling primary atomization*, Annual Review of Fluid Mechanics. 2008, 40(1), pp. 343-366, 2008. 20

[31] Spyrou, N., Choi D., Sadiki, A., and Janicka J., (2010): *Large eddy simulation of the breakup of kerosene jet in cross-flow*, Proceedings of International Conference of Multiphase Flow, 2010, Tampa, FL, May 30 -June 4, 2010. 20

[32] Befrui, B., Corbinelli, G., Robart, D., and Reckers, W. (2008): *LES Simulation of the Internal Flow and Near-Field Spray Structure of an Outward-Opening GDI Injector and Comparison with Imaging Data*, SAE paper, 2008-01-0137. 20

[33] Reitz, R.D.; Diwakar, R., (1987): *Structure of high-pressure fuel sprays*, SAE Papers 870598-1987. 20, 21

[34] Dorfner, V., Domnick, J., Durst, F., and Koehler, N., (1995): *Viscosity and surface tension effects in pressure swirl atomization*, Atomization and Sprays, vol. 5, pp. 261-285, 1995. 21

[35] Han, Z., Parrish, S.C, Farell, P.V., and Reitz, R.D., (1997): *Modeling atomization processes of pressure-swirl hollow-cone fuel sprays*, Atomization and Sprays, vol. 7, pp. 663-684, 1997. 21

[50] Schmidt, D.P., Nouar, I., Senecal, P.K., Rutland, C.J., Martin, J.K., and Reitz, R.D., (1999): *Pressure-swirl atomization in the near field*, SAE Technical Papers 1999-01-0496, 1999. 21, 22

[37] Patterson, M.A., and Reitz R.D., (1987): *Modeling the effects of fuel spray characteristics on diesel engine combustion and emission*, SAE Technical Paper, 980131, 1998. 21, 43

[38] O'Rourke, P.J. , Amsden A.A., (1987): *The TAB method for numerical calculation of spray droplet breakup*, SAE Technical Paper 87-2089, 1987. 21, 38, 39

[39] Taylor, G.I., (1963): *The Shape and Acceleration of a Drop in a High Speed Air Stream*, Technical report, In the Scientific Papers of Taylor, G. I., ed., Batchelor, G. K., 1963. 21

[40] Chigier, N., Reitz, R.D., (1997), *Liquid jet atomization and droplet breakup modeling of non-evaporating diesel fuel sprays.*, SAE Transactions. J. Engines 106, pp. 127-140, 1997. 21

[41] Park, S.W., and Lee, C.S., (2004): *Investigation of atomization and evaporation characteristics of high-pressure injection diesel spray using Kelvin-Helmholtz instability/droplet deformation and break-up competition model*, Proceedings of the Institution of Mechanical Engineers, Part D: Journal of Automobile Engineering 2004 vol. 218(7), pp. 767-777, 2004. 21

[42] Amsden, A.A., O'Rourke, P.J., and Butler, T.D., (1989): *KIVA-II A computer program for chemically reactive flows with sprays*, Los Alamos National Laboratory, LA-11560-MS. 21, 26, 31, 36, 37, 41

[43] O'Rourke, P.J., (1981): *Collective drop effects in vaporizing liquid sprays*, PhD. Thesis, Dept. Mech. Aerospace Engg., Princeton University, Princeton, NJ, 1981. xi, 22, 39, 40, 46

[44] Munnannur A., and Reitz R., (2007): *A new predictive model for the fragmenting and non-fragmenting binary droplet collisions*, International Journal of Multiphase Flow, vol. 33, pp. 873-896, 2007. xi, xii, 22, 23, 40, 46, 47, 48, 49

[45] Munnannur A., and Reitz R.D., (2007): *Droplet collision modeling in multi-dimensional spray computations*, International Multidimensional Engine Modeling, SAE Congress, April 15, 2007, Detroit, MI USA. 22, 47, 48

[46] Schmidt D.P., Rutland C.J., (2004):*Reducing grid dependency in droplet collision modeling*, Journal of Engineering for Gas Turbines and Power, vol. 126, pp. 227-233, 2004. 22, 40, 47, 48

[47] Hieber, S.E., (2001): *An investigation of the mesh dependence of the stochastic discrete droplet model applied to dense liquid sprays*, Master Thesis, Department of Mathematical Science, Michigan Technological University. 22

[48] Nordin, N., 2000: *Complex Chemistry Modeling of Diesel Spray Combustion*, Ph.D. Dissertation, Chalmers University of Technology, 2000. 22

[49] Aneja, R., Abraham, J., (1998): *How far does the liquid penetrate in a diesel engine: computed results vs. measurements* Combustion Science and Technology vol. 138, pp. 233-255, 1998. 22

[50] Schmidt, D.P., Rutland, C.J., 2000: *A new droplet collision algorithm*, Journal of Computational Physics vol. 164, pp. 62-80, 2000. 21, 22

[51] Hou S,and Schmidt, D. P., (2006):*Adaptive collision meshing and satellite droplet formation in spray simulations*, International Journal of Multiphase Flow, Vol. 32, pp. 935-956, 2006: 22

[52] Brazier-Smith, P., Jennings, S., and Latham, J., (1971): *The interaction of falling rain drops: coalescence*, Proceedings of Royal Society of London A326, pp. 393-408, 1971. 22

[53] Qian, J., and Law, C.K., (1997): *Regimes of coalescence and separation in droplet collision*, Journal of Fluid Mechanics, vol. 331, pp. 59-80, 1997. 22

[54] Ashgriz, N., and Poo, J.Y., (1990): *Coalescence and separation in binary collisions of liquid drops*, Journal of Fluid Mechanics, vol. 221, pp. 183-204, 1990. 22

[55] Pischke, P., Martin, D., and Kneer, R., (2010): *Combined spray model for gasoline direct injection hollow-cone sprays*, Atomization and Sprays, vol. 20(4), pp. 345-364, 2010. xi, xii, xiii, xvii, 22, 23, 40, 46, 47, 48, 65, 66, 68, 70, 72, 74, 100

[56] Bardon, M. F., Rao, V. K., and Gardiner, D. P., (1987):*Intake manifold fuel film transient dynamics*, SAE Paper, 870569, 1987. 23, 50

[57] Xiong T.Y., YUEN M.C., (1991): *Evaporation of a liquid droplet on hot plate*, International Journal of Heat and Mass Transfer, vol. 34(7), pp. 1881-1894, 1991. 23

[58] Habchi, C. (2011): *New correlations for Leidenfrost and Nukiyama temperatures with gas pressure application to liquid film boiling simulation*, ILASS-Europe, 2011, Brno, Czech Republic, Sept. -2010. 23

[59] Castanet, G., Lienart, T., and Lemoine, F., (2009): *Dynamics and temperature of droplets impacting onto a heated wall*, International Journal of Heat and Mass Transfer, vol. 52, pp. 640-679, 2009. 23

[60] Cossali, G. E., Marengo, M., and Santini, M., (2005): *Single-drop empirical models for spray impact on solid walls: a review*, Atomization and Sprays, vol. 15, pp. 699-736, 2005. xi, xii, 23, 24, 50

[61] Cossali, G. E., Marengo, M., and Santini, M., (2005): *Secondary atomization produced by single drop vertical impacts onto heated surfaces*, Experimental Thermal and Fluid Science, Vol. 29(8), pp. 937-946, 2005. xi, 23, 24

[62] Richter, B., Dullenkopf, K., and Bauer, H. J., (2005): *Investigation of secondary droplet characteristics produced by an isooctane drop chain impact onto a heated piston surface*, Experiments in Fluids, Vol. 39, 351-363, 2005. xii, 65, 70

[63] Amiel, C., (2002): *Application de techniques optiques á l'étude du comportement dynamique et thermique de gouttes en interaction avec une paroi chauffée*, Ph.D. Thesis, École Nationale Supérieure de l'Aéronautique et de l'Espace, Toulouse, 2002. 23

[64] Dewitte, J., Berthoumieu, P., and Lavergne, G., (2005): *An experimental study of droplet hot wall interactions and a Survey of the splashing regime*, 5^{th} International Symposium on Multiphase Flow, Heat Mass Transfer and Energy Conversion, ISMF 5, Xi'an, China, 3-6 July, 2005. xi, xii, 23, 24, 50

[65] Mülhbauer, M., (2010): *Modeling wall interactions of a high-pressure, hollow cone spray*, Ph.D. Thesis, Mechanical Engineering, Technical University Darmstadt 2010. 23

[66] Rosa, N.G., Villedieu, P., and Lavergne, G., (2006): *A statistical model for droplet-wall interaction*, 2^{nd} Colloque INCA, Oct. 23-24, 2008. xii, 23, 50

[67] O'Rourke, P.J., and Amsden, A.A., (1996): *A particle numerical model for wall film dynamics in port-injected engine*, SAE Paper, 961961, 1996. 23, 50

[68] O'Rourke, P.J., and Amsden, A.A., (2000): *A spray/wall interaction sub-model for the KIVA-3 wall film model*, SAE Paper, 2000-01-0271, 2000. 23

[69] Heywood, J.B., (1998): *Internal Combustion Engine fundamentals*, New York: McGraw-Hill. 24, 29

[70] Arcoumanis, C., and Kamimoto, T., (2009): *Flow and Combustion in Reciprocating Engines*, Springer-Verlag Berlin Heidelberg, 2009. 24

[71] Khalighi, B., (1991): *Study of the intake tumble motion by flow visualization and particle tracking velocimetry*, Experiments in Fluid, vol. 10, pp. 230-236, (1991). 24

[72] Gurupatham, A., and Teraji, A., (2011): *A Study of Rich Flame Propagation in Gasoline SI Engine Based on 3-D Numerical Simulations*, SAE Technical Paper 2011-28-0125, 2011. 24, 25

[73] Lee, K.H., and Lee, C.S., (2003): *Effects of tumble and swirl flows on turbulence scale near top dead centre in a four-valve spark ignition engine*, Proceedings of the Institution of Mechanical Engineers, Part D: Journal of Automobile Engineering, vol. 217. Part D: J. Automobile Engineering, vol. 217, pp. 607-615, 2003. 24

[74] Lee, K., Bae, C., and Kang, K., (2007): *The effects of tumble and swirl flows on flame propagation in a four-valve S.I.engine*, Applied Thermal Engineering 27, pp. 2122-2130, 2007. 24

[75] Murali Krishna B, and Mallikarjuna M J, (2009): *Tumble Flow Analysis in an Unfired Engine Using Particle Image Velocimetry*, World Academy of Science, Engineering and Technology, vol. 54, pp. 430-435, 2009. 24

[76] Sullivan P., Ancimer R., and Wallace J., (1999): *Turbulence averaging within spark ignition engines*, Experimental Fluids, vol. 27, pp. 92-101, 1999. 24

[77] Roudnitzky S., Druault P., and Guibert P., (2006): *Proper orthogonal decomposition of in-cylinder engine flow into mean component, coherent structures and random Gaussian fluctuations*, Journal of Turbulence, vol. 7, pp. 1-19, 2006. 24

[78] Liu, Z., Liu, X., and Zhang, Z., (1999): *Reducing exhaust emissions from an automotive DI diesel engine by means of air injection variable swirl inlet system*, Proceedings of the IEEE International, Vehicle Electronics Conference, 1999. 25

[79] Keromnes, A., Dujol, C., and Guibert, P., (2010): *Aerodynamic control inside an internal combustion engine*, Measurement Science and Technology, vol. 21, pp. 125404-125415, 2010. 25

[80] Adomeit, P., Jakob, M., Pischinger, S., Brunn, A. and Ewald, J., (2011): *Effect of Intake Port Design on the Flow Field Stability of a Gasoline DI Engine*, SAE Technical Paper 2011-01-1284, 2011. 25

[81] Han, Z., and Reitz, R. D., (1995): *Turbulence modeling of internal combustion engines using RNG* $k-\epsilon$ *models* Combustion Science Technology vol. 106, pp. 267-295, 1995. 25

[82] Celik, I., Yavuz, I., and Smirnov, A., (2001): *Large eddy simulations of in-cylinder turbulence for IC-engines: a review*, International Journal of Engine Research, Vol. 2(2), pp. 119-148, 2001. 25

[83] Rutland, C.J., (2011): *Large-eddy simulations for internal combustion engines - a review*, International Journal of Engine Research, vol. 12, pp. 421-431, 2011. 25

[84] Rodi W., (2006): *DNS and LES of some engineering flows*, Fluid Dynamics Research, Vol. 38:(2-3), pp. 145-173, 2006. 25

[85] Temmerman, L., Hadziabdic, H., Leschziner, M. A., and Hanjalic, A., (2005): *A hybrid two-layer URANS-LES approach for large eddy simulation at high Reynolds numbers*, International Journal of Heat Fluid Flow, vol. 26(2), pp. 173-190, 2005. 25

[86] Menter, F. R., and Egorov, Y., (2010): *The scale adaptive simulation method for unsteady flow prediction, Part 1: Theory and model description*, Flow Turbulence and Combustion, vol. 85(1), pp. 139-165, 2010. 25

[87] Janicka, J., and Sadiki, A., (2005): *Large eddy simulation of turbulent combustion system*, Proceedings of Combustion Institute, vol. 30, pp. 537-547, 2005. 25

[88] Apte, S. V., Mahesh, K., and Moin, P., (2009): *Large eddy simulation of evaporating spray in coaxial combuster*, Proceedings of Combustion Institute, vol. 32, pp. 2247-2256, 2009. 25

[89] Nishad K P, and Sadiki A, (2011): *LES and RANS comparison study of atomization process in hollow cone gasoline injector using KIVA-4 code*, ILASS, Europe, Estoril, Portugal, 5-7th Sep., 2011. 25, 100

[90] Nishad K P, Sadiki A, and Janicka J, (2011): *A comprehensive modeling and simulation of gasoline direct injection using KIVA-4 code*, SAE Technical Paper 2011-01-1899 , 2011. 39, 46, 66, 100

[91] Nishad, K.P., Pischke, P., Goryntsev, D., Sadiki, A., and Kneer, R., (2012): *LES based Modeling and Simulation of Spray Dynamics including Gasoline Direct Injection (GDI) Processes using KIVA-4 code,* SAE Technical Paper, 2012-01-1257, , 2012. 25, 100

[92] Nishad, K.P., Sadiki, A., and Janicka, J., (2012): *Large Eddy Simulation of GDI Spray Evolution in a Realistic Engine,* ICLASS 2012, Heidelberg, Germany, 2-6 Sept. 2012. 26

[93] Sone, K., and Menon, S. (2003): *Effect of Sub-grid Modeling on the In-Cylinder Unsteady Mixing Process in a Direct Injection Engine*, Journal of Engineering for Gas Turbine and Power, 2003, vol. 125, pp. 435-443, 2003.

[94] Banerjee, S., Bharadwj, N., and Rutland, C. J., (2009): *Investigation of In-cylinder Mixing Using Large Eddy Simulation Models for LTC Diesel Applications*, ASME IC Engine Div. 2009, Wisconsin, USA.

[95] Torres D., and Trujillo M. (2006): *KIVA-4: An unstructured ALE code for compressible gas flow with sprays*, Journal of Computational Physics, 2006, vol. 21, pp. 943-975, 2006. 26, 41

[96] Senecal P., Schmidt D., Nouar I., Rutland C., Reitz R., and Corradini M. (1999): *Modeling of high speed viscous liquid sheet atomization*, International Journal Multiphase Flow, 1999, vol. 25, pp. 1073-1097, 1999. 21, 38, 45

[97] Dombrowski, N., Johns, W. R., (1963): *The aerodynamic instability and disintegration of viscous liquid sheets*, Chemical Engineering Science, vol. 18, pp. 203-214, 1963. 45

[98] Beale, J. C., and Reitz, R. D., (1999): *Modeling spray atomization with the Kelvin-Helmholtz/Rayleigh-Taylor hybrid model*, Atomization and Sprays, vol. 9, pp. 623-650, 1999. 44, 45

[99] Chaves, H., Knapp, M., Kubitzek, A., and Obermeier, F., (1995): *Experimental study of cavitation in the nozzle hole of diesel injectors Using transparent nozzles*, SAE Paper 950290, 1995.

[100] Soteriou, C., Smith, M., and Andrews, R.J., (1998): *Diesel injection - Laser light sheet illumination of the development of cavitation in orifices*, IMechE Paper C529/018/98, 1998.

[101] Afzal, H., Arcoumanis, C., Gavaises, M., and Kampanis, N., (1999): *Internal flow in diesel injector nozzles: Modeling and experiments*, IMechE Paper S492/S2/99, 1999.

[102] Arcoumanis, C., Badami, M., Flora, H., and Gavaises, M., (2000): *Cavitation in real-size multi-hole diesel injector nozzles*, SAE Paper 2000-01-1249.

[103] Arcoumanis, C., Gavaises, M., Flora, H., and Roth, H., (2001): *Visualization of cavitation in diesel engine injectors* Mecanique & Industries, vol 2(5), pp. 375-381, 2001.

[104] Roth, H., Gavaises, M., and Arcoumanis, C., (2002): *Cavitation initiation, its development and link with flow turbulence in diesel injector nozzles*, SAE Paper 2002-01-0214,

[105] Reitz, R.D., (1993): *Modeling atomization processes in high.pressure vaporizing sprays*, Atomization and Spray Technology, vol. 3, pp. 309-337, 1993. 21

[106] Ibrahim, E. A., Yang, H. Q., and Przekwas, A. J. (1993): *Modeling of spray droplets deformation and breakup*, Journal of Propulsion, vol. 9, pp.651-654, 1993.

[107] Rosa, N.G., Villedieu, P., Dewitte, J:, and Lavergne, G., (2006): *A new droplet-wall interaction model*, Proceedings of the 10th International Conference on Liquid Atomization and Spray System (ICLASS), Tokyo, Japan, 2006. xi, 23, 24

[108] B. Xavier and F. Alain (1997): *Investigation of the in-cylinder tumble motion in a multi valve engine: Effect of piston shape*, SAE Technical Paper 971643.

[109] Arcoumanis, C., Bae, C., and Hu, Z., (1994): *Flow and Combustion in a Four-Valve, Spark-Ignition Optical Engine*, SAE Technical Paper 940475, 1994.

[110] Haworth, D., C., and Jansen, K., (2000): *Large-eddy simulation on unstructured deforming meshes towards reciprocating IC engines*, Computers & Fluids, Vol. 29(5), pp. 493-524,2000. 25

[111] Hess, D., Tag, S., and Brücker, (2012): *Volumetric flow studies in a 4-stroke water-analogue IC-engine using high-speed scanning-PIV*, International Symposium on Applications of Laser Techniques to Fluid Mechanics Lisbon, Portugal, 09-12 July, 2012.

[112] Hasse C, Sohm V, Durst B (2010): *Numerical investigation of cyclic variations in gasoline engines using a hybrid URANS/LES modeling approach*, Computers and Fluids, 39, pp. 25-48, 2010.

[113] Pera, C., Richard, S., and Angelberger, C., (2012): *Exploitation of Multi-Cycle Engine LES to Introduce Physical Perturbations in 1D Engine Models for Reproducing CCV*, SAE Technical Paper 2012-01-0127, 2012.

[114] Keskinen, J., Vuorinen, V., Kaario, O., and Larmi, M., (2012): *"Large Eddy Simulation of the Intake Flow in a Realistic Single Cylinder Configuration*, SAE Technical Paper 2012-01-0137, 2012.

[115] Pera, C. and Angelberger, C., (2011): *Large Eddy Simulation of a Motored Single-Cylinder Engine Using System Simulation to Define Boundary Conditions: Methodology and Validation*, SAE International Journal of Engines 4(1), pp. 948-963, 2011.

[116] Lacour PhD, C. and Pera, C., "An Experimental Database Dedicated to the Study and Modeling of Cyclic Variability in Spark-Ignition Engines with LES," SAE Technical Paper 2011-01-1282, 2011,

[117] Laget, O., Reveille, B., Martinez, L., Truffin, K., Habchi C., and Angelberger, C., (2011): *LES Calculations of a Four Cylinder Engine*, SAE Technical Paper 2011-01-0832, 2011.

[118] Liu, K. and Haworth, D., "Development and Assessment of POD for Analysis of Turbulent Flow in Piston Engines," SAE Technical Paper 2011-01-0830, 2011

[119] Bird, G.A., (1994): *Molecular gas dynamics and the direct simulation of gas flows*, Oxford University Press, 1994.

[120] Reynolds O., (1984): *On the dynamical theory of incompressible viscous flows and the determination of the criterion*, Philosophical Transaction of Royal Society, QA 186, 123-164, 1894. 27, 29

[121] Schlichting, H., (1979): *Boundary Layer Theory*, McGraw-Hill, New York, 1979. 28

[122] Bradshaw P., (1976): *An Introduction to turbulence and its measurement*, Pergamon Press, London, 1976. 28

[123] Pope, S.B, (2000): *Turbulent flows*, Cambridge University Press, Cambridge, 2000. 28, 29, 33

[124] Kolmogorov, A.N., (1941): *The local structure of turbulence in incompressible viscous fluids for very large Reynolds numbers*. C. r. Acad. Sci USSR, 30, 301-305, in Russian, 1941. 28

[125] Kolmogorov, A.N., (1941): *Dissipation of energy in locally isotropic turbulence*, C. r. Acad. Sci USSR, 32, 19-21, in Russian, 1941. 28

[126] Shah P., and Markatos, N.C., (1987):*Computer-simulation of turbulence in internal-combustion engines*, International Journal for Numerical Methods in Fluids, Vol. 7(9), pp. 927-952, 1987. 29

[127] Yavuz, I., (2000):*Refined turbulence models for simulation of IC engine cylinder flows*, Dissertation, Mechanical and Aerospace Engineering Department, West Virginia University, 2000. 29

[128] Hoffmann, G., (1995):*Engineering application of large eddy simulation to turbulent free and wall-bounded shear layers*, Von Karman Institute for Fluid Dynamics, 1995. 33, 34, 35

[129] Smagorinsky, J.S., (1963): *General circulation experiments with the primitive equations, 1. The Basic Experiment*, Monthly Weather Review, Vol. 91(3), pp. 99-164, 1963. 34

[130] Germano, M., Poimelli, U., Moin, P., and Cabot, W.H., (1991): *A dynamic subgrid-scale eddy viscosity model*, Physics of Fluid, Vol. 3(7), pp. 1760-1765, 1991. 35

[131] Patankar, S.V., (1980): *Numerical heat transfer and fluid flow* Hemisphere Publication Corporation, Waschington D.C., 1980.

[132] Williams, F.A., (1958): *Spray Combustion and Atomization*, Physics of Fluids, Vol. 1, pp. 541-545, 1958. 36

[133] Gupta, H. C., Bracco, F. V., (1978): *Numerical computations of two-dimensional unsteady sprays for application to engines*, AIAA Journal, vol. 16, pp. 1053-1061, 1978. 36

[134] Schneider, L., (2009): *A concise moment method for the unsteady poly-dispersed sprays*, PhD. Thesis, Department of Mechanical Engineering, Technical University Darmstadt, Germany, 2009. 37

[135] Schneider, L., LeLostec, N., Villedieu, P., and Sadiki, A., (2010): *A moment method for splashing and evaporation processes of polydisperse sprays*, International Journal of Multiphase Flow, vol. 36, pp. 261-272, 2010. 37

[136] Nishad, K.P., Schneider, L., and Sadiki, A., (2010): *Eulerian Multi-fluid Method for Spray and Wall Interaction*, International Conference on Multiphase Flow, ICMF-2010, Tampa, FL, May 30- June 4, 2010. 37

[137] Dukowicz, J.K., (1980): *A particle-fluid numerical model for liquid sprays* Journal Computational Physics, vol. 35: 229, 1980. 37, 38

[138] Reitz, R., (1996):*Computer modeling of spray*, Spray Technology: Short cource,Pittsburgh, PA, May 7, 1996 xi, 37

[139] Mundo, C., Sommerfeld, M, and Tropea, C., (1995): *Droplet-wall collisions: experimental studies of the deformation and break-up process*, International Journal of Multiphase Flow, 21(2), pp. 151-173, 1995. 50

[140] Marengo, M., Sikalo, S., and Tropea, C., (1998): *Impact of drops on inclined dry surfaces*, Proceedings of ILASS Europe Manchester (United Kingdom) 1998. 51

[141] Sick V., Ruess D., Rutland C., Haworth D., Janicka J., Oefeleln J., Kuo T. W., Yang X., Freitag M., (2010): *A Common Engine Platform for Engine LES Development and Validation*, IFP-LES, Nouvelles, Rueil-Malmaison, France, Nov. 18-19, 2010. xii, xiii, 56, 75, 78, 79

Publications

Journals/Conferences

D Goryntsev, K P Nishad, A Sadiki, and J Janicka, *Application of LES for Aanalysis of Unsteady Effects on Spray Combustion and Misfires in DISI Engine,* Oil & Gas Science and Technology - Revue d'IFP Energies Nouvelles (accepted), 2013.

K P Nishad, A Sadiki, and J Janicka, *Large Eddy Simulation of GDI Spray Evolution in a Realistic Engine,* ICLASS 2012, Heidelberg, Germany, 2-6 Sept. 2012.

K P Nishad, P Pischke, D Goryntsev, A Sadiki, and R Kneer, *LES based Modelling and Simulation of Spray Dynamics including Gasoline Direct Injection (GDI) Processes using KIVA-4 code,* SAE Paper, 2012-01-1257, , 2012.

K P Nishad; A Sadiki and J Janicka, *A comprehensive Modeling and Simulation of Gasoline Direct Injection using KIVA-4 Code,* SAE Paper 2011-01-1899 , 2011.

K P Nishad; A Sadiki, *LES and RANS Comparison Study of Atomization Process in Hollow Cone Gasoline Injector using KIVA-4 Code,* ILASS, Europe, Estoril, Portugal, 5-7th Sep., 2011.

K P Nishad, and A Sadiki, *Numerical Analysis of High Speed Fuel Spray Breakup in Automobile Applications,* SPRAY 2010. 9th Workshop über Sprays, Techniken der Fluidzerstäubung und Untersuchung von Sprühvorgängen, 3-5th May 2010, Heidelberg, Germany, 2010.

K P Nishad, L Schneider, and A Sadiki, *Eulerian Multi-fluid Method for Spray and Wall Interaction,* 7th International Conference on Multiphase Flow, ICMF 2010, Tampa, FL, May 30-June 4, 2010, 2010.

K P Nishad, L Zealouk, and A Sadiki, *Comparison of 2D and 3D Modeling of Mold Filling of Aluminum Casting ,* 7th International Conference on Multiphase Flow, ICMF 2010, Tampa, FL, May 30-June 4, 2010, 2010.

K P Nishad, L Schneider, A Sadiki, and J Janicka, *Investigation of Interaction of Spray with Heated Wall using New Eulerian Multi-fluid Method,* International Workshop on Near-Wall Reactive Flows , 18-19th Nov 2010, Seeheim-Jugenheim, Darmstadt, Germany, 2010.

K P Nishad, U Agrawal , R Pardeshi, and A K Singh, *Influence of Bag Design on Flow, and Thermal Parameters in DC Casting,* International Symposium on Energy Related Materials, November 13-16, 2007, Mumbai, India., 2007.

V H Arakeri, and K P Nishad, *Influence of Argon Gas Content on Intensity of Multi-Bubble Sonoluminescence,* 2006, 11th Asian Congress of Fluid Mechanics, 22-25 May 2006, Kuala Lumpur, Malaysia.

K P Nishad, and A K Singh, *Modeling of Mold Filling of Aluminum Casting (keynote)* Advanced Processing of Metals and Materials: Volume 4: 263-270, New, Improved and Existing Technologies: Nonferrous Materials Extraction and Processing: TMS-ISBN: 978-0-87339-637-0, in: F. Kongoli; R.G. Reddy (ed.): Advanced Processing of Metals and Materials: Volume 4: New, Improved and Existing Technologies: Nonferrous Materials Extraction and Processing, ISBN: 978-0-87339-637-0. edition, TMS, 2006, pp. 263-270.

K P Nishad, and A K Singh, *Modeling of Gas Entrainment During Mold Filling,* International Symposium on Steels for Automotives, Indian Institute of Metals (IIM), NMD-ATM 2006, 13th-16th Nov 2006, Jamshedpur, India., 2006.

K P Nishad, (Advisor: Prof. V H Arakeri) *Influence of Noble Gas Doping in Multi-bubble Sonoluminescence,* ME Thesis, Department of Mechanical Engineering, Indian Institute of Science, Bangalore, India, 2005.

Curriculum Vitae

Name	Kaushal Prasad Nishad	
Birthdate	01.01.1980	
Birthplace	Akoli (Durg), Chhattisgarh, India	
Highschool	07/1993- 06/1995	Janata Higher Secondary School, Bhimbhouri, Durg, CG, INDIA High school certificate
Highschool	07/1995 - 06/1997	Janata Higher Secondary School, Bhimbhouri, Durg, CG, INDIA Higher secondary school certificate
Diploma	07/1997 - 06/2000	M. P. Board of Technical Education, Bhopal, MP, INDIA Diploma in Mechanical Engineering
Bachelor	07/2000 - 06/2003	Pt. Ravishankar Shukla University Raipur, CG, INDIA Bachelor in Mechanical Engineering
Master	07/2003 - 06/2005	Department of Mechanical Engineering, Indian Institute of Science, Bangalore, INDIA Master in Mechanical Engineering
Employer	07/2005 - 01/2009	Tata Research Development & Design Centre, Pune, INDIA an innovation lab of Tata Consultancy Services (TCS)
Employer	02/2009 - present	Technische Universität Darmstadt at the department of Energy and Power Plant Technology (EKT) Prof. Dr.-Ing. Johannes Janicka